



Politechnika Wroclawska



POLITECHNIKA WROCLAWSKA
WYDZIAŁ PODSTAWOWYCH
PROBLEMÓW TECHNIKI
KATEDRA OPTYKI I FOTONIKI

UNIVERSITÉ
BOURGOGNE-FRANCHE-COMTÉ
LABORATOIRE INTERDISCIPLINAIRE
CARNOT DE BOURGOGNE

Field of science: natural sciences

Discipline of science: physical sciences

Doctoral dissertation in Physics

Experimental investigation of spatiotemporal nonlinear phenomena in multimode optical fibers

Karolina Stefańska

supervised by:

dr hab. inż. Karol Tarnowski *and* dr hab. Bertrand Kibler

Wrocław & Dijon, 2024

Maćkowi

*Science is not a collection of firmly established truths.
It is a continuing exploration of mysteries.*

— Freeman John Dyson

I would like to express my deepest appreciation to Bertrand Kibler and Karol Tarnowski, for your guidance and immense support during the past few years. Your insightful feedback, patience, and encouragement have been crucial in shaping this dissertation and my growth.

I am grateful for the opportunity to work under your mentorship.

I am also extremely grateful to Pierre B ejot and Tadeusz Martynkien, for your invaluable assistance that contributed significantly to the successful completion of this research. Thank you for your time, insights, and guidance.

I would like to acknowledge my defense committee, for dedicating time and effort to evaluating my work.

Sincere thanks go to all the members of the Fiber Optics Group at WUST and Laboratoire Interdisciplinaire Carnot de Bourgogne in Dijon. It has been a pleasure to work with you all, especially Kasia, Manon, Killian, Alex, Anastasiia, Alix, Erwan, Mo ise, Edyta, Marta, Grzesiek, Magda, Rafa l, and Kinga.

I am especially grateful to my Mom, Dad, and Brother for continuous encouragement and always believing in me. Finally, Maciek, thank you for unwavering support and understanding.

The research in the thesis was funded by:

- Bourses du Gouvernement Français – Doctorat cotutelle fellowship, Campus France;
- Polish National Science Centre, project Sonata Bis (2018/30/E/ST7/00862);
- InterDocSchool project co-financed by Polish National Agency for Academic Exchange NAWA within the STER Programme “Internationalisation of doctoral schools”;
- French-Polish Polonium Hubert Curien Partnership co-financed by Polish National Agency for Academic Exchange NAWA (PPN/BIL/2022/1/00017 and PPN/BIL/2018/1/00021), French Ministry for Europe and Foreign Affairs, and French Ministry for Higher Education and Research;
- Erasmus+ EU funds;
- French programs “Investments for the Future” operated by the National Research Agency (EIPHI Graduate School, contract ANR-17-EURE-0002; EQUIPEX+ Smartlight, contract ANR-21-ESRE-0040).



Eksperymentalne badania czasowo-przestrzennych zjawisk nieliniowych w światłowodach wielomodowych

Słowa kluczowe: wielomodowe światłowody, nieliniowa optyka światłowodowa, mieszanie czterech fal, pułapkowanie solitonów, dyskretna emisja stożkowa, światłowód gradientowy, światłowód typu step-index, światłowód fotoniczny, czasowo-przestrzenne pakiety falowe

Streszczenie: Praca doktorska poświęcona jest eksperymentalnej charakterystyce nieliniowych zjawisk zachodzących w światłowodach wielomodowych. Hipoteza badawcza streszcza się w pytaniu, w jaki sposób i w jakim stopniu dynamika zjawisk nieliniowych o skorelowanych cechach czasowych i przestrzennych może być kontrolowana przez kształtowanie właściwości światła wprowadzanego do światłowodu. Rozprawa zaczyna się od ogólnej prezentacji światłowodów wielomodowych wraz z charakteryzującymi je parametrami używanymi do opisu badanych zjawisk nieliniowych. Wyniki w pracy są przedstawione według rosnącej liczby oddziałujących modów. W pierwszej kolejności badane są dwójłomne włókna mikrostrukturalne prowadzące dwa mody polaryzacyjne. W szczególności analizowana jest konwersja polaryzacji i zjawisko pułapkowania impulsów w związku z dwójłomnością grupową i ortogonalnym rozpraszaniem Ramana. Następnie badana jest nieliniowa konwersja częstotliwości do dalekich zakresów spektralnych zachodząca przez procesy mieszania czterech fal wewnątrz- i międzymodowego w kilkumodowym włóknie gradientowym. Jako ostatnia analizowana jest nieliniowa propagacja ultrakrótkich, intensywnych impulsów w wielomodowym światłowodzie o skokowym profilu współczynnika załamania. Uzyskane wyniki dowodzą spontanicznej emisji dyskretnej fali stożkowej, którą można opisać jako quasi-niezmienniczy czasowo-przestrzenny pakiet falowy. Pomimo że w rozważanych systemach dominują różnego typu czasowo-przestrzenne nieliniowe efekty, to składowe spektralne, przestrzenne i czasowe światła wychodzącego ze światłowodu mogą być deterministycznie kontrolowane przez kompozycję modową pola wejściowego. Uzyskane wyniki przyczyniają się do fundamentalnego zrozumienia zjawisk nieliniowych w wielomodowych światłowodach i wskazują drogę do sposobów kontrolowania nowych strukturyzowanych wiązek światła, które mogą prowadzić do ekscytujących nowych kierunków badań i zastosowań.

Experimental investigation of spatiotemporal nonlinear phenomena in multimode optical fibers

Keywords: multimode optical fibers, nonlinear fiber optics, four-wave mixing, soliton trapping, discretized conical emission, graded-index fiber, step-index fiber, photonic crystal fiber, space-time wavepackets

Abstract: This thesis work is devoted to the experimental characterization of nonlinear phenomena taking place in multimode optical fibers. The research hypothesis concerns how the dynamics of nonlinear phenomena with correlated spatial and temporal features can be governed by the input light properties. The dissertation begins with a general presentation of multimode optical fibers, and their parameters used to describe the nonlinear effects under study. The results and chapters are presented according to the increasing number of optical modes involved. The case of birefringent microstructured fibers supporting two polarization modes is studied first. In particular, pulse trapping and polarization conversion phenomena are analyzed through fiber group birefringence and orthogonal Raman scattering. Secondly, far-detuned nonlinear frequency conversion is investigated through intramodal and intermodal four-wave mixing processes in a few-mode graded-index fiber. Thirdly, the nonlinear propagation of ultrashort, intense pulses in a step-index multimode fiber highlights the spontaneous emission of discretized conical waves, which can be described as quasi-invariant space-time wave packets. Although distinct spatiotemporal nonlinear phenomena are involved in the systems considered, the spectral, spatial and temporal components of the output light are deterministically controlled by the modal composition of the input optical field. The obtained results contribute to the fundamental understanding of nonlinear phenomena in multimode optical fibers and pave the way for the control of new structured light states that could lead to exciting new research directions and applications.

Etude expérimentale de phénomènes non-linéaires spatiotemporels dans les fibres optiques multimodes

Mots clés: fibres optiques multimodes, optique non-linéaire fibrée, mélange à quatre-ondes, piégeage de solitons, émission conique discrète, fibre à gradient d'indice, fibre à saut d'indice, fibre microstructurée, paquets d'ondes spatiotemporels

Résumé: Ce travail de thèse est consacré à la caractérisation expérimentale de phénomènes non-linéaires se produisant dans les fibres optiques multimodes. L'hypothèse de recherche concerne la manière dont la dynamique des phénomènes non-linéaires avec des caractéristiques spatiales et temporelles corrélées peut être régie par les propriétés de la lumière en entrée de fibre. La thèse commence par la présentation générale des fibres optiques multimodes et de leurs paramètres utilisés pour décrire les effets non-linéaires étudiés. Les résultats et chapitres sont présentés en fonction du nombre croissant de modes optiques mis en jeu. Le cas de fibres microstructurées biréfringentes supportant deux modes de polarisation est d'abord étudié. En particulier, les phénomènes de piégeage d'impulsions et de conversion de la polarisation sont analysés à travers la biréfringence de groupe de la fibre et la diffusion Raman orthogonale. Deuxièmement, la conversion non-linéaire de fréquences ultra-décalées est étudiée par le biais de processus de mélange à quatre-ondes intra-modaux et intermodaux dans une fibre à gradient d'indice à quelques modes. Troisièmement, la propagation non-linéaire d'impulsions ultracourtes et intenses dans une fibre multimode à saut d'indice met en évidence l'émission spontanée d'ondes coniques discrètes, qui peuvent être décrites comme des paquets d'ondes spatio-temporels quasi-invariants. Bien que des phénomènes non-linéaires spatio-temporels distincts soient impliqués dans les systèmes considérés, les composantes spectrales, spatiales et temporelles de la lumière émise sont contrôlées de manière déterministe par la composition modale du champ optique d'entrée. Les résultats obtenus contribuent à la compréhension fondamentale des phénomènes non-linéaires dans les fibres optiques multimodes et ouvrent la voie au contrôle de nouveaux états de lumière structurée pouvant conduire à de nouvelles directions de recherche et des applications passionnantes.

Contents

1	Introduction	1
2	Light coupling and propagation in multimode fibers	5
2.1	Multimode optical fibers	5
2.1.1	Step-index fibers	6
2.1.2	Graded-index fibers	7
2.1.3	Photonic crystal fibers	8
2.2	Fiber modes and free space coupling	9
2.2.1	LP modes	10
2.2.2	Optimization of the launch system to excite the LP _{0,1} mode	13
2.2.3	Shaping the beam to excite OAM modes	16
2.2.4	Excitation of OAM modes	17
2.3	Linear properties and phenomena	20
2.3.1	Propagation constant and effective refractive index	20
2.3.2	Group refractive index	21
2.3.3	Dispersion	23
2.3.4	Birefringence	25
2.3.5	Attenuation	27
2.4	Nonlinear properties and phenomena	28
2.4.1	Effective mode area	29
2.4.2	Nonlinear parameter gamma	29
2.4.3	Nonlinear refractive index	30
2.4.4	Self-phase modulation	30
2.4.5	Formation of solitons	31
2.4.6	Self-focusing	31
2.4.7	Cross-phase modulation	31
2.4.8	Four-wave mixing	32
2.4.9	Modulation instability	33
2.4.10	Raman scattering	34
3	Soliton trapping in birefringent photonic crystal fibers	37
3.1	Study conditions	39
3.2	Energy conversion for pump pulses polarized along fiber axis	42
3.2.1	Investigation for increasing pump power	42
3.2.2	Investigation along the propagation distance	46
3.3	Energy conversion for other polarization azimuths of pump pulses	50
3.4	Soliton positions, group velocity matching, and Raman gain	54
3.5	Conclusions	57

4	High gain far-detuned four wave mixing in a graded-index fiber	59
4.1	Remarks on theoretical analysis of FWM processes in GRIN fibers	61
4.2	Study conditions	68
4.2.1	Fiber properties	68
4.2.2	Experimental setup	70
4.3	Intramodal four wave mixing study	70
4.4	Intermodal four wave mixing study	74
4.5	FWM in other fiber designs	77
4.6	Conclusions	82
5	Spatiotemporal wavepackets in a multimode step-index fiber	83
5.1	Theoretical description of ST wavepackets	84
5.2	Study conditions	88
5.3	Conical emission in bulk media	91
5.4	Discretized conical emission in a multimode fiber	95
5.5	Helicon wavepackets in multimode fiber	103
5.6	Conclusions	109
6	Conclusions and perspectives	111
	Bibliography	115
	List of Figures	133
A	Academic achievements	141

Chapter 1

Introduction

The field of nonlinear optics was opened with Theodore Maiman's invention of laser in 1960 [1]. This breakthrough allowed to produce optical fields with intensities that rival those of the atomic electric field, enabling displacing the electric charges. Consequently, a high-intensity laser light alters the properties of the medium in which it travels, thereby affecting its own propagation and, for instance, resulting in generation of new spectral components. In the wake of the laser's invention, numerous nonlinear processes were observed in bulk media for the first time during the 1960s, beginning with the demonstration of the second harmonic generation of light at 347 nm from a ruby laser beam with a wavelength of 694 nm focused into a quartz sample [2].

Simultaneously, the field of optical fibers developed rapidly, initially for the purpose of transmitting images through bundles of glass fibers [3]. Following pivotal studies that suggested the possibility of drastically reducing fiber losses [4, 5, 6], optical fibers brought a revolution in the field of telecommunication [7], leading to Charles Kao being awarded the Nobel Prize in Physics in 2009 for "groundbreaking achievements concerning the transmission of light in fibers for optical communication".

At the intersection of nonlinear optics and fiber optics, the new field of nonlinear fiber optics emerged [8, 9]. The optical fibers turned out to be an excellent platform for exploring nonlinear phenomena, since the guided light is confined in a small area and the propagation distances are very large, resulting in significant nonlinearity even at relatively low pulse powers. In the following years, various nonlinear processes were observed in optical fibers: stimulated Raman emission [10], optical Kerr effect [11], parametric wave mixing processes [12, 13, 14], self-phase modulation [15], and formation of optical solitons [16]. With advancements in fabrication technology facilitating the production of single-mode fibers (SMF) and their structural simplicity that proved extremely advantageous in 1980s for telecommunication applications [17, 18], the majority of the conducted research concentrated on the nonlinear phenomena in single-mode fibers, and the nonlinear properties of multimode fibers (MMF) have remained largely unexplored.

However, starting from 2010 the nonlinear effects in MMF receive a substantial renewed attention [19, 20]. This is driven by promising applications that surpass the possibilities of single-mode fibers, including space-division multiplexing in telecommunication systems [21, 22], high-power lasers [23] and high-resolution biomedical imaging [24]. At the same time, multimode optical fibers support a rich variety of coupled spatial and temporal phenomena that are extremely interesting to study from the fundamental point of view. In present days, thanks to innovative characterization techniques, improved light sources, and better computing power to support experimental observations with numerical modeling, this subject has become a central

issue in the field of nonlinear fiber optics [25].

Multimode fibers offer a natural platform to bridge the gap between the nonlinear phenomena that have been examined over the past 50 years in both single-mode fibers and bulk media. Each of those types of structures is distinct in terms of the way it guides light. Single-mode fibers support only one spatial mode, whereas bulks support a dense and infinite number of modes. A continuous mode structure in bulks enables investigation of fascinating space-time correlations during nonlinear pulse propagation. As multimode fibers support a discretized mode structure, it is very interesting to explore how the spatiotemporal dynamics can be transposed from each of the two limiting cases, namely a single discrete mode in SMF, and a continuous set of modes in bulk.

Very recently, spatiotemporal pulse dynamics in multimode fibers have led to exciting observations of qualitatively new phenomena, such as spatial beam self-cleaning that reshapes the transverse spatial beam pattern at the fiber output via the nonlinearity [26, 27, 28] and multimode solitons [29, 30, 19], in which nonlinearity balances both chromatic dispersion and modal dispersion. However, further research is still necessary to reach a complete understanding of the complex interactions of light between multiple fiber modes.

For example, extensive studies on optical solitons in SMF are driven by their ability to maintain the pulse shape during propagation due to an interplay between dispersive and nonlinear effects. The possibility of avoiding temporal broadening of pulses transmitted over the distances of thousands of kilometers has profound implications for modern high-speed high-capacity telecommunication systems [18]. Such as conventional single-mode solitons play a key role in understanding pulse temporal dynamics in single-mode fibers, multimode solitons might provide an intuitive tool to understand the pulse spatiotemporal dynamics in multimode systems. Recent studies indicate that nonlinear couplings between many modes of MMF can mitigate the issue of intermodal dispersion, leading to formation of synchronized, non-dispersive pulses in multiple spatial modes [29, 31]. Nevertheless, many aspects of the behavior and properties of multimode solitons remain unexplored. By examining simpler structures, such as bimodal solitons, we can gain a perspective on the underlying principles and dynamics that govern multimode solitons in more complex systems.

From another perspective, it is interesting to consider the spatiotemporal dynamics of light in MMF as the pulse power approaches the critical threshold for self-focusing [32]. In bulk media, the transverse size of the beam at high intensities can progressively reduce during propagation due to the Kerr effect overcoming diffraction [33]. Self-focusing has been extensively studied in bulk materials such as glasses, liquids, and gases [34, 35, 36] for its capability to counteract diffraction, which could result in diffraction-free optical beams that maintain shape during propagation [37, 38]. Such ultrafast pulses with a localized transverse profile are termed light bullets: stable pulses that are confined in both time and space. Nonlinear light couplings in MMF could lead to Kerr nonlinearity balancing both chromatic dispersion and diffraction at the same time. Light bullets in fibers remain experimentally unexplored despite focused efforts. Besides their fundamental appeal, they hold potential for use as complex data bits in high-capacity telecommunication and data processing systems.

Finally, frequency conversion processes have been explored in both SMF and bulks.

However, various modes of MMF offer more degrees of freedom in enabling phase-matching of nonlinear wave-mixing processes. After several experimental studies of intermodal four-wave mixing at the onset of nonlinear fiber optics [12, 13, 14, 39], this subject reemerged around 2010 [40, 41] and has remained in the center of interest from that time, in particular for generating a broadband supercontinuum through a series of cascaded intermodal four-wave mixing processes [42, 43, 44, 45, 46]. Highly-multimode graded index fibers are particularly interesting in this context, as their relatively low intermodal dispersion can lead to formation of a broad supercontinuum through the phenomenon known as geometric parametric instability, characterized by the presence of a series of distinct spectral peaks [47, 48, 49, 50]. Its analytical description is based on a simplified picture of degenerated mode groups in graded-index fibers. Nevertheless, deeper analyses are still required to provide a complete overview of the potential of multimode interactions.

Such nonlinear intermodal interactions have the potential to shape the spatiotemporal spectrum in relatively simple experimental configurations. This could provide a welcome alternative to a more complex experimental approach of engineering the desired three-dimensional ST pulse structure through a coherent wave shaping combined with linear spatial mode multiplexing. The primary focus of this dissertation is the experimental investigation of novel spatiotemporal nonlinear effects in multimode fibers. I aim to show that *spectral, spatial, and temporal dynamics of nonlinear phenomena can be controlled through the modal composition of the excited field by managing the polarization, spatial distribution, and phase profile of the input optical field in a conceptually simple experimental arrangement.*

The research hypothesis is evaluated by detailed studies of pulse trapping by soliton in birefringent photonic crystal fibers, intramodal and intermodal four-wave mixing in a graded-index fiber, and discretized conical emission and generation of helicon wavepackets in a highly multimode step-index fiber. The choice of each subsequent investigated topic is driven by the potential to explore more complex interactions resulting from the increasing number of interacting modes. Initially I study birefringent photonic crystal fibers that support two polarization modes. This is followed by investigation of a few-mode graded-index fiber. In the end I explore the nonlinear dynamics in a highly multimode step-index fiber.

This dissertation is organized as follows. Chapter 2 describes fundamental principles governing both linear and nonlinear regimes of light propagation in different modes of optical fibers. The introduced concepts are illustrated with experimentally and numerically characterized properties of the fibers that are used for the subsequent investigations of nonlinear processes. Chapters 3-5 contain the results of my studies on spatiotemporal nonlinear effects. Chapter 3 presents the experimental investigation of pulse trapping in two birefringent photonic crystal fibers characterized by different magnitudes of group birefringence. The polarization conversion phenomena I study result from the fiber group birefringence and orthogonal Raman scattering of the pump pulse. Chapter 4 provides the theoretical predictions and experimental characterizations of intramodal and intermodal four-wave mixing processes in a few-mode graded-index fiber. I reveal the potential to obtain high-gain frequency conversion with far-detuned peaks whose spectral position is determined by the fiber dispersion. Chapter 5 contains the experimental confirmation and detailed study of spontaneous emission of a discretized

conical wave in a step-index multimode fiber, as well as preliminary results of the experimental study of the formation of helicon wavepackets.

The doctoral thesis has been realized under the international cotutelle scheme. The research work was carried out alternately at the Wrocław University of Science and Technology (WUST) and at the University Bourgogne-Franche-Comté (UBFC). During the three academic years 2021/2022 - 2023/2024 I spent 4 months each year at UBFC.

Selected findings discussed in this dissertation have been published in three peer-reviewed journal articles:

- [K. Stefańska](#), P. Béjot, J. Fatome, G. Millot, K. Tarnowski, B. Kibler, *High-gain far-detuned nonlinear frequency conversion in a few-mode graded-index optical fiber*, Scientific Reports, 2024, 10.1038/s41598-024-65873-w;
- [K. Stefańska](#), P. Béjot, K. Tarnowski, B. Kibler, *Experimental observation of the spontaneous emission of a space-time wavepacket in a multimode optical fiber*, ACS Photonics, vol. 10, 3, 2023, 10.1021/acsp Photonics.2c01863;
- [K. Stefańska](#), S. Majchrowska, K. Gemza, G. Soboń, J. Sotor, P. Mergo, K. Tarnowski, T. Martynkien, *Soliton trapping and orthogonal Raman scattering in a birefringent photonic crystal fiber*, Optics Letters, vol. 47, 16, 2022, 10.1364/OL.463643.

Additionally, I have contributed as the presenting author to 6 international conferences (1 poster, 6 oral presentations, including one invited), with one more oral presentation scheduled for September 02-06, 2024, as well as 2 workshops and 3 schools (1 presentation and 5 posters). A detailed list of all scientific contributions made during the PhD thesis can be found in the Appendix at the end of the dissertation.

Chapter 2

Light coupling and propagation in multimode fibers

Conventional optical fibers guide light by the phenomenon of total internal reflection (TIR), which was first demonstrated in the *light fountain* experiment of Jean-Daniel Colladon [51] and described by John Tyndall [52] in the nineteenth century. When light arrives at the interface from one medium with a higher refractive index to another medium with a lower refractive index, it can be fully reflected back into the first medium if the incidence angle is sufficiently large. A dominating material used in fiber optics due to its robustness is fused silica. It is characterized by a number of favorable properties: broad spectral region of optical transparency [53, 54], superior resistance to mechanical stresses such as pulling and bending compared to other optical glasses [55, 56, 57, 58], high damage threshold against laser-induced breakdown [59, 60, 61, 62], and possibility of doping with other materials to achieve efficient light guidance and improve various properties. In particular, certain dopants are used to increase the refractive index in the core, such as germania [63] or alumina [64], and others, like fluorine, are used to decrease the refractive index in the cladding [65]. The contrast of refractive index is essential in achieving TIR of light within the fiber on its core-cladding boundary instead of on its outer surface, which was first proposed by Abraham van Heel in 1954 [66] and proved to be highly beneficial in reducing the losses and in preserving a high quality of the light beam.

If the difference between the refractive index of fiber core and cladding is sufficiently high, or the core area is large enough, the fiber becomes multimode. Multimode fiber supports multiple transverse guided modes for a given wavelength. Each of them is characterized by a certain set of properties, such as: transverse amplitude profile of electric field distribution, effective refractive index, propagation constant, and optical losses. In this chapter, I discuss different types of multimode optical fibers, their fundamental linear and nonlinear properties that give rise to distinct phenomena, and the mode structure of multimode fibers.

2.1 Multimode optical fibers

Multimode fibers with a single core can be divided into two main categories: step-index fibers and graded-index fibers. In step-index fibers, a glass core with constant refractive index n_0 is surrounded by a cladding layer with constant refractive index $n_{cl} < n_0$. In graded-index fibers, the refractive index value decreases gradually from the center of the core to its boundary with cladding. Various special designs of fibers have been developed to enhance their properties making them particularly useful for specific applications [67, 68, 69, 70]. In the following,

besides describing step-index and graded-index fibers, I also focus on one particular specialty fiber design: microstructured fibers, also referred to as photonic crystal fibers. In the later chapters, I study different nonlinear phenomena in the three introduced fiber types, therefore it is essential to comprehend their distinct design features to understand how it affects their unique properties.

2.1.1 Step-index fibers

A step profile of refractive index is the most basic design of a fiber. Figure 2.1 provides a schematic illustration of this refractive index profile. Fiber core with a radius R is made of a material with refractive index n_0 . Fiber cladding is made of a material with slightly lower refractive index n_{cl} . To ensure compatibility with various fiber connectors and components, the cladding radius R_{cl} is typically equal to $62.5 \mu\text{m}$.

The photograph of the crosssection of the step-index (SI) fiber which I use in the later investigations is displayed on the right side of Fig. 2.1. This fiber has a large silica core with $R = 52.5 \mu\text{m}$, and a fluorine-doped glass cladding.

The contrast of refractive index between the fiber core and cladding is often characterized by the relative index difference:

$$\Delta = \frac{n_0^2 - n_{cl}^2}{2n_0^2}. \quad (2.1)$$

Another very useful parameter in assessing fiber properties is V number defined as:

$$V = k \cdot R \cdot \text{NA} = k \cdot R \cdot \sqrt{n_0^2 - n_{cl}^2}, \quad (2.2)$$

where $k = 2\pi/\lambda$, λ is the wavelength in vacuum, and NA is the numerical aperture. V number is a dimensionless normalized optical frequency. It determines the number of modes supported by the fiber. If $V < 2.405$, fiber supports only a single mode (two modes when polarization degeneracy is included). For larger values, fibers supports higher-order modes as well. When the number of modes is large, it can be estimated as:

$$M \approx V^2/2, \quad (2.3)$$

if modes are accounted for both polarization directions [71]. The step-index fiber used in my investigations is characterized by the following parameters provided by its manufacturer

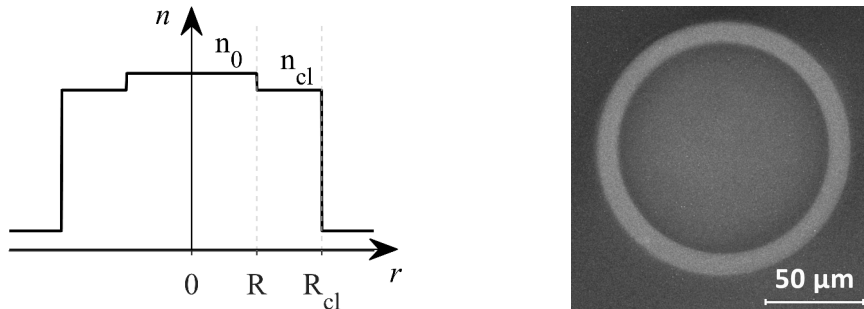


Figure 2.1: Schematic illustration of refractive index profile of a step-index fiber and a photograph of the fiber used in later experiments.

(Thorlabs, fiber FG105LCA): $R = 52.5 \mu\text{m}$ and $\text{NA} = 0.22$. I therefore estimate that it supports over 2450 modes at the pump laser wavelength 1035 nm. The provided formula indicates that fibers support more modes as the wavelength decreases, as M shows inverse quadratic dependence on λ . For example, the investigated fiber supports propagation of over ten thousand different modes at $\lambda = 500 \text{ nm}$.

2.1.2 Graded-index fibers

The refractive index of graded-index (GRIN) fiber decreases radially inside the core of radius R from the value n_0 at the core center to the cladding refractive index n_{cl} [72]. The refractive index profile, illustrated schematically in Fig. 2.2, is given by:

$$n^2(r) = n_0^2 \left[1 - 2\Delta \left(\frac{r}{R} \right)^\alpha \right], \quad (2.4)$$

where $\alpha \approx 2$ is a typically assumed near parabolic index profile in the core ($r \leq R$) [73], and $\alpha = 0$ is a flat index profile in the cladding ($R < r \leq R_{\text{cl}}$). The near parabolic shape of the core refractive index profile is due to the typical near parabolic germanium doping concentration [74]. Remarkably, such profile of refractive index results in an almost equal distribution of effective refractive indices of the guided modes. In this case, all modes propagate with (approximately) the same group velocity, and the intermodal dispersion is much smaller than in other designs of multimode fibers [74].

The refractive index profile of the GRIN fiber which I use in the later investigations can be approximated with the following parameters: a core radius $R = 8 \mu\text{m}$ with a parabolic index profile, a 5 mol% Ge doping in the core center, and a pure silica cladding. In addition, this profile features a region of depressed index, called trench, which is doped with fluorine at ($10 \mu\text{m} < r < 15 \mu\text{m}$). The photograph of the fiber's cross-section is displayed on the right side of Fig. 2.2, and the measured refractive index profile is shown in Fig. 4.5.

The general formula for a total number of guided modes (accounting for both polarizations) for a fiber with an arbitrary index profile can be written as [75]:

$$M \approx \frac{2\pi}{\lambda^2} \int_0^R 2\pi r (n^2(r) - n_{\text{cl}}^2) dr, \quad (2.5)$$

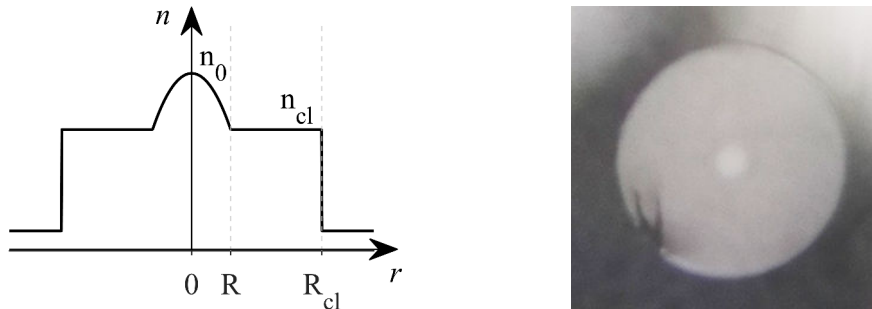


Figure 2.2: Schematic illustration of refractive index profile of a graded-index fiber and a photograph of the fiber used in later experiments.

and in a GRIN fiber it can be estimated as [74]:

$$M \approx \frac{\alpha}{\alpha + 2} \Delta \left(\frac{2\pi}{\lambda} n_0 R \right)^2. \quad (2.6)$$

2.1.3 Photonic crystal fibers

Photonic crystal fibers (PCFs) obtain their waveguide properties not from a radially varying material composition but from a microstructure of air holes. Since the pioneering research led by the group of Philip Russel [76], various designs have been proposed to achieve modification of different properties, as this type of fiber offers many degrees of freedom.

In its most basic form, a PCF is entirely composed of silica, with the glass core region surrounded by multiple rings of periodic air holes that effectively reduce the refractive index of the cladding region. In different designs, the core region can be further doped with additional materials, and the size and arrangement of air holes varies from one structure to another [77, 78]. For example, the PCF used in later experiments is characterized by a Ge-doped core, a set of smaller air holes arranged in a honeycomb lattice, and two regions with larger air holes arranged symmetrically on two sides of the core, see the image of the fiber's cross-section in Fig. 2.3. This kind of structure is fabricated using a preform, which consists of multiple stacked capillaries and solid rods arranged in a pre-ordered manner and inserted in a larger tube. The preform is then drawn into a fiber in a way similar to the standard fiber fabrication process [79].

The arrangement of air holes in PCF affects how the fiber modes are guided. Significant design flexibility permits achieving different combinations of desirable properties. For instance, it is possible to reach small effective mode areas, which enhance the fiber nonlinearity [80]. Moreover, the fiber's dispersive properties are highly sensitive to the size and spacing of air holes, enabling much more customization of the chromatic dispersion compared to the other fiber designs and reaching unique outcomes [81, 82, 83].

It should be mentioned that calculating the modal and dispersive properties of PCF requires a numerical approach because there is no radial symmetry and the cladding refractive index is not homogeneous. For that reason, an advanced mode solver is required: the transmission properties of the fiber can be obtained for example using the Comsol Multiphysics software.

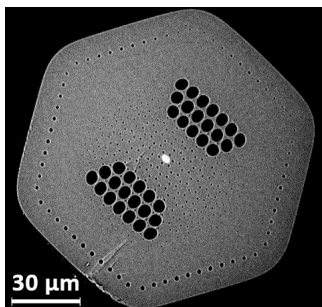


Figure 2.3: Image from a scanning electron microscope showing the photonic crystal fiber used in the later experiments.

2.2 Fiber modes and free space coupling

Fiber modes are obtained by solving the wave equation, which takes the following form in cylindrical coordinates [84]:

$$\frac{\partial^2 E}{\partial r^2} + \frac{1}{r} \frac{\partial E}{\partial r} + \frac{1}{r^2} \frac{\partial^2 E}{\partial \phi^2} + \frac{\partial^2 E}{\partial z^2} + n^2 k^2 E = 0, \quad (2.7)$$

where $k = 2\pi/\lambda$, z is the direction of propagation, n is the local refractive index value, and $E(r, \phi)$ is the complex electric field profile. The following assumes a cylindrically symmetric fiber, which means that the refractive index depends only on the radial coordinate r and not on the azimuthal coordinate ϕ . The described step-index and graded-index fibers satisfy this requirement.

The next useful simplification is considering the weakly guiding approximation, valid for fibers with relatively small index contrast $\Delta \ll 1$. In this case, the axial components of the electric and magnetic fields become negligible, so that the fields are considered transverse to the fiber axis [85]. Under such assumption, the above equation can be solved using an ansatz expressed either as:

$$\begin{aligned} E(r, \phi) &= F_{lm}(r) \cos(l\phi), \\ E(r, \phi) &= F_{lm}(r) \sin(l\phi), \end{aligned} \quad (2.8)$$

or as:

$$\begin{aligned} E(r, \phi) &= F_{lm}(r) \exp(+il\phi), \\ E(r, \phi) &= F_{lm}(r) \exp(-il\phi), \end{aligned} \quad (2.9)$$

with $F_{lp}(r)$ satisfying the following equation:

$$F_{lp}''(r) + \frac{1}{r} F_{lp}'(r) + \left(n^2(r)k^2 - \frac{l^2}{r^2} - \beta^2 \right) F_{lp}(r) = 0. \quad (2.10)$$

For $F_{lp}(r)$ to be physically meaningful, it has to converge toward zero for $r \rightarrow \infty$. Such solutions exist only for certain discrete values of β_{lp} , each of them representing the specific guided mode. This eigenvalue β is the propagation constant of the mode, which governs its propagation in the fiber.

In order to preserve continuity of the ϕ -dependent factor in Eqs. 2.8 and 2.9, the index l , called the azimuthal mode number, must be an integer $l = 0, 1, 2, \dots$. For selected l , the index p , which is an integer called the radial mode number, starts from 1 for the highest possible β and increases until no more solutions can be found.

When the mode basis is established using the ansatz from Eq. 2.8, the guided modes are referred to as LP (linearly polarized) modes, which is the typically assumed mode basis in optical fibers. I describe their selected properties in Section 2.2.1. When the mode basis is established using the ansatz from Eq. 2.9, the guided modes carry orbital angular momentum (OAM) [86]. The value of OAM depends on the integer l , which in this mode basis is often called the *topological charge*. It is evident from Eqs. 2.8 and 2.9 that a superposition of modes from one basis can form modes from another basis. The discussion of OAM fiber modes can be found in Section 2.2.3.

2.2.1 LP modes

The electric field of the LP mode has one predominant direction of polarization. In a cylindrically symmetric fiber, this direction can be arbitrarily selected. Consequently, fiber modes can be divided into two orthogonally polarized groups. One group has electric field aligned along the x axis, while the other has electric field aligned along the y axis, making the two sets of modes degenerate. Another type of mode degeneracy results from the choice of ansatz, which according to Eq. 2.8 makes use of either $\cos(l\phi)$ or $\sin(l\phi)$. These two solutions are known as even and odd modes of the fiber, respectively, and are degenerate for any $l \neq 0$. Consequently, all spatial $LP_{0,p}$ modes are 2-fold degenerate due to polarization degeneracy, and all $LP_{l,p}$ modes with $l > 0$ are 4-fold degenerate in the weakly guiding approximation.

The solutions to the wave equation vary based on the refractive index profile $n(r)$. In the following, I present key observations about modes in step-index and graded-index fibers and devote a section to the challenge of efficiently coupling the input beam into the selected mode.

LP modes in step-index fibers

Equation 2.10 has analytical solutions for step-index fibers, whose core refractive index remains constant. The solution for the core part involves a Bessel function $J_l(r\sqrt{n_0^2k^2 - \beta^2})$, while the solution for the cladding part involves a modified Bessel function $K_l(r\sqrt{\beta^2 - n_{cl}^2k^2})$. The two functions must be balanced to ensure continuity at the boundary between the core and the cladding, and the entire procedure is detailed in Ref. [84].

Obtaining the eigenvalue β and the corresponding mode field distributions for each $LP_{l,p}$ mode requires a numerical approach. I have solved the wave equation numerically for the step-index fiber used in the study in Chapter 5, considering the $l = 0$ modes at the pump laser wavelength $\lambda = 1.035 \mu\text{m}$. At this wavelength, the fiber supports propagation of 23 $LP_{0,p}$ modes. The calculated amplitude and intensity profiles for the first four $LP_{0,p}$ modes are shown in Fig. 2.4. The fundamental mode $LP_{0,1}$ has a Gaussian-like intensity distribution with a maximum at the center of the core. Higher-order modes have more complex field distributions with the number of lobes determined by the radial number p .

On the right side of Fig. 2.4 I show the mode propagation constant β as a function of the radial number for all found guided $LP_{0,p}$ modes. The fundamental mode is characterized by the highest β , with its value approaching n_0k (indicated with a black horizontal line). The propagation constants of higher-order modes decrease at an increasing rate, and the highest-order guided mode has β approaching $n_{cl}k$.

LP modes in graded-index fibers

Core refractive index of GRIN fibers changes according to Eq. 2.4. For such $n(r)$ distribution, the analytic solution of the radial mode equation 2.10 involves Laguerre polynomials, as detailed in Ref. [84]. I have used a numerical mode solver to determine the mode field distributions of the $l = 0$ modes for the same wavelength as in the previous example $\lambda = 1.035 \mu\text{m}$. To better illustrate the unique features of the graded-index design, I consider the parabolic

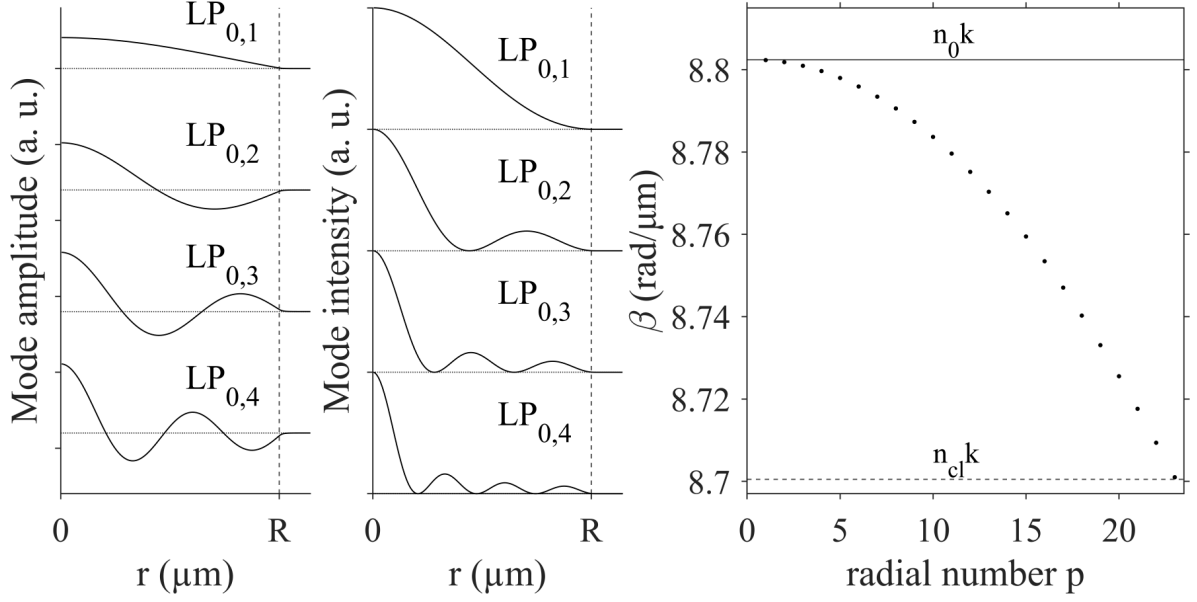


Figure 2.4: Calculated amplitude and intensity profiles of the first few $\text{LP}_{0,p}$ modes (left) and mode propagation constant (right) as a function of the radial mode number for the step-index fiber characterized by a $R = 52.5 \mu\text{m}$ pure-silica core and $\text{NA}=0.22$, assuming $\lambda = 1.035 \mu\text{m}$. In the left panels, the vertical dashed line at $r = R$ indicates the core-cladding boundary.

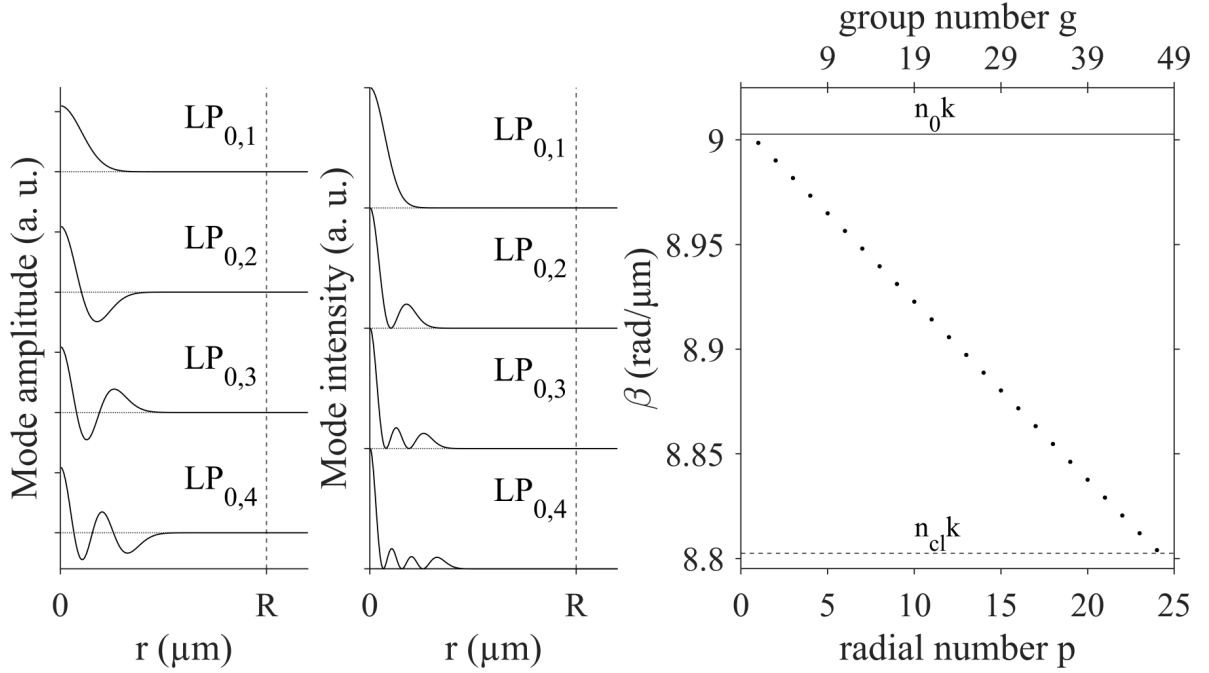


Figure 2.5: Calculated amplitude and intensity profiles of the first few $\text{LP}_{0,p}$ modes (left) and mode propagation constant as a function of the radial mode number for the graded-index fiber characterized by a $R = 50 \mu\text{m}$ core with a 24 mol % Ge doping in the core center, a parabolic index profile, and a pure silica cladding, assuming $\lambda = 1.035 \mu\text{m}$. In the left panels, the vertical dashed line at $r = R$ indicates the core-cladding boundary.

Table 2.1: First 15 mode groups of GRIN fibers with the associated $LP_{l,p}$ modes. The mode count #ndeg (#deg) excludes (includes) mode degeneracy.

g	modes	#ndeg	#deg
1	$LP_{0,1}$	1	2
2	$LP_{1,1}$	1	4
3	$LP_{0,2}; LP_{2,1}$	2	6
4	$LP_{1,2}; LP_{3,1}$	2	8
5	$LP_{0,3}; LP_{2,2}; LP_{4,1}$	3	10
6	$LP_{1,3}; LP_{3,2}; LP_{5,1}$	3	12
7	$LP_{0,4}; LP_{2,3}; LP_{4,2}; LP_{6,1}$	4	14
8	$LP_{1,4}; LP_{3,3}; LP_{5,2}; LP_{7,1}$	4	16
9	$LP_{0,5}; LP_{2,4}; LP_{4,3}; LP_{6,2}; LP_{8,1}$	5	18
10	$LP_{1,5}; LP_{3,4}; LP_{5,3}; LP_{7,2}; LP_{9,1}$	5	20
11	$LP_{0,6}; LP_{2,5}; LP_{4,4}; LP_{6,3}; LP_{8,2}; LP_{10,1}$	6	22
12	$LP_{1,6}; LP_{3,5}; LP_{5,4}; LP_{7,3}; LP_{9,2}; LP_{11,1}$	6	24
13	$LP_{0,7}; LP_{2,6}; LP_{4,5}; LP_{6,4}; LP_{8,3}; LP_{10,2}; LP_{12,1}$	7	26
14	$LP_{1,7}; LP_{3,6}; LP_{5,5}; LP_{7,4}; LP_{9,3}; LP_{11,2}; LP_{13,1}$	7	28
15	$LP_{0,8}; LP_{2,7}; LP_{4,6}; LP_{6,5}; LP_{8,4}; LP_{10,3}; LP_{12,2}; LP_{14,1}$	8	30

index profile with a $R = 50 \mu\text{m}$ core, a 24 mol % Ge doping in the core center, and a pure silica cladding, to obtain a larger number of guided modes than in the few-mode GRIN fiber that is actually used in the later study. The calculated amplitude and intensity profiles for the first four $LP_{0,p}$ modes are shown in Fig. 2.5. The mode field distributions resemble those obtained for the step-index profile, however the key distinction is that the modes in the GRIN fiber are localized closer to the core center. This is due to the radial dependence of the core refractive index.

Assuming a parabolic index profile $\alpha = 2$, propagation constant of the $LP_{l,p}$ mode is expressed as [87]:

$$\beta = n_0 k \left[1 - \frac{2(l + 2p - 1)\sqrt{2\Delta}}{n_0 k R} \right]^{1/2}. \quad (2.11)$$

Clearly, modes with the same value of the integer $l + 2p - 1 \equiv g$ have the same propagation constant, where g is referred to as the group mode number of a $LP_{l,p}$ mode. Consequently, modes belonging to the same group g are degenerate in the weakly-guiding approximation. Table 2.1 presents all the modes belonging to the first 15 groups, illustrating that the mode degeneracy escalates as g increases - each group g includes $2g$ degenerate modes.

Remarkably, the propagation constant of the mode characterized by the mode group number g can be approximated as a simple sum of the material dispersion and waveguide contribution [87]:

$$\beta_g = n_0 k \left[1 - \frac{2g\sqrt{2\Delta}}{n_0 k R} \right]^{1/2} \approx n_0 k - g\sqrt{2\Delta}/R. \quad (2.12)$$

It is important to note that the first term in the above equation depends solely on the

wavelength-dependent refractive index in the center of the fiber core, and the second term is a waveguide contribution that depends on the mode group number and parameters of the fiber design. Consequently, for a given wavelength all modes with the same group number have the same value of the propagation constant, whereas modes with increasing group numbers have propagation constants separated by a factor of $\sqrt{2\Delta}/R$. This is evident in Fig. 2.5, where β is a linear function of g .

The equidistant distribution of mode propagation constants is a very useful feature of graded-index fibers. It creates conditions for the emergence of new phase-matched processes through the self-imaging effect [73]. In particular, collective spectral sidebands (associated with numerous intermodal four-wave mixing combinations) can emerge on both sides of the pump wavelength in a phenomenon called geometric parametric instability (GPI) [47]. Section 4.1 includes the analysis of the spectral positions of phase-matched nonlinear wave mixing processes predicted using the presented assumption.

2.2.2 Optimization of the launch system to excite the $LP_{0,1}$ mode

In general, launching the optical beam into the multimode fiber results in excitation of a superposition of many different modes. The efficiency of excitation of the specific mode is determined by the overlap of its amplitude with the complex amplitude of the pump field incident on the fiber.

The dynamics of the investigated nonlinear processes significantly depend on the amount of energy contained in various modes of the fiber. In particular, the discretized conical wave studied in Chapter 5 emerges as intermodal dispersive wave emitted from an unsteady localized wave structure, and to assure optimal observation and easy interpretation of the phase-matching conditions it is crucial that the ultrashort pump pulses initially propagate in a single fiber mode. Typical laser beam is well approximated by a Gaussian intensity profile, therefore the best overlap can potentially be achieved for the fundamental $LP_{0,1}$ mode. For that reason, I developed a light coupling scheme aimed at enhancing the excitation of the fundamental mode, while reducing the energy coupling into the higher-order modes of the used multimode fiber, which, it is worth highlighting, supports close to 2500 modes at the pump wavelength.

The developed launch system consists of a focusing lens in conjunction with a multiaxis platform that provides 5 degrees of freedom and serves to support the entire, sub-10-cm-long fiber used in this study. In addition, I precisely controlled the path of the input beam using two mirrors arranged in a Z configuration and ensured the exact alignment of the focusing lens's center with the laser beam by using an adjustable XY translation mount.

It is worth to mention the importance of carefully performing the fiber cleaving process. As evident in Fig. 2.1, the cladding layer is quite thin - it measures only 10 μm . Consequently, the score, which is a scratch at the surface of the glass made by the cleaving blade, must be very precise and cannot go too deep, otherwise the core integrity might be compromised which impacts the optical field distribution and prevents pure excitation of the fundamental mode (note that the $LP_{0,1}$ mode intensity profile in Fig. 2.4 extends relatively close to the core-cladding boundary). To achieve a clean breaking along the score line the force applied by

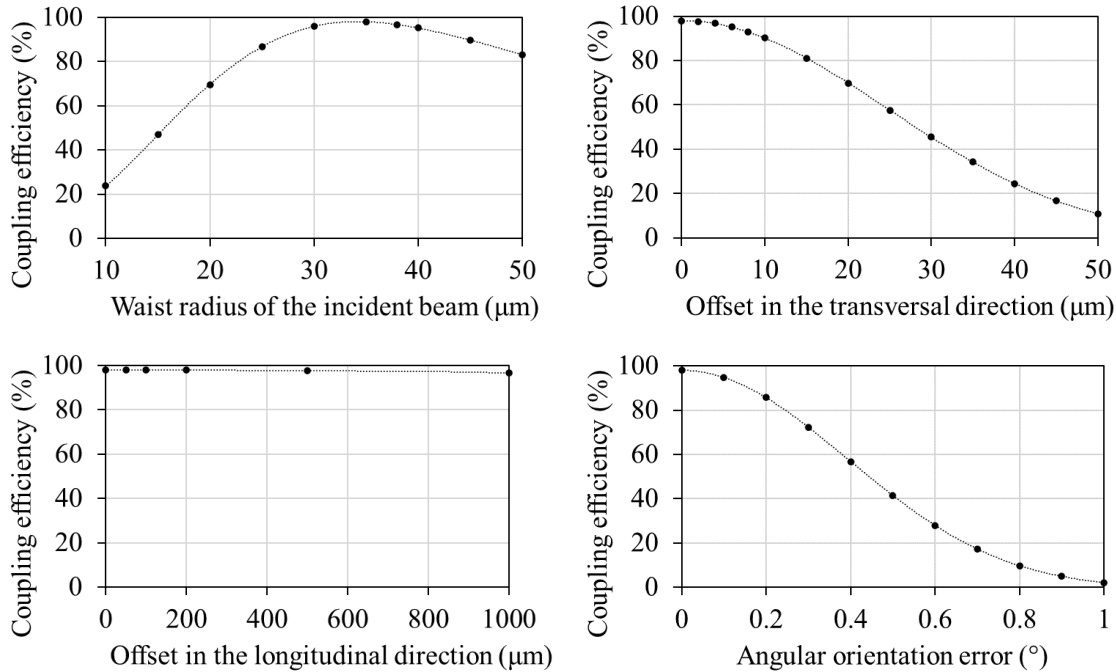


Figure 2.6: Calculated efficiencies of power coupling into the fundamental fiber mode for the beam with a Gaussian intensity profile launched into the investigated step-index MMF. The points show the calculated results as a function of incident beam radius, offset in the longitudinal and transverse directions, and error in angular orientation. The lines serve to guide the eye.

the cleaver to the scored fiber must be precisely managed. After cleaving I inspect both ends of the fiber under the microscope to confirm the clean cut. The segment of the fiber that is an exposed glass is approximately 2-4 mm long from both sides, and the rest remains in the protective polymer coating.

I have found that specific properties of the incident beam should be precisely managed to efficiently launch light into the fundamental mode of this highly multimode fiber. In order to better understand how strong the fiber misalignment influences the launch efficiency into the fundamental fiber mode, I have calculated complex overlap integrals containing the transverse input beam profile and the mode profile using the *RP Fiber Calculator* software. The results, shown in Fig. 2.6, are analyzed below.

Waist radius of the incident beam

The size of the beam at the focus should match the size of the fundamental mode. The waist radius of the beam with a Gaussian intensity profile compared to the intensity profile of the $\text{LP}_{0,1}$ mode shown in Fig. 2.4 should then be around 35 μm (at $1/e^2$). A deviation of 5 μm causes a decrease of power coupling from 98% to 95-96%. However, larger discrepancies from the optimal beam size have a stronger impact on light launch efficiency. As a result, the choice of the lens used for light coupling into the fiber is crucial to ensuring preferential excitation of the selected mode. Consequently, I characterized different available lenses with

the use of a scanning slit optical beam profiler (Thorlabs, BP104IR) to optimize the beam diameter at the focal point to fit the calculated intensities of the fiber modes. The inspection was performed with the pump laser in the continuous mode to avoid damaging the beam profiler. A bi-convex lens (Thorlabs, LB1904-C) was chosen because of the optimal beam waist radius of this element; however, it should be noted that a plano-convex lens would be a better choice as it has lower spherical aberrations. The parameters analyzed in the following assume the optimized beam waist radius of 35 μm .

Transverse and longitudinal alignment of the fiber

The fiber input end should be well-aligned with respect to the beam focus. In terms of alignment in the transverse direction, the position error of the incident beam should be small compared to the radius of the mode. The offset by several micrometers is acceptable in this case. The error of 10 μm allows for the launch efficiency of 90%, while the error of 30 μm results in a twice lower efficiency. Consequently, high precision of the optical-mechanics (preferably with sub-micron accuracy) is important for optimizing transversal alignment of the fiber.

Moreover, the distance from the focal spot should ensure a flat wavefront of the incident beam. However, as shown in Fig. 2.6, the coupling efficiency into the fundamental mode is less prone to errors related to misalignment of the fiber input end in the longitudinal direction, compared to the other analyzed cases. Even a large longitudinal offset of 1 mm does not significantly change the obtained coupling, dropping the efficiency to 96.5%.

Angular orientation of the beam

Finally, it is crucial to ensure the correct direction of the input beam so that it hits the fiber input face perpendicularly. I have found that for such highly-multimode fiber the error of even fraction of a degree can significantly impact the beam launch efficiency. Consequently, ensuring the parallel orientation of the beam with respect to the optical table, and controlling the tilt and yaw of the fiber input end is crucial for optimized light launching. In addition, I should highlight the importance of the inspection performed after cleaving the fiber to verify whether the cut is perpendicular to the fiber axis.

The optimization of the mentioned beam parameters according to the performed analysis allows to achieve high coupling efficiency. In the linear regime, 82% of the beam power is coupled into the fiber.

In the end, it is important to note that even if the pump field is coupled entirely into the fundamental mode, some amount of random mode mixing might occur during propagation due to various factors, including, but not limited to:

- manufacturing irregularities causing non-circularity of the core radius, variations in the material composition, and roughness at the core-cladding boundary [88],
- bending-induced coupling [89],
- applied mechanical stress [90].

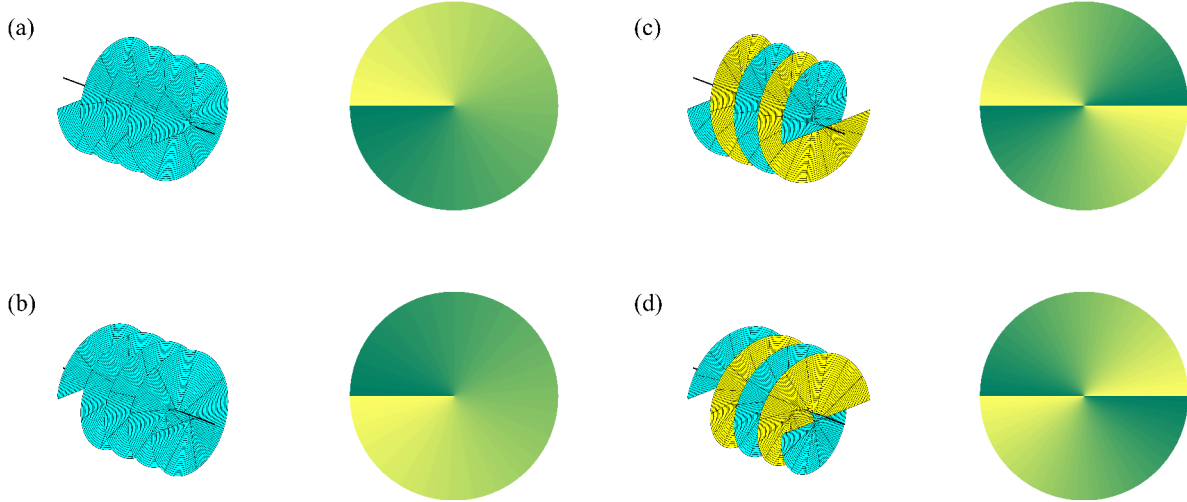


Figure 2.7: Helical structures and phase fronts of OAM beams with (a) $l = +1$, (b) $l = -1$, (c) $l = +2$, (d) $l = -2$.

It is impossible to eliminate the coupling caused by the inherent structure of the fiber. In order to mitigate the mode mixing resulting from the remaining disturbances, it is important to keep the fiber segment straight. In the context of this specific experiment, it is achievable, as merely a few centimeters of nonlinear propagation in the MMF are enough to observe the effect under investigation, therefore the entire fiber segment can be placed on the multi-axis platform. It is also critical to avoid exerting mechanical force on the fiber and to forego the use of conventional fiber clamps or magnetic holders that cause unwanted energy couplings.

2.2.3 Shaping the beam to excite OAM modes

OAM modes are another mode basis to represent spatial modes of fibers, see Eq. 2.9. They are characterized by a helical phase front $\exp(il\phi)$ varying around the axis, where the topological charge l indicates the amount of orbital angular momentum $l\hbar$ carried by each photon [91]. The polarization states associated with this mode basis are left and right circular polarization, σ_{\pm} , which indicates the spin angular momentum carried by each photon [86]. Consequently, OAM modes are denoted as $\text{OAM}_{\pm l, p}^{\pm}$, with the superscript indicating the polarization state, l indicating the number of phase steps in the intensity profile and simultaneously the number of intertwined helical surfaces, see Fig. 2.7, and p indicating the number of concentric rings in the intensity profile. Each $l \neq 0$ OAM mode carries a non-zero orbital angular momentum and has a donut-shaped intensity with a dark central spot since its phase is undefined at the center. Under weakly guiding approximation, each $l > 0$ OAM mode is 4-fold degenerate including polarization and direction of phase rotation, while $\text{OAM}_{0, p}^{\pm}$ mode is 2-fold degenerate including only polarization. The OAM modes can be formed by superposing the even and odd $\text{LP}_{l, p}$ modes with correct phase shifts [92]. Clearly, the total count of modes guided in the specific fiber remains identical, irrespective of whether the LP basis or the OAM basis is considered. OAM modes in the GRIN fibers form degenerate groups [93], similarly to the LP modes.

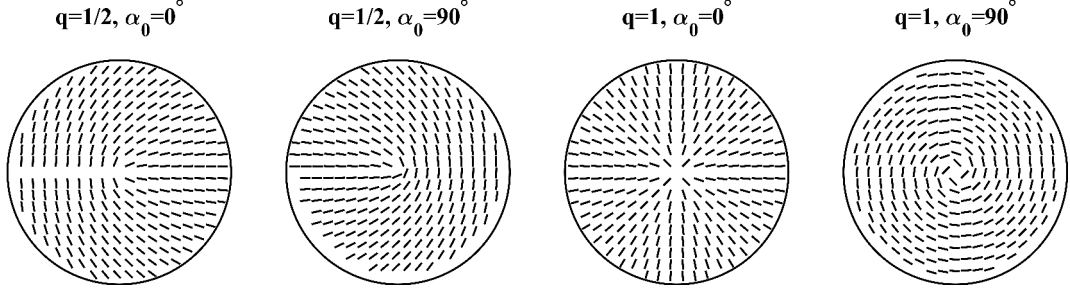


Figure 2.8: Examples of q plates. Lines indicate the local direction of the optical axis.

2.2.4 Excitation of OAM modes

Common methods used for creating the OAM beams include spatial light modulators (SLM) [94, 95], spiral phase plates [96, 97, 98], and q plates [99, 100]. To form the OAM beam for the study described in Chapter 5, I used a q plate, which is an element allowing direct conversion of the optical angular momentum from the spin to the orbital. This implies a possibility of obtaining an OAM beam from a circularly polarized beam passing the q -plate, as demonstrated in Ref. [99]. I elaborate on this below, additionally describing the method developed to shape the beam for exciting simultaneously both the fundamental $l = 0$ and the first order $l = 1$ OAM fiber modes in the desired proportion.

A q plate is a uniaxial birefringent flat plate with a homogeneous birefringent phase retardation ϑ . In the following, I focus on two typical phase retarders: half-wave plate ($\vartheta = \pi$) and quarter-wave plate ($\vartheta = \pi/2$). The q plates have an inhomogeneous orientation of the fast (or slow) optical axis. Assuming that light impinges at normal incidence on the surface of the plate, which is parallel to the xy coordinate plane, the orientation of the optical axis of the q plate can be written as:

$$\alpha(r, \phi) = q\phi + \alpha_0, \quad (2.13)$$

where α is the angle of optical axis orientation with the x axis, q is an integer or a semi-integer, and α_0 is a constant indicating the angle of optical axis orientation with the x axis at $\phi = 0$. Figure 2.8 demonstrates a few examples of q plate geometries for different values of q and α_0 .

The effect applied on an optical field by a q plate with a birefringent phase retardation of ϑ can be conveniently analyzed using Jones formalism [101] with the following Jones matrix \mathbf{M}_q^ϑ applied on the optical field at each point of the q plate transverse plane:

$$\mathbf{M}_q^\vartheta = \mathbf{R}(-\alpha) \cdot \mathbf{M}^\vartheta \cdot \mathbf{R}(\alpha), \quad (2.14)$$

where $\mathbf{R}(\alpha) = \begin{pmatrix} \cos(\alpha) & \sin(\alpha) \\ -\sin(\alpha) & \cos(\alpha) \end{pmatrix}$ is the standard 2×2 rotation matrix by angle α , and \mathbf{M}^ϑ is the Jones matrix for the phase retarder with a homogeneous orientation of the optical axis. The considered half-wave and quarter-wave plates with a homogeneous orientation of the

optical axis are characterized by the following Jones matrices \mathbf{M}^θ :

$$\begin{aligned}\mathbf{M}^\pi &= \exp(-i\pi/2) \begin{pmatrix} 1 & 0 \\ 0 & -1 \end{pmatrix}, \\ \mathbf{M}^{\pi/2} &= \exp(-i\pi/4) \begin{pmatrix} 1 & 0 \\ 0 & i \end{pmatrix},\end{aligned}\tag{2.15}$$

assuming that their fast axis lies parallel to the x axis. Applying Eqs. 2.15 and 2.13 to 2.14 allows obtaining the following Jones matrices for the half-wave and quarter-wave q plates:

$$\begin{aligned}\mathbf{M}_q^\pi &= \begin{pmatrix} \cos(2\alpha) & \sin(2\alpha) \\ \sin(2\alpha) & -\cos(2\alpha) \end{pmatrix}, \\ \mathbf{M}_q^{\pi/2} &= \frac{\sqrt{2}}{2} \left[\begin{pmatrix} 1 & 0 \\ 0 & 1 \end{pmatrix} + \exp(i \cdot 3\pi/2) \begin{pmatrix} \cos(2\alpha) & \sin(2\alpha) \\ \sin(2\alpha) & -\cos(2\alpha) \end{pmatrix} \right],\end{aligned}\tag{2.16}$$

neglecting the terms that represent a global phase shift, which is irrelevant for this discussion.

I will first analyze the influence of a half-wave q plate on the optical field, which can be described by the Jones electric field vector \mathbf{E}_{in} . A left-circular polarized plane wave $\mathbf{E}_{\text{in}} = E_0 \times (1, i)$ will be transformed into the following output field:

$$\begin{aligned}\mathbf{E}_{\text{out}} &= \mathbf{M}_q^\pi \cdot \mathbf{E}_{\text{in}} = E_0 \begin{pmatrix} \cos(2\alpha) & \sin(2\alpha) \\ \sin(2\alpha) & -\cos(2\alpha) \end{pmatrix} \cdot \begin{pmatrix} 1 \\ i \end{pmatrix} = E_0 \begin{pmatrix} \cos(2\alpha) + i \sin(2\alpha) \\ \sin(2\alpha) - i \cos(2\alpha) \end{pmatrix} = \\ &= E_0 \exp(i2\alpha) \begin{pmatrix} 1 \\ -i \end{pmatrix} = E_0 \exp(i2q\phi) \exp(i2\alpha_0) \begin{pmatrix} 1 \\ -i \end{pmatrix}.\end{aligned}\tag{2.17}$$

After passing the q half-wave plate, a left-circular polarized wave becomes uniformly right-circular polarized, just as it would with a regular half-wave plate. Interestingly, the wave also acquires a phase factor $\exp(i2q\phi)$, which indicates its transformation into a helical wave with an orbital helicity of $2q$ and an orbital angular momentum $2q\hbar$ per photon. It is easy to confirm that for a right-circular polarized input wave, the sign of the orbital helicity and angular momentum of the output field is inverted. This technique enables generation of a circularly polarized OAM beam from a circularly polarized laser beam with a standard Gaussian intensity profile. The sign of the orbital helicity of the output wave front can be selected by the input polarization handedness, while its magnitude can be controlled by the q plate geometry.

Next, I analyze the influence of a quarter-wave q plate on the optical field, again considering a left-circular polarized input plane wave. This results in the following output electric field:

$$\begin{aligned}\mathbf{E}_{\text{out}} &= \mathbf{M}_q^{\pi/2} \cdot \mathbf{E}_{\text{in}} = E_0 \frac{\sqrt{2}}{2} \left[\begin{pmatrix} 1 & 0 \\ 0 & 1 \end{pmatrix} + \exp(i \cdot 3\pi/2) \begin{pmatrix} \cos(2\alpha) & \sin(2\alpha) \\ \sin(2\alpha) & -\cos(2\alpha) \end{pmatrix} \right] \cdot \begin{pmatrix} 1 \\ i \end{pmatrix} = \\ &= \frac{\sqrt{2}}{2} E_0 \begin{pmatrix} 1 & 0 \\ 0 & 1 \end{pmatrix} \cdot \begin{pmatrix} 1 \\ i \end{pmatrix} + \frac{\sqrt{2}}{2} E_0 \exp(i \cdot 3\pi/2) \begin{pmatrix} \cos(2\alpha) & \sin(2\alpha) \\ \sin(2\alpha) & -\cos(2\alpha) \end{pmatrix} \cdot \begin{pmatrix} 1 \\ i \end{pmatrix} = \\ &= \frac{\sqrt{2}}{2} E_0 \cdot \begin{pmatrix} 1 \\ i \end{pmatrix} + \frac{\sqrt{2}}{2} E_0 \exp(i \cdot 3\pi/2) \exp(i2q\phi) \exp(i2\alpha_0) \begin{pmatrix} 1 \\ -i \end{pmatrix}.\end{aligned}\tag{2.18}$$

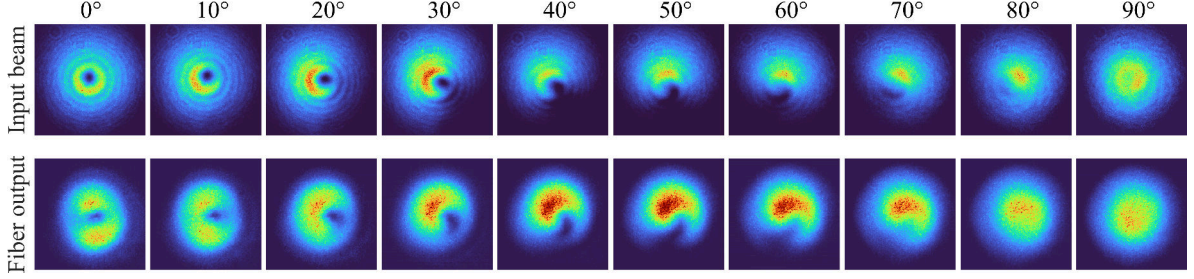


Figure 2.9: Input beam (top row) and near-field images of the fiber output (bottom row) for different rotations of circular polarizer selecting the launched beam composition.

After passing the q quarter-wave plate, a left-circular polarized wave produces a right-circular polarized helical wave with an orbital helicity of $2q$ (just as it would after passing the q half-wave plate) superposed with the initial left-circularly polarized wave. This results from the expression for the q quarter-wave plate Jones matrix $\mathbf{M}_q^{\pi/2} = \sqrt{2}/2[I + \exp(i \cdot 3\pi/2)\mathbf{M}_q^\pi]$ in Eq. 2.16, which consists of the identity matrix that returns the input field vector \mathbf{E}_{in} unchanged, and the Jones matrix corresponding to the q quarter-wave plate with a respective phase shift $3\pi/2$. It is evident that for a right-circular polarized wave, half of the input field will pass the q plate unchanged, and the rest will produce a left-circular polarized OAM beam with an orbital helicity $-2q$.

Consequently, the goal of controllably launching the laser beam into the $l = 0$ and $l = 1$ OAM fiber modes is realized as follows. First, the polarization of the laser beam is converted from linear to circular by a simple quarter wave plate. Next, the beam is passed through a $q = 1/2$ plate to obtain a superposition of a circularly polarized $l = 0$ beam and a $l = 2q = 1$ helical beam polarized circularly with the opposite handedness to the incident beam. Finally, the desired composition of the beam is controlled with a circular analyzer, which can select either one circular polarization component, or any combination of the two. The resulting beam is linearly polarized and contains a specific mix of $l = 0$ and $l = 1$ components. Finally, the beam is launched into the fiber under study using a similar procedure to the one detailed in the previous section concerning the excitation of the $\text{LP}_{0,1}$ mode. This allows to selectively control the excitation of the fundamental and the first-order OAM fiber mode, as shown in Fig. 2.9 for different rotations of the quarter-wave plate in the circular analyzer.

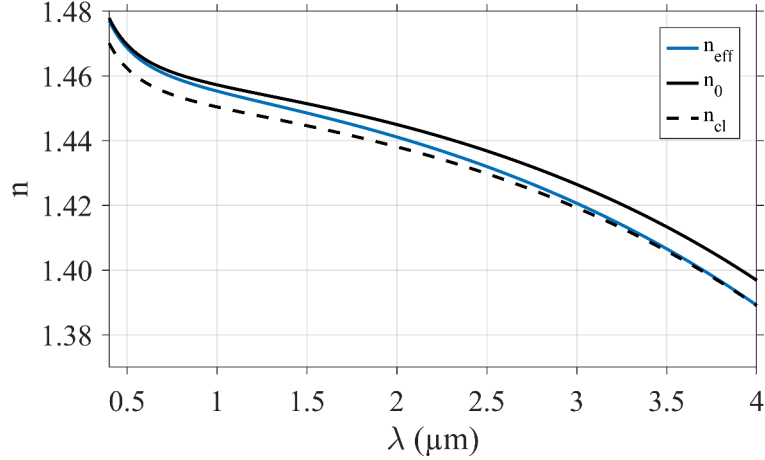


Figure 2.10: Refractive index calculated for the core center and cladding of the investigated GRIN fiber, along with the effective refractive index of the fundamental fiber mode.

2.3 Linear properties and phenomena

In this section, I introduce the fundamental principles governing the linear propagation of light in optical fibers. I discuss the key concepts such as the mode propagation constant, dispersion, birefringence, and attenuation mechanisms. This part aims to provide a theoretical foundation, bolstered by experimental and numerical characterization of the linear parameters of the fibers used in various studies throughout this doctoral thesis. Through the analysis of theoretical models complemented by practical examples, this section lays the groundwork for the exploration of nonlinear effects in the subsequent section.

2.3.1 Propagation constant and effective refractive index

The propagation constant β of a mode describes how the phase of the light with a given frequency varies along the propagation direction z :

$$A(z) = A(0) \exp(i\beta z), \quad (2.19)$$

where $A(z)$ is the complex amplitude of the light field at position z , and the medium is assumed to be lossless. The propagation constant depends on the wavelength λ and the optical frequency, which is written as $\omega = 2\pi c/\lambda$.

Propagation constant is given by the product of the effective refractive index n_{eff} and the vacuum wavenumber $k = 2\pi/\lambda$, therefore $\beta = n_{\text{eff}}k = n_{\text{eff}}\omega/c$. The effective index of a mode is a similar concept to the refractive index of a material; it quantifies the decrease of phase velocity of a particular wavelength compared to its phase velocity in vacuum, $n = c/v_{\text{ph}}$. The wavelength-dependent effective refractive index of the fundamental mode of the studied GRIN fiber, calculated using a mode solver software, is shown in Fig. 2.10, together with the refractive indices of the core (n_0) and cladding (n_{cl}) material. At shorter wavelengths, the mode effective index is closer to n_0 , while at longer wavelengths it approaches n_{cl} . This trend is also observed for higher-order fiber modes, although their effective indices approach the

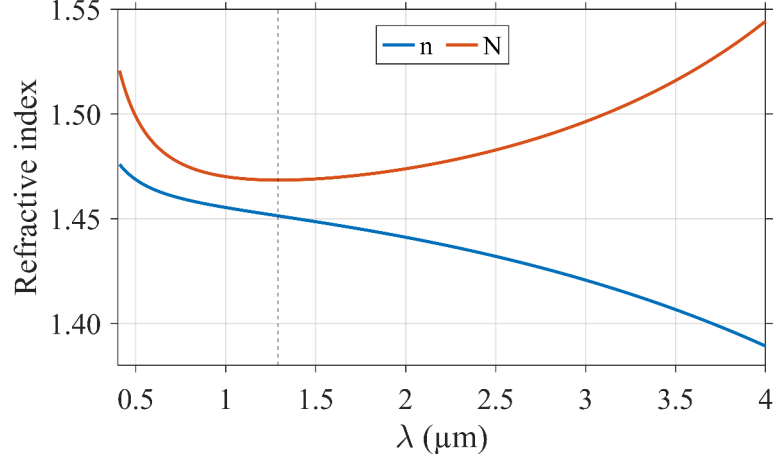


Figure 2.11: Calculated phase and group effective refractive index for the fundamental mode of the investigated GRIN fiber.

cladding index at shorter wavelengths than those of the fundamental mode, after which they cease to be guided in the fiber (the cut-off wavelengths).

Dispersion (dependence of effective index and propagation constant on wavelength) plays a crucial role in light propagation in fibers, especially for short pulses. That is because different spectral components associated with the pulse travel at different speeds, and undergo different phase change per unit length. The different effects of dispersion can be accounted for by expanding the mode propagation constant in a Taylor series around the central frequency of the pulse ω_0 :

$$\beta(\omega) = \beta_0 + \beta_1 \cdot (\omega - \omega_0) + \frac{1}{2} \beta_2 \cdot (\omega - \omega_0)^2 + \dots, \quad (2.20)$$

where

$$\beta_m = \left(\frac{\partial^m \beta}{\partial \omega^m} \right)_{\omega=\omega_0}, \quad m = \{0, 1, 2, \dots\}. \quad (2.21)$$

The terms corresponding to the different orders of derivatives have the following physical meaning:

- β_0 describes a phase shift;
- $\beta_1 = \frac{1}{v_g}$ is the inverse group velocity, which describes the speed of the pulse envelope;
- β_2 is the group velocity dispersion responsible for the pulse broadening;
- higher-order derivatives describe higher-order dispersion.

2.3.2 Group refractive index

In a manner analogous to the phase refractive index, the group refractive index can be defined as the ratio of the velocity of light in vacuum to its group velocity in the medium:

$$N = \frac{c}{v_g} = c\beta_1 = c \frac{\partial \beta}{\partial \omega} = \frac{\partial}{\partial \omega} (\omega \cdot n(\omega)) = n(\omega) + \omega \frac{\partial n}{\partial \omega}. \quad (2.22)$$

Consequently, the group index at a specific wavelength consists of the combined information on the value of the phase refractive index, but also its frequency dependence. If the wavelength

dependence of the phase index is known, for example by calculating the mode effective index with a mode solver software, the group index can also be easily determined, see Fig. 2.11.

In order to experimentally determine the frequency dependence of the group index I employ a method based on the white-light spectral interferometry [102], which involves recording a set of spectral interferograms in a Mach-Zehnder interferometer with an adjustable path length of the reference arm. The other arm contains the fiber segment of a known length. The technique is based on measuring the equalization wavelength as a function of the path length difference, or equivalently the differential group refractive index dispersion in the fiber. It does not deliver the direct value of N , but the group index related to its value at an arbitrarily chosen length of the reference arm L_{MZ}^0 . The measured dependence of the differential group index can then be fitted to a function $\Delta N(\lambda)$, which can be used for calculating the chromatic dispersion, or group birefringence, as detailed in the following sections. As an illustration, the measured values of differential group index for two modes of the studied PCF are shown in Fig. 2.12.

Walk-off of short pulses due to group velocity mismatch

The walk-off effect plays an important role in the description of the nonlinear phenomena involving two or more co-propagating pulses. The investigated nonlinear processes are typically efficient for short pulses due to their high intensities even for low average powers. However, a short pulse duration imposes a limit of the useful interaction length due to the temporal walk-off. If the interacting pulses have different wavelengths, they travel with different group velocities, losing their temporal overlap after the distance when the faster pulse completely walks through the slower pulse. The strength of the pulse walk-off depends on the group velocity mismatch, and is evaluated with the relative inverse group velocity of the pulses in two optical fields:

$$\text{RIGV} = \beta_1^i - \beta_1^j = \frac{1}{v_g^i} - \frac{1}{v_g^j} = \frac{1}{c} (N^i - N^j), \quad (2.23)$$

where i, j indicate different wavelengths or different fiber modes. After final transformation, it is evident that the group velocity mismatch can be easily determined by the difference in group indices of the two optical fields. For example, the measurements of the differential group indices in the PCF allow to simultaneously determine RIGV, see the right axis in Fig. 2.12. The results for both modes are shown in relation to the value of β_1 of the $\text{LP}_{0,1}^x$ mode at the pump laser wavelength $\lambda = 1560$ nm, marked with a vertical line. The obtained results show that in the analyzed spectral region the pulses at longer wavelengths travel slower in both fiber modes than the pulses at shorter wavelengths, and the $\text{LP}_{0,1}^x$ mode (blue) travels faster than the $\text{LP}_{0,1}^y$ mode (red).

In practice, it is useful to define the walk-off length:

$$L_W = T_0/\text{RIGV}, \quad (2.24)$$

where T_0 is the pulse width. In the considered example, assuming that the pump laser pulse (which is characterized with $T_0 = 13$ fs in the PCF study) is exciting both modes of the PCF, the walk-off length is approximately 5 millimeters. This demonstrates that the intermodal

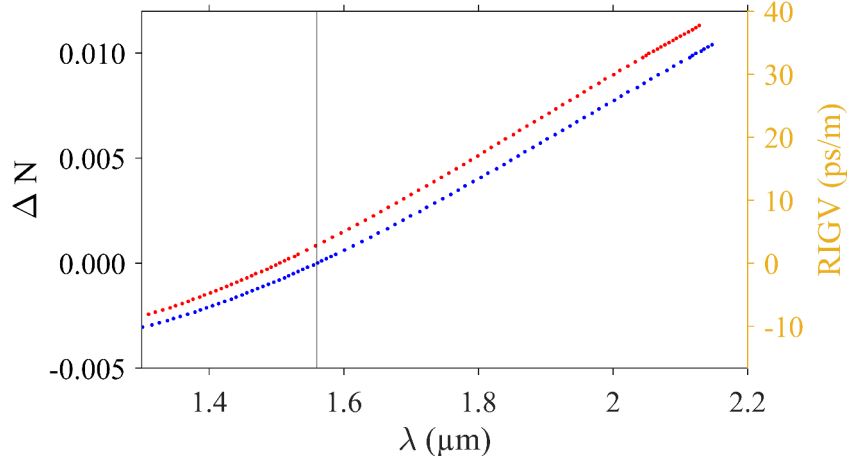


Figure 2.12: Measured linear parameters of two modes $LP_{0,1}^x$ (blue) and $LP_{0,1}^y$ (red) of the investigated PCF: differential group refractive index and relative inverse group velocity.

interactions of ultrashort pulses can be significantly limited because of their different group velocities, unless nonlinear mode couplings lead to changes of pulse group velocities.

2.3.3 Dispersion

Group velocity dispersion is the phenomenon that the group velocity of light in a medium depends on the frequency or wavelength. The term can also be used as a precisely defined parameter, namely the derivative of the inverse group velocity with respect to the angular frequency, just as indicated in Eq. 2.21:

$$\beta_2 = \frac{\partial}{\partial \omega} \frac{1}{v_g} = \frac{\partial}{\partial \omega} \beta_1 = \frac{\partial}{\partial \omega} \left(\frac{\partial \beta}{\partial \omega} \right) = \frac{\partial^2 \beta}{\partial \omega^2}. \quad (2.25)$$

Group velocity dispersion can alternatively be expressed as a derivative with respect to wavelength, in which case it is typically referred to as the chromatic dispersion parameter D . It can be written in relation to β_2 :

$$D = \frac{\partial}{\partial \lambda} \frac{1}{v_g} = -\frac{2\pi c}{\lambda^2} \beta_2, \quad (2.26)$$

or to the derivatives of refractive index:

$$D = \frac{1}{c} \frac{\partial N}{\partial \lambda} = -\frac{\lambda}{c} \frac{\partial^2 n}{\partial \lambda^2}, \quad (2.27)$$

The chromatic dispersion expressed as a derivative of group index with respect to wavelength can be retrieved from the experimental characterization of differential group refractive index. When the experimental points are approximated with a function $\Delta N(\lambda)$, a simple numerical derivation allows to obtain the dependence $D(\lambda)$ and, consequently, $\beta_2(\lambda)$. As an illustration, both dispersion parameters calculated as a function of wavelength are shown for one of the modes of another studied PCF in Fig. 2.13. Notably, both β_2 and D vanish at a wavelength of 1.24 μm . This wavelength, marked with dashed line both in Fig. 2.13 for PCF and

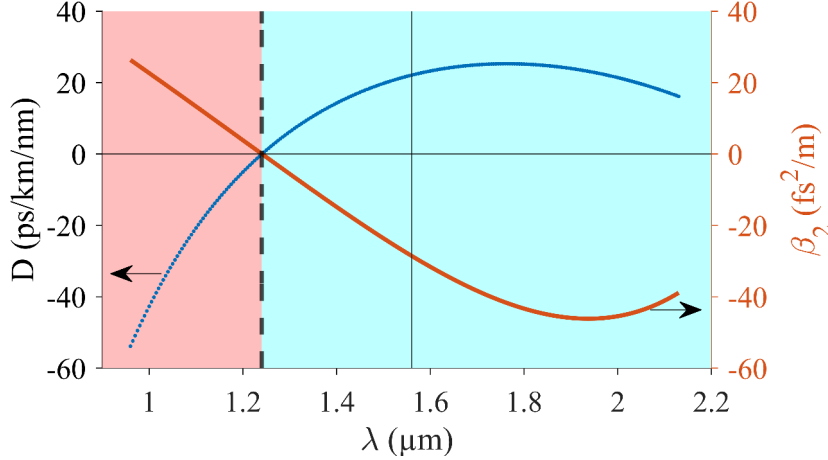


Figure 2.13: Measured chromatic dispersion of the investigated PCF.

in Fig. 2.11 for GRIN fiber is referred to as the zero-dispersion wavelength λ_{ZDW} . Typically, in silica fibers $\lambda_{\text{ZDW}} \approx 1.3 \mu\text{m}$, however the design flexibility of PCF allows to significantly modify the dispersion curve: flatten it [82], shift the λ_{ZDW} , and even achieve $D > 0$ in the visible spectral region [81].

Using the terms "positive" or "negative" dispersion might be confusing due to the different signs of β_2 and D , hence, the terms normal and anomalous dispersion are used instead. Normal dispersion ($D < 0$, marked with a red region in Fig. 2.13) implies that the group velocity decreases for increasing optical frequency and increases with wavelength (blue-shifted components of the optical pulse travel slower than the red-shifted components of the same pulse); anomalous dispersion ($D > 0$, marked with a blue region in Fig. 2.13) implies that the group velocity increases for increasing frequency. Nonlinear effects in fibers manifest qualitatively different behavior depending on the dispersion region.

Because of group velocity dispersion, various frequency components of the pulse travel with different velocity. As a result, the pulse width increases during propagation. The fiber length over which this effect starts to play a significant role is called the dispersion length:

$$L_D = \frac{T_0^2}{|\beta_2|}. \quad (2.28)$$

At this distance, a Gaussian pulse broadens by a factor of $\sqrt{2}$ [84]. When a $T_0 = 13 \text{ fs}$ pulse is injected into the investigated PCF at $1.56 \mu\text{m}$ in the anomalous dispersion region with $\beta_2 = -28.5 \text{ fs}^2/\text{m}$, the dispersion length is less than 10 meters. This might potentially lead to a significant dispersive pulse broadening over a longer distance of propagation; however, as I describe in the later sections, this might be balanced by nonlinear effects if the pulse intensity is sufficiently high.

Finally, it is worth to highlight that the term "chromatic" is employed to distinguish that type of dispersion from other types. This is especially significant for multimode fibers, which also show intermodal dispersion that pertains to the different group velocities of various fiber modes. In particular, polarization mode dispersion is associated with the distinct propagation characteristics of light fields with orthogonal polarizations, as detailed below.

2.3.4 Birefringence

In an ideal, cylindrically-symmetric, and stress-free fiber, light field polarized in the x direction does not interact with the orthogonal polarization state. However, in practice, random variations in the core shape along the fiber and anisotropic stress lead to an uncontrollable coupling to other polarizations [103]. This issue can be addressed by using birefringent fibers, where a large birefringence is deliberately introduced to overshadow the relatively minor birefringence fluctuations and maintain the polarization state of the input field. Introducing birefringence leads to a significant difference of the effective refractive indices of the orthogonal polarization modes, thus reducing the probability of linear coupling. Such polarization-maintaining fibers are achieved by altering the geometry of the core [104], introducing anisotropic stresses [105], or most commonly by combining both methods. The investigated PCF combines the two methods with three rows of large air holes arranged on the two sides of the core as shown in Fig. 2.3. High pressure deployed during the fiber drawing process results in lattice squeezing, modification of the core shape, and consequently high birefringence.

In birefringent fibers, the phase effective refractive index of the mode polarized along the so-called *slow* axis (x axis by convention) is higher, and the index of the mode polarized along the *fast* axis (y axis by convention) is lower. This results in a slower and faster light propagation in terms of phase velocity, respectively. The difference between the effective indices of the orthogonally polarized modes is the phase birefringence:

$$B = n_x - n_y = \frac{\lambda|\beta_x - \beta_y|}{2\pi} = \frac{\lambda}{L_B}. \quad (2.29)$$

L_B denotes the beat length, defined as the distance over which the phase difference between the polarization modes changes by 2π .

As the dispersion of the two polarization modes may vary, phase birefringence is also frequency-dependent. This is characterized by the group birefringence:

$$G = B - \lambda \frac{\partial B}{\partial \lambda}, \quad (2.30)$$

which can be also interpreted as the difference in group indices of the polarization modes $N_x - N_y$. In birefringent photonic crystal fibers, the second term in the above equation is typically dominant, leading to opposite signs of B and G .

I used two independent experimental techniques to determine the birefringence of both studied PCFs. First, I measured differential group refractive index in the previously described experiment while controlling which fiber polarization mode is excited. Because the measurements are performed with the same L_{MZ}^0 length of the reference arm, calculating the difference of the fitted functions $\Delta N_x - \Delta N_y$ allows to determine directly the group birefringence G , see blue lines in Fig. 2.14.

Another approach [106] is to simply excite both polarization modes in the fiber with a spectrally broad light, aligning the polarization azimuth of the input beam at an angle of around 45° with respect to one of the fiber axis. This way, two equally excited polarization modes propagate through the fiber of length L and accumulate the relative phase shift $\Delta\phi = 2\pi LB/\lambda$.

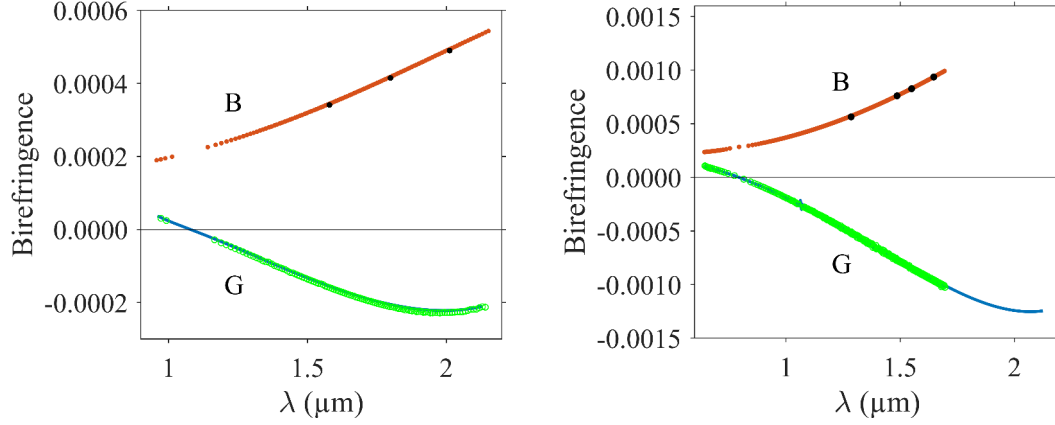


Figure 2.14: Measured phase and group birefringence determined using various techniques in the two investigated PCFs.

At the fiber output, the two modes are mixed by an analyzer with the azimuth adjusted at 45° with respect to the polarization axes and the mode spectral interference is resolved by an optical spectrum analyzer. The average birefringence of the fiber segment can be determined from the spectral fringe period $\Delta\lambda$, as each single period corresponds to a 2π phase shift between the two polarization modes. Group birefringence can be determined using the following relationship:

$$G = -\frac{\lambda^2}{L\Delta\lambda}. \quad (2.31)$$

This method was used to obtain results marked with green points in Fig. 2.14 which follow very well the blue line indicating an excellent agreement with the results obtained using the previous technique.

It is also worth noting that the registered spectral interferogram allows to reconstruct the relative phase birefringence between two wavelengths from the number of spectral fringes m that separates them. As each consecutive fringe corresponds to a phase difference of 2π , the phase birefringence can be written as [107]:

$$B = \frac{m\lambda}{L}. \quad (2.32)$$

It should be noted that the fiber length needs to be carefully selected to ensure that the interference pattern can be resolved using the spectral analyzer, and that the results can be obtained at sufficiently dense spectral intervals. I measured the phase birefringence using the conventional lateral point force method [108] at a few selected wavelengths (represented by black markers in Fig. 2.14). The obtained value was then used to calculate the fringe number m in absolute terms, enabling to retrieve the full $B(\lambda)$ dependency (orange points in Fig. 2.14).

The performed measurements allow to confirm high birefringence of the two photonic crystal fibers used in the study described in Chapter 3. The obtained magnitude of fiber birefringence in the range from 10^{-4} to 10^{-3} is considered to be very high [84], as the conventional (meaning: not microstructured) birefringent fibers with an elliptical core are characterized by $B \sim 10^{-6}$ [104], and the conventional birefringent fibers with stress-induced birefringence typically achieve $B \sim 10^{-4}$ [105]. Finally, the high dispersion of phase birefringence indeed results in the negative

group birefringence at wavelengths longer than $1.1\ \mu\text{m}$ ($0.8\ \mu\text{m}$) for PCF 1 (PCF 2) on the left (right) of Fig. 2.14. The opposite signs of phase and group birefringence indicate that the x polarization mode of the fiber travels faster in terms of group velocity than the y polarization mode, even though it has a lower phase velocity. The respective group velocities of the two modes are important when considering the nonlinear effects occurring in that study.

2.3.5 Attenuation

In practice, optical fibers are not a lossless medium, contrary to the assumption made in Eq. 2.19. To account for fiber losses, the equation needs to be modified to include the attenuation coefficient α :

$$A(z) = A(0) \exp((i\beta - \alpha/2)z), \quad (2.33)$$

which quantifies the power loss originating from various sources, leading to attenuation of optical signals transmitted inside the fiber. This coefficient links the transmitted power P , the injected power P_0 and the length of propagation in the fiber L :

$$\begin{aligned} P &= P_0 \exp(-\alpha L), \\ \alpha &= -\frac{1}{L} \ln \frac{P}{P_0}, \end{aligned} \quad (2.34)$$

and is usually expressed in units of dB/km or dB/m, $\alpha_{\text{dB/km}} = 4.343\alpha$ [84]. The factor $1/2$ in the equation for field amplitudes results from the fact that the optical power or intensity is proportional to the square of the amplitude.

The attenuation coefficient can be determined using a conventional cut-back method, which involves measuring the power at the end of a long fiber segment, followed by reducing the fiber length by L , and repeating the power measurement. Provided that the launch conditions remain unchanged, the power ratio allows to determine the light attenuation in the cut-back segment. By adjusting the length of the cut-back segment, different orders of magnitude of loss can be measured. For high loss, the fiber length after the cut-back must be sufficiently short; otherwise, the fiber attenuation might reduce the signal below the detector sensitivity threshold.

The attenuation coefficient measured in PCF as a function of wavelength is shown in Fig. 2.15. There are different factors contributing to the attenuation of light as it travels in the fiber. The primary loss mechanisms in the near-infrared and mid-infrared spectral regions are material loss, Rayleigh scattering (providing a fundamental limit and varying as λ^{-4}), and mode confinement loss [84]. Rayleigh scattering is dominant at shorter wavelength, and at $1.55\ \mu\text{m}$ it results in attenuation of 0.12-0.15 dB/km. Silica glass exhibits minimal absorption in the spectral range from $0.5\ \mu\text{m}$ to $2\ \mu\text{m}$. However, the presence of OH ions can significantly affect the light absorption in this spectral window [54]. The fundamental vibrational OH absorption peak at $2.72\ \mu\text{m}$, its overtone at $1.38\ \mu\text{m}$ and combinations with vibrational mode of SiO_4 tetrahedron at $2.21\ \mu\text{m}$ result in distinct absorption bands that significantly contribute to the fiber attenuation. The relative intensities of OH absorption bands [54] can be used to estimate the fiber attenuation at their spectral positions based on the characterization of

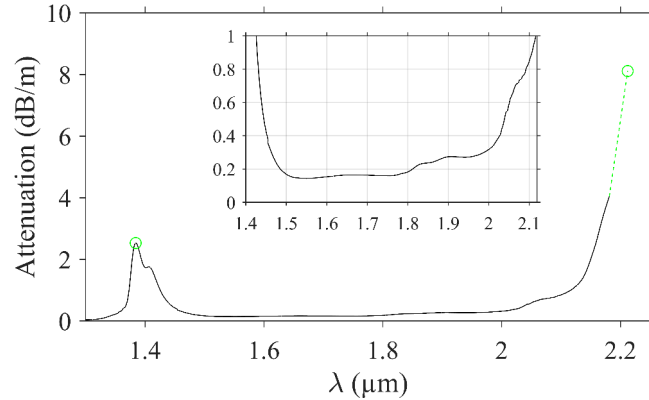


Figure 2.15: Measured attenuation coefficient in PCF (black) and its estimation for longer wavelengths (green).

only a single absorption band. By determining the loss related to the OH absorption band at $1.38\ \mu\text{m}$ (reaching $2.53\ \text{dB/m}$), I can find the corresponding loss at $2.21\ \mu\text{m}$, which should be $201/62.7$ times higher and reach $8.11\ \text{dB/m}$.

It should be mentioned that state-of-the-art fibers, produced in dry conditions to minimize the OH ion content in the fiber preform exhibit an OH absorption peak around $1.4\ \mu\text{m}$ that is below $0.5\ \text{dB/km}$ [109], which is highly desirable for telecommunication applications. Although similar results are also possible in photonic crystal fibers [110], the PCF used in our study is characterized by a higher OH content, resulting in a significant OH absorption band compared to the transmission-optimized PCF in the referenced work.

The final factor contributing to the fiber attenuation is mode confinement loss, which stems from the leaky nature of fiber modes. It affects especially the higher-order modes near their cut-off, causing them to continuously radiate a small amount of carried energy into the fiber cladding during the propagation. The extent of confinement loss is influenced by the fiber structure, and is particularly pronounced in photonic crystal fibers due to their complex design [111]. Reducing core size of PCF can lead to significant confinement loss which can even surpass material losses [80], thus restricting the usable fiber lengths to less than a kilometer. The measured PCF attenuation shown in the inset of Fig. 2.15 is higher in the spectral range from $1.5\ \mu\text{m}$ to $1.8\ \mu\text{m}$ compared to standard silica fibers, which can be attributed to confinement loss resulting from the fiber design.

2.4 Nonlinear properties and phenomena

Light in an optical fiber is confined to a small transverse area, resulting in high intensities even at moderate beam powers. Furthermore, the waveguiding property of fibers enables light to travel considerable distances, leading to accumulation of effects of fiber nonlinearities. Consequently, optical fibers exhibit significant nonlinear effects, especially when the light propagates in the form of short, high-intensity pulses. In the subsequent sections, I introduce fundamental fiber properties and associated nonlinear effects, which are relevant to the subjects explored in the later chapters.

2.4.1 Effective mode area

To assess the strength of nonlinear effects, it is necessary to determine the size of the transverse area occupied by the light beam in the fiber. Fiber modes have smooth transverse profiles with no well-defined boundaries. Therefore, determining the area of a mode is not particularly straightforward, especially for complex profiles of higher-order modes. Hence, effective mode area is a very useful concept. It is defined as:

$$A_{\text{eff}} = \frac{\left(\iint_{-\infty}^{\infty} |F(x, y)|^2 dx dy \right)^2}{\iint_{-\infty}^{\infty} |F(x, y)|^4 dx dy}, \quad (2.35)$$

where $F(x, y)$ is the spatial distribution of the fiber mode across the transverse coordinates.

The shape of the mode, and consequently the effective mode area depend on both the core size and the doping levels that determine how tight is the localization of mode in the core [112]. Standard single-mode fibers, such as SMF-28, have effective mode areas on the order of $100 \mu\text{m}^2$. The effective mode areas of the large mode area fibers sometimes exceed $1000 \mu\text{m}^2$. On the other hand, photonic crystal fibers are sometimes characterized by mode areas below $10 \mu\text{m}^2$. Typically, effective mode area increases with wavelength. The calculated effective areas of the selected modes in two fibers used for later experiments are displayed as a function of wavelength in Fig. 2.16.

Nonlinear effects depend on the light intensity. For a given power level, the optical intensity is larger when a mode area is smaller, leading to more significant nonlinearities. Consequently, the fiber nonlinearity can be enhanced by reducing the core diameter, while ensuring that the mode remains well-confined, particularly in the long wavelength range.

2.4.2 Nonlinear parameter gamma

The strength of the nonlinear interaction can be expressed by the nonlinear parameter γ :

$$\gamma = \frac{2\pi n_2}{\lambda A_{\text{eff}}}. \quad (2.36)$$

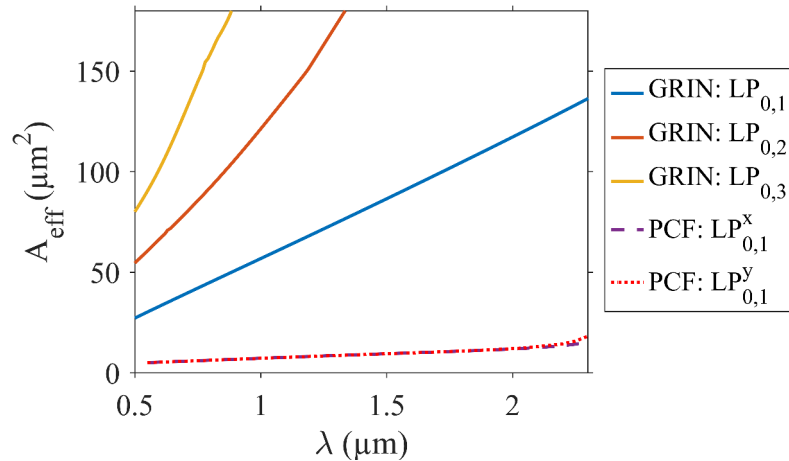


Figure 2.16: Calculated effective areas of the fundamental and higher-order modes of the investigated GRIN and photonic crystal fiber.

The mode area A_{eff} depends on the fiber design and can be reduced as explained in the previous section. The Kerr coefficient n_2 is a material parameter of a given glass explained in more detail in the following section.

It should be mentioned that for some of the nonlinear processes, choosing the value of calculated effective mode area is not so straightforward. More specifically, in the case of four-wave mixing, the occurring effects result from interactions of different modes at different wavelengths. As presented in Fig. 2.16, the value of A_{eff} changes with wavelength and from mode to mode. Consequently, the nonlinear parameter can instead of $1/A_{\text{eff}}$ be driven by the overlap integral of the fields distribution [84]:

$$f_{i,j,k,l} = \left| \frac{\langle F_i^* F_j^* F_k F_l \rangle}{\sqrt{\langle |F_i|^2 \rangle \langle |F_j|^2 \rangle \langle |F_k|^2 \rangle \langle |F_l|^2 \rangle}} \right|, \quad (2.37)$$

where angle brackets denote integration over the transverse coordinates and subscripts indicate four interacting waves. F_i is the spatial distribution of the fiber mode in which the i th field propagates inside the fiber.

2.4.3 Nonlinear refractive index

A large number of nonlinear effects in optical fibers originate from Kerr effect, which is an intensity-dependent increase of refractive index, meaning that the phase delay of light gets larger as the intensity of light increases [113]. This nonlinear correction to refractive index can be written as:

$$\Delta n = n_2 I, \quad (2.38)$$

and it plays an important role in various processes that involve generation of new frequencies. Kerr coefficient n_2 , also referred to as nonlinear refractive index, varies for different materials [114]. Its value is relatively small in silica compared to other transparent glasses, reaching approximately $2.6 \times 10^{-20} \text{ m}^2/\text{W}$ for wavelengths around $1 \mu\text{m}$ [115, 116, 117, 118].

2.4.4 Self-phase modulation

Self-phase modulation (SPM) is one of the consequences of the Kerr effect [84]. In this phenomenon, an ultrashort pulse of light traveling in a fiber experiences a nonlinear phase shift that results from its own intensity. The phase shift increases with the length of the fiber. The fiber length over which SPM starts to play a significant role during pulse propagation is called the nonlinear length:

$$L_{\text{NL}} = \frac{1}{\gamma P_0}, \quad (2.39)$$

where P_0 is peak power of the pulse. The nonlinear length indicates the distance over which the phase shift at the peak of the pulse is equal to 1 rad. SPM causes generation of new frequency components as the pulse propagates in the fiber, leading to its spectral broadening. The new frequency components are shifted to longer wavelengths at the leading edge of the pulse, and to shorter wavelengths at the trailing edge of the pulse.

Pulse self-steepening and formation of optical shock

Self-steepening is related to the distortion of the optical pulse caused by the group velocity's dependence on the intensity [119, 120]. The peak of the pulse travels slower than both its edges. As a result, the trailing edge of the pulse becomes increasingly steeper during propagation. Eventually, pulse self-steepening leads to formation of optical shock in an analogue manner to creation of acoustic shock on the leading edge of a sound wave [121, 122]. For femtosecond pulses and peak powers in the kW range, pulse self-steepening can impact the nonlinear propagation in short sub-meter segments of single-mode fibers [84].

2.4.5 Formation of solitons

It should be noted that chromatic dispersion can also significantly affect ultrashort light pulses, as discussed in Section 2.3.3. If the effects of Kerr nonlinearity and dispersion are comparable and the fiber is sufficiently long ($L > L_D \sim L_{NL}$), the interplay between GVD and SPM can lead to qualitatively new results, which differ based on the dispersion regime [84]. In the anomalous dispersion region, the combined influence of self-phase modulation and dispersion can mitigate the temporal and spectral broadening caused by each of them individually, resulting in the formation of a soliton pulse. The propagation of soliton is governed by its order N , defined as:

$$N^2 = \frac{L_D}{L_{NL}} = \frac{\gamma P_0 T_0^2}{|\beta_2|}. \quad (2.40)$$

Solitons generated in the investigated PCFs from the pulses of the used pump laser are characterized by $N \approx 1$ for the average pump powers ranging from 50 mW to 100 mW. Such fundamental solitons ($N = 1$) do not change their shape during propagation, in contrast to higher-order solitons, which exhibit periodic oscillations [123].

2.4.6 Self-focusing

Nonlinear self-focusing is another consequence of the Kerr effect, following SPM. This time, the impact of the intensity-dependent refractive index is observed in the transverse spatial dimensions, as the beam size is reduced during propagation. This occurs because the higher optical intensity at the center of the beam causes a local increase of refractive index for the central part of the beam compared to the outer parts of the beam. The altered refractive index distribution acts as a focusing lens [124]. This mechanism is triggered when the peak power exceeds a threshold value [32]:

$$P_{\text{crit}} = \frac{3.72\lambda_0^2}{(8\pi n_0 n_2)}, \quad (2.41)$$

enabling self-focusing to overcome diffraction of the beam.

2.4.7 Cross-phase modulation

Cross-phase modulation (XPM), occurring alongside SPM, describes interactions between two or more pulses that propagate simultaneously in a fiber at distinct wavelengths or polariza-

tions [84]. Fiber nonlinearity causes each pulse to undergo a nonlinear phase shift influenced by the intensity of the other pulses. If the two co-propagating optical fields i and j are co-polarized, the phase modulation of one field by the second field can be written as:

$$\Delta n_i = 2n_2 I_j. \quad (2.42)$$

The factor of 2 shows that XPM is twice as effective as SPM for the same intensity of light. This factor is valid for fields with the same polarization. For orthogonally linearly polarized fields it should be replaced by 2/3 [125]. The XPM mechanism does not result in transfer of energy between the interacting pulses, however it leads to coupling of the optical fields. Notably, it can cause trapping of pulses that initially travel at different speeds, but due to the XPM-induced nonlinear spectral shifts, they begin to propagate at common velocity [126, 127].

2.4.8 Four-wave mixing

Kerr effect provides a mechanism for a mutual interaction of four optical fields. For example, if two wavelength components travel together through a fiber, four-wave mixing (FWM) may cause the generation of two new frequency components. This process requires conservation of net energy, which can be written as:

$$\omega_{p1} + \omega_{p2} = \omega_s + \omega_{as}. \quad (2.43)$$

In the general case in which $\omega_{p1} \neq \omega_{p2}$, two pump beams must travel together for FWM to occur. Interestingly, degenerate FWM can be initiated with a single pump beam at a frequency $\omega_p = \omega_{p1} = \omega_{p2}$, and is often observed in optical fibers. The low-frequency sideband generated at ω_s and the high-frequency sideband generated at ω_{as} are referred to as the Stokes and anti-Stokes bands, respectively.

FWM is a phase-sensitive process, which means that the interaction depends on the relative phases of the four beams. Its effect will accumulate efficiently over longer distances only if the amplitudes added to the sidebands at one point in the fiber add constructively to those generated at other points. Hence, any (intra- or intermodal) FWM process requires satisfaction of the following linear phase-matching condition in order to efficiently generate FWM sidebands [87, 13]:

$$\Delta\beta = \beta_\mu^s + \beta_\eta^{as} - \beta_\nu^{p1} - \beta_\kappa^{p2} = 0, \quad (2.44)$$

where β_κ^{p2} represents the propagation constant of the spatial mode κ at the frequency ω_{p2} .

The phase-matching condition is driven by dispersion, but it can also be substantially modified by nonlinear phase shifts in the case of high involved optical intensities. For a completely degenerate pump fields (indistinguishable on the basis of their frequencies, polarization, or spatial profile), assuming undepleted pump, the effective phase-mismatch involving the effects of nonlinear phase changes becomes:

$$\Delta k = \Delta\beta - 2\gamma_{p,p}P_0 + 2\gamma_{s,p}P_0 + 2\gamma_{as,p}P_0, \quad (2.45)$$

where $\Delta\beta = \beta_\mu^s + \beta_\eta^{as} - 2\beta_\kappa^p$ is the phase-matching condition in the linear regime; P_0 is the input peak power; and $\gamma_{p,p}$, $\gamma_{s,p}$ and $\gamma_{as,p}$ denote the effective nonlinear parameters for pump's

self-phase modulation, pump-induced cross-phase modulation of Stokes and anti-Stokes bands, respectively, which take the form of:

$$\gamma_{i,j,k,l} = \frac{2\pi n_2}{\lambda_i} f_{i,j,k,l} \quad (2.46)$$

driven by the overlap integral of the field distributions defined in Eq. 2.37 and where $\gamma_{i,j} = \gamma_{i,j,i,j}$. It is noteworthy to emphasize that for the far-detuned FWM process investigated in Chapter 4, the integration involves the wavelength-dependent field distributions.

It is worth to note that if solely the pump wave is incident at the fiber, and the phase-matching condition is satisfied, the Stokes and anti-Stokes sidebands can be emerge from noise (vacuum fluctuations), on which I elaborate in the following section. Conversely, if a weak signal at either Stokes or anti-Stokes frequency is launched together with the pump, it is amplified while a new idler is simultaneously generated at the phase-matched frequency. The gain responsible for amplification (for either noise or the injected signal) can be written as:

$$g = \sqrt{(\gamma_{\text{FWM}} P_0)^2 - (\Delta k/2)^2}, \quad (2.47)$$

until the gain saturation occurs because of pump depletion. The maximum gain (g_{max}) is achieved for $\Delta k = 0$, thus $g_{\text{max}} = \gamma_{\text{FWM}} P_0$, with $\gamma_{\text{FWM}} = \sqrt{\gamma_{s,as,p,p} \gamma_{as,s,p,p}}$ being the effective nonlinearity for the FWM process.

2.4.9 Modulation instability

Modulation instability (MI) can be interpreted as a FWM process which occurs with a quasi-CW beam acting as a pump for the two noise-seeded sidebands. It leads to amplification of a small fluctuations of the constant pump due to the Kerr nonlinearity, typically acting in conjunction with anomalous dispersion. This leads to increasing oscillations of the optical power and amplification of sidebands in the optical spectrum proportional to the power of the optical beam, see Eq. 2.47.

Interestingly, when this process involves two different pump optical fields (at different wavelengths, orthogonal polarizations, or spatial modes), it can also occur in the normal dispersion region [128]. In Chapter 4, I observe the intermodal MI sidebands around the pump centered at 1.064 μm that arise due to bimodal interaction between the $\text{LP}_{0,1}$ and $\text{LP}_{0,2}$ modes, which are both excited due to the beam launching conditions. Phase-matching of the MI sideband peak depends on the ratio of powers injected into each mode, therefore it is possible to estimate the initial power distribution between the two spatial modes involved at the pump wavelength by analyzing the experimentally-observed frequency detuning of the sideband peaks. This method is based on the stability analysis of the stationary solutions of the two incoherently coupled nonlinear Schrödinger equations (for the modes involved) in the presence of small amplitude and phase perturbations, which is developed in Ref. [129]. The corresponding stability matrix $[M]$ of the system provides the following dispersion relation:

$$K_{\pm}^2 = \pm \sqrt{Y^2(U^2 - 2UX + 4V^2 + X^2) + Y(U + X + Y)}$$

with $U = n_2\omega_p f_{\nu,\nu,\nu} P_\nu/c$, $V = 2n_2\omega_p f_{\nu,\kappa,\nu} \sqrt{P_\nu P_\kappa}/c$, $X = n_2\omega_p f_{\kappa,\kappa,\kappa} P_\kappa/c$, and $Y = \beta_2 \Omega^2/2$. Subscripts ν and κ refer to the spatial modes involved at the pump frequency ω_p , $P_{\nu/\kappa}$ is power injected into the respective mode, overlap integral $f_{i,j,k,l}$ is defined in Eq. 2.37, and dispersion coefficient β_2 is assumed to be the same for both modes. The MI phenomenon occurs when the wave number K of the perturbation possesses a nonzero imaginary part, and manifests itself by the exponential growth of the amplitude of the perturbation with the power gain $G = 2|\text{Im}(K)|$, where K is the eigenvalue of the matrix $[M]$ with the highest imaginary part.

2.4.10 Raman scattering

Raman scattering leads to transfer of power from one optical field, which acts as a pump, to another Stokes field with a lower frequency. The frequency difference between the pump and the Stokes is determined by the vibrational modes of the medium (optical phonons), and lies in the terahertz range for fused silica. This effect, first described in 1928 [130], can be viewed as the conversion of a photon with energy $\hbar\omega_p$ by a molecule to a photon with lower energy $\hbar\omega_s$ as the molecule makes the transition to a vibrational excited state [84].

Raman scattering is characterized by the gain spectrum $g_R(\Delta f)$, where $\Delta f = \frac{\omega_p - \omega_s}{2\pi}$ represents the frequency difference between the pump and Stokes waves. The Raman response of the medium for either co-polarized or orthogonally polarized optical fields can be determined with commonly used models that consider contributions from isotropic and anisotropic molecular responses $g_a(\Delta f)$ and $g_b(\Delta f)$ [131]:

$$g_{\parallel}(\Delta f) = g_a(\Delta f) + g_b(\Delta f), \quad (2.48)$$

$$g_{\perp}(\Delta f) = g_b(\Delta f)/2, \quad (2.49)$$

where $g_\epsilon(\Delta f) = 2\gamma f_R \text{Im}(\tilde{R}_\epsilon(\Delta f))$ ($\epsilon = a, b$), $\tilde{R}_\epsilon(\Delta f)$ is the Fourier transform of $R_\epsilon(\tau)$, $R_a(\tau) = f_a h_a(\tau)$, $R_b(\tau) = f_b h_b(\tau) + f_c h_a(\tau)$, and Raman response functions for silica glass are expressed as:

$$h_a(t) = \frac{\tau_1^2 + \tau_2^2}{\tau_1 \tau_2^2} \cdot \exp\left(-\frac{t}{\tau_2}\right) \cdot \sin\left(\frac{t}{\tau_1}\right), \quad (2.50)$$

$$h_b(t) = \frac{2\tau_3 - t}{\tau_3^2} \cdot \exp\left(-\frac{t}{\tau_3}\right), \quad (2.51)$$

where $f_a = 0.75$, $f_b = 0.21$, $f_c = 0.04$, $f_R = 0.245$, $\tau_1 = 12.2$ fs, $\tau_2 = 32$ fs, and $\tau_3 = 96$ fs.

The Raman gain spectra calculated according to the described model are shown in Fig. 2.17. In silica fibers, the Raman gain spectrum extends over a broad range of frequencies. When considering transfer to the same polarization as the pump, the gain spectrum g_{\parallel} extends up to 40 THz and has a broad peak around 13 THz. Transfer to the polarization orthogonal to the pump is characterized by a significantly lower Raman gain spectrum g_{\perp} with a maximum around 3 THz and a flat plateau up to 15 THz.

Raman gain can act over long propagation distance and lead to a substantial transfer of power to the Stokes wave. When a probe beam is launched together with the continuous-wave pump into the fiber, it is amplified in a process of stimulated Raman scattering as long as

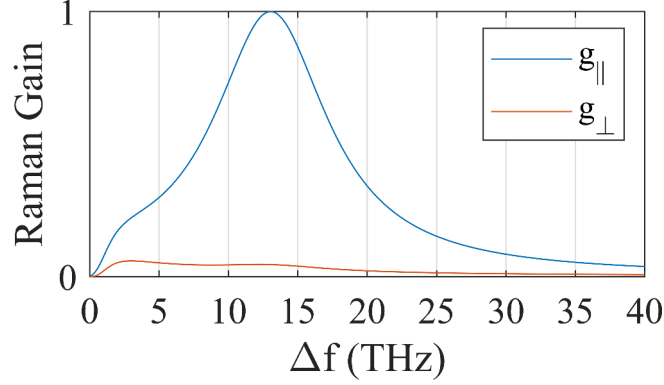


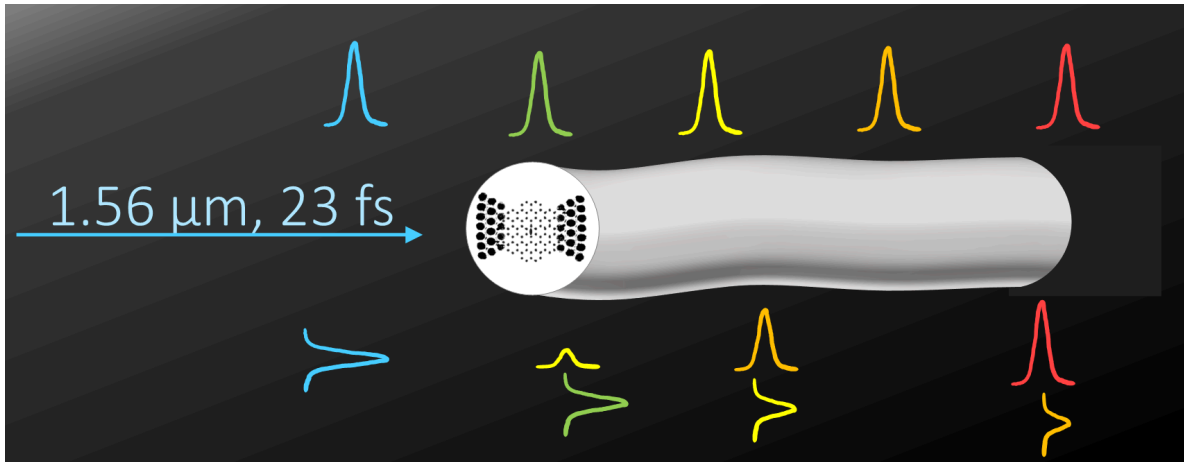
Figure 2.17: Normalized Raman gain in silica fibers calculated for co-polarized ($g_{||}$) and orthogonally polarized (g_{\perp}) pump and Stokes pulses.

its frequency lies in the bandwidth of the gain spectrum. If only the pump beam is present, spontaneous Raman scattering generates photons within the entire bandwidth of the Raman gain spectrum, and the frequency component with the highest gain builds up most rapidly. Interestingly, for pulses with a sufficiently large spectral bandwidth, such as ultrashort solitons, Raman scattering acts within the spectrum of the single pulse, leading to redistribution of energy from the components at higher frequencies to the components at lower frequencies. This leads to a shift of the pulse spectrum towards longer wavelengths, in the case of solitons known as the Raman soliton self-frequency shift (SSFS) [132].

It should be highlighted that for short pulses with duration of less than 100 ps, the Stokes generation might be limited due to the group velocity mismatch. Since the pump and Stokes pulses have different frequencies, they travel at different velocities and lose temporal overlap at propagation distances exceeding the walk-off length, which hinders amplification of the Stokes pulse. Interestingly, Raman scattering into a Stokes mode different than the pump mode potentially allows to obtain much closer group velocities of the two pulses, allowing Stokes amplification to occur over longer distances of propagation [133, 134]. In Chapter 3, I study the effects of orthogonal Raman scattering between two polarization modes on ultrashort pulses propagating in photonic crystal fibers.

This chapter outlined the basic designs of optical fibers and the fundamental phenomena that govern their light-guiding properties. It is important to acknowledge that the silica based step-index, graded-index, and photonic crystal fiber introduced here represent only a subset of the wide range of available types of optical fibers. Other fiber types, such as hollow-core, Bragg, or twisted fibers, and fibers fabricated from different materials (including chalcogenide, tellurite, or ZBLAN fibers) are undoubtedly important in the field of fiber optics and have found a specific range of applications. The decision to focus on introducing the three selected designs is based on their use in the investigations detailed in the subsequent chapters.

Chapter 3



Soliton trapping in birefringent photonic crystal fibers

The optical solitons are intense light pulses that propagate in a nonlinear medium in anomalous dispersion regime. They retain shape due to balance between chromatic dispersion and self-phase modulation. The possibility of transmission of such undistorted pulses in optical fibers was predicted by Hasegawa and Tappert in 1973 [135]. In 1986, Mitschke and Mollenauer discovered that an ultrashort soliton undergoes self-frequency shift caused by energy transfer from the higher to the lower frequency part of the spectrum due to Raman scattering [132] (SSFS – soliton self-frequency shift). This phenomenon allows for continuous tuning of the soliton’s spectral position and facilitates reaching wavelengths not available with typical laser sources. In recent years, the possibility of effectively tuning solitons was investigated in photonic crystal fibers (PCFs). They appeared to be perfect media for spectral tuning of solitons as they provide control over the shape of dispersion curve and allow to obtain a small effective mode area which results in high effective nonlinearity [136, 137, 138, 139].

The second thread of the recent research related to solitons in optical fibers is focused on few-mode fibers (FMFs) and multimode fibers (MMFs) [140]. In reference to photonic crystal fibers, the FMFs and MMFs have relatively high effective area, thus they can guide high-intensity pulses. Moreover, they enable more complex dynamics by providing additional degrees of freedom to the system. Propagation of solitons in higher-order modes of MMF was investigated by Rishøj et al. [141] in a step-index silica fiber with a 100 μm core. The conversion is enabled by Raman scattering and group velocity matching of distinct spatial modes. When the two modes have identical group velocities at spectral separation corresponding to the frequency difference at which nonlinear Raman gain is maximized, a new, spectrally separated

ultrashort pulse is initiated in a second mode from quantum noise. This process is consecutively repeated several times during the propagation in the 12-meter-long fiber, when the generated mode undergoes the SSFS and reaches the group-velocity matched wavelength with another mode at the frequency separation within the Raman gain bandwidth.

Raman scattering is not the only phenomenon that is important in describing nonlinear pulse propagation. Due to cross-phase modulation (XPM), the intense pulse can force the common group velocity causing trapping of the other copropagating pulse. When two copropagating pulses are orthogonally polarized, the XPM induces nonlinear phase shifts in both polarization components which depend on the intensity of the orthogonal polarization component [84]. This kind of mutual interaction can lead to trapping of orthogonally polarized pulses. The first studies on soliton trapping showed a numerical investigation of XPM in conventional birefringent fibers [126, 127]. They were followed by the experimental demonstration of soliton trapping in low-birefringent optical fiber in the low power regime [142]. In this experiment, the linearly polarized pulse with azimuth angle $\theta = 45^\circ$ excited two polarization components. The x (slow)-axis component propagated at shorter wavelength to increase the group velocity, and the y (fast)-axis component propagated at longer wavelength to decrease the group velocity. Finally, both components propagated with a common group velocity.

Interestingly, there exists a mechanism that can transfer energy from one polarization component to the other. This mechanism is provided by orthogonal Raman scattering. The energy from the shorter wavelengths in one polarization is transferred to the longer wavelengths in orthogonal polarization. The gain spectrum for orthogonally polarized (g_\perp) pulses is shown in Fig. 3.1, normalized to the maximum of g_\parallel (see Fig. 2.17 for both g_\parallel and g_\perp). The normalized orthogonal Raman gain exceeds 0.03 for frequency shifts between 1.2 and 17.4 THz and its maximum is located around 3 THz. Although the orthogonal Raman response is weaker than co-polarized Raman response, it plays a key role in the pulse trapping observed in the conventional birefringent fiber by Nishizawa [143, 144]. In those experiments, the soliton polarized along the slow fiber axis transferred part of its energy to the fast axis. The generated pulse polarized along the fast fiber axis was trapped by slow-axis component and fed by the trapping pulse through the Raman scattering. The authors confirmed that the pulses overlapped temporally and copropagated along the fiber. In the following work, the authors also investigated pulse trapping of co-linearly polarized pulses across zero-dispersion wavelength [145]. Additionally,

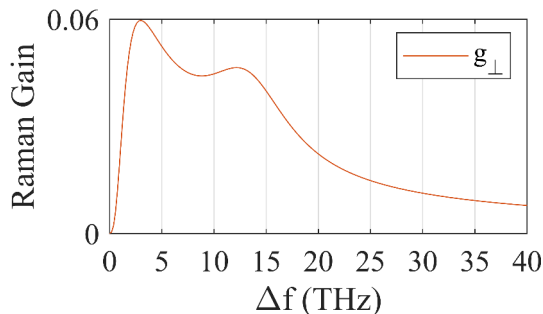


Figure 3.1: Raman gain in silica fibers calculated for orthogonally polarized pulses based on model from Ref. [131]. Gain is normalized to the maximum of Raman gain for co-polarized pulses.

trapping of an orthogonally polarized continuous wave [146] and even pulse trapping and amplification of incoherent light from a super-luminescent diode [147] were demonstrated in birefringent fibers.

In the referenced works [143, 144, 146, 147], a conventional birefringent fiber was used. In this type of fiber, the group velocity matching of polarization modes is possible between a shorter wavelength aligned to the slow (x) axis and a longer wavelength aligned to the fast (y) axis. Consequently, pulse trapping is possible when the trapping pulse is aligned to the slow axis and the generated trapped pulse is aligned to the fast axis.

In the following chapter I investigate soliton trapping in two birefringent photonic crystal fibers with a group birefringence on the order of 10^{-4} and 10^{-3} . Such detailed experimental study is conducted for the first time in fibers exhibiting a negative value of group birefringence, achieved due to the specific fiber design. Through control of the azimuth angle of the linearly polarized input pulse, pulse peak power, and fiber length, I obtain different detunings and energy transfers to the two polarization components of the output pulse. Interestingly, I observed that the characteristics of the wavelength shifts of the two output polarization components differ qualitatively depending on the magnitude of fiber birefringence.

3.1 Study conditions

To observe the effect of Raman scattering on solitons, I used a mode-locked Er-doped fiber laser (FemtoFiber pro IR, TOPTICA Photonics) operating at $1.56\ \mu\text{m}$ and generating 23 fs pulses (at FWHM, corresponding to $T_0 = 13\ \text{fs}$) with a repetition rate of 80 MHz and average output power of about 200 mW. The laser beam was passed through a polarizer and half-wave plate to control its power level and polarization state. I monitored the beam average power with a thermal power sensor (Thorlabs, S401C). I recorded the output spectrum with an optical spectrum analyzer (Yokogawa AQ6376). The pulses were injected into the fiber with an aspheric lens (Thorlabs, C230TMD-C).

I used PCF designed for SSFS and manufactured in-house through stack-and-draw method from a single preform in the Laboratory of Optical Fibers Technology at the Maria Curie Skłodowska University (Lublin, Poland). A germanium-doped core (with 18 mol % doping level) is surrounded by rings of air holes arranged in a honeycomb lattice. Three rows of larger air holes arranged in a bow-tie centered on the core assist in achieving high birefringence. Modification of conditions during the drawing process influenced the geometrical parameters along the fiber's length, leading to varying guiding properties for different segments. For the investigation of soliton trapping, I selected two sub-100-meter-long segments from different parts of the drawn fiber, to which I will refer as PCF 1 and PCF 2. The SEM images of the two fibers cross-sections in the core region are shown in the insets of Fig. 3.2(a-b). Elliptical core of PCF 1 has a major axis of $4.5\ \mu\text{m}$ and a minor axis of $2.9\ \mu\text{m}$, while the core of PCF 2 is more elongated with a major axis of $5.1\ \mu\text{m}$ and a minor axis of $2.5\ \mu\text{m}$. The lattice pitch of the air hole microstructure is $3.0\ \mu\text{m}$ in both PCFs and the average diameter of the holes closest to the core is $0.9\ \mu\text{m}$ in PCF 1 and $1.5\ \mu\text{m}$ in PCF 2.

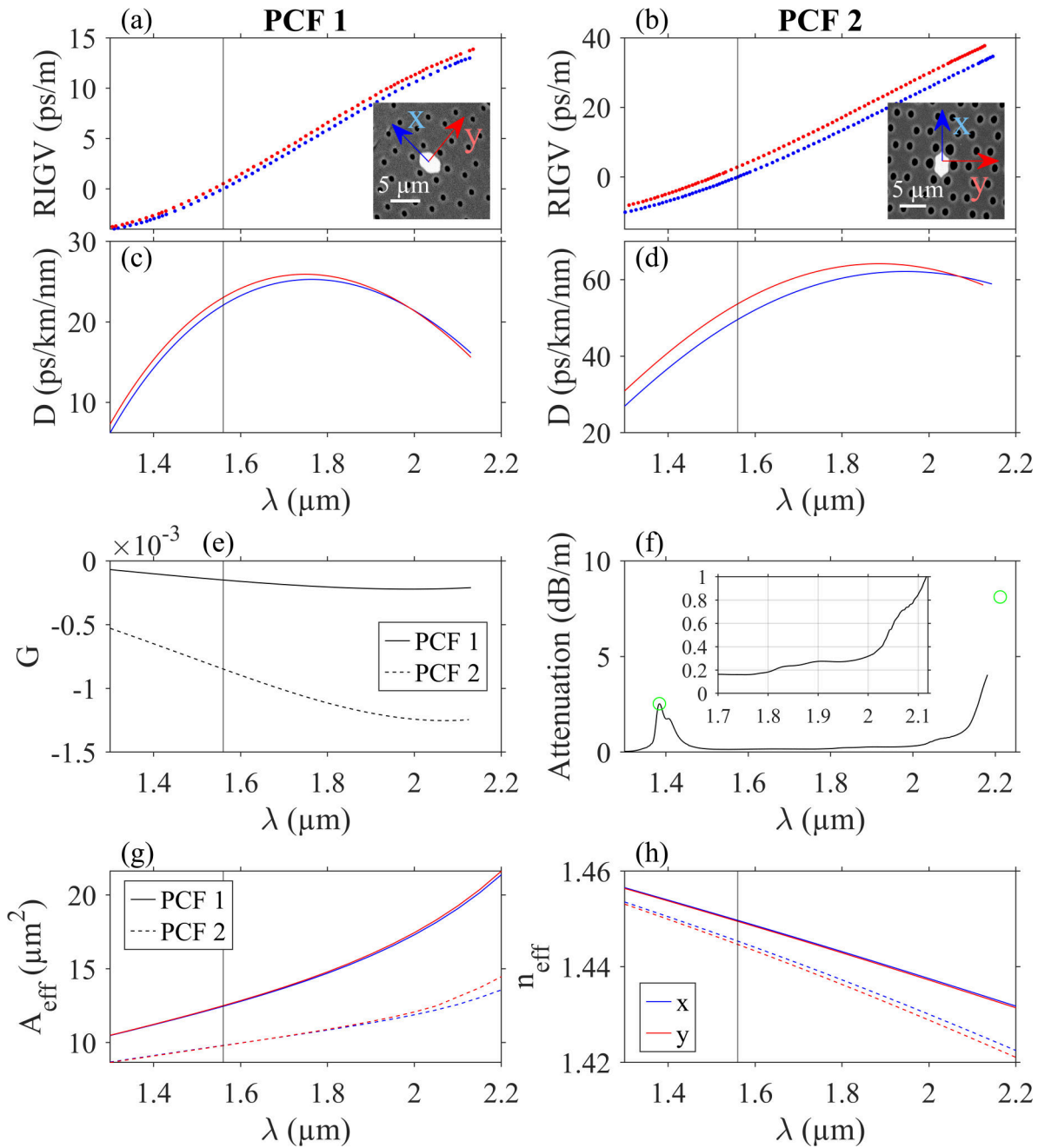


Figure 3.2: Transmission properties of the two photonic crystal fibers. Measured related inverse group velocities RIGV (a-b) and calculated chromatic dispersion D (c-d) of the mode polarized along x axis (blue) and y axis (red) in PCF 1 (a,c) and PCF 2 (b,d). Insets in (a,b) show SEM images of the fiber cross-section with arrows indicating direction of x and y axis and a white scale bar of $5\ \mu\text{m}$. Group birefringence (e) measured in PCF 1 and PCF 2. Measured attenuation (f) with an estimated maximum at $2.21\ \mu\text{m}$ indicated with green circle. Calculated mode effective area (g) and effective refractive index (h) of the two polarization modes of both PCFs. A vertical black line indicates a $1.56\ \mu\text{m}$ pump wavelength.

The fibers' geometry results in their birefringence and different modal parameters depending on the direction of the linear polarization of light. Blue and red arrows on the cross-sections indicate orientation of the polarization axis of the slow (x) and fast (y) mode. I employed several experimental characterization techniques to gain insight into the transmission properties of the two polarization modes of both fibers. The measured and calculated parameters are shown in Fig. 3.2.

I used white-light interferometry [102] to characterize relative inverse group velocities (RIGV, $\Delta\beta_1^{(x/y)}$) of the two polarization modes in a short fiber section, see Fig. 3.2(a,b) for RIGV related to inverse group velocity of the x polarization mode at the pump wavelength. This allowed to calculate dispersion, shown in panels (c,d), and group birefringence, shown in panel (e). Chromatic dispersion is simply the slope of RIGV. In PCF 1, it reaches $22.1 \text{ ps km}^{-1} \text{ nm}^{-1}$ ($23.0 \text{ ps km}^{-1} \text{ nm}^{-1}$) at $1.56 \mu\text{m}$ pump wavelength for the pulses polarized along x (y) axis. In PCF 2, it reaches $49.6 \text{ ps km}^{-1} \text{ nm}^{-1}$ ($53.7 \text{ ps km}^{-1} \text{ nm}^{-1}$) at the pump wavelength for the pulses polarized along x (y) axis.

The difference between RIGV measured for the two polarization modes allows to determine the group birefringence: $G = (\Delta\beta_1^x - \Delta\beta_1^y)c$, where c is the speed of light in vacuum. In PCF 1, $G = 1.5 \times 10^{-4}$ at the pump wavelength, and 2.2×10^{-4} at $2 \mu\text{m}$. PCF 2 is characterized by a more elongated core, which results in a higher group birefringence, reaching 8.5×10^{-4} at the pump wavelength, and 1.25×10^{-3} at $2 \mu\text{m}$.

I used the cut-back technique to measure fiber attenuation in the near-infrared spectral region, see Fig. 3.2(f). To evaluate the low-loss spectral region I used a 100-meter-long segment between PCF 1 and PCF 2, which should be characterized by similar attenuation as both PCFs. In the long wavelength range, attenuation exceeds 1 dB/m for wavelengths longer than $2.12 \mu\text{m}$. The used source provided light only up to $2.18 \mu\text{m}$, at which the attenuation exceeded 4 dB/m. I was able to gain insight into attenuation at longer wavelengths by determining loss related to the OH absorption band at $1.38 \mu\text{m}$ (reaching 2.53 dB/m) and using relation provided in Ref. [54] to find corresponding loss level at $2.21 \mu\text{m}$, which should be 201/62.7 times higher and reach 8.11 dB/m. The intensities of the measured and estimated maxima of two absorption bands are marked with green points in panel (f).

In addition, the geometrical parameters determined from the SEM images were used in the numerical modeling of the transmission properties performed using the Comsol Multiphysics software by the team from the Department of Optics and Photonics at Wrocław University of Science and Technology. In Fig. 3.2(g-h), I show the mode effective area A_{eff} and effective refractive indices determined as a function of wavelength.

The two birefringent PCFs are characterized by negative values of group birefringence. In Fig. 3.2(a-b) we clearly see that pulses polarized along the y fiber axis have a higher RIGV and group refractive index (lower group velocity) than pulses polarized along the x fiber axis. This observation aligns with other reports on PCFs [148], but is contrary to reports on conventional birefringent fibers [143, 144, 146, 147]. Consequently, group-velocity-matching could be achieved if the polarization of a shorter wavelength is aligned to the y axis and the polarization of a longer wavelength is aligned to the x axis. In the next section, I investigate the dynamics of pulses polarized along x or y axis propagating in birefringent PCFs.

3.2 Energy conversion for pump pulses polarized along fiber axis

In the following I investigate the influence of input pulse power and distance of propagation in fiber on spectral pulse dynamics in the two birefringent PCFs. I found that the soliton dynamics significantly depends on whether the input beam is polarized along the x or y axis of the fiber.

3.2.1 Investigation for increasing pump power

Figure 3.3 shows the optical spectra recorded at the output of 20-meter-long sections of PCF 1 and PCF 2 for different pump powers. The power level is displayed in the top left corner for each panel, and represents the input beam average power measured before the lens used for coupling light into the fiber. I used polarizer to separate the signal components polarized along the x (blue line) or y (red line) fiber axis.

The input pulse forms a soliton, which undergoes Raman SSFS. The soliton wavelength increases with power, but the soliton can be tuned hardly beyond $2.1\ \mu\text{m}$ due to the abrupt increase of attenuation. When the input pulse is polarized along the x axis (top panels), the soliton pulse is generated with a well-defined central wavelength, indicated with blue dashed lines. However, when the input pulse is polarized along the y axis (bottom panels), the generated soliton pulse polarized along the y axis, indicated with red dashed lines, is accompanied by an orthogonally polarized component at longer wavelengths. To improve clarity, the central wavelengths of the soliton generated when the input pulse is polarized along the x axis and of both polarization components generated when the input pulse is polarized along the y axis are plotted as a function of pump power in Fig. 3.4.

The intensity of the signal starts to decrease when it is shifted beyond $2.05\ \mu\text{m}$. When PCF 1 is pumped by 100 mW beam polarized along the y axis, the signal component polarized orthogonally to the input pulse is even attenuated below the noise level. This occurs due to high transmission loss, which, based on the measurements shown in Fig. 3.2(f), results in a power decrease of 12 dB at $2.05\ \mu\text{m}$, 17 dB at $2.10\ \mu\text{m}$, and 40 dB at $2.15\ \mu\text{m}$ over 20 meters of the fiber. However, it should be noted that these values represent an upper limit, and the actual soliton attenuation is lower, as its wavelength continuously shifts during propagation, meaning that high loss affects it on a distance shorter than 20 meters. The relationship between the soliton shift and the fiber length will be discussed in the next section.

In top right corners of each panel in Fig. 3.3 I provide the polarization extinction ratio (PER) of solitons. It ranges from 9.1 dB to 11.5 dB in PCF 1, and from 22.2 dB to 37.8 dB in PCF 2. It is evident that PER of solitons is significantly higher when the pulse propagates in PCF 2. This is as anticipated, because the increased birefringence of PCF 2 decreases linear couplings between orthogonal polarizations caused by the fiber's imperfections, which aids in preserving the pulse polarization. There appears to be no clear correlation between the polarization purity of the solitons and the pulse power. This indicates that polarization extinction is limited by linear couplings.

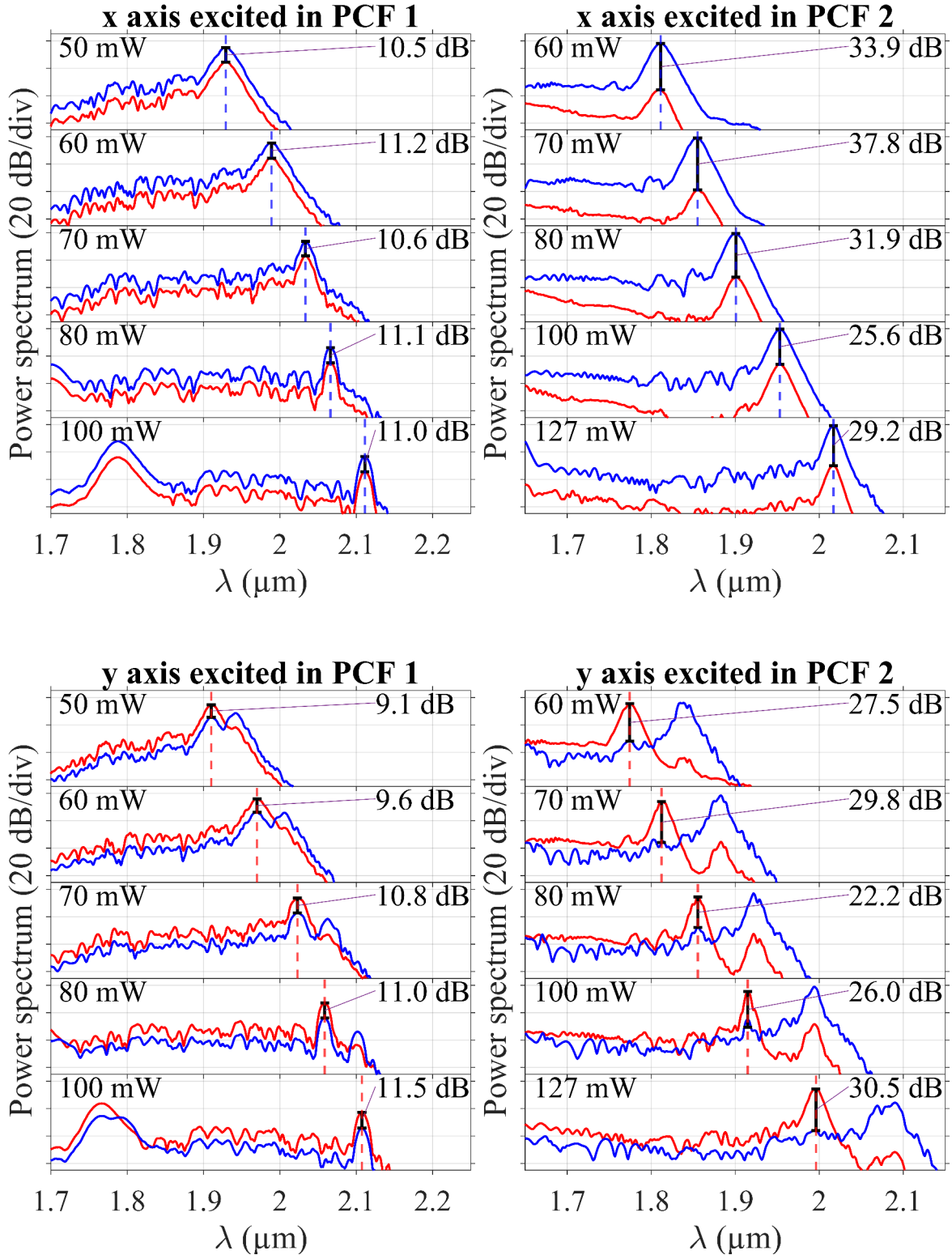


Figure 3.3: Optical spectra recorded at the output of 20-meter-long section of PCF 1 (left) or PCF 2 (right) for increasing power of pump beam polarized along the x (top) or y (bottom) axis of the fiber. Line colors denote signal components polarized along the x (blue) or y (red) axis. Average power of the input beam is indicated in the top left corner of each panel. Polarization extinction ratio of solitons is given in the top right corner of each panel.

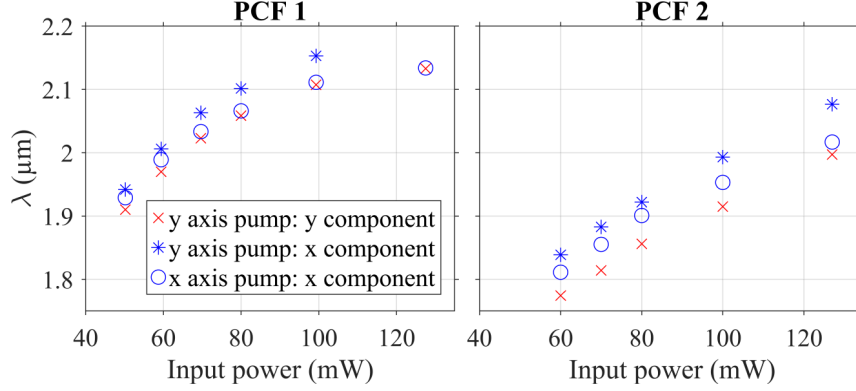


Figure 3.4: Central wavelength of solitons from Fig. 3.3 as a function of pump power for PCF 1 (left) and PCF 2 (right) after 20 m of propagation in the fiber. When x axis is excited, only the signal component polarized along the x axis is observed (blue circles). When y axis is excited, the signal component polarized along the x axis (blue asterisks) is observed in addition to the original component polarized along the y axis (red crosses).

Figure 3.4 allows to easily compare the soliton detunings depending on the polarization direction of the input beam. The soliton generated from the input beam polarized along the x axis (blue circles) is more detuned than the soliton generated with the same input power from the beam polarized along the y axis (red crosses). This can be attributed to the lower dispersion of the x polarization mode. As both solitons are characterized by $N = 1$ (see Eq. 2.40), and carry a similar energy (as shown in Fig. 3.5), which is proportional to $P_0 T_0$, the duration of soliton in x polarization mode must be shorter to maintain $N = 1$. A shorter soliton duration corresponds to a higher peak power P_0 , resulting in a larger SSFS for the soliton carried by the mode with a lower dispersion. The difference in the detunings of orthogonally polarized solitons decreases with the soliton wavelength shift (particularly after passing 2 μm), which is related to the fiber attenuation. This observation is valid for both fibers.

Furthermore, for the input pulse polarized along the y axis, the difference between the spectral positions of the generated soliton (red crosses) and the orthogonally polarized signal component (blue asterisks) increases very slowly with power (and with the soliton wavelength): from 32 nm to 46 nm in PCF 1; and from 64 nm to 80 nm in PCF 2. Notably, the difference is smaller in PCF 1 than in PCF 2. This topic will be examined more thoroughly in the later sections.

When comparing the central wavelengths of the solitons in PCF 1 and PCF 2 for a specific power level of the input beam, it is evident that the solitons shift approximately 150-200 nm further when propagating in PCF 1. For instance, when the x (y) axis is excited with an input power of 70 mW, the soliton shifts to 2066 nm (2059 nm) in PCF 1, compared to 1855 nm (1814 nm) in PCF 2. At first impression, this seems unexpected, as PCF 1 has a lower nonlinearity coefficient γ owing to the larger mode effective area A_{eff} (by almost 30%), as shown in Fig. 3.2(g). Two key factors account for the observed dynamics.

The first factor is related to the significant difference in dispersion between the two fibers: the dispersion of PCF 1 is less than half the dispersion of PCF 2 at the pump wavelength. Using again the analytical formula 2.40, I have verified that the fundamental solitons ($N = 1$)

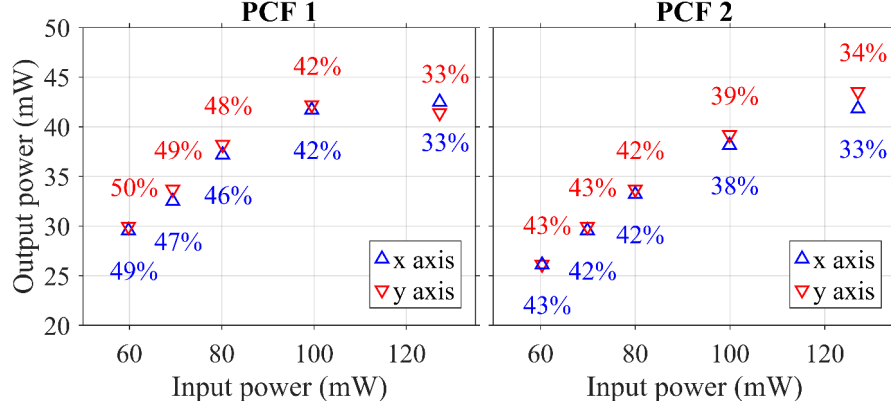


Figure 3.5: Relationship between the fiber output power and the power of the input beam in short, 2-meter-long sections of PCF 1 (left) and PCF 2 (right) for input beam polarization aligned along x and y axis of the fiber. The calculated ratio of powers is indicated below markers for x polarization and above markers for y polarization.

emerge in both fibers for the lower investigated powers. Assuming that both solitons carry the same energy proportional to $P_0 T_0$, it can be deduced that due to the higher $\gamma/|\beta_2|$ ratio in PCF 1 compared to PCF 2, the soliton duration T_0 must be shorter, leading to higher peak power and the shift to longer wavelengths. This explains the greater soliton shift observed in PCF 1, assuming the energy level of the two solitons in both fibers is the same.

However, the light coupling efficiencies differ, favoring PCF 1 even further (higher soliton energy requires even shorter soliton duration to maintain the same N). Due to the different geometry of the fiber cores, optimal alignment with respect to the input beam allows more light to be coupled into PCF 1 than into PCF 2. This is confirmed by analyzing the power of the collimated fiber output as a function of the input beam power for short 2-meter-long sections of both fibers in Fig. 3.5. In PCF 1 the ratio between output and input powers reaches 50% for 60 mW power of the input beam, and in PCF 2 this ratio is equal to 43%. The measured ratio does not depend on the beam polarization. The results are similar for input powers of 60 mW, 70 mW, and 80 mW, however the power ratios decrease for higher investigated input powers, namely 100 mW and 127 mW. This might result from soliton crossing spectral regions characterized by increased losses - for example, due to absorption bands of combination modes of OH and SiO₄ tetrahedron vibrations around 1.894 μm [54]. It should be mentioned that the actual coupling efficiency is higher than the provided values, because the pulse energy decreases after passing the coupling lens at the fiber input and the collimating lens at the fiber output and during the 2 meters of propagation due to Raman scattering leading to SSFS as well as attenuation. Nevertheless, the similar power ratios obtained for input powers of 60 mW, 70 mW, and 80 mW confirm that it is possible to couple more energy into PCF 1, which aids in obtaining larger soliton shifts in this fiber than in PCF 2 for the same power of the input beam.

Finally, it is worth remarking that the data presented in Fig. 3.5 can be used to determine the approximate level of power coupled into the fiber from the average power of the input beam that is provided in this study. I have decided to refer to the power of the input beam, because

the fiber output power significantly changes with the fiber length, and is also influenced by soliton dynamics (when the SSFS occurs, part of the photon energy is lost due to Raman scattering). The input beam powers for which similar levels of power are obtained at the output of 2-meter-long fiber sections are 60 mW in PCF 1 and 70 mW in PCF 2 (with 30 mW output power) or 70 mW in PCF 1 and 80 mW in PCF 2 (with 33 mW output power). In the subsequent section, where I investigate soliton detunings in cutback experiments, I compare the results obtained for both PCFs with the two indicated sets of input powers.

3.2.2 Investigation along the propagation distance

In this section I investigate the spectral pulse dynamics with propagation distance, studied via cutback of the original 20-meter-long PCF 1 and 100-meter-long PCF 2. I took special care to keep the fiber launch conditions unchanged. Figure 3.6 presents the spectra registered at the output of fiber sections of different lengths: 2 m, 8 m, 20 m, and 100 m; for the fixed input beam average powers of 60 mW for PCF 1 and 70 mW for PCF 2, which correspond to the same average power of 30 mW measured at the output of 2-meter-long sections of both PCFs. A second set of similar characterizations is shown in Fig. 3.7 for increased input powers: 70 mW for PCF 1 and 80 mW for PCF 2, which correspond to 33 mW measured at the output of 2-meter-long fiber sections. The data in Fig. 3.7 serves to qualitatively support the analysis performed in the subsequent paragraphs, in which I refer to Fig. 3.6.

In both excitation cases in the two fibers, the solitons shift toward longer wavelengths during propagation. This shift occurs due to the energy transfer from the shorter to the longer wavelength part of their spectrum, driven by the scalar Raman gain (see g_{\parallel} in Fig. 2.17). The soliton spectra narrow during propagation, and the SSFS efficiency generally decreases. The SSFS efficiency η , defined as the ratio of the soliton power (measured using the bandpass filter Thorlabs FB2000-500) to the total output power, is provided in Fig. 3.6. The data for the 2-meter-long PCF 2 is not included, as the soliton shifts insufficiently far to avoid cutting it off by the bandpass filter. The spectral narrowing and decrease of SSFS efficiency are direct consequences of the attenuation [149]. As the soliton peak power decreases its duration must increase to satisfy Eq. 2.40, and soliton narrows spectrally.

Interestingly, the polarization extinction ratio of solitons does not exhibit the same dynamics in the two PCFs. In PCF 1, the PER steadily declines as the propagation distance increases from 2 m to 20 m: dropping from 24.5 dB to 11.2 dB for the x axis excitation, and from 31.5 dB to 9.6 dB for the y axis excitation. In PCF 2, the soliton PER does not follow the same trend over the initial 20 meters of propagation. Instead, it varies between 21.5 dB and 37.8 dB, without any apparent correlation to the propagation distance. It is only after 100 meters of propagation that the PER drops to 13.1 dB for the x axis excitation, and to 18.9 dB for the y axis excitation, which still remains a better extinction ratio than after 20 meters of propagation in PCF 1. This relatively superior performance of PCF 2 in terms of preserving the polarization of the soliton pulses can be attributed to its high birefringence. However, maintaining a high polarization extinction ratio of the main soliton is not the only requirement for ensuring pure polarization of the output pulses.

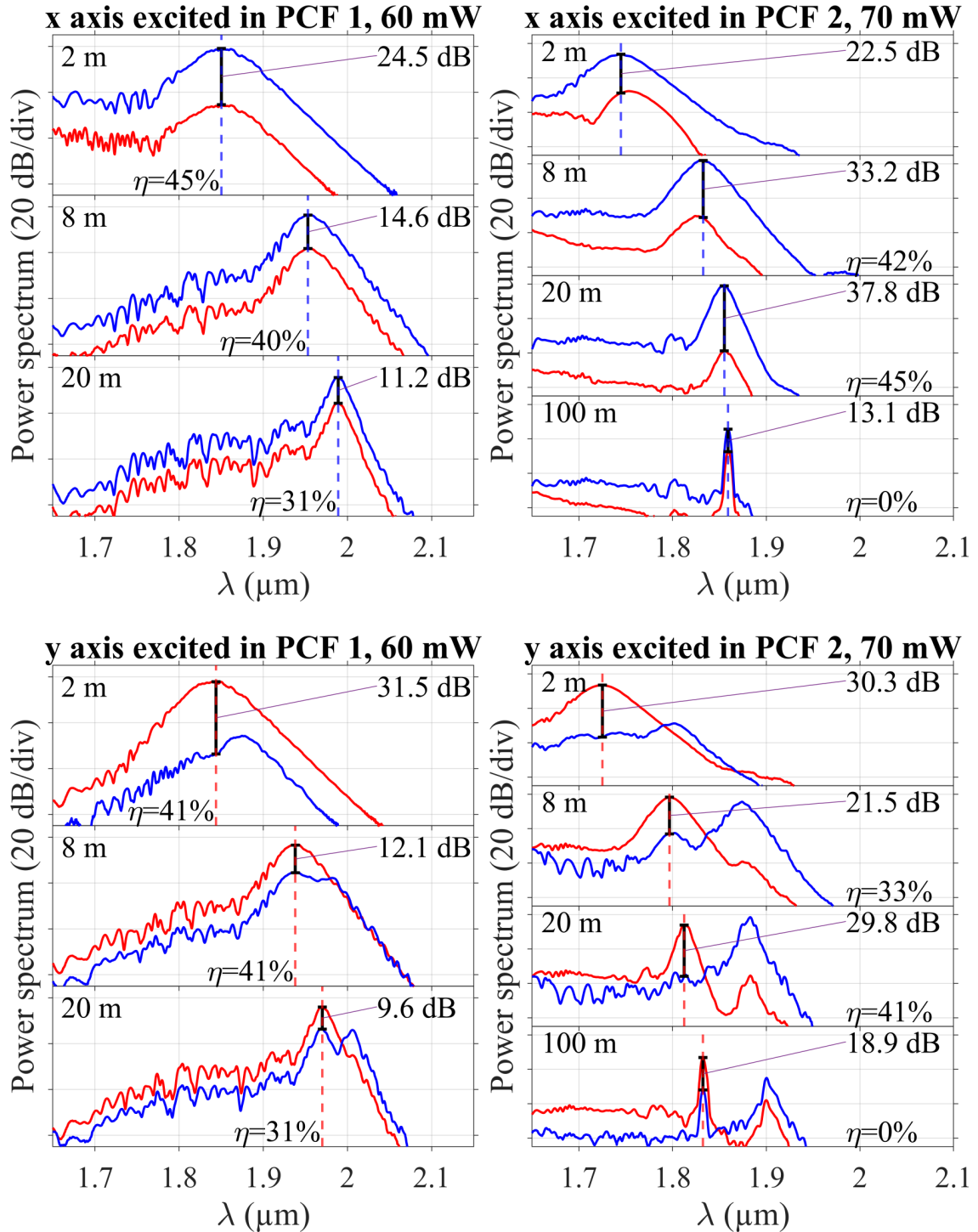


Figure 3.6: Optical spectra recorded at the output of fiber sections of increasing lengths with an average power of the input beam equal to 60 mW for PCF 1 (left) or 70 mW for PCF 2 (right). The direction of the input beam polarization is along the x axis (top) or y axis of the fiber. Line colors denote signal components polarized along the x (blue) or y (red) axis. Fiber length is indicated in the top left panel of each panel. Polarization extinction ratio of solitons is given in the top right corner of each panel, and η denotes ratio of output soliton power to total output power.

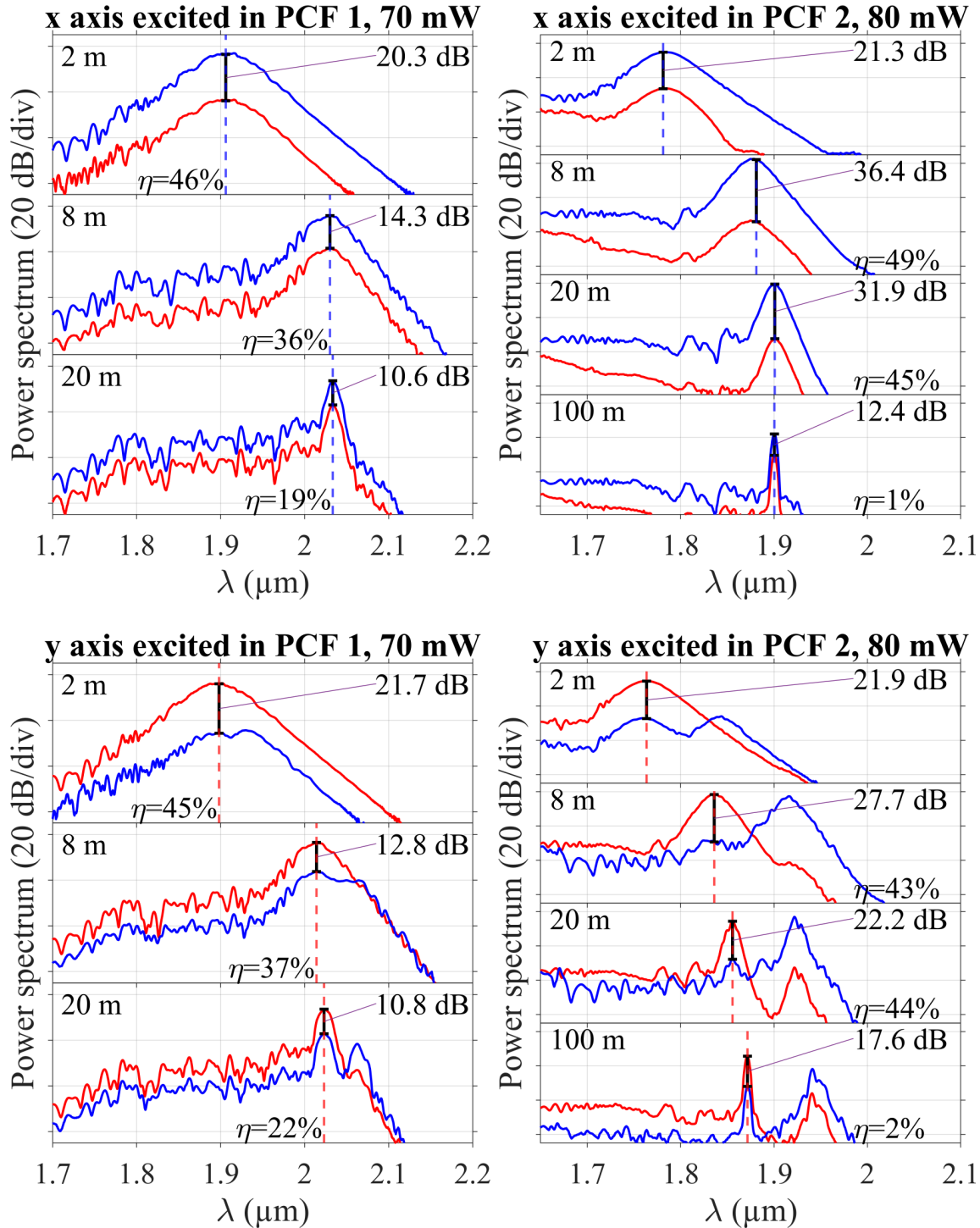


Figure 3.7: Optical spectra recorded at the output of fiber sections of increasing lengths with an average power of the input beam equal to 70 mW for PCF 1 (left) or 80 mW for PCF 2 (right). The direction of the input beam polarization is along the x axis (top) or y axis of the fiber. Line colors denote signal components polarized along the x (blue) or y (red) axis. Fiber length is indicated in the top left corner of each panel. Polarization extinction ratio of solitons is given in the top right corner of each panel, and η denotes ratio of output soliton power to total output power.

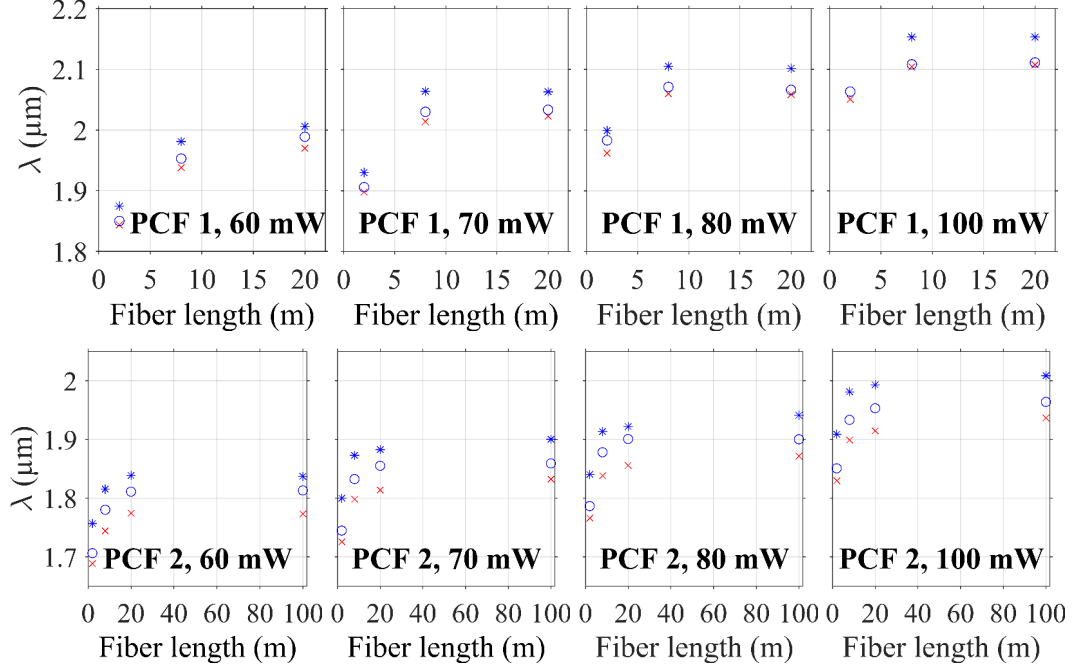


Figure 3.8: Central wavelength of polarization components of the solitons as a function of propagation distance in PCF 1 (top row) and PCF 2 (bottom row) for four power levels of the input beam. When the x axis is excited, only the signal component polarized along the x axis is observed (blue circles). When the y axis is excited, the signal component polarized along the x axis (blue asterisks) is observed in addition to the original component polarized along the y axis (red crosses).

As noted in the previous section, when the input pulse is polarized along the y axis, the generated soliton polarized along the y axis is accompanied by an orthogonally polarized component at longer wavelengths, which affects the polarization purity of the fiber output. The intensity of this second component increases with propagation distance, with an exception for 100-meter-long PCF 2, where it is affected by losses accumulated over a long propagation distance. The observed gradual increase of intensity indicates that the pulse component polarized along the x axis emerges due to orthogonal Raman scattering, which enables the simultaneous conversion of wavelength and polarization.

Figure 3.8 illustrates the soliton wavelength shifts as a function of propagation distance in PCF 1 and PCF 2, respectively. The most significant wavelength shift occurs within the initial few meters of propagation. At later stages, the rate of spectral shift decreases considerably, primarily due to the reduction of soliton energy (as indicated by the calculated η) caused by attenuation. Furthermore, the solitons shift further in PCF 1 than in PCF 2. The reasons for this behavior are discussed in the paragraphs related to Fig. 3.4.

Finally, for the input pulse polarized along the y axis, the difference between the spectral positions of the generated soliton (red crosses) and the orthogonally polarized signal component (blue asterisks) does not appear to be correlated with propagation distance, and is very similar no matter the fiber length. As noted in the previous sections, this difference is smaller in PCF 1 than in PCF 2. In the following, I investigate how the spectral positions of the different pulse components depend on the azimuth of the input beam polarization.

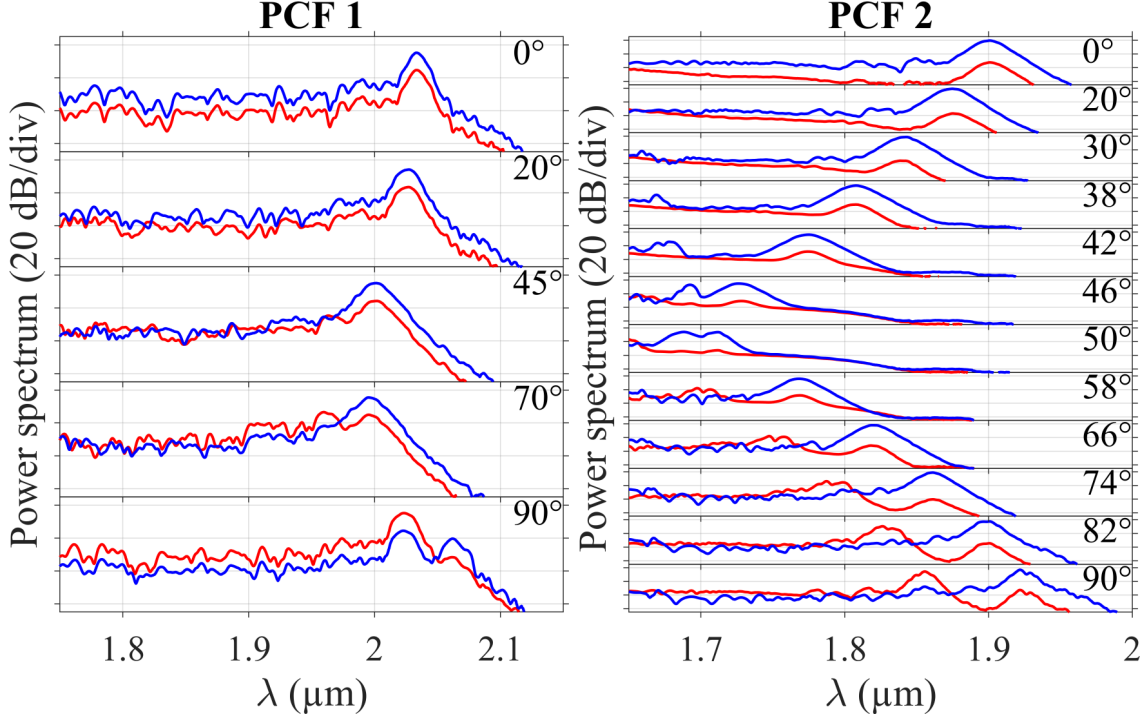


Figure 3.9: Optical spectra recorded at the output of 20-meter-long fiber sections with an average power of the input beam equal to 70 mW for PCF 1 (left) and 80 mW for PCF 2 (right) for different direction of the input pulse polarization with respect to the x fiber axis. Line colors denote signal components polarized along the x (blue) or y (red) axis.

3.3 Energy conversion for other polarization azimuths of pump pulses

In the previous sections I analyze the soliton dynamics using linearly polarized pulses with the azimuth aligned along the x or y fiber axis. However, I obtained additional interesting results as the polarization direction of the input beam is rotated. Those findings are detailed in this section. Figure 3.9 shows the spectra registered at the output of 20-meter-long sections of PCF 1 and PCF 2 for different azimuths of input polarization θ with respect to the x axis of the fiber.

When the polarization azimuth is not exactly aligned to the x axis, the soliton shifts to shorter wavelengths: in PCF 1 (PCF 2) for $\theta = 20^\circ$ it shifts to 2027 nm (1875 nm) instead of 2033 nm (1901 nm) for $\theta = 0^\circ$. Similar observation can be made when the polarization azimuth is not exactly aligned to the y axis: in PCF 1 (PCF 2) for $\theta = 70^\circ$ the soliton polarized along the y axis shifts to 1960 nm (1775 nm) instead of 2024 nm (1856 nm) for $\theta = 90^\circ$ and the second pulse component polarized along the x axis shifts to 1995 nm (1844 nm) instead of 2062 nm (1922 nm). This can be explained by less energy from the input pulse participating in generation of the soliton polarized along the specific fiber axis, which results in its lower peak power and smaller shift over the 20 meters of propagation. The intensity of the soliton polarized along the y axis is lower for the excitation at $\theta = 70^\circ$ than at $\theta = 90^\circ$, contrary to

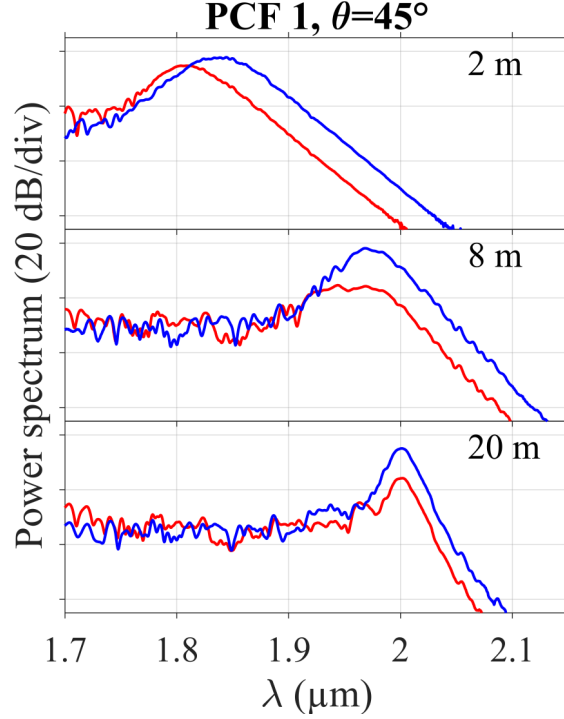


Figure 3.10: Optical spectra recorded at the output of increasing lengths of PCF 1 with 70 mW input beam average power for equal excitation of the two fiber axes. Line colors denote signal components polarized along the x (blue) or y (red) axis.

the intensity of the second pulse component, which outgrows the soliton, even at $\theta = 82^\circ$ in PCF 2. This is because the energy coupled into the x axis facilitates the transfer from the original soliton to the trapped pulse.

An interesting set of results is obtained for the excitation at $\theta \approx 45^\circ$, when an equal amount of energy is coupled into both fiber axes. At the beginning of propagation, this leads to generation of two orthogonally polarized soliton components that carry almost the same energy, resulting in their similar intensities. This is illustrated in the top panel of Fig. 3.10, which shows spectral dynamics characterized in experiments for increasing length of PCF 1. When the two polarization modes are excited with an equal amount of energy, linear coupling between polarizations does not affect the energy distribution, since a net balance is zero. However, Fig. 3.10 shows that the component polarized along the x axis gradually dominates the component polarized along the y axis as the propagation distance increases. The mechanism providing transfer of energy between the two orthogonal polarizations only in one direction from shorter to longer wavelength is orthogonal Raman scattering. The presented results indicate that orthogonal Raman scattering is the mechanism that transfers the energy between two polarization modes of the fiber and consequently affects the polarization state of the propagating solitons. This is further confirmed by numerical simulations performed by other team members with the use of a self-developed solver¹ based on the software implemented in Ref. [150]. The simulations are performed for $\theta = 45^\circ$ in PCF 1 assuming the Raman polarization mixing

¹<https://github.com/WUST-FOG/cgnlse-python>

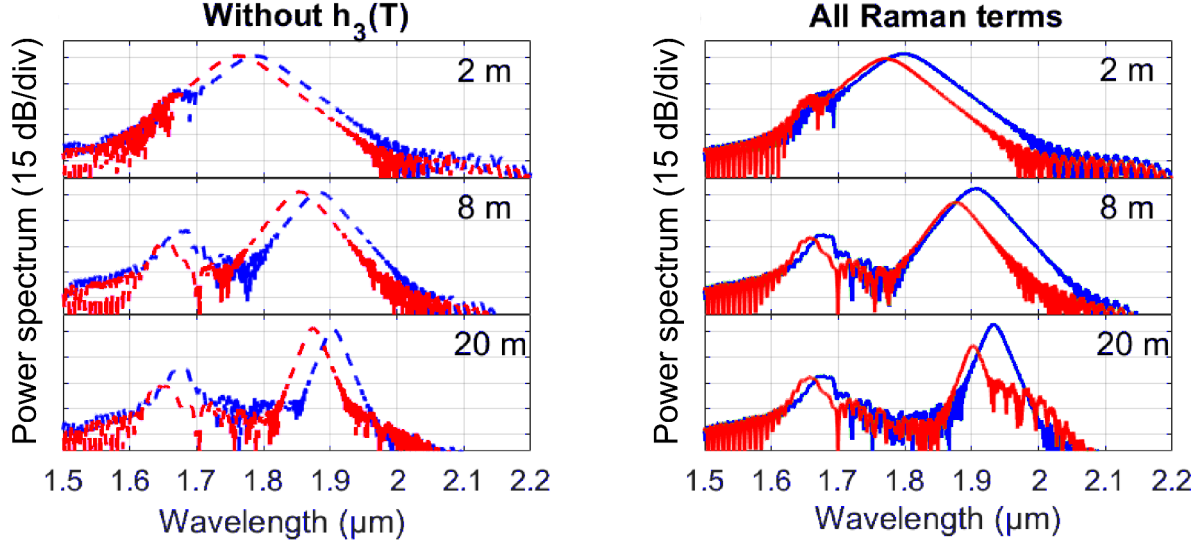


Figure 3.11: Optical spectra calculated at the output of increasing lengths of PCF 1 for equal excitation of the two fiber axes assuming 80 mW input beam average power coupled with 50% efficiency. Line colors denote signal components polarized along the x (blue) or y (red) axis. Simulations performed assuming the orthogonal Raman polarization mixing term is turned off (dashed lines) or turned on (solid lines). Figure reproduced from [151].

term $h_3(T)$ set to zero (left panel of Fig. 3.11) or turned on (right panel of Fig. 3.11). When the orthogonal Raman polarization mixing term is turned off, both polarization components have equal intensities at each investigated propagation distance. When the orthogonal Raman polarization mixing term is turned on, the polarization component polarized along the x axis gradually dominates the other component, as I observe in the experiments. The characteristic frequency of the maximum orthogonal Raman gain $\Delta\omega_{\perp} \approx 3$ THz [131] can be retrieved from Fig. 3.1. In the subsequent section I show that the spectral positions of the two orthogonally polarized components are separated by a value close to $\Delta\omega_{\perp}$.

Before that, it is interesting to point out that the characteristics of the soliton wavelength shifts for the simultaneous excitation of the two polarization modes differ qualitatively in experiments using PCF 1 and PCF 2. Each of the two generated orthogonally polarized soliton components propagates with the specific group velocity according to its spectral position and polarization. The group velocity difference between the two polarization modes is smaller in PCF 1 than in PCF 2, see Fig. 3.2(e) for measured group birefringence. In PCF 1, the group velocity difference between the two polarization modes is not large enough to cause a temporal separation of the two orthogonally polarized pulse components. Their temporal overlap over a sufficiently long distance allows the mechanism of cross-phase modulation (XPM) to force their common group velocity, causing their trapping and shift of each polarization component to a wavelength that is matched in terms of group velocity to the wavelength of the orthogonally polarized copropagating pulse. The results of numerical simulations performed by other team members confirm that the two orthogonally polarized pulse components are localized at the same time after 20 meters of propagation [151], see Fig. 3.12. During propagation, orthogonal Raman scattering leads to transfer of energy from one polarization component to the other.

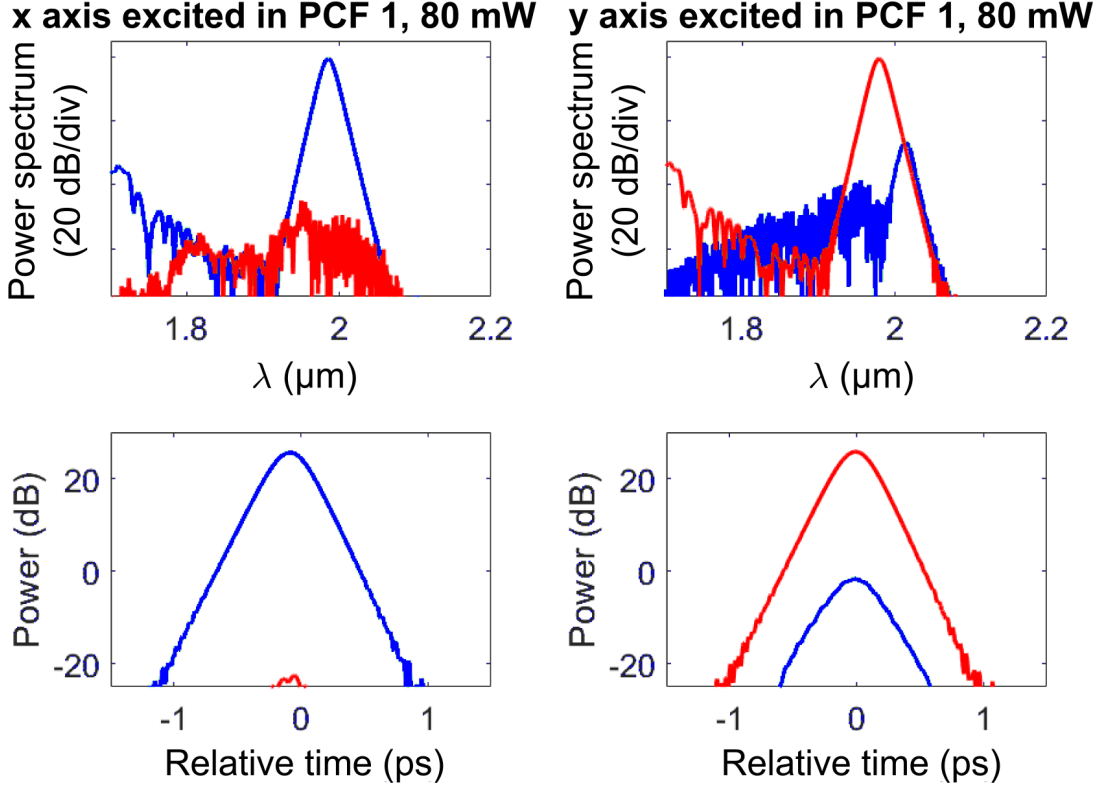


Figure 3.12: Calculated spectra (top) and temporal profiles (bottom) of generated soliton pulses at the output of 20-meter-long section of PCF 1, assuming 80 mW input power with 50% coupling efficiency. Line colors denote signal components polarized along the x (blue) or y (red) axis. Figure reproduced from [151].

Conversely, PCF 2 is characterized by more than 5 times higher group birefringence. The pulses in two orthogonal polarizations separate in time before they are trapped through the mechanism of XPM. As a result, the soliton generated from the pump energy polarized along the x axis does not overlap temporally with the soliton generated from the pump energy polarized along the y axis. Nevertheless, the linear coupling of energy from the soliton pulse polarized along the y axis to the orthogonal polarization is amplified by the orthogonal Raman scattering. This leads to the generation of copropagating pulse component at a longer wavelength, polarized along the x axis. As the group velocity becomes lower at longer wavelengths (see Fig. 3.2(a-b)), the component polarized along the x axis propagates with a more similar group velocity to the soliton that is feeding it, compared to the soliton generated from the part of pump pulse energy polarized along the x axis. This leads to trapping of the long-wavelength component to the soliton polarized along the y axis through the mechanism of XPM. Its intensity gradually increases during propagation at the expense of the original soliton. As a result, two signal components polarized along the x axis are observed at different spectral positions for several θ in Fig. 3.9: the pulse trapped to the soliton polarized along the y axis and amplified through the orthogonal Raman scattering, and the soliton generated from the pump pulse energy polarized along the x axis of the fiber. It should be noted that those two components polarized along the x axis do not belong to a single pulse and are separated in time.

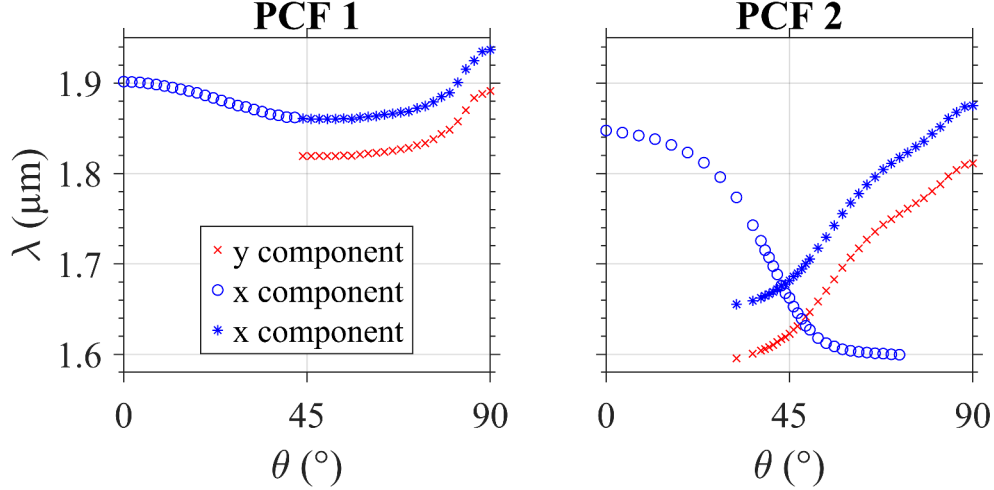


Figure 3.13: Central wavelength shift of polarization components of the solitons as the input pulse polarization is rotated with respect to the x axis of the fiber in PCF 1 (left) and PCF 2 (right). The input beam average power is 66 mW, and the fiber sections are 80 meter long in both cases.

The characteristics of the wavelength shift of each polarization component as a function of azimuth of the input pulse polarization are illustrated in Fig. 3.13 for longer 80 m sections of the two PCFs. In PCF 1, the two trapped pulse components are located at 1.82 μm and beyond. The largest shifts occur when the input pulse polarization is aligned along one of the fiber axis. In PCF 2, the amount of energy in the y polarization mode is just enough around $\theta \approx 30^\circ$ to generate a soliton in this mode, which is shifted to 1.60 μm after 80 meters of propagation. It is accompanied by a trapped, orthogonally polarized pulse component located at 1.66 μm . When θ increases, more energy is coupled into y polarization, leading to further shift of the two trapped pulse components. In a similar way, at $\theta \approx 70^\circ$ the amount of energy polarized along the x axis is just enough to lead to the generation of soliton in this polarization mode. When θ decreases, more energy is coupled into x polarization, and the soliton polarized along the x axis is shifted toward longer wavelengths. Finally, it is worth to point out that around $\theta \approx 45^\circ$ the energy of any of the two solitons in PCF 2 is lower compared to the combined energy of the two copropagating trapped pulses in PCF 1, therefore the two solitons in PCF 2 shift to wavelengths much closer to the pump compared to the soliton in PCF 1.

3.4 Soliton positions, group velocity matching, and Raman gain

In this section, I analyze the relation between spectral positions of the main and trapped pulse components for excitation at $\theta = 90^\circ$, $\theta = 70^\circ$, and $\theta = 45^\circ$. I summarize the results obtained for different propagation distances and power levels in Fig. 3.14. I relate the retrieved spectral positions to the group velocity matched wavelengths of x and y polarization modes calculated from the measured relative inverse group velocities of the two polarization modes of each fiber, shown in Fig. 3.2(a-b) and to the spectral gain of orthogonal Raman scattering shown in Fig. 3.1.

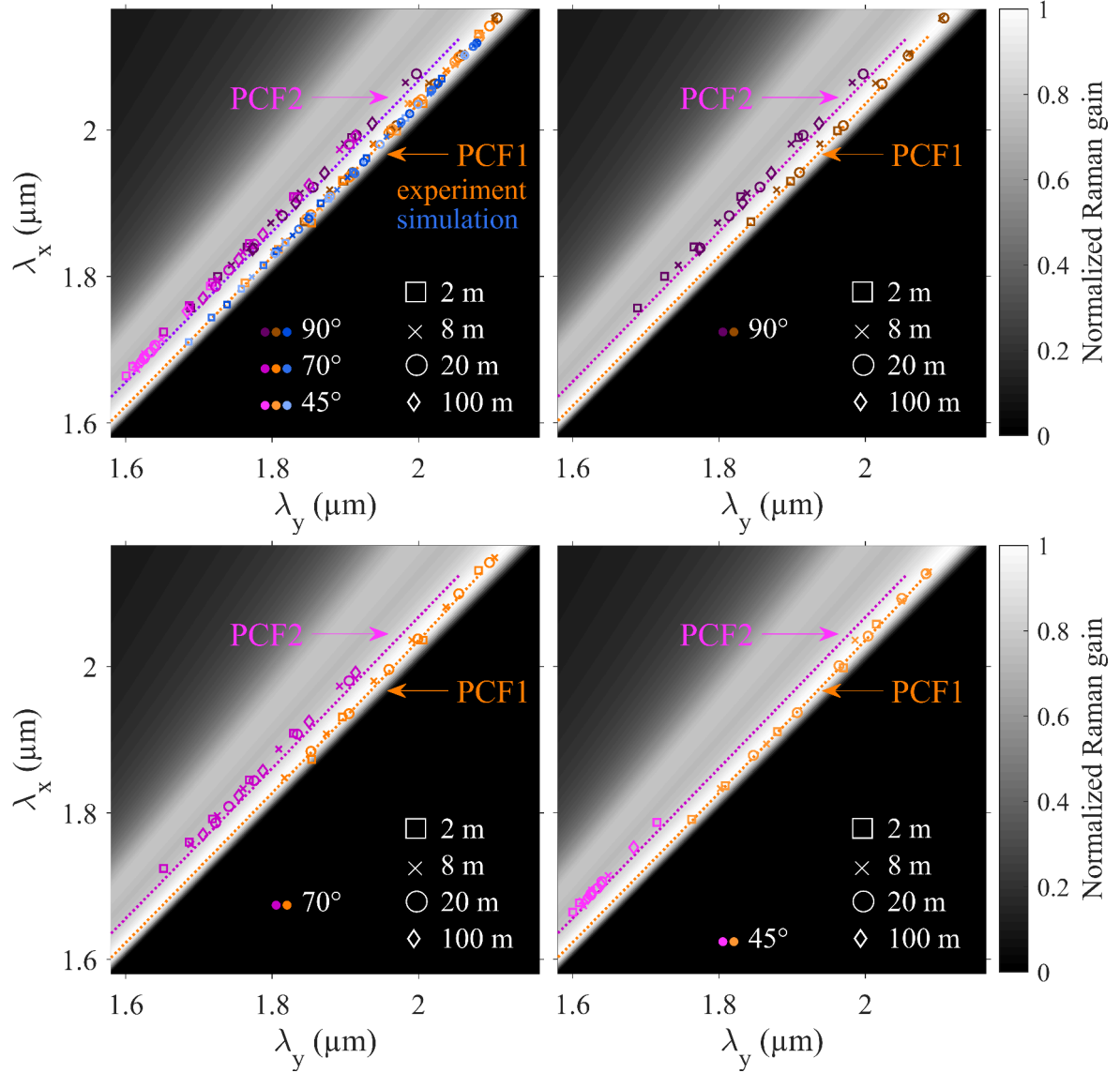


Figure 3.14: Relation between central wavelengths of two polarization components of the soliton pulse investigated for different propagation distances (indicated in the legend) and pump average powers between 60 and 127 mW in PCF 1 (orange markers) and PCF 2 (pink markers) when the input pulse polarization is rotated 90°, 70°, and 45° with respect to the x axis of the fiber. Results for simulations performed for PCF 1 are indicated with blue markers. Two lines indicate group velocity matched wavelengths of the two polarization modes in each fiber (based on Fig. 3.2(a-b)). Background intensity indicates normalized orthogonal Raman gain from the pulse component polarized along the y axis (the gain spectrum is shown in Fig. 3.1).

Figure 3.14 shows dependence of central wavelength of the trapped pulse component polarized along the x axis λ_x on the central wavelength of the original soliton polarized along the y axis λ_y . Orange markers are used for PCF 1 and pink markers are used for PCF 2. In addition, blue markers are used for results of simulations performed for PCF 1 by other team members. Different shapes of markers indicate lengths of the fiber sections. The markers for the two fibers follow two separate lines, and the experimental results agree well with the simulations. As noted in the previous sections, the spectral separation of the two pulse components is larger for PCF 2, therefore the markers belonging to PCF 2 are located higher than the markers belonging to PCF 1.

Shades of markers indicate the value of θ . To enhance clarity, additional plots are provided in which data for only a single excitation angle is displayed (the top right plot and the two bottom plots). In PCF 1, the markers for each analyzed excitation angle spread relatively evenly along the line (limited by the pump wavelength and the saturation of shift due to the fiber attenuation). The markers with larger λ_x and λ_y are related to higher pulse powers and longer fiber lengths. In PCF 2, the markers are also spread along the line for the excitation angle $\theta = 90^\circ$. However, for lower θ I observe a threshold to values of λ_x and λ_y . For $\theta = 45^\circ$ neither exceeds $1.8\ \mu\text{m}$, even for the highest pulse powers. This is due to a lower energy of the generated soliton pulse, as discussed in the preceding section.

The two dotted lines have an additional function besides serving as a visual guide. They denote the group velocity matched wavelengths of x and y polarization modes of each fiber, retrieved from measurements shown in Fig. 3.2(a-b). The markers indicating the central wavelengths of the pulse polarization components follow group velocity matching lines, which confirms that the two orthogonally polarized pulse components have matched group velocities.

In the background of Fig. 3.14, I plot the grayscale map of normalized gain spectrum of the orthogonal Raman scattering from λ_y . It can be clearly observed that in both investigated fibers the pulse components polarized along the x axis are located at spectral regions for which relatively strong orthogonal Raman gain is obtained from the component polarized along the y axis. This confirms that the trapped component originates from the soliton formed initially in the y polarization mode of the fiber. Interestingly, the spectral positions of the two pulse components follow the group velocity matching lines rather than the line with a maximum Raman gain. This indicates that in the investigated process, it is crucial for the pulse component fed by the Raman scattering from the original soliton to match its group velocity to that feeding soliton, as the relatively low values and the plateau in the orthogonal Raman gain spectrum lead to favoring the components that overlap temporally over long distances, meaning that they must propagate with the same group velocities.

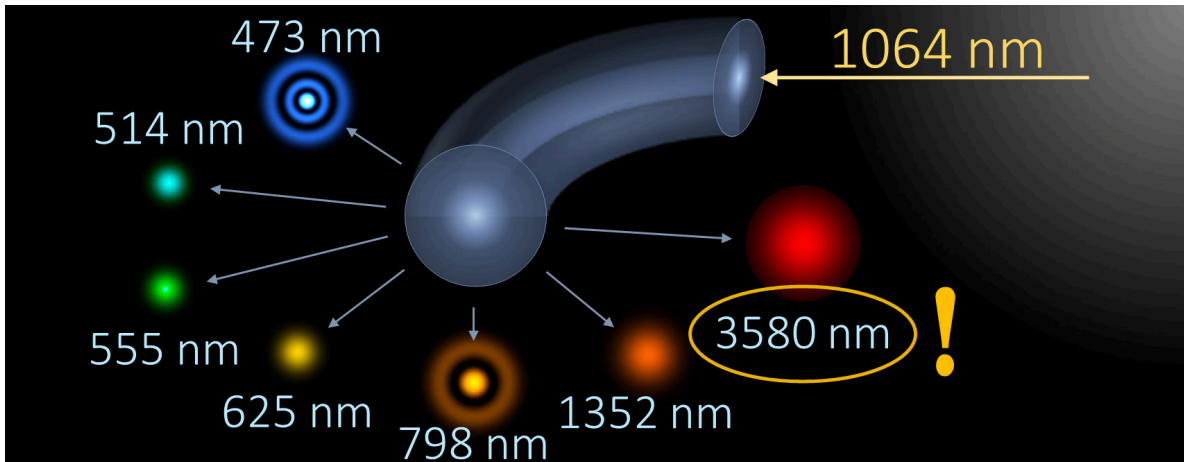
3.5 Conclusions

In this chapter I investigated soliton trapping in two birefringent photonic crystal fibers. I found that due to a negative sign of group birefringence, pumping the fiber with pulses polarized along the x (slow) axis assures higher polarization purity of the output signal than pumping with pulses polarized along the y (fast) axis, which leads to transferring part of the pulse energy to the orthogonal polarization. I confirmed that orthogonal Raman scattering provides the mechanism of energy transfer between the two polarization components of the soliton. The polarization conversion efficiency depends on the initial excitation of the fiber, which proves the research hypothesis that managing the polarization of the input optical field results in control of the nonlinear dynamics. By changing azimuth angle of linearly polarized light while managing the pulse power or fiber length, it is possible to achieve various polarization components at distinct spectral positions. Furthermore, controlling the input field's polarization allows to generate either a single soliton pulse, or two separate pulses with distinct spectral separations in the fiber whose birefringence is sufficiently high. Importantly, I found that the x mode is favored for most of excitation angles. The obtained results are particularly important for the tunable sources of polarized light which are based on Raman SSFS in the birefringent PCFs [152].

Additionally, the presented analysis of a soliton propagating in two fiber polarization modes might be useful in understanding the dynamics of a more complex multimode solitons. For example, the temporal separation of solitons propagating in the two polarization modes of PCF 2, which is characterized by high group birefringence, highlights the important influence of intermodal dispersion, which, if too large, can hinder the formation of a single pulse from the various excited modes.

Finally, it is worth to note that the group velocity matching analyzed in this study is also satisfied in the self-mode conversion investigated by Rishøj et al. [141]. In the case of the polarization conversion reported here, the process takes place over a longer distance than in the mode conversion. This is due to the smaller gain of orthogonal Raman scattering compared to the gain of co-polarized Raman scattering, as shown in Fig. 2.17. The study presented here provides important results regarding Raman-assisted energy transfer between different modes of the fiber. The observed effects of Raman scattering change drastically depending on the interaction of co-polarized or orthogonally-polarized fiber modes.

Chapter 4



High gain far-detuned four wave mixing in a graded-index fiber

Intermodal nonlinear wave mixings in graded-index (GRIN) fibers have been a subject of recent detailed investigations. A particular focus has been placed on the peaks emerging on the short-wavelength side of the pump laser (in the near-infrared and visible spectral regions) in fibers with relatively large core diameter (50-100 μm) [47, 49, 45, 153, 50, 154]. In such fibers, discrete spectral sidebands appear as a result of a refractive index grating enabled by equidistant distribution of mode propagation constants and induced by the nonlinear Kerr effect that leads to periodic self-imaging of the beam along propagation [73, 155]. As predicted in [156] the wave propagating in a GRIN fiber may undergo so-called geometric parametric instability (GPI), which causes exponential amplification of small perturbations in the frequency domain. The process is characterized by a specific phase matching condition [156] on which I expand in equation 4.1. The first experimental demonstrations in standard 52 μm core GRIN fibers showed multiple spectral bands in the short wavelength side of 1.064 μm pump, but only the first order sideband detuned by approximately 125 THz has been observed on the long wavelength side of the pump [47, 49]. In subsequent experiments, GPI has been studied in seeded configuration [45], in fibers with periodically modulated core [48], in varying spatial coupling conditions [157], in various fiber designs which revealed control over the the frequency shifts [158], and using a distinct methodology to analyze the generated sidebands [153].

To the best of my knowledge, the possibility of generating sidebands far from the pump wavelength in the mid-infrared (mid-IR) region has not been experimentally investigated in such fibers to date. The commonly accepted limit of the transparency window of silica fibers (0.4 to 2.4 μm) prevents their practical use in mid-IR [159, 160]. The two types of

nonlinear phenomena that allow to generate wavelengths longer than the pump and to access this spectral region are four wave mixing (FWM), which gives rise to spectral peaks at specific wavelengths and supercontinuum (SC) generation, which can lead to a significant spectral broadening of the original pump. Interestingly, despite high fiber losses, several studies demonstrated SC generation up to $3\ \mu\text{m}$ in short meter-long [161, 162] and centimeters-long [163, 164, 165] segments of germanium-doped silica fibers. Introducing germanium to the core region shifts the fiber transmission window toward longer wavelengths while also increasing fiber nonlinearity [160, 166]. In [162] it was theoretically predicted that a cm-long segment of heavily germania-doped fiber (97%) pumped at $2\ \mu\text{m}$ could produce a broadband spectrum extending up to $3.5\ \mu\text{m}$. Subsequent experiments demonstrated the possibility of using short segments of germania-core fibers pumped by systems based on thulium-doped fiber amplifiers to obtain mid-IR radiation spanning up to $3.5\ \mu\text{m}$ [167, 168], and $3.6\ \mu\text{m}$ [166]. For completeness, I should mention that to achieve longer wavelengths fibers made of soft-glass materials, including fluoride [169, 170, 171], telluride [172] and chalcogenide [173, 174], are used.

Moreover, several studies have explored the possibility of achieving mid-IR in silica photonic crystal fibers, which enable easy engineering of dispersion properties through control of the fiber design [82]. In pure silica PCF mid-IR generation up to $4\ \mu\text{m}$ was investigated numerically [175], and the authors concluded that accessing the wavelengths beyond $3.5\ \mu\text{m}$ is in principle possible but it poses a major practical challenge due to requiring very short, sub-cm fiber segments. Experimentally, a 1.4 m of endlessly single-mode (ESM) large mode area PCF was used to convert picosecond pulses from a $1.064\ \mu\text{m}$ pump to $2.54\ \mu\text{m}$ Stokes with a 6% efficiency, and according to theoretical predictions utilizing a tunable Yb-doped fiber amplifier source could result in obtaining up to $3\ \mu\text{m}$ in this fiber [176]. In a subsequent work [177], the same group studied FWM in similar fibers, and observed a 180 THz conversion from $1.064\ \mu\text{m}$ pump to $0.65\ \mu\text{m}$ anti-Stokes and $2.93\ \mu\text{m}$ Stokes in a 60 cm fiber segment. Another study [178] investigated shorter-than-1 m segments of PCFs pumped by a $1.064\ \mu\text{m}$ picosecond pulses for achieving $0.65\ \mu\text{m}$ anti-Stokes, which corresponds to the Stokes generated at $2.77\ \mu\text{m}$. Finally, a conversion of $1.064\ \mu\text{m}$ nanosecond pulses was investigated in two ESM PCFs [179], resulting in the most far-detuned FWM into the mid-IR region in a silica fiber. In that study, a Nd:YAG laser pump was converted to $3.11\ \mu\text{m}$ Stokes with a 0.2% efficiency.

In the following I investigate, both theoretically and experimentally, far-detuned nonlinear frequency conversion in a few-mode silica GRIN fiber pumped at $1.064\ \mu\text{m}$. The fiber core is moderately doped with germanium, reaching a concentration of 5% in the center of the core. I report the wave mixing processes extending towards both the visible and the mid-IR, achieving gains of hundreds of dB per meter below $0.65\ \mu\text{m}$ and record-far detuning beyond $3.5\ \mu\text{m}$. This remarkably high-gain wavelength conversion is obtained in short fiber segments of less than one meter. My results highlight the potential of graded-index fibers in terms of high modal overlap over an ultrabroad spectral range.

4.1 Remarks on theoretical analysis of FWM processes in GRIN fibers

First, I offer some perspectives on how to accurately analyze the spectral positions of the peaks generated in a FWM process. As an example, I analyze FWM processes in a simple GRIN fiber with a $1.064\ \mu\text{m}$ pump in the fundamental mode. I assume that the fiber has a parabolic profile of refractive index, $22\ \mu\text{m}$ core diameter, 5% Ge doping in the center of the core, and cladding made of pure silica. This fiber has been studied earlier in [44]. The design assumed here is simplified with respect to an actual fiber profile featuring a trench as shown in Fig. 4.5(a). Nevertheless, for the purpose of comparing results obtained using different techniques, a simplified design is considered in this section. This eliminates any variations that may arise from the introduction of a trench, which can be accounted for in one technique but not in another.

As outlined in Chapter 2, any (intra- or intermodal) FWM process that occurs in an optical fiber can be described by a phase-matching condition 2.44. The FWM process is the most efficient when the effective phase mismatch vanishes, which means $\Delta\beta = 0$. For a given combination of spatial modes μ, η, ν, κ (Stokes, anti-Stokes, and two pump waves, respectively), knowing their propagation constants, one can find the phase mismatch and establish the wavelengths of Stokes and anti-Stokes in a phase-matched process. To do that, I calculated mode propagation constants for the assumed fiber design using a rigorous model that takes into account the impact of the varying concentration of germanium doping in the fiber core. Knowing mode propagation constants as a function of wavelength, I used equation 2.44 to obtain phase mismatch for different combinations of modes. Here I analyze three combinations of Stokes (μ) and anti-Stokes (η) in $\text{LP}_{0,1}$ or $\text{LP}_{0,2}$ modes, assuming that pump is in $\text{LP}_{0,1}$ mode, and ignoring the issue of estimating the cutoff of $\text{LP}_{0,2}$ mode. In Fig. 4.1(a) solid lines represent the calculated $\Delta\beta$ as a function of either Stokes or anti-Stokes wavelength. Among these lines, only the purple one crosses zero, which means that phase-matching is achieved only when both Stokes and anti-Stokes waves are in the fundamental mode, rather than one of them being in the $\text{LP}_{0,2}$ mode. The spectral positions of where the line crosses zero, namely $3.52\ \mu\text{m}$ and $0.63\ \mu\text{m}$, correspond to the wavelengths of Stokes and anti-Stokes of this intramodal process.

Here, it is worth to mention and discuss the applicability of some frequently employed techniques that simplify the procedure of obtaining phase-matched wavelengths. A common practice is using Taylor expansion of the refractive index or the mode propagation constant around the pump frequency to approximate it to the second (or higher) order in ω , as in Eq. 2.20. This method is convenient and used very often in theoretical investigations of FWM processes [44, 47, 87]. However, it is important to be aware of the limitations of this approach and of the possible mistakes it could cause. To illustrate, I used second order Taylor expansion of propagation constants of $\text{LP}_{0,1}$ and $\text{LP}_{0,2}$ modes to again calculate phase mismatch curves for the previously analyzed FWM processes. The results are plotted with dotted lines in Fig. 4.1(a). The dotted lines follow the solid lines in the spectral range near the $1.064\ \mu\text{m}$

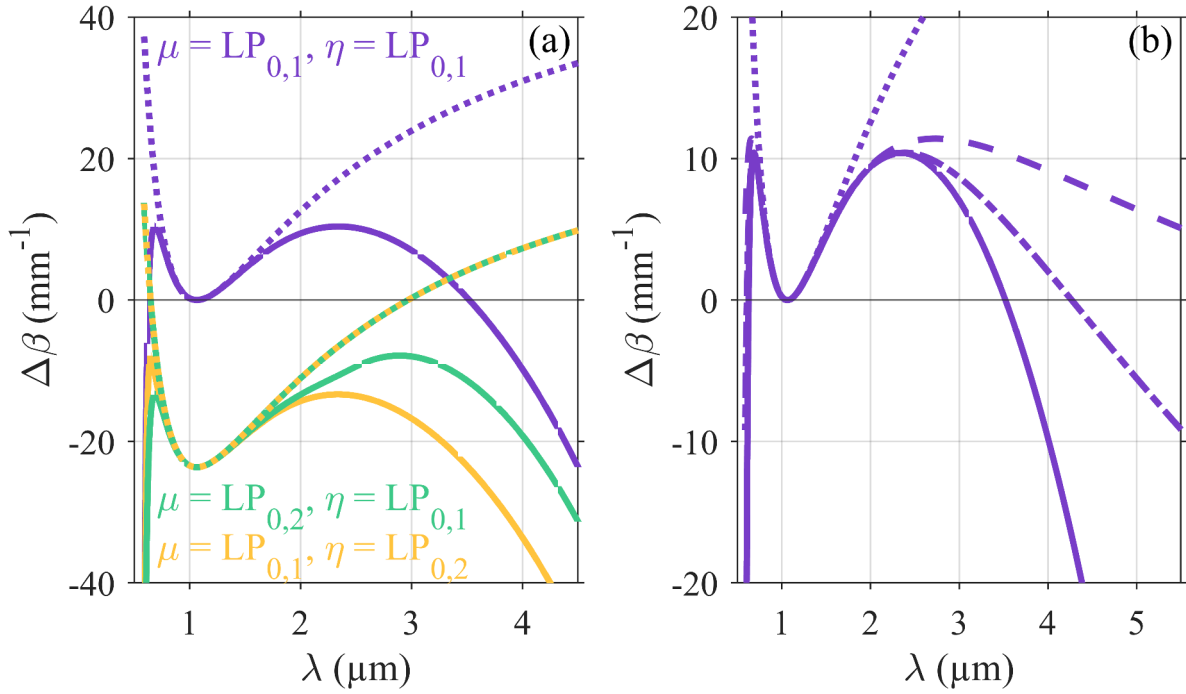


Figure 4.1: (a) Phase-mismatch curves for FWM process with a selected spatial modes in Stokes (μ) and anti-Stokes (η) assuming pumping at $1.064 \mu\text{m}$ in the fundamental mode in a $22 \mu\text{m}$ -core GRIN fiber with a 5% Ge doping in the core center. Solid lines: obtained using calculated mode propagation constants; dotted lines: obtained using second order Taylor expansion of mode propagation constants around pump wavelength. (b) Phase-mismatch for intramodal FWM process with a Stokes, anti-Stokes, and pump in the fundamental mode, assuming pumping at $1.064 \mu\text{m}$, calculated using full mode propagation constant (solid line), or second-order (dotted line), fourth-order (dashed line), or sixth-order (dashed-dotted line) Taylor expansion of mode propagation constant around pump wavelength.

pump wavelength, but they deviate notably when the wavelengths are significantly different from the pump. As a result, the purple dotted line does not cross zero, which indicates that there are no phase-matched wavelengths for the intramodal FWM process. The orange and green dotted lines cross zero at the same points, leading to conclusion that Stokes in LP_{0,1} (LP_{0,2}) should be generated at 2.97 μm, and anti-Stokes in LP_{0,2} (LP_{0,1}) should be generated at 0.65 μm. Clearly, the conclusions drawn here differ significantly from those reached in the preceding paragraph. While the phase-matched wavelengths are quite similar (albeit it is coincidental), the anticipated modal composition is incorrect. It is important to emphasize that when the FWM peaks being studied are far-detuned from the pump, relying on the Taylor expansion of mode propagation constants to analyze phase-matching conditions can lead to significant mistakes. This approach has been taken to study the same fiber that is investigated in this chapter [44]. Due to the application of the Taylor approximation in their analysis, the authors inaccurately identified the FWM process originating the anti-Stokes peak. One possible improvement could involve using a higher-order Taylor expansion to enhance the accuracy of the fit [154]. However, this necessitates the numerical calculations of higher-order derivatives, increasing the susceptibility to numerical errors. Moreover, it involves more complex derivations to obtain the equation for phase-matching. In Fig. 4.1(b) I have verified that using fourth- and sixth-order Taylor expansion did not yield satisfactory approximations of the propagation constants in the spectral regions so far away from the pump. Consequently, due to the possibility of inaccurate predictions of the spectral positions and modes in the far-detuned FWM processes, this technique will not be suitable for far-detuned frequency conversion investigated in the following.

The second technique that allows simplifying the calculations takes advantage of the specific feature of the GRIN fibers, which have nearly equally-spaced effective refractive indices of guided modes. In practice, while investigating a GRIN fiber, the phase-matching condition 2.44 is often reformulated by expressing the propagation constants of the modes as a simple sum of the material dispersion and wavelength-independent waveguide contribution, as in Eq. 2.12. After undergoing this transformation and a few rearrangements, this leads to deriving an approximate phase-matching condition [74]:

$$\begin{aligned}
 \Delta\beta &= \beta_\mu^s + \beta_\eta^{as} - \beta_\nu^{p1} - \beta_\kappa^{p2} \approx \\
 &= \left(n_0^s k^s - \frac{g_\mu \sqrt{2\Delta}}{R} \right) + \left(n_0^{as} k^{as} - \frac{g_\eta \sqrt{2\Delta}}{R} \right) - \left(n_0^{p1} k^{p1} - \frac{g_\nu \sqrt{2\Delta}}{R} \right) - \left(n_0^{p2} k^{p2} - \frac{g_\kappa \sqrt{2\Delta}}{R} \right) \\
 &= \underbrace{n_0^s k^s + n_0^{as} k^{as} - n_0^{p1} k^{p1} - n_0^{p2} k^{p2}}_{\Delta k_M} - \underbrace{(g_\mu + g_\eta - g_\nu - g_\kappa) \sqrt{2\Delta}/R}_{\Delta k_W} = 0, \tag{4.1}
 \end{aligned}$$

which consists of phase mismatch occurring due to material dispersion (Δk_M) and due to waveguide dispersion (Δk_W). It should be noted that the expression $(g_\mu + g_\eta - g_\nu - g_\kappa)$ depends on the group numbers of interacting modes and is equal to a certain integer G . Moreover, different combinations of modes $\{\mu, \eta, \nu, \kappa\}$ can yield identical values of G . For instance, $G = 2$ for each of the following combinations of Stokes, anti-Stokes and two pump modes interacting in a FWM process: $\{\text{LP}_{0,1}, \text{LP}_{0,2}, \text{LP}_{0,1}, \text{LP}_{0,1}\}$, $\{\text{LP}_{0,2}, \text{LP}_{0,1}, \text{LP}_{0,1}, \text{LP}_{0,1}\}$,

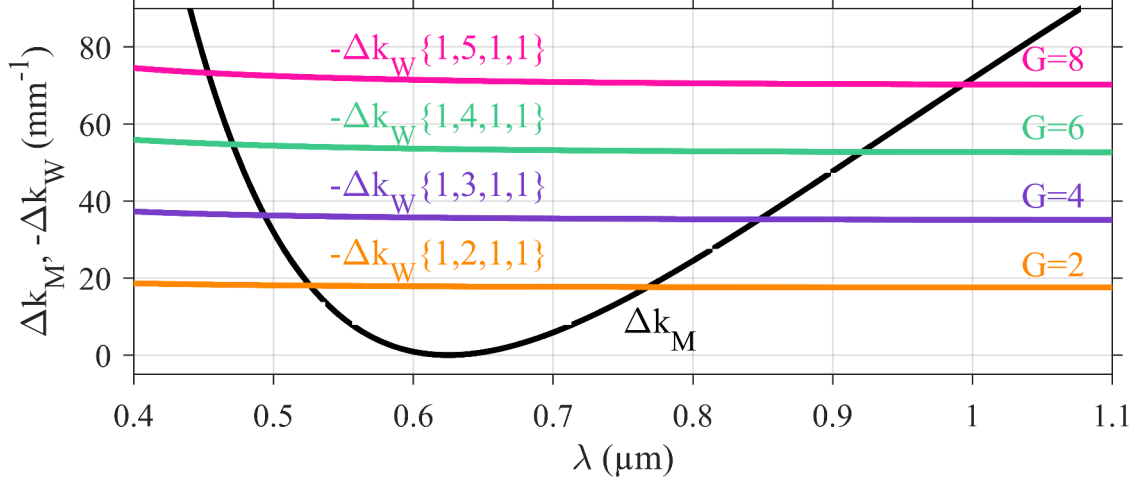


Figure 4.2: Phase-matching curves for FWM processes with a pump wavelength of $0.625 \mu\text{m}$. The Δk_M and $-\Delta k_W$ curves represent the material and waveguide dispersion contributions, respectively. $-\Delta k_W$ were calculated for several allowed values of integer G . Numbers in brackets represent example values of p of $\text{LP}_{0,p}$ modes that could be selected for Stokes, anti-Stokes, and two pump modes interacting in a FWM process and be characterized by a given G .

$\{\text{LP}_{0,2}, \text{LP}_{0,2}, \text{LP}_{0,2}, \text{LP}_{0,1}\}$, $\{\text{LP}_{0,3}, \text{LP}_{0,1}, \text{LP}_{0,2}, \text{LP}_{0,1}\}$, $\{\text{LP}_{1,1}, \text{LP}_{0,2}, \text{LP}_{1,1}, \text{LP}_{0,1}\}$. The remaining parts of the equation 4.1 depend solely on the material and geometric parameters of the fiber. As a result, each of the combinations listed above has similar phase-matching conditions. However, it is worth to underline that although these combinations are nearly equivalent wavelength-wise (result in nearly identical Stokes and anti-Stokes wavelengths if a FWM process occurs), their FWM efficiencies differ. This arises from the fact that different combinations of spatial modes exhibit varying overlap integrals, leading to different nonlinear coupling coefficients $\gamma_{1,2,3,4}$ (defined in Eq. 2.46) and different relative strengths of the interaction. It is also important to mention that the possible values of G are limited by the requirement to conserve the spatial angular momentum of the modes [87]. For that reason, G has to be an even integer. As my subsequent analysis is restricted to the $\text{LP}_{0,p}$ modes, I will simplify the labeling of mode combinations by using only the radial mode number p of the four interacting modes $\{p_\mu, p_\eta, p_\nu, p_\kappa\}$. For instance, the combination $\{\text{LP}_{0,3}, \text{LP}_{0,1}, \text{LP}_{0,2}, \text{LP}_{0,1}\}$ will be denoted as $\{3, 1, 2, 1\}$.

The approach outlined above is a simple yet powerful tool that provides the possible conditions of the FWM process occurring in a GRIN fiber. Knowing just the material dispersion of the fiber and the group numbers of the participating modes, one is able to predict the approximate phase-matched wavelengths of Stokes and anti-Stokes waves for a given pump. I illustrate this with the fiber design that has already been introduced, but assuming that the pump is now at a shorter wavelength of $0.625 \mu\text{m}$, which results in more guided modes in the considered spectral region around the new pump wavelength. In Fig. 4.2 I show the phase mismatch contribution of the material (Δk_M) and waveguide ($-\Delta k_W$) dispersion for several mode combinations characterized by different values of G . Phase matching occurs at the intersection of the curves. With every (even) value of G , a pair of sidebands is generated, which

become more detuned from the pump as G increases. It can be shown [87] that approximating the material dispersion using a second order Taylor expansion and solving equation 4.1 for the FWM frequency shift gives an expression that scales as \sqrt{G} . In practice, numerous studies on nonlinear wave mixing processes in multimode GRIN fibers have combined the two described approximations to analyze the generated sidebands, for instance: [47, 49, 156]. In certain works the authors include higher-order dispersion terms to gain better insight into the origin of the sidebands emerging in experiments [45, 154], or perform a rigorous analysis accounting for all orders of material dispersion [153]. Setting aside the method of introducing the contribution of material dispersion, the approach that collectively includes the waveguide contribution from different combinations of modes to a specific sideband is indeed very useful when addressing a large number of possible intermodal interactions in a highly multimode fiber. As each mode requires a pre-computed propagation constant, analyzing a complex multimode environment on a mode-by-mode basis rapidly becomes impractical. The collective approach is also particularly beneficial when considering a largely multimode input pumping condition, or when the input modal content is not known.

However, when dealing with a few-mode fiber, the number of intermodal couplings is significantly reduced and easier to analyze. In this scenario, using the above described collective approach to investigate FWM processes may be less favorable due to certain limitations that I will discuss below. First, it fails to provide information on the modal content of the emerging FWM peaks. As noted previously, although various mode configurations have equivalent phase-matching conditions, they vary in terms of FWM efficiencies. Consequently, experimental characterization of the modal content of the peaks generated in a FWM process typically reveals that certain modes tend to dominate over the rest [44, 180]. When each combination of four modes is analyzed individually, in the way described in the beginning of the section 4.1, they are characterized by a certain overlap integral defined in Eq. 2.37. This integral can be compared with the overlap integrals of other mode combinations, which offers insight into relative effectiveness of the FWM processes contributing to a given sideband. In contrast, the collective analysis provides only the estimated phase-matched wavelengths, and information about the interaction strength cannot be retrieved. As a result, it is unfeasible to gain any insight into the modal composition of the Stokes and anti-Stokes waves using this approach.

The next issue is that the propagation constants of the modes in the GRIN fibers are not perfectly equidistant. Because of that, the derived equation 4.1 is not precise, resulting in the collective approach allowing to obtain only approximated positions of phase-matched wavelengths. I illustrate this in Fig. 4.3, where I compare the phase-matching curves obtained with the two approaches. The thick dashed lines represent the collective approach explained above. They are obtained by summing the Δk_M and Δk_W curves from Fig. 4.2. The remaining phase mismatch curves are calculated by directly adding the propagation constants of Stokes, anti-Stokes, and two pump modes in various combinations of spatial modes (similarly to solid lines in Fig. 4.1(a)). Figure 4.3 clearly demonstrates that employing the collective approach allows to correctly estimate the phase-matched wavelengths of only a limited number of possible mode combinations (the ones marked with thin solid lines).

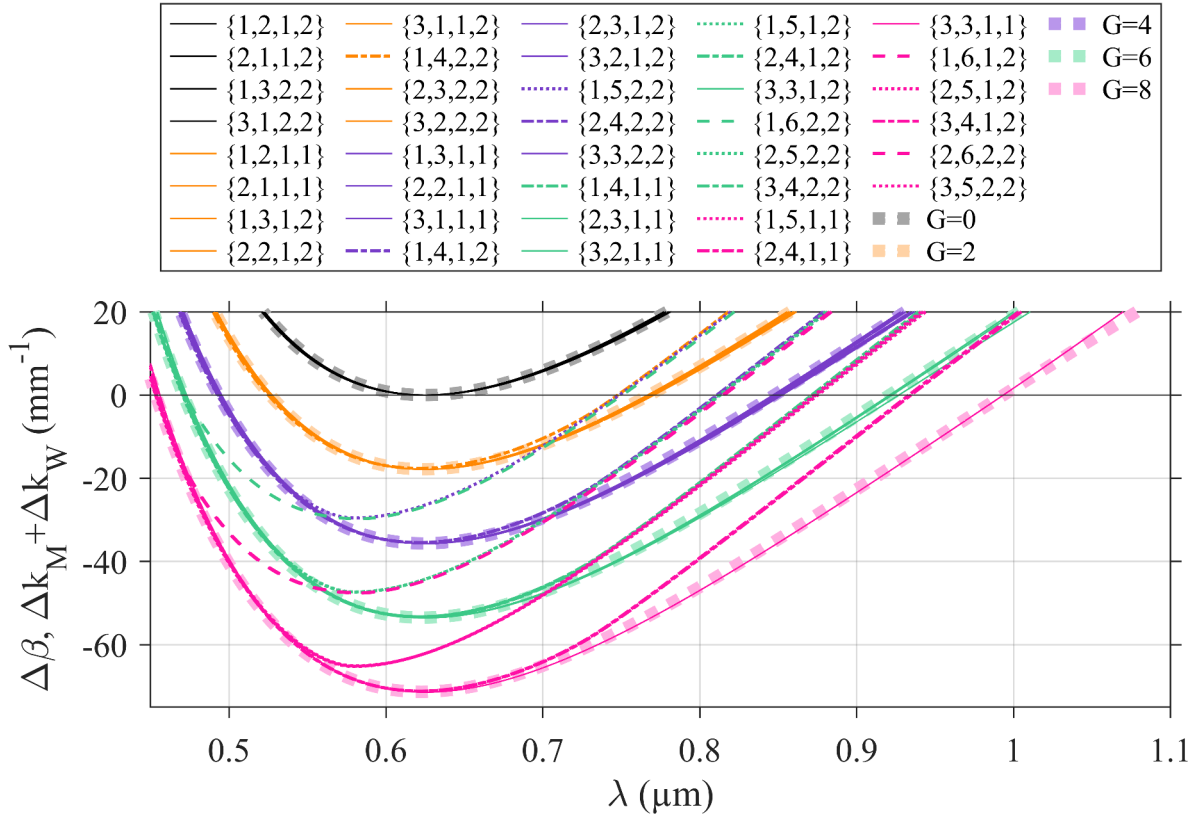


Figure 4.3: Phase-matching curves for FWM processes involving different combinations of Stokes, anti-Stokes, and pump modes calculated using two approaches: a collective approach that accounts for material and waveguide dispersion contribution (thick dashed lines), and a rigorous approach that accounts for the effective refractive index of each mode (thin lines). The considered mode combinations are grouped by linestyle according to their phase-matched wavelength.

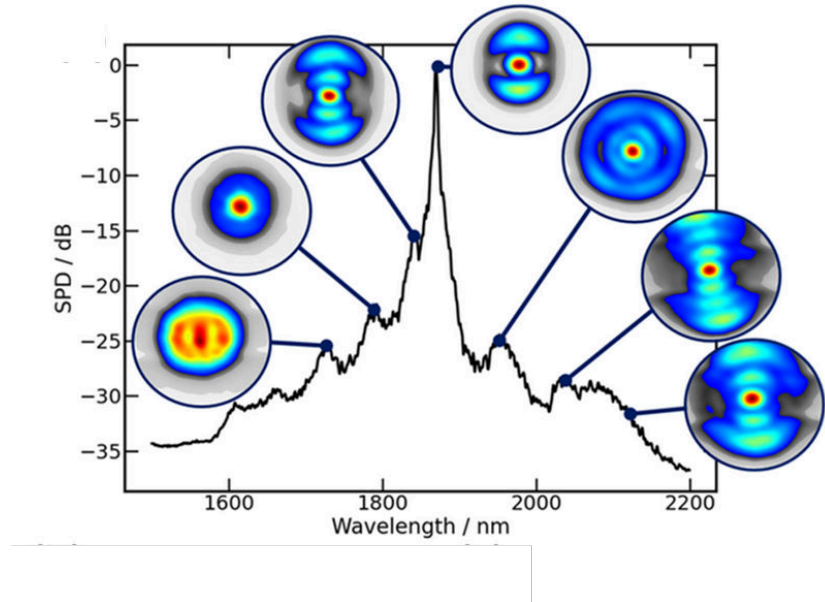


Figure 4.4: Experimental characterization of the Stokes peak generated in nonlinear wave mixing process in a 62.5 μm core fiber pumped at 1.064 μm reveals different modal components at offset wavelengths [Reprinted with permission from Leventoux *et al.*, *Opt. Lett.* 46, 3717-3720 (2021). Copyright 2021 Optical Society of America].

The phase mismatch curves corresponding to the other groups of mode combinations (represented by dashed, dotted, and dash-dotted lines) deviate from the trajectory of the phase-mismatch curve obtained using the collective approach, and have notably different zero-crossing wavelengths in the long wavelength side of the pump. For example, the anticipated Stokes wavelengths corresponding to the following FWM processes: $\{1, 4, 1, 2\}$, $\{2, 4, 2, 2\}$ (purple dashed-dotted lines), $\{1, 5, 1, 2\}$, $\{2, 5, 2, 2\}$ (green dotted lines), and $\{1, 6, 1, 2\}$, $\{2, 6, 2, 2\}$ (magenta dashed lines) are all in proximity of 0.815 μm , rather than approximately 0.848 μm , 0.921 μm , and 0.994 μm , as implied by the values of G for the first, second, and third pair of the listed combinations, respectively.

Another example considers a different perspective: FWM processes indicated by purple lines have Stokes waves around 0.749 μm , 0.811 μm , and ranging from 0.846 μm to 0.853 μm , which is a much more rich and complex dynamic compared to the wavelength of 0.848 μm indicated by the $G=4$ phase mismatch curve. A recent experimental study [180] employed a 3D beam mapping technique to analyze the spatial-spectral structure of the Stokes peak generated in nonlinear wave mixing process in a multimode, 62.5 μm core GRIN fiber. Figure 4.4 reproduced from that publication shows the wavelength-dependent spatial profiles of the beam around the Stokes peak. Combining those experimental findings with the conclusions from my theoretical investigations above, it becomes evident that generation of different modes at offset wavelengths is the result of varying phase-matching conditions of the different FWM processes, and cannot be addressed by the approach that takes into account general contribution of waveguide dispersion.

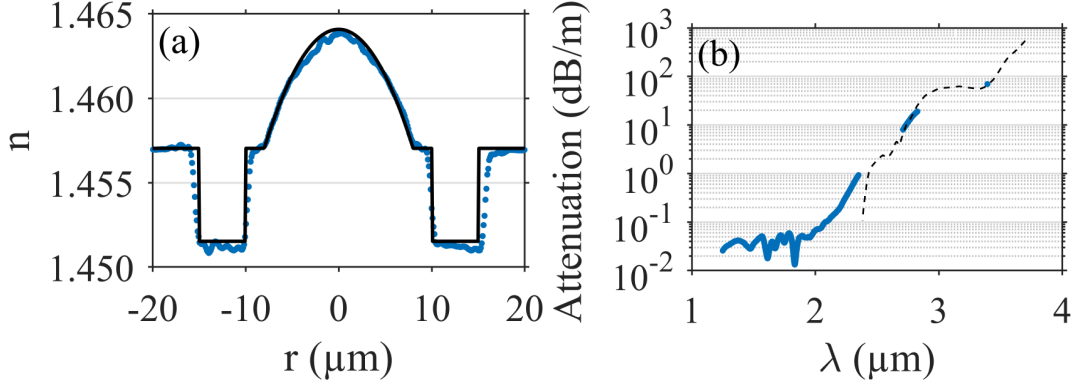


Figure 4.5: Measured parameters of the fiber: (a) Refractive index profile measured at $0.632\ \mu\text{m}$ (blue dots) and corresponding fit used for the numerical analysis (black line). (b) Measured attenuation (blue dots) and absorption spectrum of bulk silica (Suprasil F300) from Ref. [54] (dashed line) in the mid-IR.

As explained above, the commonly used picture of the equidistant distribution of mode propagation constants, together with the use of a finite-order Taylor series expansion of propagation constants, could fail to correctly describe my observations in the few-mode fiber without implying a misinterpretation of mode combinations involved in FWM processes. Consequently, all the phase-matching curves presented in the following are obtained by taking into account the full frequency dependence of the mode propagation constants.

4.2 Study conditions

In this section, I present a detailed description of the conditions of my investigation of nonlinear four wave mixing in a few-mode graded-index fiber. First, I provide the measured and calculated parameters of the fiber that actually has a slightly more intricate refractive index profile than the one assumed in the preceding section. Next, I elaborate on the experimental setup and light coupling conditions.

4.2.1 Fiber properties

I used a commercially available few-mode GRIN fiber [44]. The photograph of the fiber cross section is shown in Fig. 2.2. The refractive index profile, measured at $632\ \text{nm}$ by other team members, is shown in blue in Fig. 4.5(a). To approximate it (see black line), I assumed the following fiber design. The core has a radius of $8\ \mu\text{m}$ and is doped with GeO_2 with a parabolic profile and a maximum concentration in the center equal to $5\ \%$ mol. The core is surrounded by a $2\ \mu\text{m}$ thick layer of pure silica and a $5\ \mu\text{m}$ thick fluorine doped trench followed by a pure silica cladding. I used the Sunak material dispersion model to calculate wavelength-dependent refractive indices of pure and GeO_2 -doped silica [181]. I assumed a constant refractive index shift induced by the fluorine doping to pure silica, $\delta n_F = -5.5 \cdot 10^{-3}$. The refractive indices of the center of the core, the pure silica cladding, and the fluorine-doped trench calculated as a function of wavelength are shown in Fig. 4.6(c).

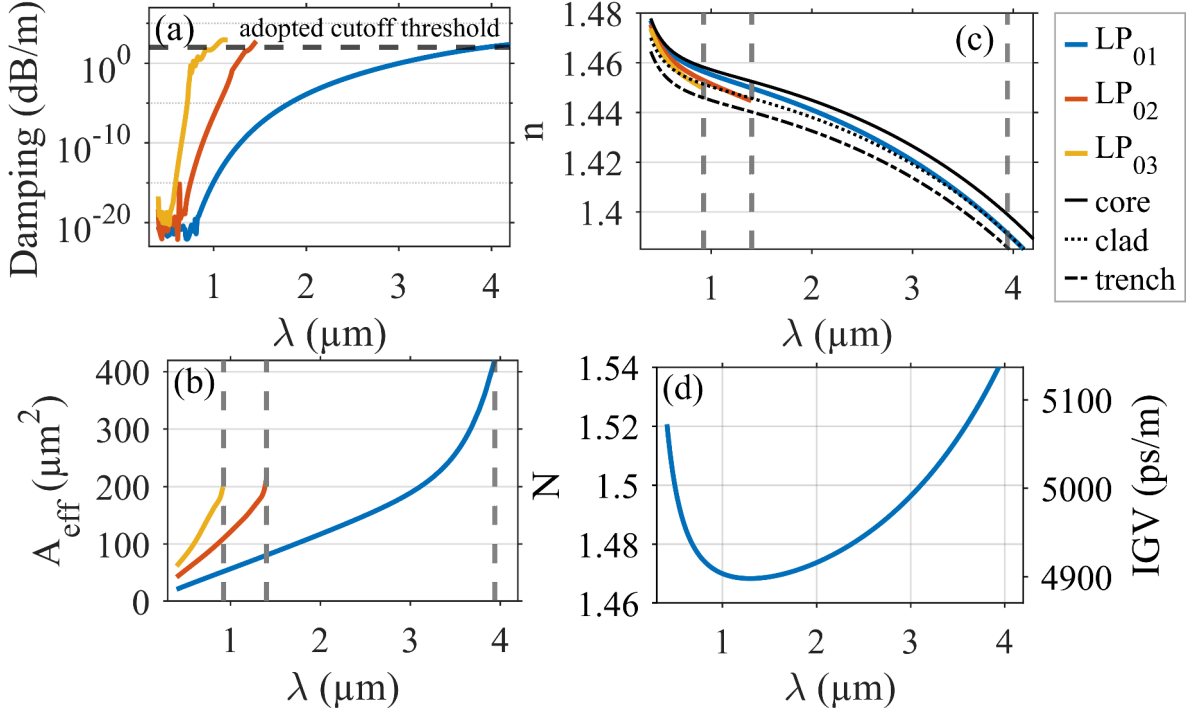


Figure 4.6: Calculated mode damping (a), effective area (b), and effective refractive index (c) of the first three LP_{0,p} modes of the GRIN fiber under study. Calculated effective group refractive index and corresponding inverse group velocity of the LP_{0,1} mode (d).

For silica-based fibers such as the one studied, material linear losses in the visible and near-infrared spectral regions are negligible for meters-long fiber segments. However, when approaching the 2-μm spectral region, the silica transparency significantly drops. To gain more insight, I measured fiber losses using the common cutback method described in Section 2.3.5. As a light source I used a home-developed fiber supercontinuum that emits wavelengths up to 2.8 μm (with a spectral gap around 2.7 μm due to OH absorption band in the fiber) and a He-Ne laser that emits at 3.392 μm. The measurement results are shown in Fig. 4.5(b) in semi-log scale, and are compared to the attenuation of bulk silica glass [54], reproduced with black dashed line. The good agreement allows to use the bulk attenuation as an estimation of the fiber losses in the mid-IR. The measured attenuation reaches 1 dB/m at 2.4 μm and 70 dB/m at 3.39 μm, and it would exceed 200 dB/m for wavelengths beyond 3.54 μm. To put this result in perspective, I also checked the attenuation of a standard multimode GRIN fiber (Nufern, core diameter of 50 μm). It reaches 62 dB/m at 3.392 μm, which confirms that such a high attenuation is mainly due to material losses rather than fiber design.

Modal properties of the fiber were obtained using the COMSOL Multiphysics software. I consider only linearly polarized LP_{0,p} modes. The calculated damping coefficient, effective areas, and effective refractive indices of the first three LP_{0,p} modes are plotted in Fig. 4.6(a), (b), and (c) respectively. In addition, in Fig. 4.6(d) I plot the group refractive index and corresponding inverse group velocity for the fundamental mode. Modal attenuation exceeds 100 dB/m at 0.92 μm for LP_{0,3}, at 1.40 μm for LP_{0,2}, and at 3.94 μm for LP_{0,1} mode. I assumed that the

modes are cut off at this level of attenuation (the corresponding wavelengths are marked with gray dashed lines in Fig. 4.6(b-c)). The effective mode area grows linearly with wavelength and reaches $200 \mu\text{m}^2$ close to cutoff. For the $\text{LP}_{0,1}$ mode, the linear behavior changes drastically around $3.5 \mu\text{m}$. Noticeably, close to the cutoff the effective refractive index drops below the material refractive index of the silica cladding. The above observations regarding the two fiber parameters indicate that the modes at indicated wavelengths start to propagate in the cladding, and this can be associated with increasing confinement losses. For the fundamental mode, the calculated damping coefficient reaches 16 dB/m at $3.5 \mu\text{m}$. This value is still only a small fraction (less than 20%) of the measured attenuation (Fig. 4.5(b)) which indicates that material losses are the main contribution to the fiber's attenuation in the mid-infrared.

4.2.2 Experimental setup

I used a high-power laser source (Teem Photonics, PNP-M08010-1x0) operating at $1.064 \mu\text{m}$ with a maximum peak power 220 kW . It delivers 400 ps pulses with a repetition rate of 1 kHz . The beam passed through a polarizer and a half-wave plate to control the power and polarization, and was coupled to the fiber using a $\times 10$ microscope objective with a numerical aperture $\text{NA} = 0.25$. The fiber was placed on a pitch & yaw tilt platform combined with a 3-axis stage system to ensure precise fiber adjustments. Light coupling was handled with care to maximize excitation of the fundamental mode $\text{LP}_{0,1}$ by ensuring that the laser beam goes straight and exactly through the center of the microscope objective and by focusing the beam on the center of the fiber core. The fiber output spectrum was monitored using two optical spectrum analyzers (Yokogawa, AQ6374 and AQ6377), and the associated spatial content was analyzed using two beam profilers (Cinogy, CinCam CMOS-1202 IR; FLIR, SC7300) and a set of suitable spectral filters. The power was monitored by using a thermal power sensor (Thorlabs, S401C). In the following sections, I present and analyze two typical fiber output spectra obtained for slightly different average powers but similar spatial light coupling conditions into a 70 cm -long fiber segment.

4.3 Intramodal four wave mixing study

Here, I maximized the coupling into the fundamental mode by monitoring the modal content of the fiber output. The corresponding output spectrum for an average power of 27.5 mW (equivalent to more than 60% coupling factor of the input laser beam whose power measured just before the input microscope objective was 46 mW) is plotted in Fig. 4.7(b). The pump spectrum is broadened around $1.064 \mu\text{m}$ due to the intermodal modulation instability arising from the bimodal interaction with the $\text{LP}_{0,2}$ mode [129, 13]. By finely analyzing the MI peak frequency and gain recorded for several fiber lengths (see Fig. 4.8(b)), I can estimate the initial power distribution between the two spatial modes involved at the pump wavelength, as described in Section 2.4.9. My analysis reveals that more than 85% of the total power was injected into the fundamental mode. The residual peaks around 0.8 and $1.4 \mu\text{m}$ in the overall spectrum in Fig. 4.7(b) arise from the laser source. However, a striking observation here is the

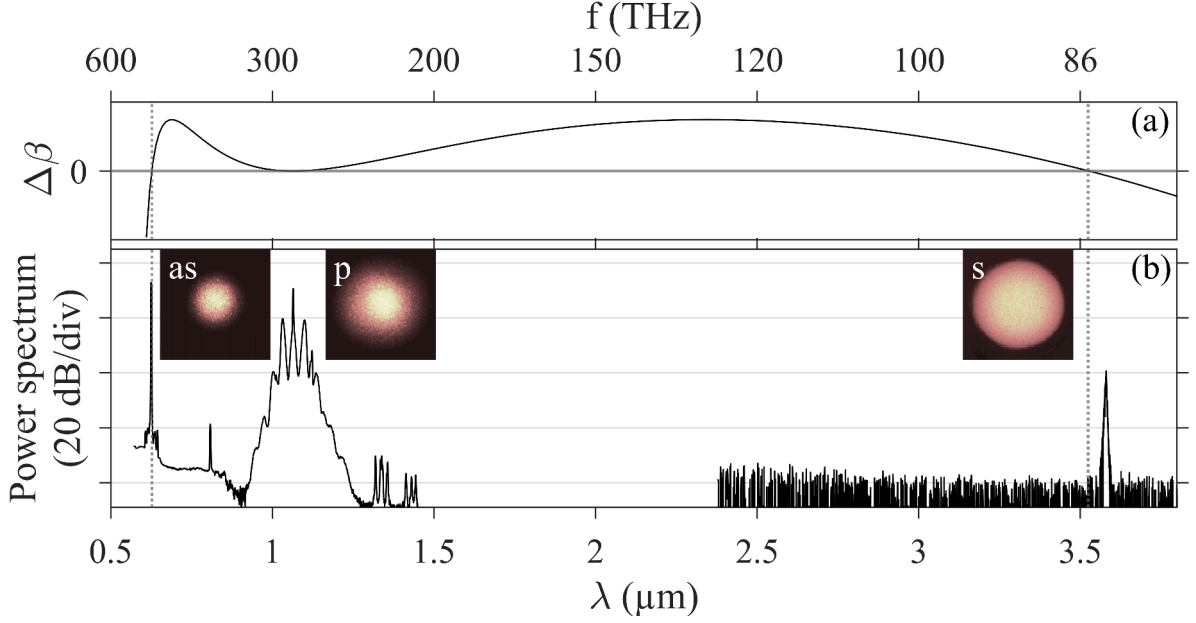


Figure 4.7: (a) Phase mismatch $\Delta\beta$ calculated for the FWM process in the fundamental mode. (b) Experimental spectrum recorded at the output of a 70 cm-long fiber segment when the aforementioned FWM process in the fundamental mode is optimized. Insets: near-field images of the three spectral peaks (anti-Stokes, pump, and Stokes waves) captured using appropriate spectral filters.

emergence of two far-detuned peaks located at 3.580 μm and 0.625 μm . The peaks' spectral positions represent a symmetric 200 THz detuning from the pump, which corresponds to the wavelengths of the Stokes and anti-Stokes of a FWM process involving solely the fundamental $\text{LP}_{0,1}$ mode. The near-field spatial characterization of filtered spectral peaks (see insets in Fig. 4.7(b)) corroborates the intramodal nature of this FWM process. More specifically, I used a shortpass 0.95 μm spectral filter to capture the anti-Stokes wave at 0.625 μm , a bandpass 1.064 μm spectral filter to capture the pump wave, and a longpass 2 μm spectral filter to capture the Stokes wave at 3.580 μm . The spatial intensity patterns can all be attributed to the fundamental mode $\text{LP}_{0,1}$, whose full-width at half-maximum significantly broadens over the fiber core with increasing wavelength. The power contained in the mid-infrared peak was measured to be 40 μW when the total average power at the fiber output was 27.5 mW. Comparing to a 0.2% efficiency of conversion of 1.064 μm pump pulses to 3.105 μm Stokes reported in a meter-long PCF [179], I measured a comparable but slightly lower conversion efficiency, while observing Stokes at much longer wavelength (which results in higher losses). To the best of my knowledge, the described observation is the most far-detuned frequency conversion into the mid-IR range performed in a silica-based fiber.

Using Eq. 2.44, I calculated the phase mismatch for the FWM process involving only the fundamental mode and plot the obtained $\Delta\beta$ in Fig. 4.7(a). My results corroborate that the phase-matching of the far-detuned frequency peaks observed at ± 200 THz can be fully driven by the higher-order dispersion of solely the $\text{LP}_{0,1}$ mode (i.e., a degenerate FWM that transfers energy from a strong pump wave to two waves). Indeed, the corresponding linear phase-matching accurately predicts the spectral positions of the Stokes and anti-Stokes at

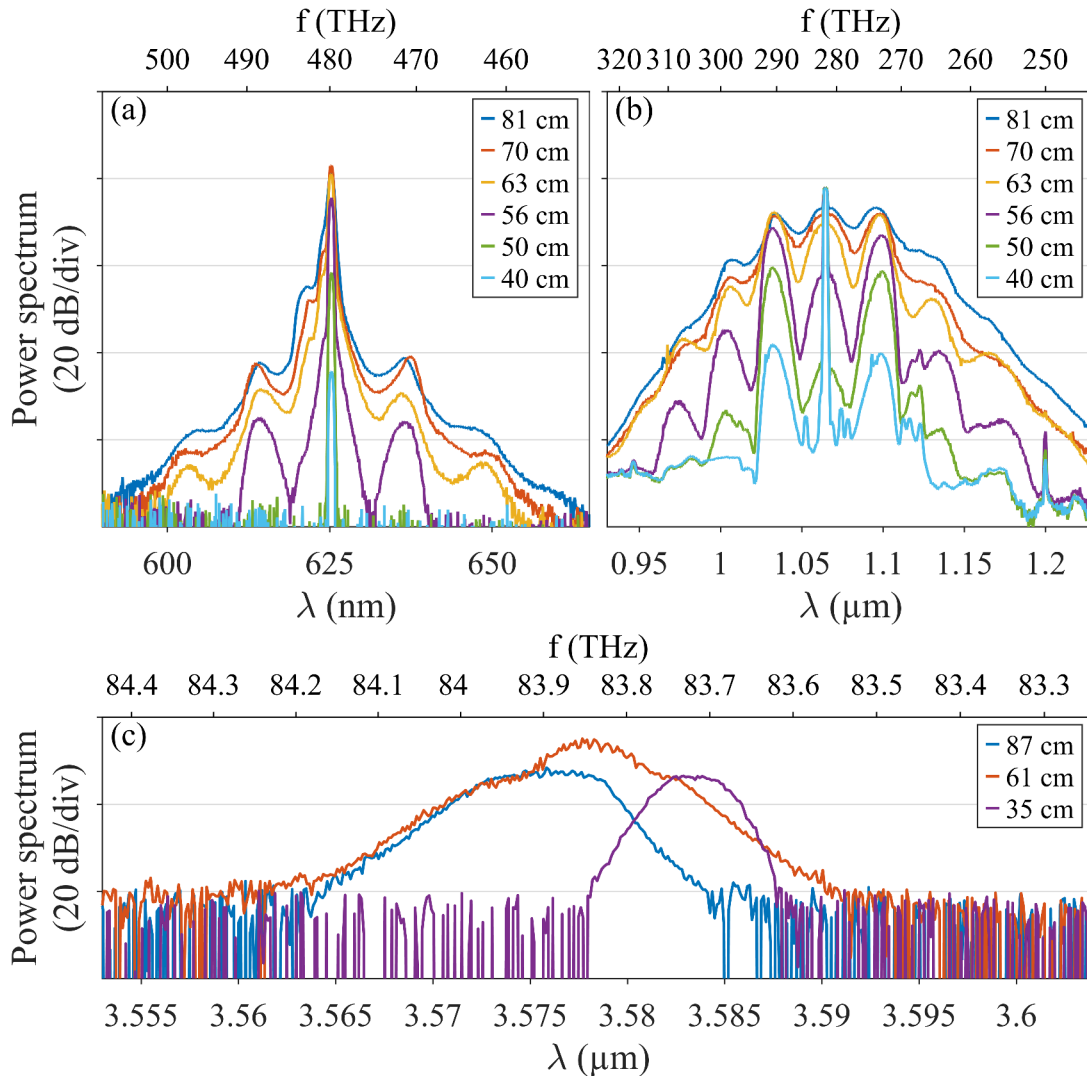


Figure 4.8: Corresponding spectra of anti-Stokes (a), pump (b), and Stokes (c) waves recorded at the output of fiber segments of increasing lengths. In (a-b), the input beam launch conditions were kept unchanged. In (c), for each fiber length the launch conditions were adjusted to obtain the highest intensity of the Stokes peak.

$3.524\ \mu\text{m}$ and $0.627\ \mu\text{m}$, respectively (marked with dotted lines in Fig. 4.7). Note that the disagreement in frequency with experiments remains in the order of 1 THz for both peaks (see also Fig. 4.8(a and c) for zoomed in measured spectra).

To further study this FWM process, I carried out a cutback experiment to compare the power spectra of anti-Stokes and pump waves at different propagation distances. I plot selected spectra of anti-Stokes in Fig. 4.8(a), obtained for different fiber lengths with input beam launch conditions kept unchanged (except average power here equals to 24 mW). Notably, the anti-Stokes power grows significantly with propagation distance. The estimation of this growth rate along the propagation distance is analyzed later (see Fig. 4.9(a)). After approximately 70 cm, the spontaneous gain for the anti-Stokes saturates and further propagation leads solely to spectral broadening. The broadening is induced by the cascaded broadening of the pump

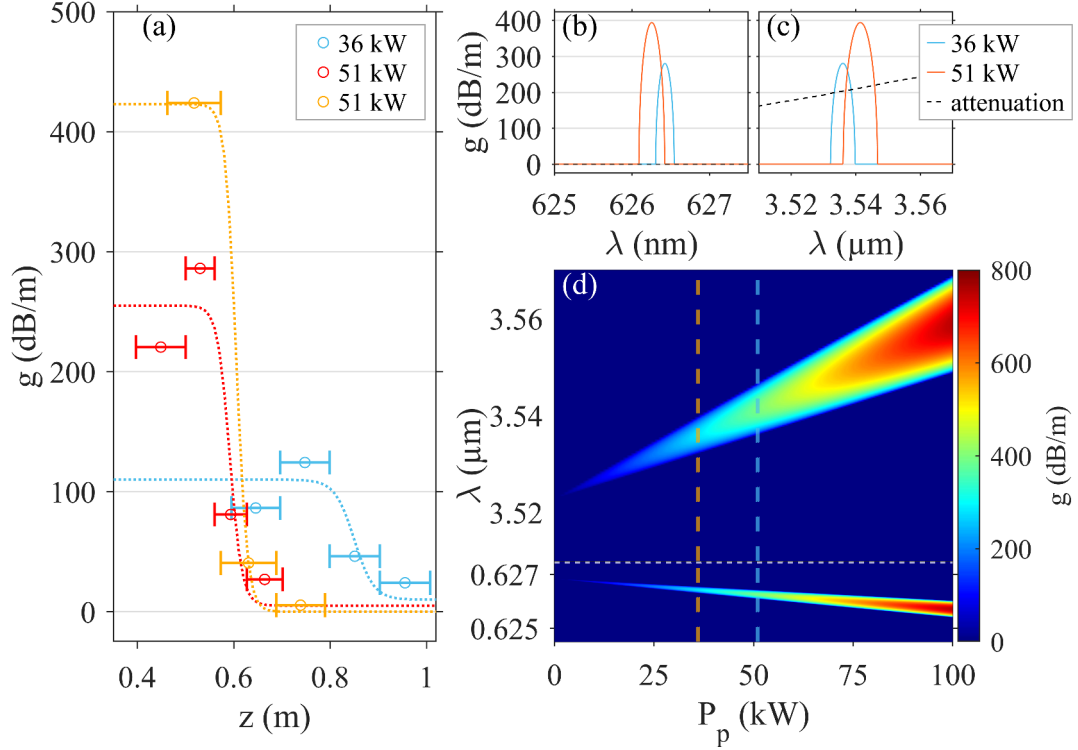


Figure 4.9: (a) Experimental gain measurements for the anti-Stokes wave centred at $0.625\ \mu\text{m}$ as a function of propagation distance z , obtained for peak powers in the fundamental mode equal to 51 kW (red and yellow) and 36 kW (blue) (with fitting curves in dashed lines as guides to the eye). Horizontal solid segments also indicate the cutback fiber lengths. (b and c) Theoretical gain calculations for the anti-Stokes (b) and Stokes (c) waves for 36 kW (blue) and 51 kW (orange) peak power. Black dashed line indicates the estimated fiber attenuation in this spectral region. (d) Theoretical gain calculations for the anti-Stokes and Stokes waves as a function of peak power. Dashed orange and blue lines indicate peak powers plotted in (b-c).

spectrum, as observed in Fig. 4.8(b), through cross-phase modulation effects. Note that the same frequency detuning of spectral sidebands is observed (approximately 8.5 THz).

Additionally, in Fig. 4.8(c), I present some selected spectra of the mid-IR Stokes wave obtained for different fiber lengths. After each cutback the fiber alignment was optimized to achieve the highest intensity of the mid-IR peak (for a constant average power of 27.5 mW). Clearly, the Stokes power is limited by the strong fiber losses in this spectral region (see Fig. 4.5(b)). After exceeding approximately 70 cm of propagation, the Stokes power begins to drop as the fiber losses overcome the already saturated gain of the FWM process. In this study, I observe a small detuning by a fraction of 1 THz of the Stokes central wavelength and a change in its bandwidth for different lengths of the fiber. This may result from small variations of the input conditions which were optimized each time to achieve the highest intensity of the Stokes peak.

In the following, I characterize the dynamics of gain of the observed spontaneous far-detuned FWM process. In Fig. 4.9 I compare some experimental gain measurements along the fiber length (a) with theoretical predictions for the two analyzed peak powers (b-c). In addition,

in Fig. 4.9(d) I display gain calculated as a function of peak power, obtained using Eq. 2.47. To compare my measurements performed for the higher power with theoretical values, I estimate the value of the input peak power P_0 equal to 85% of 60 kW. Peak power of 60 kW corresponds to average power of 24 mW that was measured in two cutback experiments indicated with yellow and red points in Fig. 4.9(a), and 85% is the estimate for the power contained in the fundamental mode by analyzing the frequency detuning of MI peaks around the pump. Estimation of experimental gain is possible only for the anti-Stokes wave in the visible region, based on several spectra recordings, as shown in Fig. 4.8(a). Such a gain estimation over very short propagation distances is challenging. As shown by the two data sets for the same power of 51 kW in the fundamental mode, the obtained gain strongly depends on the cutback increment (indicated by horizontal segments). Nevertheless, the gain measurements agree well with the theoretical predictions. The measurements also show the complete saturation of the FWM process after 0.7 m as the gain rapidly drops to zero. It is worth mentioning that the theoretical phase-matching Δk , which involves the nonlinear phase changes due to pump power and is defined in Eq. 2.45, better predicts the spectral positions of the Stokes and anti-Stokes at 3.545 μm and 0.626 μm , respectively.

In the third cutback experiment (marked with blue in Fig. 4.9(a)), the output average power is 17 mW, and analysis of the MI peaks around the pump (not shown here) again indicates that 85% of the power is contained in the fundamental mode. The gain measured here agrees well with the theory for $P_0 = 36$ kW. Several effects can impact the gain efficiency of this FWM process, namely the higher mid-IR losses accumulated during propagation, the competition with other FWM processes such as intermodal MI around the pump, and the temporal walk-off between the generated peaks and the pump [84]. I checked the group velocity mismatch using equation 2.23 and a calculated IGV of the $\text{LP}_{0,1}$ mode from Fig. 4.6(d). GVM between the pump and anti-Stokes wavelengths is 48 ps/m, and GVM between the pump and Stokes wavelengths is 168 ps/m. Subsequently, I verified the corresponding walk-off lengths L_W for a characteristic duration of the pump pulse $T_0 \approx 240$ ps. I found $L_W = 5$ and 1.4 m, respectively, which is longer than the fiber segments under study. A clear identification of the involved detrimental effects would require further numerical studies based on complex modeling as a function of modal excitation [182].

4.4 Intermodal four wave mixing study

To study intermodal FWM processes, I increased the input peak power into the 70-cm-long GRIN fiber by slightly adjusting the position of the fiber around the input focal plane, after which I collected the output spectrum shown in Fig. 4.10(g). The average power at the fiber output is now 29.8 mW, thus corresponding to a coupling efficiency of more than 65%. Here, I obtained a similar spectrum characterized by a pump broadened around 1.064 μm and two far-detuned frequency peaks at ± 200 THz. However, a new set of frequency peaks has emerged in the visible region, similarly to previously reported in Ref. [44] in a slightly longer fiber segment (1 meter). The minor adjustment in the input conditions modified the characteristic frequency of intermodal MI bands around the pump (now about 10 THz detuning). Consequently, I

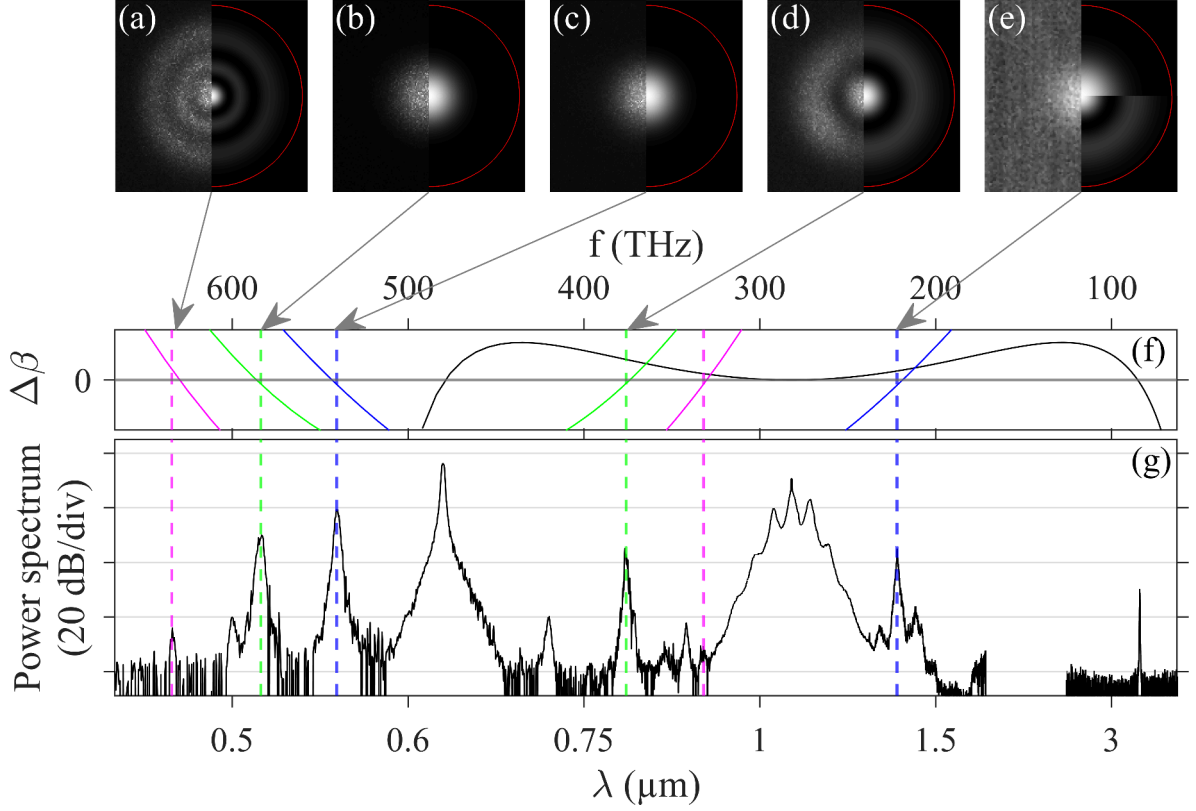


Figure 4.10: (a-e) Near-field images of the spectrally filtered peaks indicated by arrows and colored dashed lines. Left sections are experimental measurements, whereas right sections provide corresponding calculated mode distributions for a given wavelength. In panel (e), both calculated $LP_{0,1}$ and $LP_{0,2}$ modes are shown. Red line in right sections indicates the inner edge of the fluorine-doped trench. (f) Phase mismatch $\Delta\beta$ calculated for intra- and intermodal FWM processes - details provided in text. (g) Experimental spectrum recorded at the output of a 70 cm-long fiber segment with an average power of 29.8 mW when a cascaded FWM process is optimized.

estimate that no more than 80% of the total power is now injected into the fundamental mode (and the remaining into the $LP_{0,2}$ mode). However, as previously shown, the fundamental mode remains the main mode involved in the distinct FWM processes studied below.

A detailed investigation of each FWM at the origin of the spectral peaks was performed both experimentally and theoretically. I characterized the spatial content for the newly emerged spectral peaks by near-field imaging as shown in Figs 4.10(a-e). I analyzed various configurations of intermodal FWM processes and listed them in Table 4.1. As very similar phase-matched frequencies can be found, beyond the necessary condition of phase-matching for the FWM interactions for distinct mode combinations, I determined the relative strength of the interaction using the nonlinear coupling coefficient $\gamma_{1,2,3,4}$ which is driven by the overlap integral of the field distributions $f_{1,2,3,4}$. It is noteworthy to emphasize that integration for far-detuned processes should involve wavelength-dependent field distributions.

For the case of far-detuned peaks at ± 200 THz studied in detail in the previous section, there are two possible FWM processes involving $LP_{0,1}$ mode only, or a combination of the two modes: $LP_{0,1}$ and $LP_{0,2}$. In Table 4.1 those are: $\{p_\mu, p_\eta, p_\nu, p_\kappa\} = \{1, 1, 1, 1\}$, or $\{1, 2, 1, 2\}$.

Table 4.1: FWM combinations with the highest overlap integrals. For comparison, the self-phase modulation coefficient at the pump wavelength in the fundamental mode is $0.0165 \mu\text{m}^{-2}$.

$\{p_\mu, p_\eta, p_\nu, p_\kappa\}$	λ_μ^s	λ_η^{as}	λ_ν^{p1}	λ_κ^{p2}	$f_{s,as,p1,p2} (\mu\text{m}^{-2})$
$\{1, 1, 1, 1\}$	3.524	0.627	1.064	1.064	0.0111
$\{1, 2, 1, 2\}$	3.475	0.629	1.064	1.064	0.0045
$\{2, 1, 1, 1\}$	1.351	0.556	1.064	0.625	0.0135
$\{2, 2, 2, 1\}$	1.364	0.554	1.064	0.625	0.0059
$\{1, 3, 1, 2\}$	1.373	0.552	1.064	0.625	0.0054
$\{1, 2, 1, 1\}$	1.372	0.552	1.064	0.625	0.0054
$\{2, 2, 1, 2\}$	1.354	0.555	1.064	0.625	0.0050
$\{1, 3, 2, 1\}$	1.384	0.550	1.064	0.625	0.0036
$\{2, 1, 1, 1\}$	0.799	0.513	0.625	0.625	0.0171
$\{3, 1, 1, 2\}$	0.791	0.517	0.625	0.625	0.0111
$\{1, 2, 1, 1\}$	0.802	0.512	0.625	0.625	0.0106
$\{3, 2, 2, 2\}$	0.793	0.516	0.625	0.625	0.0093
$\{1, 3, 1, 2\}$	0.804	0.511	0.625	0.625	0.0084
$\{2, 2, 1, 2\}$	0.801	0.513	0.625	0.625	0.0072
$\{2, 3, 1, 3\}$	0.804	0.511	0.625	0.625	0.0057
$\{3, 2, 1, 3\}$	0.795	0.515	0.625	0.625	0.0048
$\{2, 3, 2, 2\}$	0.802	0.512	0.625	0.625	0.0037
$\{2, 2, 1, 1\}$	0.906	0.477	0.625	0.625	0.0119
$\{3, 1, 1, 1\}$	0.894	0.480	0.625	0.625	0.0113
$\{2, 3, 1, 2\}$	0.909	0.476	0.625	0.625	0.0073
$\{1, 4, 1, 2\}$	0.911	0.476	0.625	0.625	0.0034
$\{1, 3, 1, 1\}$	0.911	0.476	0.625	0.625	0.0029

Clearly, these combinations exhibit different overlap integrals, which translate into different FWM efficiencies. This confirms that the process under-study predominantly involves the fundamental mode (the corresponding $\Delta\beta$ is indicated by a black line in Fig. 4.10(f)). In this regard, it is also worth to point out that the resulting FWM efficiency also depends on the power contained in the two pumping modes $\{p_\nu, p_\kappa\}$. I recall that based on my estimations, around 80% of the pump power is injected into the $\text{LP}_{0,1}$ mode, and 20% into the $\text{LP}_{0,2}$ mode. Such distribution of the pump power further privileges the resulting efficiency of the intramodal FWM process.

The second pair of analyzed peaks is located at $0.555 \mu\text{m}$ and $1.352 \mu\text{m}$ (blue dashed lines in Fig. 4.10). In that case, I retrieve experimentally the main signature of the fundamental mode for such peaks, see Figs. 4.10(c) and (e). Table 4.1 provides the corresponding FWM processes with the highest overlap integrals. To satisfy the condition $\omega_s + \omega_{as} = \omega_{p1} + \omega_{p2}$, the origin of the observed spectral components can only be explained by involving non-degenerate FWM with two distinct pump wavelengths, specifically $0.625 \mu\text{m}$ and $1.064 \mu\text{m}$. The mode combination $\{2, 1, 1, 1\}$ appears as the most probable scenario with the highest overlap integral

and consistent with the pump wavelengths mostly carried by the fundamental mode (the corresponding $\Delta\beta$ is marked with blue line in Fig. 4.10(f)). However, it has to be pointed out that at the Stokes wavelength the $LP_{0,2}$ mode is close to cutoff. This explains the reason behind observation of the Stokes peak in the fundamental mode with a lower intensity compared to the anti-Stokes peak. Other combinations listed in Table 4.1 provide FWM processes with lower efficiencies due to lower overlap integrals but enabling Stokes emission in the $LP_{0,1}$ mode with mixed pumping in both $LP_{0,1}$ and $LP_{0,2}$ modes. Again, it has to be pointed out that the efficiency of such FWM process with mixed pumping is additionally reduced due to the lower power of the pump contained in the higher order mode compared to the power of the pump contained in the fundamental mode.

The third pair of peaks emerges at $0.514\ \mu\text{m}$ and $0.798\ \mu\text{m}$ (green dashed lines in Fig. 4.10). These sidebands are mainly associated with the $LP_{0,1}$ and $LP_{0,2}$ modes, respectively, see Figs. 4.10(b) and (d). When checking possible phase-matched combinations, I identified a degenerate FWM with pumping in the fundamental mode at $0.625\ \mu\text{m}$ as the process with the highest overlap integral, thus giving $\{2, 1, 1, 1\}$ (the corresponding $\Delta\beta$ is marked with green line in Fig. 4.10(f)). This is in excellent agreement with my measurements. Other combinations are also listed in Table 4.1 for comparison.

Finally, the fourth pair of peaks identified at $0.473\ \mu\text{m}$ and $0.904\ \mu\text{m}$ (magenta dashed lines in Fig. 4.10) exhibits low intensities. Due to intense pump in proximity of Stokes wave I did not retrieve the Stokes spatial profile. Instead, I could record the spatial content of anti-Stokes wave, which is mainly supported by the $LP_{0,3}$ mode, as shown Fig. 4.10(a). My analysis indicates that these wavelengths can be associated with degenerate FWM processes with pump at $0.625\ \mu\text{m}$ involving the $LP_{0,1}$ and $LP_{0,2}$ modes. The one best corresponding to the experimental characterization refers to $\{2, 3, 1, 2\}$ in Table 4.1 (the corresponding $\Delta\beta$ is marked with magenta line in Fig. 4.10(f)), and confirms the low efficiency.

4.5 FWM in other fiber designs

Far-detuned frequency conversion in the normal dispersion regime has already been investigated in single-mode and small-core fibers, but it is typically rather limited to frequency shifts of tens of THz and FWM gain of tens of dB/m [183, 184]. In the performed study extended FWM features are supported by the combination of (i) the strong modal overlap across a large spectral bandwidth linked to the fiber profile and (ii) high peak powers. In Fig. 4.6(b), one can notice that the effective area of the fundamental mode remains in the 10 to $200\ \mu\text{m}^2$ range over the $3\ \mu\text{m}$ spectral bandwidth. As discussed in Section 4.2.1, the increase around $3.5\ \mu\text{m}$ can be associated with higher confinement losses and could possibly contribute to the lower measured power of the Stokes peak.

Such far-detuned phase-matchings are also theoretically possible in conventional profiles of silica step-index and graded-index fibers. I conducted numerical and experimental investigations on the FWM processes using various designs of fibers available at our laboratory. For numerical studies, I assumed a $1.064\ \mu\text{m}$ pump and each wave in the fundamental mode. The obtained results are summarized in Table 4.2. Along with the predicted Stokes and anti-Stokes

Table 4.2: Numerical investigation of intramodal FWM processes in the LP_{0,1} mode with pump at 1.064 μm evaluated in various fiber designs.

Fiber type	Core diameter (μm)	GeO ₂ doping	λ_{μ}^s (μm)	λ_{η}^{as} (μm)	$f_{s,as,p,p}$ (μm^{-2})	$f_{p,p,p,p}$ (μm^{-2})	$1/f_{s,s,s,s}$ (μm^2)
GRIN	22	5%	3.524	0.627	0.0111	0.0165	262
step-index	8.2	3.9%	3.727	0.621	0.0064	0.0207	1820
step-index	15.5	4.2%	3.297	0.634	0.0077	0.0087	189
step-index	3.6	24%	5.234	0.592	0.0167	0.1201	2322
step-index	3.4	28%	5.242	0.592	0.0221	0.1271	1384
step-index	3.2	31%	5.238	0.592	0.0271	0.1314	882
step-index	4.0	31%	4.663	0.601	0.0429	0.1020	157
step-index	6.0	31%	3.937	0.615	0.0406	0.0543	52
step-index	8.0	31%	3.951	0.615	0.0278	0.0334	60
GRIN	50	11%	3.774	0.619	0.0056	0.0079	433
GRIN	62.5	20%	4.155	0.610	0.0058	0.0085	432
GRIN	100	24%	4.333	0.607	0.0039	0.0058	654

wavelengths, I included calculated overlap integrals for FWM process and self-phase modulation coefficients at the pump wavelength in the fundamental mode. In addition, to give insight into mode confinement at mid-IR spectral range, I provided effective areas of the fundamental mode at the Stokes wavelength. The calculated parameters for the GRIN fiber under study are presented in the first row of the table.

First, I considered a step-index refractive index profile which is similar to the standard SMF-28 fiber. For the assumed 3.9% mol GeO₂-doped core with a diameter of 8.2 μm , Stokes and anti-Stokes peaks are located at 3.727 μm and 0.621 μm , respectively. However the calculated overlap integral equal to 0.0064 μm^{-2} is almost twice as low as the case of the GRIN fiber studied here, resulting in a FWM gain below the fiber attenuation. Furthermore, I observed significantly reduced modal confinement at long wavelengths comparing to the GRIN fiber (i.e., effective mode area increased substantially beyond 1000 μm^2). The fundamental mode clearly no longer remains guided in the core at that spectral range, which is not conducive to achieving high FWM gain. Experimentally, I conducted cutback measurements under pumping conditions similar to my prior research. Nevertheless, I did not detect any far-detuned FWM peaks, neither in the visible, nor in the mid-IR spectral range.

Subsequently, I investigated a few-mode step-index silica fiber which has a core almost twice the size of the standard SMF and a comparable germanium doping level. In such design, the Stokes wavelength calculated at 3.297 μm is less detuned than in the investigated GRIN fiber case. I have found that the modal confinement at this spectral range is well maintained (the mode effective area remains below 200 μm^2), and the overlap coefficient is comparable to the self-phase modulation coefficient at the pump wavelength. The calculated modal overlap coefficient equal to 0.0077 μm^{-2} is approximately 2/3 of the modal overlap of the GRIN fiber

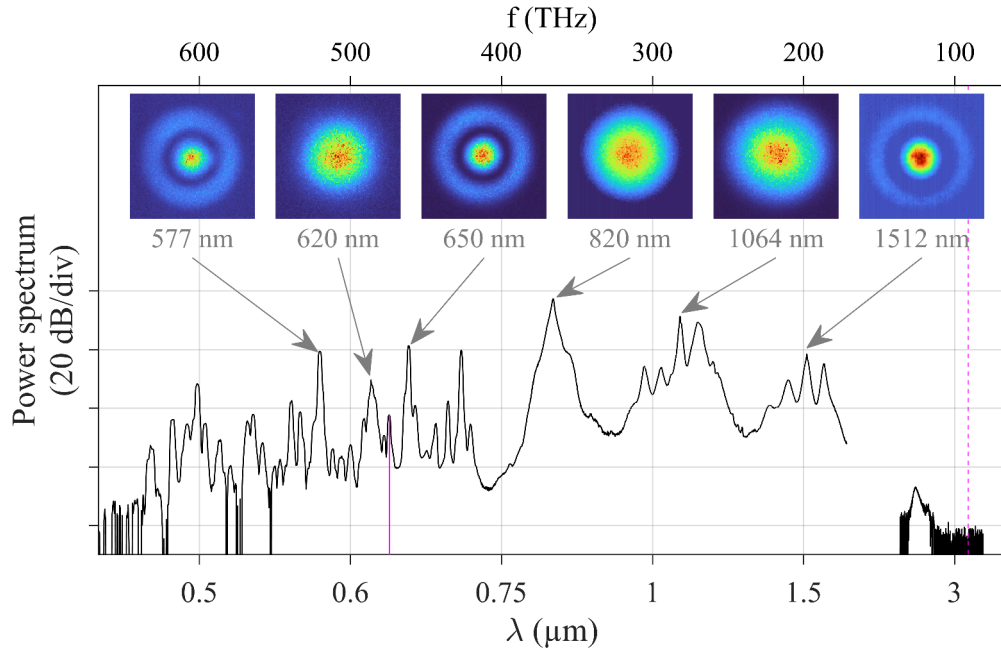


Figure 4.11: Experimental spectrum for 23 mW average power recorded at the output of a meter-long segment of step-index fiber with a $15.5\ \mu\text{m}$ core diameter with the light launching conditions optimized to excite the fundamental mode. Magenta lines indicate the Stokes and anti-Stokes wavelengths of the intramodal FWM process. Insets: near-field images of the selected peaks captured using appropriate spectral filters.

under study. In the cutback experiments, I did not detect any peak in the mid-IR spectral range beyond $3\ \mu\text{m}$ for fiber lengths between 50 and 100 cm. Instead, I observed multiple spectral peaks arising from cascaded intermodal FWM, which are located closer to the $1.064\ \mu\text{m}$ pump. The spectrum recorded at the output of a meter-long fiber segment for an average power of 23 mW is shown in Fig. 4.11. Using spectral filters with different central wavelengths, I characterized spatial content of selected spectral peaks, which revealed either $LP_{0,1}$, or $LP_{0,2}$ modes, as shown in the figure insets. The input coupling conditions were optimized to excite the fundamental mode (the captured image of spectrally filtered pump shown in one of the insets corroborates the high quality of excitation). My results are consistent with the outcomes of another study of nonlinear dynamics that has been performed in this fiber using a $1.064\ \mu\text{m}$ picosecond pump [43]. The authors used much longer segments of this fiber (50 and 5 meters) and different injection conditions to excite either a multimode mix, or fundamental mode only. Here, I validate as well as expand upon the previous study by presenting the experimental spectrum obtained at the output of a shorter, meter-long fiber segment. This offers insight into nonlinear dynamics occurring at shorter propagation distance. The increased pump power I used resulted in generation of a greater number of cascaded peaks compared to what had been reported previously. However, despite employing higher power and optimizing excitation of fundamental mode, I did not detect the Stokes peak I predicted at $3.297\ \mu\text{m}$ linked to the intramodal FWM process (the predicted Stokes wavelength is indicated by a dashed magenta line in Fig. 4.11). I identified a peak $0.633\ \mu\text{m}$, which corresponds to the predicted anti-Stokes

wavelength of the intramodal process (the peak is indicated by a magenta line in Fig. 4.11). Its intensity is relatively weak compared to the nearby peaks, which poses a challenge to retrieve its modal content and confirm whether it is indeed the expected $LP_{0,1}$ mode. The low intensity of this potential anti-Stokes peak suggests that the absence of the Stokes peak could be attributed to competition with other wave mixing processes that might have higher overlap coefficients and use up the available pump power earlier during the propagation.

Following, I performed a numerical study on a set of highly-nonlinear fibers. Our available step-index single-mode fibers are characterized by small cores of 3.2-3.6 μm and high GeO_2 doping levels. I have found that the reduced core size and the increased refractive index contrast between core and cladding result in a notable increase of the detuning of the FWM process, causing the expected wavelengths of the phase-matched Stokes peak to exceed 5 μm . In the investigated designs, the calculated overlap coefficients are higher than those in our GRIN fiber. However, it is essential to emphasize that they are only a fraction of the respective self-phase modulation coefficients, and mode effective area at calculated Stokes wavelengths is close to or exceeding 1000 μm^2 , which indicates that beyond 5 μm the mode can no longer be guided in core for any of the considered designs. Analysing those three investigated profiles, it is evident that increasing germanium doping level significantly enhances mode confinement. By conducting further numerical investigations, I have discovered that increasing the core diameter of the fiber with a 31% germanium-doped core leads to a notable reduction of mode effective area at the Stokes wavelength, which results in increase of the overlap coefficient. Simultaneously, increasing the core diameter shifts the predicted Stokes peak toward shorter wavelengths. However, for the final optimized fiber profile with a 8 μm core, the Stokes peak is expected to be generated around 4 μm , which remains an interesting potential outcome. While I did not have access to fibers with the identified designs, it could be worth to explore experimentally the possibility of generating mid-IR radiation in fibers with higher level of germanium doping in the core. I would like to recall and point out that germanium assists in extending the fiber transmission window toward longer wavelengths, which could potentially aid in generation of mid-IR wavelengths.

The last type of refractive index profiles I investigated was graded-index fiber. I considered fiber designs with larger cores than the one used for my study. For each of the analyzed designs with core diameters of 50 μm , 62.5 μm , and 100 μm the predicted Stokes is shifted towards longer wavelengths than in the 22 μm core GRIN fiber, to 3.774 μm , 4.155 μm , and 4.333 μm , respectively. However, contrary to prior findings, mode effective areas at the anticipated Stokes wavelengths exceed 400 μm^2 , which indicates insufficient mode confinement in the core. Furthermore, the overlap coefficients are half or less than in the case of the GRIN fiber in the previous study, suggesting that the FWM process may not be as efficient as in the earlier scenario. Experimentally, I checked that pumping meter-long and shorter segments of our available graded-index fibers at 1.064 μm did not result in any far-detuned FWM peaks in the mid-IR spectral range. One result worth noting was obtained in the fiber with 62.5 μm core and 20% GeO_2 doping, where at the fiber output I observed a peak at 1.870 μm , and a corresponding peak at 0.744 μm . The intensity of the peak close to the visible spectral range was high, surpassing even the pump. The spectrum recorded at the output of a 80 cm long

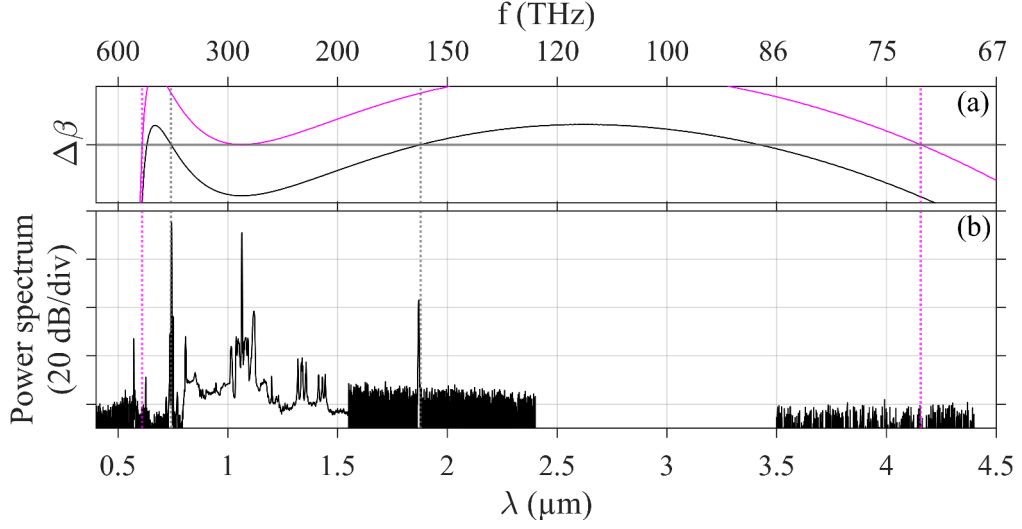


Figure 4.12: (a) Phase mismatch calculated for the FWM process in the fundamental mode (magenta) and for the FWM process with anti-Stokes in $LP_{0,1}$ and Stokes in $LP_{0,2}$ mode (black). (b) Experimental spectrum recorded at the output of a 80 cm-long, $62.5 \mu\text{m}$ core GRIN fiber for 23 mW average power coupled into the fiber with the light launching conditions optimized to excite the fundamental mode.

fiber segment for an average power of 23 mW is presented in Fig. 4.12(b). In addition, in Fig. 4.12(a) I plot using a black line the phase-mismatch curve for the intermodal FWM process corresponding to the Stokes peak in $LP_{0,2}$ mode and the anti-Stokes peak in $LP_{0,1}$ mode. The expected positions of Stokes (at $1.878 \mu\text{m}$) and anti-Stokes (at $0.742 \mu\text{m}$) agree very well with the experimental data. My results validate the findings in [180], where a mix of $LP_{0,1}$ and $LP_{1,1}$ modes had been excited in a 2.3 m long fiber and a 3D beam mapping technique was used to characterize the spatial content of the two peaks. Indeed, in that study the anti-Stokes peak was found to be composed of $LP_{0,1}$, while the main component of the Stokes peak was identified as the $LP_{0,2}$ mode (the Stokes peak characterization is reprinted here in Fig. 4.4). Compared to the results described in that article, the anti-Stokes peak I observed is significantly more intense, and both the Stokes and anti-Stokes peaks have narrower bandwidth. This discrepancy may result from my cleaner coupling into the fundamental mode and a shorter fiber used for my study. The intermodal FWM process I investigated has an overlap coefficient equal to $0.0055 \mu\text{m}^{-2}$, and a mode effective area at the Stokes wavelength of approximately $417 \mu\text{m}^2$. The values of those two parameters are close to the ones corresponding to the investigated intramodal FWM process, which are provided in Table 4.2. Nevertheless, the recorded spectrum shows no discernible peak that can be associated to either anti-Stokes or Stokes waves of the intramodal process (refer to magenta line in Fig. 4.12 for the phase-mismatch curve and dashed magenta lines for anticipated Stokes and anti-Stokes spectral positions). This absence could be explained by a much larger detuning of the Stokes wave of the intramodal process toward the mid-IR spectral region, where fiber losses prevent effective peak generation.

4.6 Conclusions

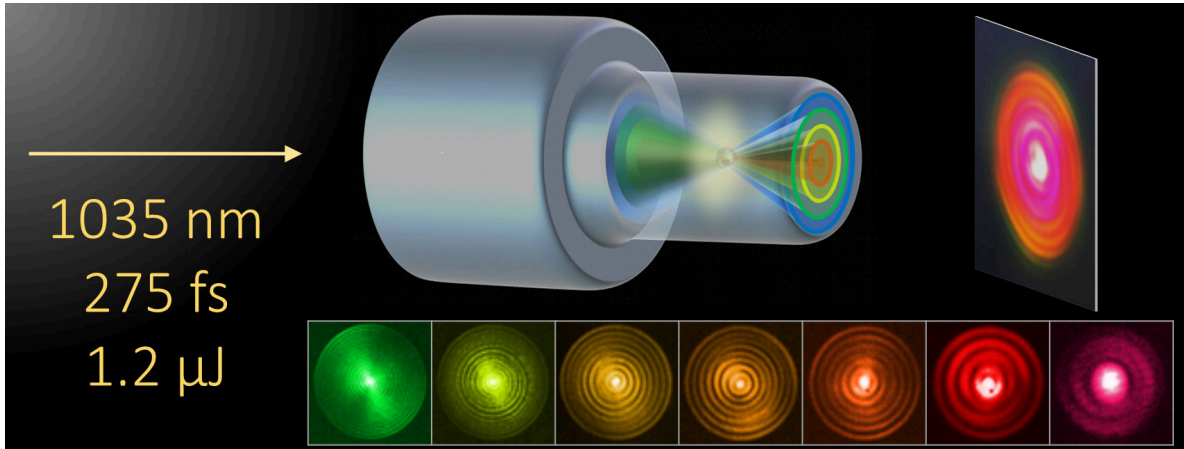
In this chapter I investigated nonlinear frequency conversion processes in a short few-mode graded-index silica fiber. I provided experimental evidence supported by theoretical analysis that four wave mixing can be used for far-detuned frequency generation leading to conversion of near-IR pump to visible and mid-IR wavelengths. The obtained results are particularly interesting as I achieved generation of mid-IR radiation well beyond the commonly accepted transparency window of silica fibers.

The conducted research clearly confirms the research hypothesis. By efficiently launching the pump into the fundamental fiber mode, I achieved generation of far-detuned peaks generated in the intramodal FWM process involving the fundamental fiber mode. By changing the modal composition of the excited field I obtained a cascade of intermodal FWM processes that arise through the combination of the secondary pump at $0.625\ \mu\text{m}$ with or without the initial pump. I performed detailed spatial investigation of the generated peaks and reached a good agreement with my theoretical predictions. The secondary pump is enabled by the significant power contained by the fundamental mode and more specifically the extremely high gain provided by the spontaneous intramodal FWM process.

The performed measurements agree very well with the calculations based on the developed theory. I clearly addressed the limits of possible application of the commonly used simplified theoretical models that allow to study nonlinear wave mixing processes in GRIN fibers.

It is worth highlighting that such high parametric gain value ($400\ \text{dB/m}$) was obtained even for far-detuned frequencies. It appears that the specific refractive index profile of the fiber that I tested allowed to observe FWM process with extremely interesting features. However, there is still room for optimization through careful engineering of the index profile or the use of infrared glasses to tailor phase-matched frequencies and parametric gain in other spectral windows of interest.

Chapter 5



Spatiotemporal wavepackets in a multimode step-index fiber

Multimode optical fibers (MMFs) provide an enabling platform for studying spatiotemporal phenomena in multidimensional systems and complex collective dynamics [20, 19]. This is due to the possible fine control and analysis of discrete set of spatial modes that can propagate and interact in MMFs, in contrast to the two limiting cases:

- single-mode waveguides supporting only one spatial mode,
- bulk media with their infinite and continuous set of modes.

Over the past decade extremely exciting observations of novel optical effects have been reported, such as geometric parametric instability [47], beam self-cleaning [27, 26], light thermalization [185, 186], multimode solitons [29], and spatiotemporal laser mode-locking [23], to name a few.

When considering the potential of multimode waveguides combined with recent technological advances in laser sources and pulse shaping, one of the most promising developments relates to the generation and application of propagation-invariant spatiotemporal (ST) wavepackets [187, 188, 189, 190, 191]. Such an ultimate control of light will pave the way to the delivery of pulsed sources with custom spatial profiles through multimode optical waveguides which could have applications in sensing, imaging, spectroscopy, and investigating novel light-matter interactions [192, 193]. Until now, invariant optical ST wavepackets have primarily been generated and characterized in free space and bulk media [194, 195, 196, 197], often limited to 1D configurations (e.g., ST light sheets).

In the following, I provide a complete analysis, from theory through numerical simulations to experiment, of the spontaneous generation of a discretized conical wave during nonlinear

propagation of an intense ultrashort pulse in a multimode fiber. The theoretical analysis draws on insights from recent publications [187, 198, 188]. In particular, I unfold that this spatiotemporal phenomenon leading to the formation of a 2D linear wavepacket corresponds to a broadband emission of intermodal dispersive waves from an unsteady localized wave structure. This structure is formed during nonlinear propagation and is driven by a characteristic phase-matching relation. Through the analysis of numerical simulations based on the linear unidirectional pulse propagation equation [182], I determine and realize the experimental conditions necessary for achieving the spontaneous generation of 2D propagation-invariant wavepackets in a commercially-available step-index multimode fiber. This research led to the first-ever documented observation of discretized conical emission in a MMF. Moreover, I present experimental characterization of spontaneous conical emission in two distinct bulk samples, which serves as a reference and provides a comparison to the discretized conical emission arising in a multimode fiber. Finally, I outline my investigations concerning the generation of 3D quadric waves in a multimode fiber, which were predicted recently in [188].

5.1 Theoretical description of ST wavepackets

In this section I provide general theoretical description of propagation-invariant 3D linear space-time wavepackets that follow spiralling trajectories in structured media such as optical fibers. Subsequently, I refine this concept to 2D linear ST wavepackets, or conical waves, which represent a special category of invariant wavepackets that do not rotate during propagation. As I show, this framework is applicable to both structured and bulk media.

In this derivation, I assume weak guidance approximation, thus limiting the study to a scalar approach. I consider structures with refractive index exhibiting cylindrical symmetry around the propagation axis z . These restrictions are met by conventional optical fibers. To represent spatial modes of the fiber, I use OAM mode basis, which is introduced in Section 2.2.3. To briefly recall, an OAM fiber mode at frequency ω can be represented by a triplet (l, p, ω) , where $l \in \{0, \pm 1, \pm 2, \dots\}$ refers to the topological charge, and p is related to radial mode number, indicating the number of concentric intensity rings in the mode intensity profile. Following theoretical derivation from [188], I define a family of modes (l, p, ω_{lp}) so that their propagation constants β satisfy the following relation:

$$\beta(l, p, \omega_{lp}) = K_0 + K_1\omega_{lp} + K_l l, \quad (5.1)$$

where constants K_0 , K_1 , and K_l can be chosen arbitrarily. A linear superposition of the modes belonging to the given family yields an electric field expressed as:

$$E(r, \phi, t) = \sum_{l,p} \bar{E}(l, p, \omega_{lp}) A_{l,p}(r, \omega_{lp}) e^{i(l\phi - \omega_{lp}t)}, \quad (5.2)$$

where $A_{l,p}(r, \omega_{lp})$ is the radial field distribution, $\bar{E}(l, p, \omega_{lp})$ is the electric field amplitude for the mode (l, p, ω_{lp}) , and phase factor contains angular and time dependencies.

Using the two above relations and considering evolution of an electric field along the propagation axis z according to the linear unidirectional pulse propagation equation (UPPE) [182],

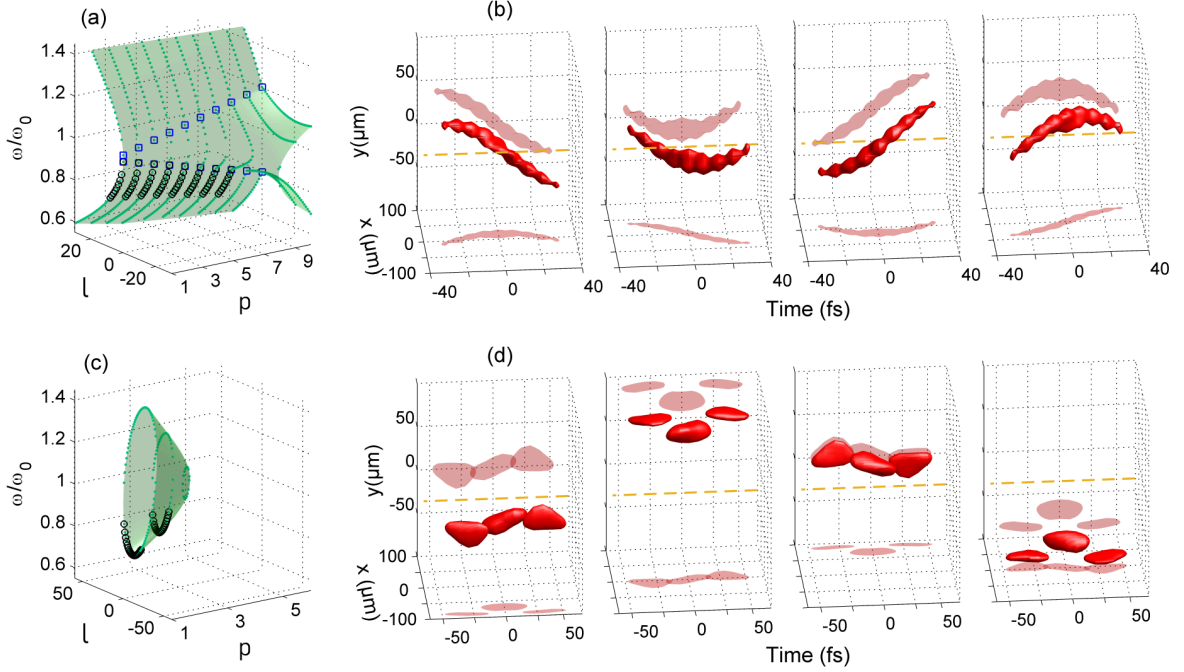


Figure 5.1: Examples of helicon wavepackets in a fused silica rod with radius $R = 100 \mu\text{m}$. (a,c) Quadric surfaces obtained in normal and anomalous dispersion regimes. Green dots indicate discretized conic sections for each p coordinate. Black circles correspond to the selected modes used for the linear construction of helicon wavepackets depicted in (b,d) through iso-surfaces of their spatiotemporal intensity pattern at half-maximum. The successive subplots obtained every $\pi/(2|K_l|)$ corroborate the invariant nature of helicon wavepackets over propagation. The dashed orange line indicates the origin ($x = 0, y = 0$). Projections on planes are provided for a clear observation of rotation [Adapted with permission from ACS Photonics 2022, 9, 6, 2066–2072. Copyright 2022 American Chemical Society].

which in the modal basis takes the form: $\partial_z \bar{E}(l, p, \omega) = i\beta(l, p, \omega) \bar{E}(l, p, \omega)$, we obtain the following solution:

$$E(r, \phi, t, z) = E(r, \phi + K_l z, t - K_1 z, 0) e^{iK_0 z}. \quad (5.3)$$

Notably, the resulting electric field propagates at a fixed group velocity $1/K_1$ and its intensity rotates around the propagation axis with a period given by $2\pi/K_l$, see Fig. 5.1 adapted from [190] for helicon wavepackets propagating in normal (b) and anomalous (d) dispersion regimes in a fused silica rod. Figure 5.1(a) (Fig. 5.1(c)) shows the 3D quadric surface corresponding to the general phase-matching pattern obtained from the relation 5.1 in the normal (anomalous) dispersion regime for arbitrarily chosen constants K_0 , K_1 , and K_l . Black circles indicate a particular selection of modes with various radial and angular indices that superposed construct the corresponding helicon wavepackets depicted in panels (b) and (d). In fact, any modes belonging to a given family and satisfying the phase-matching relation 5.1 can contribute to constructing a ST wavepacket that is free from diffraction and dispersion. Such wavepacket is an invariant field in a frame that propagates at the velocity $1/K_1$ and that rotates around the z axis with a spatial period $2\pi/K_l$. It consists of waves that oscillate at different frequencies and that carry different topological charges.

It is crucial to note that the outlined method concerns ST wavepackets composed of linear superposition of strictly monochromatic modes. Such scenario cannot align with a realistic physical situation because it would require an infinite amount of energy. In practice, a ST wavepacket could be constructed by combining multiple continuous-wave lasers (or frequency-comb lines) using wave shaping techniques and spatial mode multiplexing. In contrast, the involved modes could be spontaneously excited during the nonlinear propagation of ultrashort pulses (which I investigate in subsequent sections). This in turn implies a non-zero bandwidth of the participating frequencies ω_{lp} . Non-zero spectral bandwidth is associated with a finite temporal envelope that must be incorporated into the expression 5.2 for the electric field constructed from a given family of modes [187, 188]. As a result, the temporal envelope of the modes forming the ST wavepacket does not propagate at a one fixed group velocity. This leads to a temporal dispersion of the constructed wavepacket, meaning that it is not entirely propagation-invariant. Nevertheless, the propagation length over which the effect of dispersion of the different participating modes noticeably impacts the propagation strongly depends on the duration of the temporal envelope. Therefore, over a finite propagation distance, the wavepacket can be deemed invariant.

Regarding the spontaneous emergence during the course of nonlinear propagation, earlier works made use of the effective three-wave mixing picture developed to describe conical waves emitted in bulk and condensed media [199, 200]. This approach has recently been generalized to structured media [187] and to spontaneous emission of more general 3D wavepackets in fibers [188]. In such circumstances, the constants K_0 , K_1 , and K_l in the phase-matching condition 5.1 correspond respectively to the propagation constant, the inverse group velocity, and the rotation rate of the optical shock front that is formed in the normal dispersion regime due to the self-focusing and self-steepening of the pulsed beam. This ST shock front is followed by wavebreaking and seeds linear dispersive waves, which are then resonantly amplified in higher-order modes leading to the formation of ST wavepacket. Such dynamics will be investigated in later sections, see Fig. 5.8 and its description. The resulting wavepacket propagates with the same group velocity and rotation rate as the initial optical shock. The tolerance of the bandwidth of the generated frequencies that I mentioned in the preceding paragraph introduces a certain tolerance into the phase-matching condition 5.1:

$$\left| \beta(l, p, \omega_{lp}) - K_0 - K_1 \omega_{lp} - K_l l \right| \leq \frac{2\pi}{d_z}, \quad (5.4)$$

where d_z is related to a distance over which the optical shock seeds the emerging broadband wave structure. In subsequent sections, I compare d_z obtained from the numerical study to the bandwidth of the wave structure under investigation.

Finally, I recall that in the context of a general framework that classifies ST wavepackets localized in all dimensions and different dispersion regimes, the modes belonging to a given family lie on a specific quadric surface in the three-dimensional (l, p, ω) space [190], as seen in Fig. 5.1(a,c). In general, those surfaces are associated to ST quadrical waves (helicon wavepackets that propagate in spiraling trajectories). This model naturally embeds a special 2D case of commonly studied conical waves [200] obtained at the intersection of the quadric

surface with the plane defined by topological charge $l = 0$. The specific shape of this two-dimensional wavepacket in the (p, ω) plane depends on the chromatic dispersion of the medium and the central wavelength of the input pulse. The cross-sections of the quadric surface along the $l = 0$ plane can take the form of a hyperbola (manifesting as the so-called X-wave in the case of normal dispersion regime [199, 201, 202], for reference see blue squares in Fig. 5.1(a)), or an ellipse (O-wave for anomalous dispersion regime [203, 204, 205]). To complete this description, when the central wavelength of the input pulse is in the near-zero dispersion regime, a more complex ST dynamics results in a so-called fish-wave which exhibits characteristics common to both X- and O-waves [199, 206].

Conical waves and spontaneous conical emission have typically been studied in bulk media [194, 200, 32, 207], such as solids [205, 208], liquids [199, 204, 209, 210], gases [211, 212], or free space [210, 213, 214]. In general, the conical emission is related to the beam self-focusing overcoming diffraction when peak power exceeds a critical threshold $P_{crit} = 3.72\lambda_0^2/(8\pi n_0 n_2)$ [32]. Theoretical and numerical results from recent studies have shown evidence that MMFs are another, structured type of medium that supports spontaneous emission of discretized conical waves during propagation of intense ultrashort pulses with peak powers around the critical self-focusing threshold [187, 198, 182]. In the following, I investigate conical wavepacket generated in the normal dispersion regime, and more specifically spontaneous emergence of discretized X-wave during the propagation of ultrashort pulses in a step-index MMF. Since the considered fiber is circularly symmetric and the family of modes that satisfy this new phase-matching relation contains only modes with $l = 0$, it is reasonable to consider the linearly polarized modes of $LP_{0,p}$ class as basis for analyzing the conical emission. This yields the spatiotemporal spectrum described by the following phase-matching relation:

$$\left| \beta(p, \omega_p) - K_0 - K_1 \omega_p \right| \leq \frac{2\pi}{d_z}, \quad (5.5)$$

which is a modified version of condition 5.4, where the term $K_l l$ disappears because the conical wavepacket consists of modes that carry no topological charge, and where $\beta(p, \omega_p) = \beta(0, p, \omega_{0,p})$ refers to the full frequency-dependent propagation constant of guided mode $LP_{0,p}$. In the experimental study I optimized the conditions to achieve beam coupling into the fundamental fiber mode $LP_{0,1}$. Such configuration implies the specific values of the K_0 and K_1 parameters and properties of the generated wavepacket. Namely, the propagation constant of the optical shock front is determined by the propagation constant of the fundamental mode at the carrier central frequency ω_0 : $K_0 = \beta(1, \omega_0)$, whereas the inverse group velocity of the generated wavepacket $K_1 = 1/v_{gX}$ can be conveniently expressed as a sum $\beta_1 + \delta K_1$, where $\beta_1 = 1/v_{g_0}$ is the inverse group velocity of the fundamental mode at ω_0 . v_{g_0} is commonly used as a velocity of retarded time frame in which numerical simulations are performed. The parameter δK_1 indicates the difference of group velocities $\delta v_g = v_{g_0} - v_{gX}$. Explicitly: $\delta v_g = \delta K_1 / [\beta_1 (\beta_1 + \delta K_1)]$.

Last but not least, I should emphasize that the above relation is applicable not only to multimode waveguides but also to bulk media. In the latter case, the propagation constant is $\sqrt{k^2(\omega) - k_\perp^2}$, where wave vector $k(\omega) = n(\omega)\omega/c$, $n(\omega)$ is a material refractive index and k_\perp is a transverse component of the wave vector. However, waveguides and in particular multimode

fibers support a discrete set of modes, whereas free space, gases, and condensed media support a dense and infinite number of spatial modes. In the first case, for a given ST wavepacket, only a discrete number of frequencies ω_{lp} comply with the relation 5.4. This results in generation of ST wavepackets which are discrete in terms of possible modes that participate in a wavepacket formation, hence the term discretized conical emission. In the latter cases, any value of ω can correspond to a k_{\perp} , which is associated with a spatial mode of such media. In literature, a cone angle θ is often used in place of k_{\perp} as it corresponds to the space in which experiments are performed [200]. The two parameters are linked by a simple relation: $k_{\perp} = k \sin \theta$, which I use in the section dedicated to the study of conical emission in bulk media.

5.2 Study conditions

To study spontaneous generation of quadric and conical waves, I implemented the experimental setup depicted schematically in Fig. 5.2. I used a high-power femtosecond laser (Monaco 1035, Coherent) delivering 275 fs pulses at 1035 nm with a chosen repetition rate of 10 kHz. The pulse energy can be as high as 60 μ J. The laser output power was adjusted to μ J-level energy by means of variable attenuator composed of neutral density filters and a half-wave plate combined with a polarizer, in order to prevent damage issues [215]. The transmission axis of the polarizer P₁ was set vertically to ensure the conservation of the linear polarization after reflection from the mirror.

For the research concerning helicon wavepackets, I employed additional polarizing optical elements before the coupling lens L₁ to shape the input beam. Namely, a polarizer P₂ was used to ensure the linear polarization state of the beam and a quarter-wave plate QWP₁ was used to convert polarization from linear to circular. The circularly polarized beam then passed through a $q = 1/2$ zero-order quarter-wave q plate with an operating wavelength of 1.03 μ m (custom optical element manufactured by Thorlabs). This produced beam that can be described as superposition of a circularly polarized Gaussian intensity profile (polarized with the same handedness as the incident beam) and a circularly polarized OAM field with topological charge $l = 1$ (polarized with the opposite handedness to the incident beam), see Section 2.2.4 for a description of q plate operation. During the final stage of input beam shaping, the desired composition of the beam is selected with a circular analyzer, consisting of the quarter-wave plate QWP₂ and the polarizer P₃. By adjusting the orientation of the QWP₂ axis from 0° to 90°, the beam could be modified to contain only the $l = 1$ field, a combination of the $l = 1$ and $l = 0$ fields, or only the $l = 0$ field (like the initial laser beam). This is depicted in the top row of Fig. 5.3 (the position of the beam profiler used to obtain these captures is indicated in the *Beam shaping panel* in Fig. 5.2). I controlled the beam composition by rotating the axis of QWP₂ and keeping the P₃ polarizer axis rotation constant, in order to maintain the direction of linear polarization of the beam that was coupled into the fiber.

For the research concerning conical emission in MMF and bulk glass, I had two alternatives: either to rotate the QWP₂ to the position marked with 90° in Fig. 5.3 so that only the original beam with Gaussian intensity profile and zero topological charge passed through the circular polarizer, or to altogether remove the optical elements indicated in the *Beam shaping panel* in

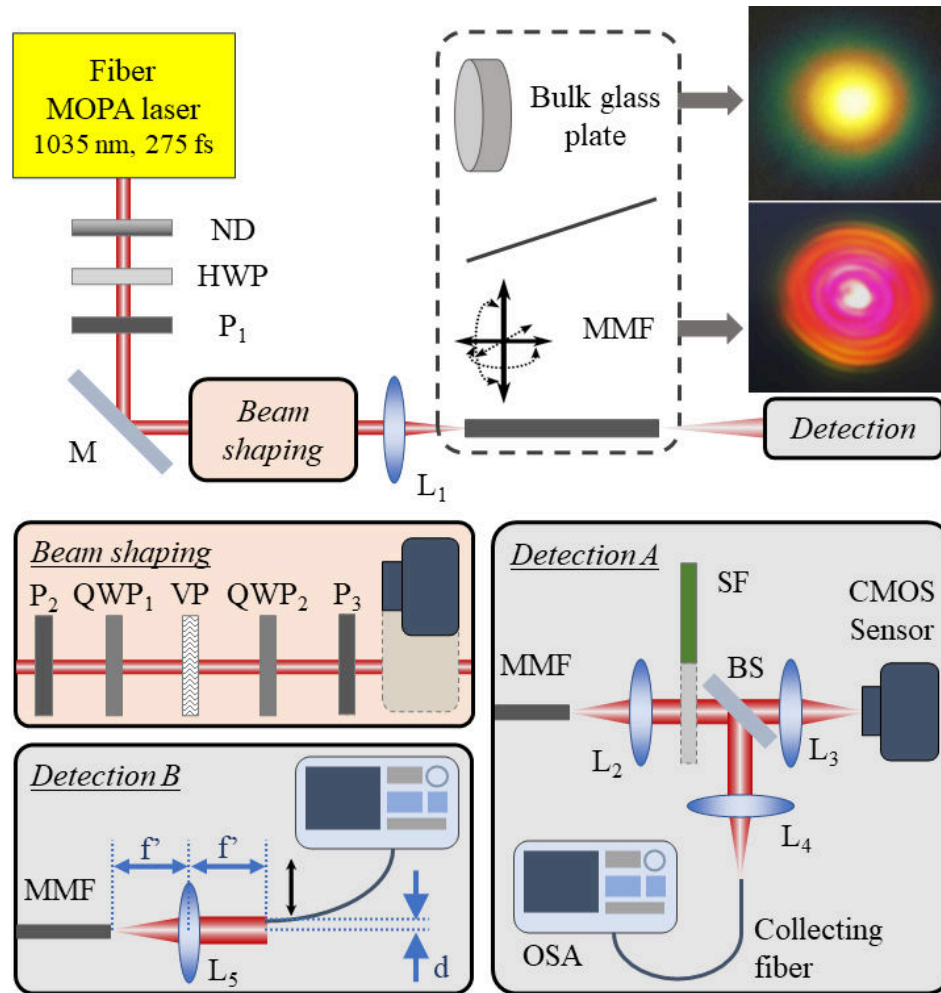


Figure 5.2: Experimental setup for investigating helicon wavepackets in MMF and for recording near-field images and angularly-resolved far-field spectra of spontaneous conical emission from a multimode fiber and bulk glass. ND: neutral density filter; HWP: half-wave plate; P: polarizer; M: mirror; L: lens; MMF: multimode fiber; QWP: quarter-wave plate; VP: *q* plate; SF: spectral filter; BS: plate beamsplitter; OSA: optical spectrum analyzer. The insets show photographs of the output beam in the far field for a bulk BK7 glass plate and MMF.

Fig. 5.2 from the setup. I chose the latter approach to reduce the setup complexity and to remove the various optical elements which might otherwise slightly affect the quality of the laser beam. This left only the neutral density filters, half-wave plate, and polarizer P₁, which allowed control over the power of the linearly polarized laser beam.

After the beam shaping stage, I carefully coupled the high-quality beam into the fiber under study using a $f = 12.5$ cm lens L₁ (Thorlabs, LB1904-C). I selected the lens through an optimization of the beam diameter at the focal point to fit the calculated intensities of the fundamental and the first OAM modes of the fiber (around $45 \mu\text{m}$ at FWHM for the $l = 0$ mode, and a ring diameter of approximately $54 \mu\text{m}$ for the $l = 1$ OAM mode) to favor their preferential excitation. I used a commercially-available step-index multimode fiber (Thorlabs, FG105LCA) with a pure silica core (core diameter $2R = 105 \mu\text{m}$), fluorine-doped silica cladding,

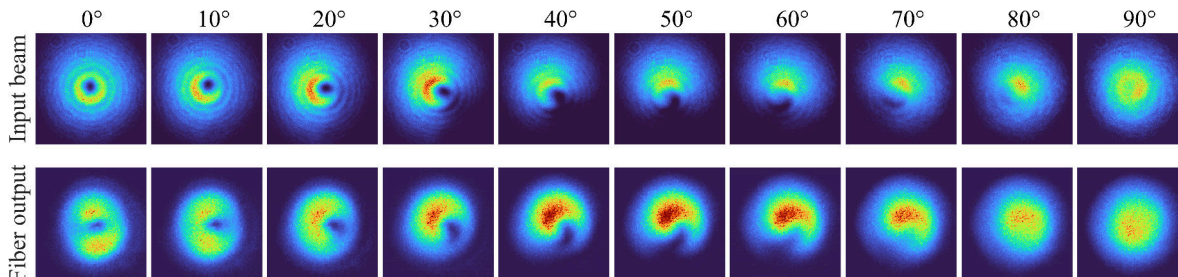


Figure 5.3: Input beam (top row) and near-field images of the fiber end face in linear regime (bottom row) for different rotations of the QWP_2 axis. The locations for the beam profiler used to capture these images are shown in Fig. 5.2: in *Beam shaping* panel for input beam characterization, and in *Detection system A* panel for fiber output characterization.

and numerical aperture $\text{NA} = 0.22$. The fiber length used in the conical emission study was 5.8 cm, and the fiber length used in the helicon wavepacket study was 5.5 cm. It was crucial to cleave the fiber with extreme care to avoid damaging the fiber core, as the cladding diameter of $125\ \mu\text{m}$ provides only a thin layer of around $10\ \mu\text{m}$ surrounding the core. The fiber segment was placed on a multi-axis platform that provides 5 degrees of freedom to ensure optimal coupling conditions. All optimization procedures outlined here and in the subsequent paragraph required detailed attention, as the process of coupling light into the fundamental mode of this highly multimode fiber presented significant challenges (the fiber supports propagation of 23 $\text{LP}_{0,p}$ modes at this wavelength; the total number of modes at the pump wavelength estimated using Eq. 2.3 is almost 2500).

I first optimized the coupling at low input powers, by controlling both output power (thermal power sensor S302C, Thorlabs) and spatial intensity distribution by near-field imaging the fiber end-face (beam profiler with a CMOS sensor, CinCam CMOS-1202 IR, Cinogy), see *Detection system A* panel in Fig. 5.2. Simultaneously, I sampled the fiber output beam using a beamsplitter plate BS to monitor the fiber output spectrum by means of a collecting multimode fiber (Thorlabs, M74L) with a very large $400\ \mu\text{m}$ core and numerical aperture $\text{NA} = 0.39$, and an optical spectrum analyzer (Yokogawa AQ6374). The lenses L_2 , L_3 , and L_4 were selected to achieve the best possible magnification for two purposes: (i) to clearly resolve the fiber end-face on the active area of the beam profiler and (ii) to gather the entire beam into the collecting fiber to analyze the total output spectrum. When the excitation was optimal in the helicon wavepacket study, I could verify that rotating QWP_2 resulted in corresponding changes of the spatial intensity distribution of the fiber output, see bottom row in Fig. 5.3. After ensuring the optimal excitation of the fundamental mode (or the desired mode combination), I was gradually increasing the input power while simultaneously checking the near-field of the fiber end-face and observing the total output spectrum and making necessary adjustments of the fiber position.

A distinctive spectral feature indicating the formation of a conical wave could be recognized as a broad and strong spectral broadening towards visible wavelengths (i.e., blue-shifted spectral shoulder) (see for instance Fig. 5.4(g)). Additional bandpass spectral filters SF could then be added in *Detection system A* to characterize the modes associated to the generated frequencies.

The discretized conical wave was also characterized in terms of angularly-resolved far field spectra (see *Detection system B* panel in Fig. 5.2). In this configuration, a lens L_5 (Thorlabs, LB1676-C, $f' = 10$ cm) is placed at the focal distance away from the MMF output, and collects the diverging output beam. The collected light is analyzed in the back focal plane of the lens, where I transversely scanned the collimated beam using the same collecting multimode fiber (Thorlabs, M74L). A large $400\ \mu\text{m}$ core of the collecting fiber prevents any additional nonlinear effects. However, it imposes a limited spatial resolution of the transverse scanning, which I performed in successive displacements with a 0.5 mm step. As the optical spectrum is measured in the Fourier plane (i.e., in the far field), the angular light distribution θ from the MMF output is simply mapped into a transverse displacement d , as follows: $\theta = \arctan(d/f')$. The used Fourier transform system allows to capture the full angular emission as shown in the following, with resolution below 0.3° . Note that I also checked that the collecting fiber's NA does not influence measurement results.

In addition, in a similar way I carried out the experimental characterization of conical waves emitted in bulk glass samples to unveil similar and distinct features between both systems. I used a sapphire plate (5 mm thick) and a BK7 glass plate (1.4 cm thick). In both the fiber and bulk plates used, the propagation of 1035 nm pulses takes place in the normal dispersion regime, leading to the generation of an X-wave. Photographs of the output beams in the far field presented in Fig. 5.2 clearly illustrates the typical frequency-angular intensity distribution of the field for the visible spectral tail for BK7 glass and MMF. In both cases, higher frequencies are observed with increasing angles (i.e., larger k_\perp). However, in the case of the MMF, discrete rings can be seen instead of a continuous concentric rainbow, as is the case for bulk BK7 glass. The rings are formed by superposition of discretized fiber modes that contain higher frequencies as the mode order increases.

In the next section, I provide detailed characterization of the conical emission observed in the two bulk samples. Following this, I perform a comprehensive analysis of the discretized conical wave that emerges during nonlinear propagation in the multimode fiber. Finally, I present the results obtained when the beam injected into the MMF carries a non-zero topological charge.

5.3 Conical emission in bulk media

In this section, I perform a detailed experimental analysis of conical emission patterns recorded for the two samples of bulk media. The studies were performed for a $1.39\ \mu\text{J}$ pulse energy (peak power of 5.0 MW for the used 275 fs pulses) of the beam focused into the sapphire plate (Fig. 5.4) and a $1.86\ \mu\text{J}$ pulse energy (peak power of 6.8 MW) of the beam focused into the BK7 glass plate (Fig. 5.5). The powers used exceed critical self-focusing threshold in those materials at the pump wavelength, which I estimate as around 2.9 MW for sapphire (assuming $n_0 = 1.749$ [216] and $n_2 \approx 3.1 \times 10^{-20}\ \text{m}^2/\text{W}$ [217]) and 3.5 MW for BK7 glass (assuming $n_0 = 1.507$ [216] and $n_2 \approx 3 \times 10^{-20}\ \text{m}^2/\text{W}$ [116, 117]).

Sapphire plate

First, a detailed analysis of conical emission pattern, shown in Fig. 5.4(a) for the sapphire plate, is reported through measured angle-resolved far-field spectrum ($\theta - \lambda$) in panel (f). It exhibits the typical X-like shape studied in the normal dispersion regime of bulks [200]. Beyond the continuous spectral broadening on-axis, the energy spreads following an increasing cone angle of emission with increasing detuning from the carrier wavelength. This is additionally confirmed by the near-field images that I recorded using distinct bandpass spectral filters with central wavelengths in the visible arm of the X-wave, reported in Fig. 5.4(b-e).

Regarding the interpretation of the full ($\theta - \lambda$) pattern observed, one can determine the central region of the angularly resolved spectrum where the energy of the dispersive waves accumulates according to the phase-matching constraints (similarly to Eq. 5.5). For bulk, the

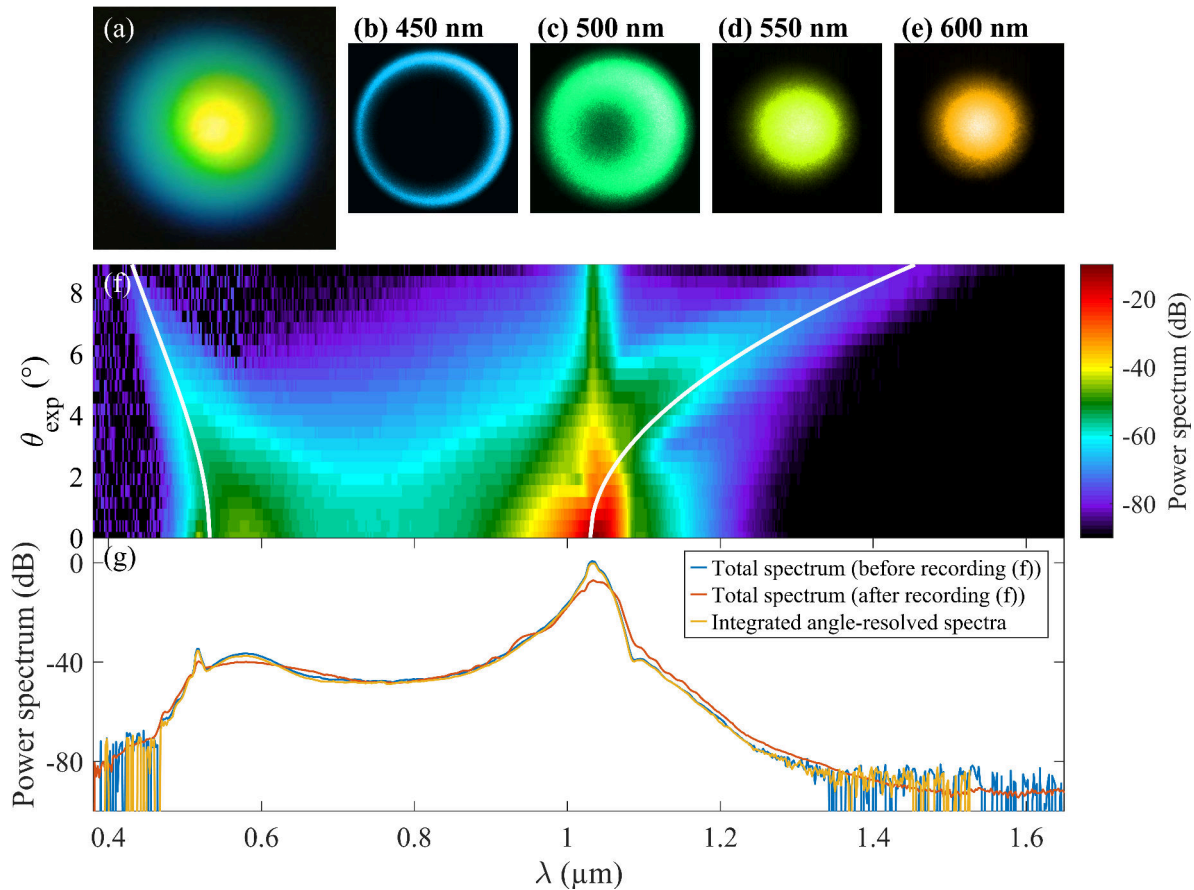


Figure 5.4: Conical emission recorded at the output of a 5-mm-thick sapphire plate. (a) Output pattern in the far field projected on a screen and photographed using a phone camera. (b-e) False-color near-field images recorded with the use of bandpass spectral filters with different central wavelengths. (f) Measured angle-resolved far-field spectrum. Solid white line provides the corresponding phase-matching using relation of $\theta(\omega)$. (g) Total spectrum measured with a focusing lens L_4 before (blue line) and after (orange line) (time separation: 45 minutes) performing the angle-resolved spectral measurements. Yellow line: integration of angle-resolved far-field spectrum from panel (f).

corresponding condition is simply: $\theta(\omega) = \arcsin(c/\omega\sqrt{k^2(\omega) - (K_0 + K_1\omega)^2})$.¹ I calculated the chromatic dispersion of the material using dispersion formula provided in [216] and I performed a simple fitting procedure to establish the values of $K_0 = k(\omega_0) \approx 10.7 \text{ rad } \mu\text{m}^{-1}$ and $K_1 \approx 5.965 \text{ ns m}^{-1}$, which provides insight into the phase velocity ω/K_0 and the group velocity $1/K_1$ of the conical wave. I retrieved the corresponding white line shown in Fig. 5.4(f) defining the theoretical phase-matching of the X-wave. A spectral gap observed on-axis between the two hyperbolic X-tails, with one of them passing through or close to ω_0 is a commonly observed situation, which arises when the group velocity of the conical wave differs from the group velocity of the input pump pulse. More specifically, the group velocity difference is $\delta v_g \approx 1.5 \text{ m } \mu\text{s}^{-1}$ for the fitted $\delta K_1 \approx 50 \text{ ps m}^{-1}$, which indicates that the X-wave is not seeded directly by the input pump pulse.

Finally, I verified that the recorded angle-resolved spectrum integrated over an area corresponds to the total spectrum acquired by focusing the entire beam exiting the MMF into the collecting fiber. This allowed me to ensure that the performed procedure of collecting angle-resolved measurements retains all important spectral information. The comparison, depicted in Fig. 5.4(g), shows excellent agreement.

BK7 plate

The second bulk sample used for my conical emission study is a plate made of BK7 glass which is almost three times thicker than the sapphire plate. Similarly to the previous material, propagation in a normal dispersion regime results in conical emission in the form of X-wave revealed through the emergence of hyperbolic tails, clearly visible in the angle-resolved far-field spectrum in Fig. 5.5(a). Comparing sapphire and BK7 glasses, I note distinct on-axis spectral broadening, and different dependence of emission angle on detuning from the carrier wavelength, which indicates that such characteristics are influenced by chromatic dispersion of the material and group velocity of the seeding structure.

Besides that, BK7 glass features a more complex $(\theta - \lambda)$ pattern. In particular, I identified several distinct possibilities for phase-matching fits in the $(\theta - \lambda)$ pattern. The two corresponding to the most intense X-tails are marked with white solid and dashed lines. Each of these lines corresponds to a different value of K_1 , as shown in Table 5.1 along with other characteristic parameters describing the generated conical wave. Here, it is clear how the value of K_1 parameter influences the shape of the phase-matching fit in the $(\theta - \lambda)$ plane. Namely, the dashed white line (indicating the phase-matching with smaller δK_1 and K_1 being closer to $1/v_{g0}$) is less steep than the solid white line and has smaller spectral gap at $\theta = 0$. I verified that if K_1 were equal to $1/v_{g0}$, there would be no spectral gap on-axis and both X-tails would start at ω_0 .

The complex shape of the registered $(\theta - \lambda)$ pattern indicates that multiple conical waves propagating with different group velocities are emitted during various stages of the nonlinear propagation of laser pulse in the plate used here. With a thinner plate, less X-tails might be visible (as is the case for the sapphire plate), because some of the less-intense tails might be

¹The strict phase-matching condition writes $\sqrt{k^2(\omega) - k_{\perp}^2} = K_0 + K_1\omega$, and the derivation provided in the text makes use of Snell's law to account for the fact that the angle θ is measured in air.

Table 5.1: Fitted parameters corresponding to the phase-matchings in BK7 plate indicated in Fig. 5.5(a) by different lines. For comparison, the group velocity of the carrier wavelength in BK7 glass is $v_{g0} \approx 197.2 \text{ m } \mu\text{s}^{-1}$ and inverse group velocity is $1/v_{g0} \approx 5.070 \text{ ps m}^{-1}$.

line	K_0 ($\text{rad } \mu\text{m}^{-1}$)	K_1 (ns m^{-1})	δK_1 (ps m^{-1})	v_{gX} ($\text{m } \mu\text{s}^{-1}$)	δv_g ($\text{m } \mu\text{s}^{-1}$)
solid	9.2	5.125	55	195.1	2.1
dashed	9.2	5.090	20	196.5	0.8

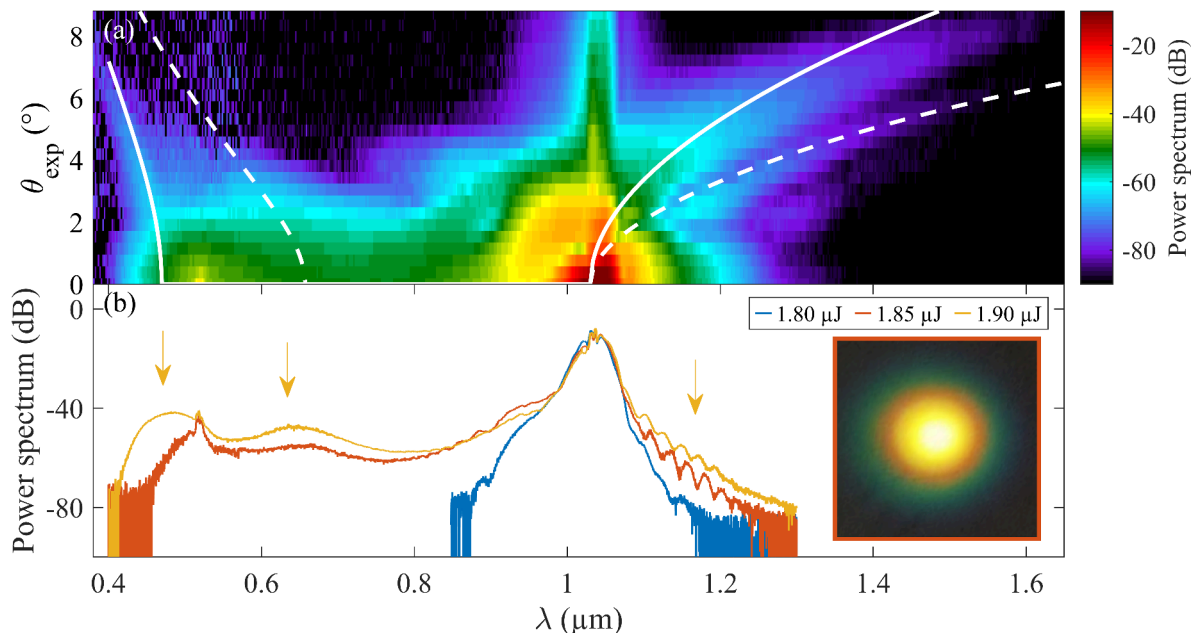


Figure 5.5: Conical emission recorded at the output of a 14-mm-thick plate made of BK7 glass. (a) Measured angle-resolved far-field spectrum for a $1.86 \mu\text{J}$ pulse energy. Solid lines provide the corresponding phase-matching. (b) Full spectrum collected with a focusing lens for different pulse energies. Inset: Output pattern for $1.85 \mu\text{J}$ projected on a screen photographed using a phone camera.

related to conical waves emitted at longer distances of the propagation in the BK7 glass plate.

I verified that the integration of angle-resolved spectrum again agrees well with the total spectrum of conical emission. In Fig. 5.5(b) I show the evolution of the total spectrum with increasing pulse energies. Clearly, the spectral broadening is very sensitive to the coupled energy. For $1.80 \mu\text{J}$, the initial laser spectrum broadens only slightly, see the blue line. For the pulse energy exceeding $1.83 \mu\text{J}$ I observed spectral broadening and a spectral shoulder forming on the short-wavelength side of the pump, corresponding to the short-wavelength X-tail marked with a white solid line in Fig. 5.5(a). For the pulse energy of $1.85 \mu\text{J}$ the spectral shoulder extends to wavelengths as short as $0.5 \mu\text{m}$, see the orange line. An increase of spectral intensity on the longer-wavelength side of the pump corresponds to the long-wavelength X-tail. I should note here that a minor artificial peak at $0.518 \mu\text{m}$ arises due to the method of signal acquisition by the optical spectrum analyzer, and is simply twice the frequency of the high-intensity pump at $1.035 \mu\text{m}$.

Higher pulse energies result in further spectral broadening and increase of spectral intensity

(see yellow line for 1.90 μJ), and particularly in three spectral regions indicated with arrows:

- generated spectrum covers the spectral range around 0.45 μm , which corresponds to the short-wavelength X-tail marked with a white solid line in Fig. 5.5(a);
- spectral intensity increases around 0.65 μm , which corresponds to the short-wavelength X-tail marked with a white dashed line in Fig. 5.5(a);
- spectral intensity increases on the long-wavelength side of the pump, which corresponds to both long-wavelength X-tails. Fringes observed in this spectral region result from interference of the two spectrally overlapping X-tails.

This analysis of spectrum evolution for increasing pulse energy concludes my study of conical emission in bulk glasses. In the next sections, I discuss findings obtained in a multimode fiber.

5.4 Discretized conical emission in a multimode fiber

In this part, I investigate conical emission in the MMF, and compare my measurements with theoretical predictions and numerical results. The experimental study is performed with 1.20 μJ pulse energy coupled into the fiber (with 1.66 μJ measured before the coupling lens, indicating that the beam coupling efficiency exceeds 72%). The coupled pulse energy corresponds to a peak power of 4.4 MW, which is around the critical self-focusing threshold of silica glass at the carrier wavelength $P_{crit} \approx 4.2 \text{ MW}$ (assuming $n_0 = 1.450$ [216] and $n_2 = 2.6 \times 10^{-20} \text{ m}^2/\text{W}$ [116, 117]). In the following, a detailed analysis of the conical emission pattern (shown in the inset of Fig. 5.2 and repeated in Fig. 5.7(h)) is reported through measured angularly resolved spectra and spectrally-filtered near-field imaging of the fiber output.

In Fig. 5.6(a), I unveil the angularly resolved spectrum recorded at the output of a 5.8 cm-long fiber segment. I retrieve the typical X-wave pattern with strong spectral broadening on-axis and hyperbolic tails clearly visible on both wavelength edges. Again, the spectral gap between the two X-tails indicates that the conical wave is not directly seeded by the input pump pulse. More details will be given in the following.

Corresponding numerical simulations are based on the multimode unidirectional pulse propagation equation (MM-UPPE) [182], which describes the evolution of the complex electric field \bar{E} :

$$\begin{aligned} \partial_z \bar{E}(p, \omega) = & i \left(\beta(p, \omega) - \frac{\omega - \omega_0}{v_{g0}} \right) \bar{E} \\ & + \frac{i n_{\text{eff}0} n_2 \omega^2}{c^2 \beta(p, \omega)} \left\{ (1 - f_R) |\bar{E}|^2 \bar{E} + f_R \left[\int h_R(\tau) |E(t - \tau)|^2 d\tau \right] \bar{E} \right\}, \end{aligned}$$

and which is expressed in a retarded frame moving at velocity v_{g0} . The function h_R is the scalar Raman response of the fiber medium with Raman fraction $f_R = 0.18$ for fused silica glass. The conducted simulations of nonlinear pulse propagation corroborate the formation of X-wave in the MMF, as shown in Fig. 5.6(b). An excellent agreement with the experiment is obtained in terms of both angular emission and spectral bandwidth over a very high dynamic range. When the $(\theta - \lambda)$ pattern is compared to the prior studies in bulk samples, differences can be noted in both the maximum emission angle and the extend of spectral broadening.

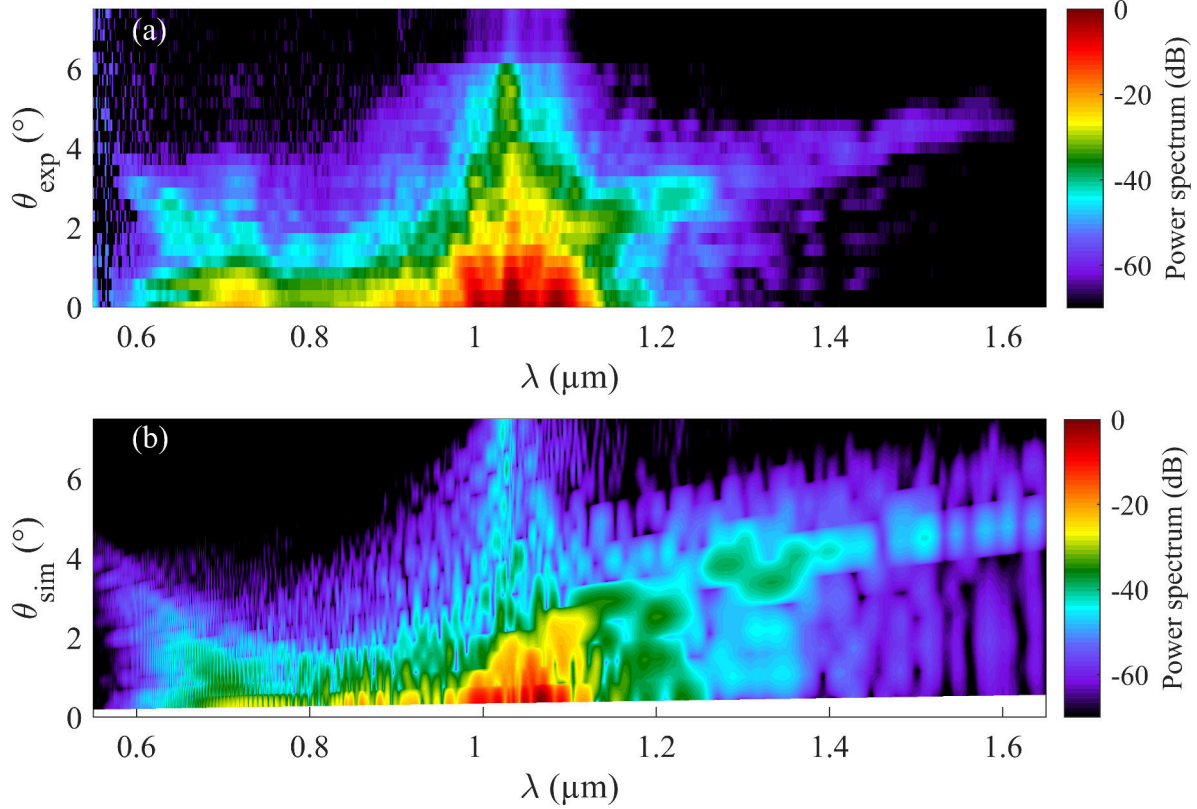


Figure 5.6: Angle-resolved far-field spectrum of conical emission obtained at the output of a 5.8 cm-long step-index MMF. (a) Experimentally measured angle-resolved far-field spectrum. (b) Corresponding numerical simulation of angle-resolved far-field spectrum based on MM-UPPE model. Calculated angles take into account the refraction taking place at the fiber output. Note that the numerical spatial grid cannot provide details for very small values of θ .

This again demonstrates that the dispersion properties of the medium along with the group velocity of the seeding wave structure significantly affect the exhibited features of the X-wave.

Moreover, it should be emphasized that in the case of the conical emission occurring in a waveguide the mode-resolved spectra could be more suitable for the investigated process than the $(\theta - \lambda)$ representation used for bulk samples. Accordingly, in the following, I investigate mode-resolved spectrum of the emerging X-wave. Figure 5.7 shows the numerical results of the distribution of the full optical spectrum (power in log scale) over the different fiber modes after propagation in the short 5.8-cm-long segment. An evident X-shaped pattern of the field distribution is very similar to those usually studied in the Fourier domain, except that the features of hyperbolic tails change on both wavelength edges, see Fig. 5.7(h). The visible tail clearly exhibits higher-order modes than the infrared one, while in θ plane it is associated with smaller cone angles. I experimentally characterized the modal composition of both visible and infrared branches by means of imaging the near-field of the fiber output face in combination with bandpass spectral filtering. Top panels in Fig. 5.7(a-g) confirm the discrete nature of the conical emission. Increasingly-detuned frequencies from the carrier wavelength are contained in higher-order modes of the fiber. In particular, for the visible branch, the phase-matching is

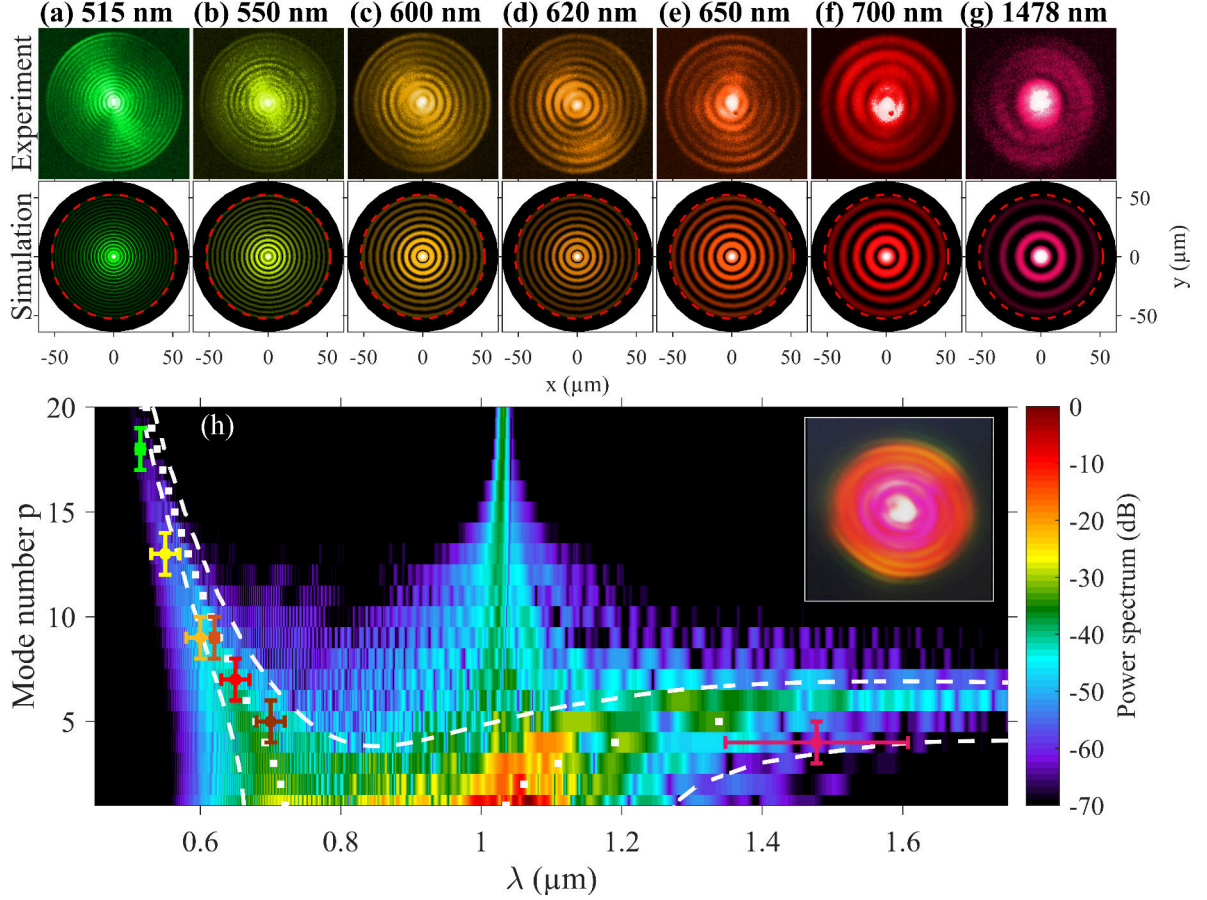


Figure 5.7: Mode-resolved spectrum of conical emission obtained at the output of a 5.8 cm-long step-index MMF. (a-g) False-color near-field images of the $\text{LP}_{0,p}$ higher-order modes involved in both X-like tails at specific wavelengths. Top panels: experimental captures with a CCD camera using bandpass spectral filters with indicated central wavelengths. Bottom panels: corresponding numerical fiber modes. (h) False-color map of the numerical mode-resolved spectrum. Colored crosses: spectral positions of the higher-order modes captured in subplots (a-g) according to the distinct bandpass spectral filters. White squares and dashed lines: theoretical phase-matching region of the discretized conical wave. Inset: Fiber output pattern projected on a screen photographed using a camera.

narrow enough in (p, λ) plane so that each filtered spectral band (10-nm bandwidth for the filters with central wavelengths 515 nm and 620 nm; 40-nm bandwidth for the remaining filters) is nearly associated with only one or a few fiber modes. For instance, at 515 nm, emission in $\text{LP}_{0,18}$ is revealed with a 10-nm bandwidth filter, see Fig. 5.7(a). And at 550 nm, emission in $\text{LP}_{0,13}$ is revealed with a 40-nm bandwidth filter, see Fig. 5.7(b). The main modal contents identified using distinct spectral filters are indicated in Fig. 5.7(h) with colored crosses at corresponding wavelengths. By contrast, the infrared part of X-wave implies almost the same few higher-order modes (i.e., the tail is flatter beyond 1200 nm), so that the modal analysis is less relevant. A longpass spectral filter with a cut-on wavelength of 1350 nm reveals a spatial profile resembling the $\text{LP}_{0,4}$ mode. The main corresponding $\text{LP}_{0,p}$ mode profiles, calculated with a scalar mode solver, are presented in the bottom panels of Fig. 5.7(a-g) to corroborate the identified main modal contents of the characterized X-tails.

It is worth noting that in addition to the two hyperbolic X-tails, another feature appears in the presented angle- and mode-resolved spectra. Namely, the carrier wavelength is present even for large angles and high mode numbers. Numerical investigations published in [187, 198] assume coupling of all pump energy into the fundamental mode. As a result, the mode-resolved spectrum includes only the two hyperbolic X-like tails, with the power contained within the region corresponding to the area surrounded by the dashed lines in Fig. 5.7(h). Such conditions can be achieved in numerical studies only. In my experiment, I aimed to excite the fundamental mode of the fiber; however, it is important to acknowledge that achieving excitation of the $LP_{0,1}$ mode only is inherently challenging. Even with a perfect alignment of the input beam with the fiber input face, part of the injected optical energy inevitably couples into higher-order modes because the Gaussian intensity profile of the beam does not align exactly with the $LP_{0,1}$ mode intensity profile. As a result, the pump residue is detected across most angles in the experimental angle-resolved spectrum shown in Fig. 5.6(a). Note the logarithmic scale of the presented power spectra, indicating that the pump energy contained at the carrier wavelength in modes of higher-orders is orders of magnitude lower compared to the pump energy contained in the fundamental mode. In contrast to the previous numerical works, the Gaussian intensity profile of the input beam is accounted for in the current numerical simulations, resulting in an excellent agreement between the numerical and experimental results.

Next, I investigate the main nonlinear dynamics at the origin of the conical emission. This analysis of the numerical results provides insight into the features of the seeding wave structure and allows to determine conditions for phase-matching indicated with white squares and dashed lines in Fig. 5.7(h). The detailed nonlinear propagation in the temporal, spectral, and spatial domains is shown in Fig. 5.8, whereas the corresponding evolution of mode-resolved spectrum is depicted in Fig. 5.9.

The retrieved nonlinear dynamics is consistent with observations regarding propagation of femtosecond pulses in a normal dispersion regime [187]. In the beginning, the injected beam propagates mainly in the fundamental mode at the pump wavelength, see Fig. 5.9(a). After one centimeter of propagation, a local increase of the refractive index across the pulse profile due to the nonlinear dependence on intensity and a spatiotemporal self-focusing (see Fig. 5.8(a,c)) leads to a decrease of pulse velocity and a self-steepening effect. As a result, an optical shock is formed at the trailing edge of the pulse (see Fig. 5.8(d) detailing the evolution of the temporal power profile and revealing the formation of the shock front, which is indicated with black lines at two propagation distances 1.2 cm and 1.4 cm). The shock front followed by wave-breaking is associated with a rapid, strong spectral broadening, clearly visible in Fig. 5.8(b) and (e) around $z_b = 1.4$ cm. This strong spectral broadening seeds linear waves in a large number of modes (see Fig. 5.9(b)), but only the phase-matched frequencies over specific higher-order modes are resonantly amplified according to the velocity of the shock front, as described by the condition 5.5. To elaborate, the inverse group velocity of the optical shock K_1 can be expressed by the sum of inverse group velocity of the pump and δK_1 correction, which can be directly read from the presented graphs. More specifically, δK_1 is simply found by comparing the temporal positions of the shock front at different propagation distances (as indicated with black lines for two values of z in Fig. 5.8(d)) or by analyzing the slope of the trailing pulse

edge in Fig. 5.8(a). The retrieved value $\delta K_1^I \approx 11.0 \text{ ps m}^{-1}$ and the distance $d_z^I \approx 1.4 \text{ mm}$ over which the seeding process occurs (between $z = 1.28 \text{ cm}$ and $z = 1.42 \text{ cm}$) well define the phase-matching and its finite bandwidth indicated with white squares and dashed lines in Fig. 5.9(b,c) which presents the mode-resolved spectrum during and after the formation of the optical shock. Here, the phase-matching parameter K_0 representing the propagation constant of the optical shock is simply the propagation constant of the fundamental mode at the pump wavelength, because the initial shock is centered at the carrier wavelength.

After undergoing the dynamics described above, the optical shock accelerates around $z_e = 1.6 \text{ cm}$ while still seeding linear waves over the higher-order fiber modes over the distance of $d_z^{II} \approx 8 \text{ mm}$. Different group velocity and updated value of correction $\delta K_1^{II} \approx 5.0 \text{ ps m}^{-1}$ lead to a new phase-matching condition indicated with white squares and dashed lines in Fig. 5.9(e-f). The second fit matches very well with the new X-tail emerging in the visible spectral region at slightly offset wavelengths compared to the previous X-tail.

Note that in the subsequent stages of the pulse propagation several less-intense optical shocks can be found around $z = 2.7 \text{ cm}$, $z = 4.0 \text{ cm}$, and $z = 5.3 \text{ cm}$, see Fig. 5.8(a). The quasi-periodicity of their occurrence can be easily linked to the beating of the first two modes of the fiber ($\text{LP}_{0,1}$ and $\text{LP}_{0,2}$) which are excited with the highest efficiency by the input beam with a Gaussian intensity profile (see Fig. 5.9(a) for the energy distribution among fiber modes at the initial stage of propagation). The period of recurring spatiotemporal self-focusing reflects the beat length $L_B = 1.28 \text{ cm}$ derived from the calculated properties of the two fiber modes. The successive optical shocks seed less-intense discretized conical waves, thus inducing some additional broadening of the mode-resolved spectrum. More specifically, the shock front formed between $z = 2.58 \text{ cm}$ and $z = 2.90 \text{ cm}$ leads to an increase of power contained in the higher-order modes at both wavelength edges, see mode-resolved spectrum before, during, and after shock formation in Fig. 5.9(g-i). The phase-matching fit and its bandwidth given by the estimated $\delta K_1^{III} \approx 12.3 \text{ ps m}^{-1}$ and $d_z^{III} \approx 3.2 \text{ mm}$ are indicated by white squares and dashed lines. Similarly, the shock front formed between $z = 3.92 \text{ cm}$ and $z = 4.10 \text{ cm}$ seeds various wavelengths in higher-order modes in Fig. 5.9(k), but only the phase-matched wavelengths remain in panel (l) according to the phase-matching determined by $\delta K_1^{IV} \approx 14.3 \text{ ps m}^{-1}$ and $d_z^{IV} \approx 1.8 \text{ mm}$, as indicated by white squares and dashed lines. The last shock formed at $z = 5.3 \text{ cm}$ does not have enough strength to significantly alter the mode-resolved spectrum, compare Fig. 5.9(k) and Fig. 5.7(h) before and after its formation.

Figure 5.7(h) shows mode-resolved spectrum after 5.8 cm of propagation in the fiber. This final map results from complex interactions between several discretized conical waves emitted subsequently during nonlinear pulse propagation, as discussed above. The theoretical phase-matching of the first, most intense discretized X-wave is transposed from Fig. 5.9(c) to Fig. 5.7(h), corroborating my experimental characterization of the generated wave structure. It is worth to remind, that the 2D ST wavepackets emitted in the nonlinear process are not truly propagation-invariant. The finite distance over which the shock front seeds the linear resonant waves leads to a spectral tolerance (indicated with dashed lines) and dispersion of the spontaneously emerging discretized conical wave.

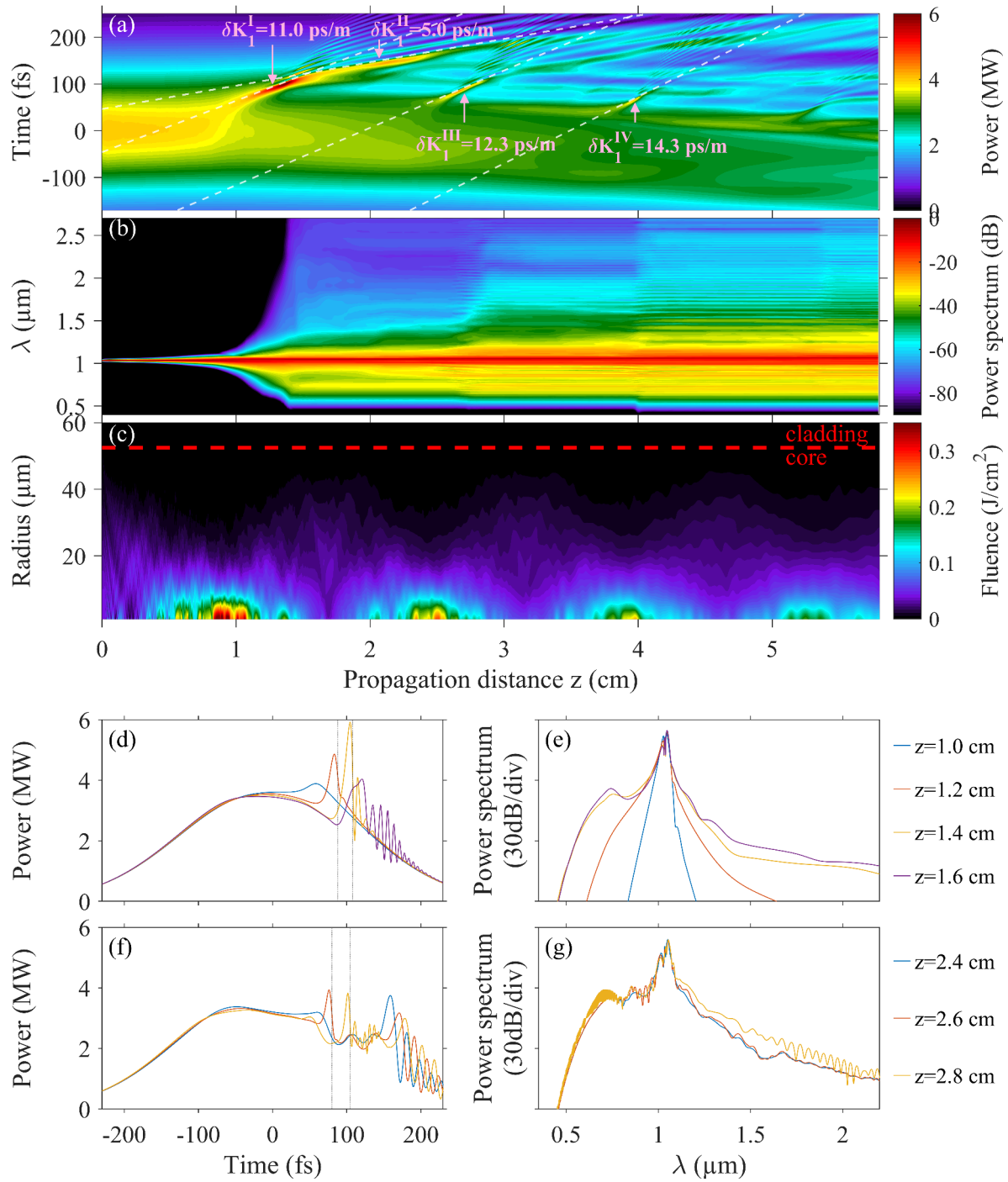


Figure 5.8: Nonlinear propagation of 275-fs pulses (1.2 μJ energy at 1035 nm) in step-index MMF. (a-c) False-color map of temporal, spectral, and spatial power profiles as a function of propagation distance z . (d-g) Snapshots of temporal (d,f) and spectral (e,g) power profiles showing formation and evolution of the first, intense optical shock (d,e) and a following, less intense shock (f,g) and corresponding spectral broadening.

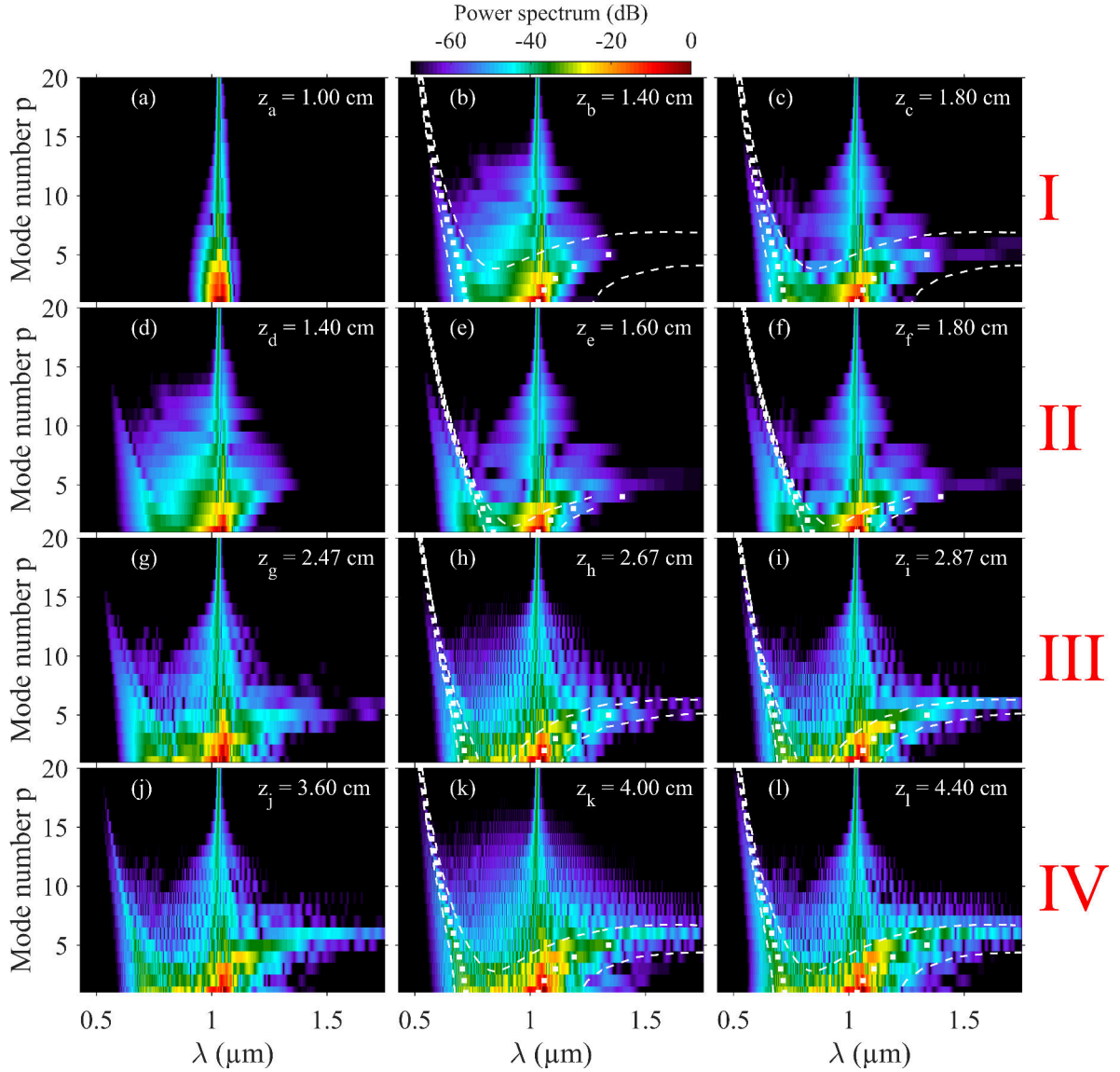


Figure 5.9: Evolution of the mode-resolved spectrum during propagation. Panels show false-color map of the numerical mode-resolved spectrum (in log. scale, dB units) calculated before (first column), during (second column), and after (third column) formation of optical shocks I-IV indicated in Fig. 5.8(a) at different propagation distances. Squares and dashed lines show theoretical phase-matching regions of the discretized conical waves corresponding to the subsequent optical shocks.

Before concluding this section, it is worth to revisit the study of conical emission in the BK7 plate, taking into account the evolution of the spectral power profile provided by numerical simulations performed for the MMF. More specifically, spectral interference fringes appear around $z = 2.8$ cm in the spectral power profile presented for the MMF in Fig. 5.8(g) (see yellow line). The spectral fringes become visible after the formation of the second optical shock. The first and second shock seed the same wavelengths (compare Fig. 5.9(d) and (h) to see that the X-tails of the two discretized conical waves overlap spectrally at both wavelength edges); therefore, fringes are observed over the entire spectrum in the fiber. The two shocks are generated at different times, and the delay between them results in spectral fringes. In the BK7 plate, spectral interference fringes appear as well, which indicates that more than one optical shock is generated during propagation of the pump pulse in the 1.4-cm-thick plate. The fringes are visible in the long-wavelength part of the output spectrum in Fig. 5.5(b), between $1.05 \mu\text{m}$ and $1.2 \mu\text{m}$, which is seeded by both conical waves. The phase-matching regions of the two conical waves are marked in Fig. 5.5(a) - the long-wavelength X-tails overlap, making it possible to observe spectral fringes; meanwhile the short-wavelength X-tails are spectrally separated, therefore the fringes cannot be observed in that spectral region.

Finally, it is necessary to discuss the stability of the nonlinear process under investigation. As I found, the conducted experiments are carried out just below the fiber damage threshold. A well-known mechanism that induces material breakdown in the ultrashort pulse regime is photoionization, which leads to modification and ablation of material [218, 62]. Ionization typically takes place when the laser intensity reaches around 10^{12} W/cm^2 [218]. The experiments described above were performed with a coupled pulse energy of $1.2 \mu\text{J}$, which, for a Gaussian beam profile, corresponds to an intensity of $1.5 \times 10^{11} \text{ W/cm}^2$. Under these conditions, the nonlinear process remained stable, with the fiber output pattern retaining its features over the course of one hour and 20 minutes when I performed its characterization, such as in the top panels of Fig. 5.10, which show stable, although not perfectly optimized visible emission. Doubling the pulse energy to $2.4 \mu\text{J}$ resulted in the process losing its stability. When the beam intensity increased, the fiber output pattern began to evolve rapidly, as shown in the middle and bottom panels of Fig. 5.10, which feature snapshots from one second of a video recorded for the coupled pulse energy of $3 \mu\text{J}$. After over ten seconds of such dynamic changes, visible emission ceased and could no longer be detected, indicating irreversible material damage. By slightly adjusting the focused beam's position at the fiber input end, I found that the visible pattern reemerged, as the beam started to propagate in an undamaged fragment of the fiber core. However, the pattern disappeared again after a similar duration, when the material in the new beam path was modified. These observations clearly indicate that for a beam intensity of approximately $3\text{--}3.5 \times 10^{11} \text{ W/cm}^2$, localized damage is induced to the material. The issue of fiber damage is particularly important in the following, where I investigate helicon wavepackets in MMF.

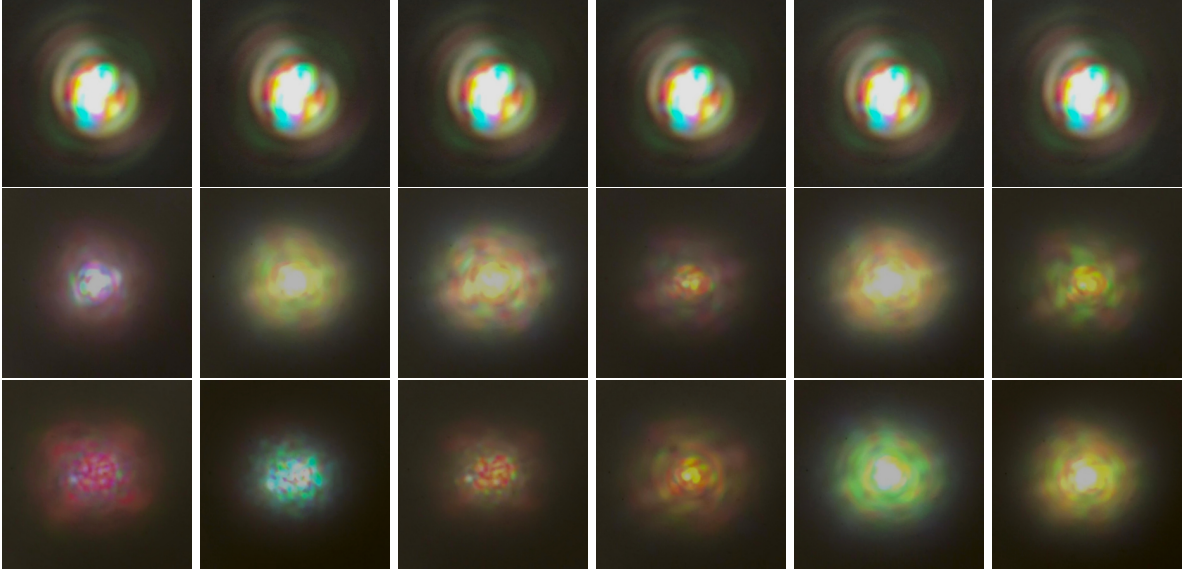


Figure 5.10: Stability of the fiber output pattern in two power regimes. Top panels: Stable fiber output pattern (snapshot every second) for $1.3\ \mu\text{J}$ pulse energy. Middle and bottom panels: Evolution of the fiber output pattern recorded over one second for a coupled pulse energy around $3\ \mu\text{J}$. The fiber output pattern is projected on a screen and recorded using a phone camera.

5.5 Helicon wavepackets in multimode fiber

In this part, I report on my work towards generation of helicon wavepackets in a multimode fiber. This is accomplished using the experimental setup presented in Fig. 5.2, by shaping the amplitude and phase of the input beam using the q plate and the rotating circular analyzer, as shown in Fig. 5.3.

First, I analyze the output spectrum and near-field profiles of the fiber output as a function of the injected pulse energy. This is done for two different compositions of the input optical field: with a mix of $l = 1$ and $l = 0$ fields, by setting the QWP_2 axis in the circular analyzer to 30° , and with a pure $l = 1$ field, by setting the QWP_2 axis to 0° . The results are shown in Fig. 5.11(a) and (b), respectively.

For the mix of $l = 1$ and $l = 0$ fields, the spectrum does not show signs of significant broadening even for the launched energy of $1.9\ \mu\text{J}$, at which it ranges from $0.9\ \mu\text{m}$ to $1.15\ \mu\text{m}$. This requires more than 1.5 the amount of energy that is used in the discretized conical emission study to reach the wavelength of $0.5\ \mu\text{m}$, see Fig. 5.7. After increasing the launched pulse energy to $2.1\ \mu\text{J}$, the spectrum undergoes a very large broadening to $0.45\ \mu\text{m}$, see purple line. However, I found that at this energy level the process becomes unstable. After only a few seconds the spectrum narrows substantially, with the initial drop of spectral intensity in the short-wavelength side of the pump visible in a green line. The process evolves too rapidly to be fully captured with the available equipment. The subsequent efforts to achieve a similar range of spectral broadening in the same fiber segment by realigning the fiber result in the same outcome, and after several attempts it is not possible to retrieve any kind of spectral broadening at all, which indicates irreversible damage of the fiber sample. This observation aligns with

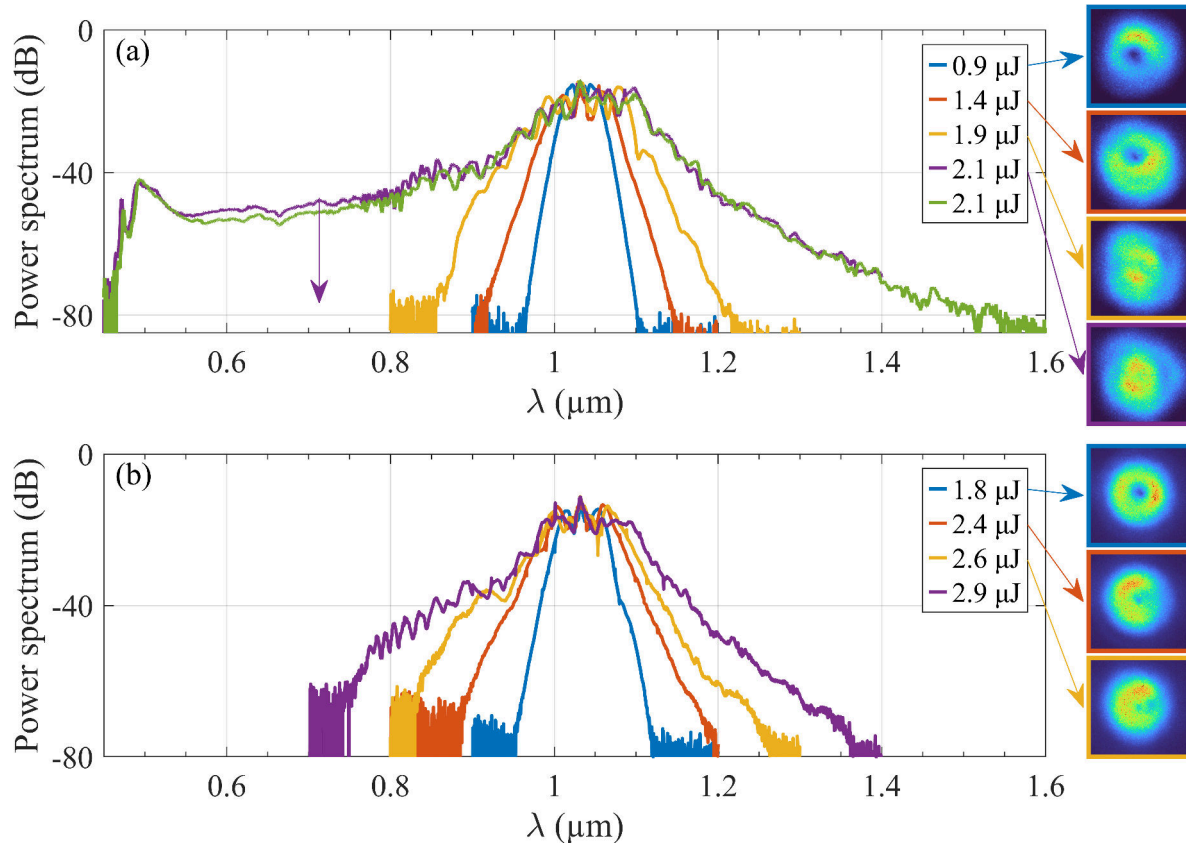


Figure 5.11: Measured output spectrum and near-field images of the fiber output as a function of the coupled pulse energy for the launched optical beam consisting of (a) a mix of $l = 1$ and $l = 0$ fields (b) a $l = 1$ field.

the stability issues mentioned at the end of the previous section, where the discretized conical emission process became unstable at a pulse energy close to $2.4 \mu\text{J}$. Here, because of different composition of the input optical field, the instability threshold appears to shift to even lower pulse energies, which are insufficient to observe the studied process.

In a subsequent experiment, I modified the composition of the launched optical field to contain only the $l = 1$ component. The study of evolution of the output spectrum in Fig. 5.11(b) shows much higher tolerance to the pulse energy in terms of the process stability, allowing to inject energy close to $3 \mu\text{J}$. This is caused by a different spatial distribution of the optical field, which does not lead to such high local beam intensity and strong subsequent self-focusing stage, thus avoiding damage of the material. At $2.9 \mu\text{J}$, the spectral broadening reaches $0.75 \mu\text{m}$, and the formation of a weak spectral shoulder in the short-wavelength part of the spectrum indicates generation of resonant radiation in higher-order modes. Near-field imaging of the fiber output shows that for increasing pulse energy the optical field changes its spatial distribution and breaks the circular symmetry, which further confirms the energy couplings to other fiber modes.

In the following, I investigate the angle-resolved spectra and the spectrally-filtered near-field images of the fiber output. The results presented in Fig. 5.12 are another set obtained in around

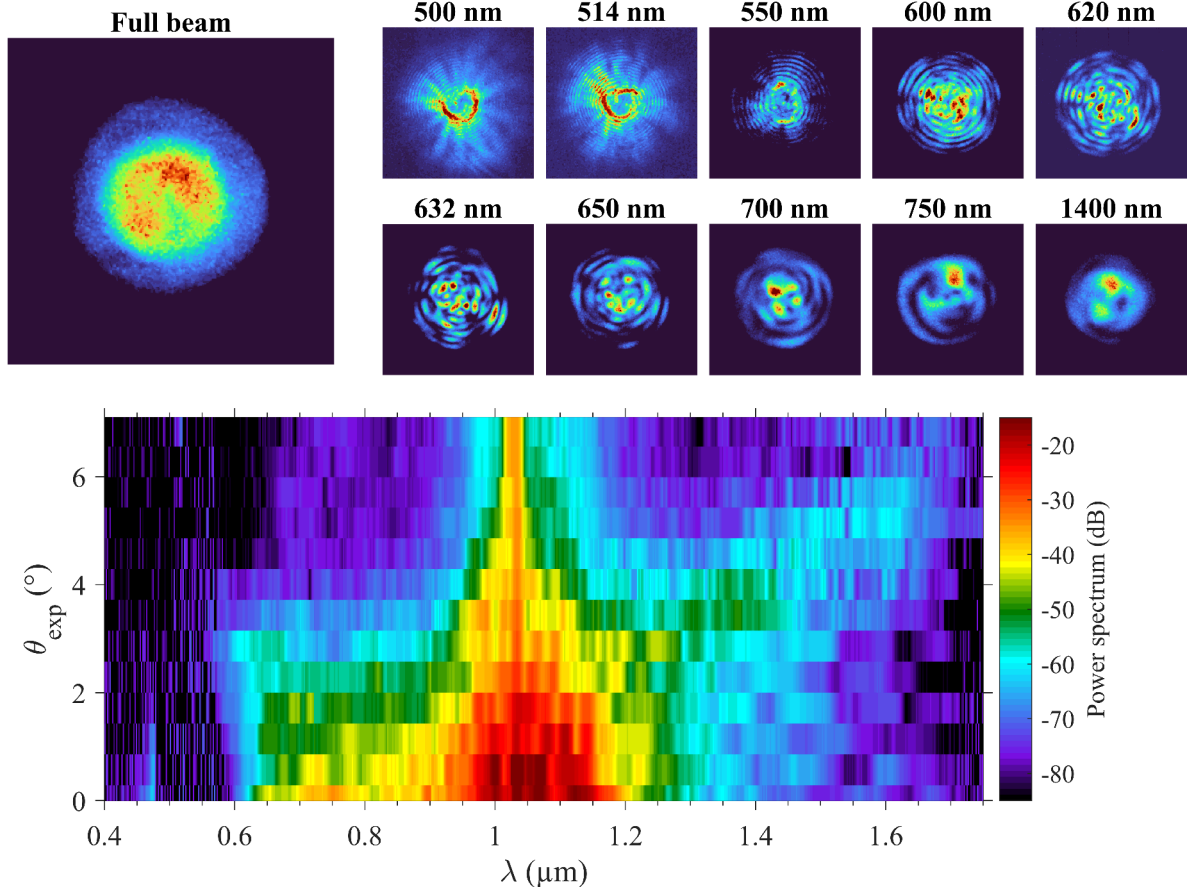


Figure 5.12: Experimentally measured angle-resolved far-field spectrum and near-field images of the fiber output captured using bandpass spectral filter. The pulse energy of the input $l = 1$ beam is $3.9 \mu\text{J}$, and $2.9 \mu\text{J}$ is measured at the output of the fiber.

6-cm-long fiber segment for the launched pulse energy of $2.9 \mu\text{J}$, with $3.9 \mu\text{J}$ measured before the coupling lens, indicating that the beam coupling efficiency exceeds 74%. When comparing these measurements to those shown in Fig. 5.6 for the pump launched into the fundamental mode, I note that more energy is coupled into the long-wavelength tail than into the short-wavelength tail. However, the observed angularly-resolved spectra still remain of X-wave type. Despite this, the visible part of the spectrum contains enough energy to characterize the output field intensity distribution at different spectral ranges. The results clearly indicate various modal components at distinct wavelengths, although the interpretation is not so straightforward as in the case of discretized conical emission with only $\text{LP}_{0,p}$ modes involved. Each spectrally filtered band contains multiple modal components, leading to their interference in the captured images. Nevertheless, a clear trend is again observed, with higher-order modes present at more-detuned wavelengths.

The experiments are supported with numerical simulations performed for two excited modal compositions. The first simulation considers excitation of the $l = 1$ OAM mode with $3.0 \mu\text{J}$ pulses (Fig. 5.13), while the second involves an equal excitation of $l = 1$ and $l = 0$ modes with $1.05 \mu\text{J}$ pulses (Fig. 5.14). The propagation in temporal, spectral, and spatial domains is

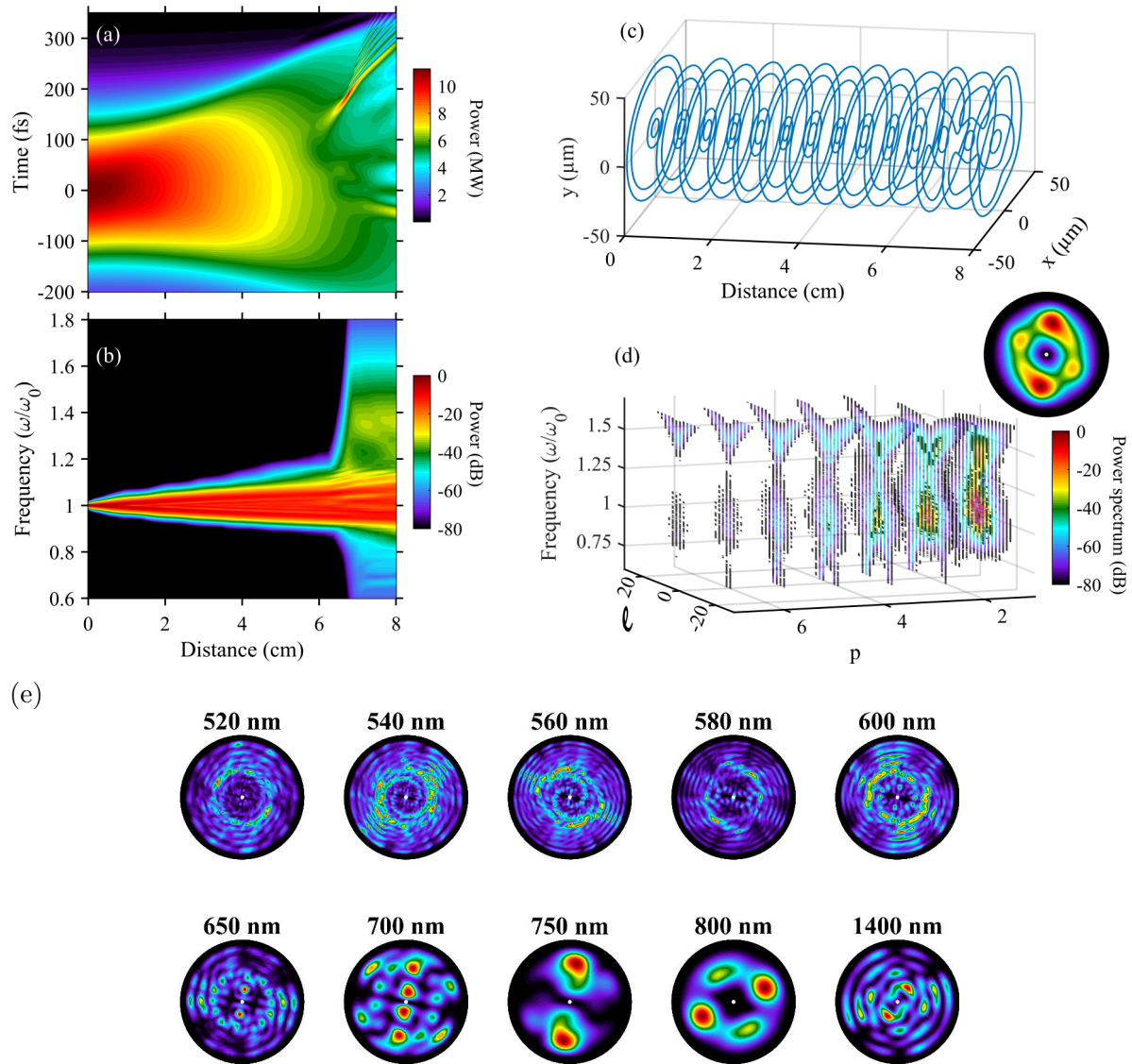


Figure 5.13: Numerical simulation for $l = 1$, $3.0 \mu\text{J}$ pulses launched into the step-index MMF. False-color map of temporal (a), spectral (b), and spatial (c) power as a function of the propagation distance. Inset shows a false-color beam intensity distribution at the fiber output. Mode-resolved spectrum (d) and calculated near-field spectrally-filtered beam intensity distributions (e) at the fiber output.

shown in panels (a), (b), and (c), respectively, the mode-resolved spectra at the fiber output are presented in panels (d), and the spatial intensity profiles at selected filtered spectral bands are presented in panels (e).

Similarly to the case of nonlinear propagation of a pulse launched into the fundamental fiber mode, an optical shock is formed and leads to wave breaking seeding a large number of modes across a broad spectrum. When a mix of $l = 1$ and $l = 0$ modes is excited, the shock is formed after less than 2 cm of propagation, as in the case of launching into the $l = 0$ mode. When only the $l = 1$ mode is excited, the shock formation occurs at a longer propagation distance, even for the increased pulse energy. This agrees well with experimental observations and results from different dynamics of spatial self-focusing.

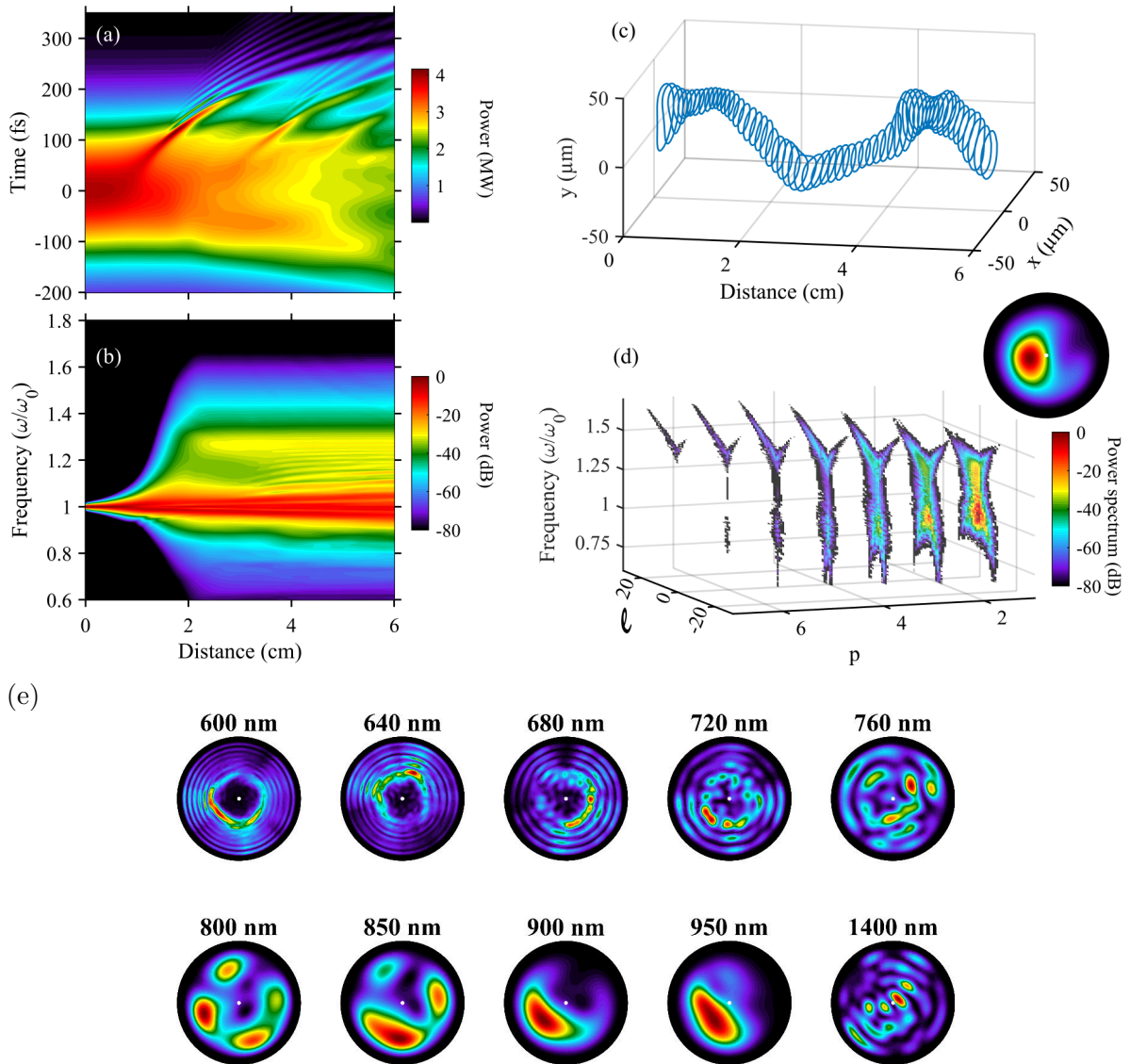


Figure 5.14: Numerical simulation for an equal mix of $l = 0$ and $l = 1$ $1.05 \mu\text{J}$ pulses launched into the step-index MMF. False-color map of temporal (a), spectral (b), and spatial (c) power as a function of the propagation distance. Inset shows a false-color beam intensity distribution at the fiber output. Mode-resolved spectrum (d) and calculated near-field spectrally-filtered beam intensity distributions (e) at the fiber output.

As seen in panels (c), the beam profile changes shape at the moment of shock formation. This is particularly accentuated for the $l = 1$ beam, where generation of higher-order modes leads to the formation of symmetric lobes in the beam cross-section, as seen in the spatial intensity distribution at the fiber output shown in the inset. For the mix of $l = 1$ and $l = 0$ modes, the beam shape at the fiber output still resembles its initial intensity distribution, however it involves different higher-order modes.

Interestingly, the mode-resolved spectra at the fiber output do not show qualitative agreement between the two analyzed excitation conditions. That is, the results shown in Fig. 5.13 for launching the $l = 1$ beam indicate the formation of only the modes that are

characterized by an odd value of l . This is related to the strong coupling from the $l = 1$ pump to $l = -1$ mode because the two modes share the value of propagation constant leading to linear phase-matching. The presence of those two modes drives the next stages of the stimulated four-wave mixing processes with emission of $l = 3$ and $l = -3$, and higher-order modes with odd l values in the next stages. The results shown in Fig. 5.14 for launching a mix of $l = 1$ and $l = 0$ beams involve the modes characterized by even values of l at the fiber output as well.

Finally, the spectrally filtered near-field images retrieve some signature features of the full beam in each investigated case. When only the $l = 1$ mode is excited, the spectrally-filtered images show 2-fold rotational symmetry, with larger symmetric lobes present for the filtered wavelengths that are closer to the pump. For more-detuned wavelengths, the spatial distribution is still symmetric, but there is greater variability along the radial coordinate. When a mix of two modes is excited, the spectrally-filtered images do not show rotational symmetry, spatial distributions of spectral bands closer to the pump resemble the full beam, but for more-detuned wavelengths there is again a greater variability along the radial coordinate.

After the performed numerical analysis, I compare the simulated spatiotemporal dynamics with the experimental results shown in Fig. 5.12. The experiment was realized with the $l = 1$ beam launched into the fiber, and the results are very close to the simulations performed for that excitation case. There appears to be a small contribution of $l = 0$ component, because the experimental spectrally-filtered near-field images of the fiber output are not symmetric (for example there is a shape of closing crescent for the spectral filtering around 500 nm, which resembles simulations for 600 nm and 640 nm in Fig. 5.14), and the full beam spatial distribution is in a shape of a bean with a non-zero intensity in the center. This contribution of $l = 0$ is linked with the imperfect excitation conditions that occur with every experiment.

The results in this section do not unequivocally demonstrate the generation of a helicon wavepacket. This could be improved by launching the beam with a different energy distribution between the two fiber modes. Injecting less energy into the fundamental mode and more into the $l = 1$ mode by setting the QWP₂ axis closer to 0° than the initial 30° could aid in achieving more stable formation of optical shock at the required power level. Finally, as observed in the numerical simulations, it might be difficult to distinguish experimentally the formation of a helicon wavepacket that evolves in a spiralling trajectory from the formation of the wavepacket formed from $l = 1$ beam by relying only on the spectrally filtered near-field images of the spatial intensity distributions at the fiber output. Considering this, further development of the part of the experimental setup devoted to the interferometric characterization of the generated wavepackets is necessary in order to determine the involved topological charges. If even values of l are detected, even for excitation very close to $l = 1$, this could confirm the formation of the helicon wavepacket. Even though the conducted research provides a significant first step towards generation of ST rotating wavepackets in multimode fibers, further investigation is still necessary to fully investigate the spontaneously emerging complex spatiotemporal pulses that carry orbital angular momentum.

5.6 Conclusions

In this chapter, I investigated nonlinear propagation of intense ultrashort pulses in a step-index multimode fiber. I experimentally demonstrated the spontaneous emission of a discretized conical wave, validating earlier theoretical predictions [187, 198]. I have identified analogies to bulk conical emission, studied in sapphire and BK7 glass plates. The experimental results agree very well with the corresponding numerical simulations, and I performed detailed analysis to explain distinct features of the investigated dynamics. Obtained results provide a general understanding of phase-matched radiations emitted spontaneously by nonlinear waves in multidimensional dispersive optical system. I have proven the research hypothesis in demonstrating that by a controlled launching of the laser beam into the fundamental mode, I achieve a spontaneous generation of a discretized conical wave formed from a linear superposition of fiber modes with an engineered spatiotemporal spectrum. The emerging ST wavepacket propagates with a deterministic group-velocity. Even if the configuration of spontaneous emergence implies that the discretized conical wave is not fully non-dispersive and non-diffractive, this simple and alternative approach appears as a welcome alternative to the exact and complex shaping of invariant fields and opens the way to future investigations of multidimensional ST wavepackets with fiber and waveguide technologies [191, 206, 219, 220]. Finally, I have explored the nonlinear dynamics when an OAM-carrying beam is launched into the fiber. The obtained results indicate the presence of different spatial and spectral components at the fiber output, even though additional experimental works are required for the full characterization of the emerging complex ST wavepacket.

Chapter 6

Conclusions and perspectives

In this dissertation, I studied how novel nonlinear phenomena with correlated spatial, temporal, and spectral features that occur in optical fibers can be influenced by shaping the input optical field in conceptually simple experimental configurations. I have investigated nonlinear couplings and energy transfer between two polarization modes in birefringent photonic crystal fibers, intramodal and intermodal four-wave mixing processes in a few-mode graded-index fiber, and spontaneous generation of three-dimensional spatiotemporal wavepackets in a highly-multimode step-index fiber.

First, particular attention was given to pulse trapping by solitons in birefringent PCFs. The study revealed that the negative sign of group birefringence plays a crucial role in polarization purity of the fiber output. Specifically, pumping the fiber with pulses polarized along the x (slow) axis ensures higher polarization purity of the output signal compared to the y (fast) axis. This is contrary to the observations of soliton trapping reported so far in conventional birefringent fibers, which are characterized by the group birefringence of the same sign as the phase birefringence. Because of the large dispersion of birefringence that is possible to achieve through the microstructured design of PCF, this phenomenon is manifested in different way.

The experiments performed in the two fibers with different magnitude of group birefringence confirmed that the spectral positions of the trapped pulse components are governed by the group velocity matched wavelengths of the two polarization modes. The trapped pulses shift to longer wavelengths with increasing pump power and propagation distance. Their spectral separation remains unchanged, dictated by the fiber's group birefringence. Furthermore, I have shown how different variables influence polarization purity. In particular, I confirmed that the high group birefringence aids in preserving the polarization extinction ratio of the soliton and the trapped pulse. However, I also revealed that only launching the light polarized along the x fiber axis can result in generation of a single polarization component at the fiber output, otherwise - two components typically emerge at separate spectral positions, characterized by distinct spectral intensities. The performed experiments highlight the importance of initial excitation conditions in achieving different spectral and polarization components at the fiber output. This is an important result in the context of multimode solitons, showing the importance of cross-phase modulation and Raman effect in pulse dynamics.

Furthermore, I confirmed that orthogonal Raman scattering is the mechanism behind energy transfer between the two polarization components when pumping with pulses polarized along the y axis. By manipulating the azimuth angle of linearly polarized light, it is possible to control the division of pulse power between polarization modes, with the x mode being favored for most excitation angles. These findings are particularly significant for developing

tunable sources of polarized light based on Raman self-frequency shift in birefringent fibers.

The performed study offers significant insights into Raman-assisted energy transfer between different fiber modes. The effects of Raman scattering vary significantly depending on whether the interaction involves orthogonally-polarized fiber modes, as reported here, or co-polarized pulses, investigated by Rishøj et al. [141]. It is worth to note that the group velocity matching is satisfied in each case. However, self-mode conversion described in the referenced work leads to a complete transfer of energy from one mode to another over a distance of less than 0.5 m, which is later followed by the soliton self-frequency shift until it reaches the group-velocity matched wavelength with another mode at the frequency separation within the bandwidth of the Raman gain, which again leads to a complete transfer of energy to another mode. In the study performed here, the polarization conversion occurs over a distance of several meters concurrently to the SSFS phenomenon, which alters the wavelengths of both polarization components. This qualitative difference results from the smaller gain of orthogonal Raman scattering compared to the gain of co-polarized Raman scattering. Consequently, when considering the more general case of the multimode soliton, the observed effects could manifest in a different manner depending on the mode polarization.

Subsequently, I investigated nonlinear frequency conversion processes in a short few-mode graded-index silica fiber. Experimental evidence, supported by theoretical analysis, demonstrated that four-wave mixing can be utilized for far-detuned frequency of the near-IR pump light to visible and mid-IR spectral range. Remarkably, mid-IR light was generated well beyond the commonly accepted transparency window of silica fibers, because the significant spatial overlap resulted in a high gain that surpassed fiber attenuation. The cutback experiments investigating the evolution of the anti-Stokes peak at 0.625 μm highlighted the significant parametric gain provided by spontaneous intramodal FWM, which allows to generate the Stokes detuned by 200 THz from the pump. The specific refractive index profile of the tested fiber played a crucial role in observing these intriguing FWM process, suggesting potential for further optimization through the engineering of the index profile or the use of infrared glasses.

The experimental results showed excellent agreement with the theoretical predictions. Furthermore, a detailed analysis addressed the limitations of simplified theoretical models commonly used to study nonlinear wave mixing processes in graded-index fibers.

In the next step, I studied a cascaded intermodal four-wave mixing processes caused by modification of the light launch conditions. The multiple observed sharp spectral peaks arise through the combination of the secondary pump in the anti-Stokes peak at 0.625 μm with or without the initial pump. I performed detailed spatial investigation of the generated peaks and reached a good agreement with my theoretical predictions. By a simple adjustment of the input conditions, instead of far-detuned intramodal FWM process extending into mid-IR, I obtained multiple spectral peaks in the visible and near-infrared spectral range. The performed study indicates an interesting direction of future research, showing potential of the realization of a new type, tunable, broadband fiber source which could be useful for many applications.

Finally, I investigated the nonlinear propagation of intense ultrashort pulses in step-index MMF close to the critical peak power threshold in silica. This study experimentally demonstrated spontaneous emission of a discretized conical wave in a structured waveguide, validating recent theoretical predictions. Analogies to bulk conical emission were identified by performing characterization of supercontinuum emitted in sapphire and BK7 glass plates. The pump pulse propagating in the normal dispersion region resulted in each case in the angle- and mode-resolved spectrum in the form of X-wave. One potential direction of future study could focus on investigation of ultrashort, high-energy pulses in other dispersion regions, which could lead to demonstration of formation of light-bullets.

This research provided a comprehensive understanding of phase-matched radiations emitted spontaneously by nonlinear waves in multidimensional dispersive optical systems. The emerging spatiotemporal wavepacket, propagating with a deterministic group velocity, results from a linear superposition of fiber modes with an engineered spatiotemporal spectrum. The numerical simulations and theoretical analysis corroborated the obtained experimental results.

This simple approach of achieving formation of propagation-invariant field offers an alternative and very useful method compared to the complex shaping of spatiotemporal properties of optical fields and opens new possibilities for future investigations of multidimensional ST wavepackets using fiber and waveguide technologies.

Although different spatiotemporal nonlinear phenomena dominate the considered systems, in each case the spectral, spatial, and temporal components at the fiber output are controlled through the modal composition of the excited field. I have shown that modifying the polarization azimuth of linearly polarized pump pulses, and the intensity and phase profile of the pump optical field, leads to qualitatively different results:

- either formation and amplification, or the absence of the pulse component polarized orthogonally to the pump and travelling at a longer wavelength with a matched group velocity to the generated soliton;
- either a cascaded four-wave mixing process leading to generation of multiple peaks in the visible and near-infrared spectral range or a far-detuned intramodal wavelength conversion below $0.65\ \mu\text{m}$ and beyond $3.5\ \mu\text{m}$ into the mid-infrared spectral region;
- spontaneous emergence of a localized space-time wavepacket that is either cylindrically-symmetric, or evolves on a complex trajectory during nonlinear propagation of ultrashort pulse.

Overall, the results presented in this dissertation improved the fundamental understanding of nonlinear phenomena observed in multimode and birefringent fibers and underscore the critical importance of which modes participate in the nonlinear interactions. The insights gained from these studies pave the way for further advancements in fiber optics, emphasizing the need for continued research to fully harness the potential of these nonlinear phenomena. This work lays a foundation for future explorations, which will undoubtedly contribute to the advancement of the optical technologies and their applications in various fields.

The exploration of nonlinear phenomena in multimode fibers has revealed and continues to reveal a wealth of complex interactions and novel spatiotemporal dynamics that significantly impact the field of fiber optics. Those recent advancements have opened up promising applications, particularly in areas requiring sophisticated control over light properties.

One such application is in the development of high-brightness laser sources. Additionally, the ability to generate complex spatiotemporal structured light could open new approaches in optical communication and signal processing, potentially improving data transmission rates and resilience to perturbations. Furthermore, the exploitation of cascaded nonlinear processes in multimode fibers allows for the creation of tunable, broadband sources, which are invaluable for advanced spectroscopic techniques and environmental sensing. Finally, structured wavepackets can also facilitate the study of nonlinear inverse-propagation, enabling the design of complex space-time input electromagnetic fields that transform optimally into the desired target output.

Despite these exciting opportunities, several significant challenges still need to be addressed. Optimization of nonlinear interactions requires designing fibers with tailored refractive index profiles through varied doping, or sophisticated structure, such as in PCF. Fabricating these specially designed fibers with high precision and consistency remains a significant challenge. Variations in manufacturing can lead to deviations from the desired fiber properties. As an example, the supercontinuum generated in a large-core graded-index fiber manifests in various ways depending on the presence of a small dip in the center of the fiber core, which is an artifact resulting from the method of the fiber fabrication [221].

Furthermore, developing accurate theoretical models to predict and understand the behavior of nonlinear phenomena in multimode fibers is complex due to the high-dimensional nature of the problem. Simulating the full spatiotemporal dynamics of multimode nonlinear interactions requires significant computational resources and advanced algorithms. Moreover, developing advanced techniques to accurately characterize the multimode nonlinear dynamics is necessary but challenging. Finally, ensuring the stability of nonlinear interactions over time and varying environmental conditions are critical for reliable applications.

Addressing these challenges is crucial and requires continued research and development in fiber design, experimental techniques, and theoretical modeling. Given the potential of these new studies, it is imperative that further research is dedicated to unraveling the underlying mechanisms, developing new numerical and experimental techniques, and optimizing their practical implementations. Continued investigation into the nonlinear behavior of multimode fibers will undoubtedly drive technological advancements and open new avenues for innovation in various scientific and industrial domains.

Bibliography

- [1] T. H. Maiman, “Stimulated optical radiation in ruby,” *Nature*, vol. 187, pp. 493–494, 1960.
- [2] P. A. Franken, A. E. Hill, C. W. Peters, and G. Weinreich, “Generation of optical harmonics,” *Phys. Rev. Lett.*, vol. 7, pp. 118–119, 1961.
- [3] N. Kapany, *Fiber Optics; Principles and Applications*. Academic Press, 1967.
- [4] K. Kao and G. Hockham, “Dielectric-fibre surface waveguides for optical frequencies,” *Proceedings of the Institution of Electrical Engineers*, vol. 113, pp. 1151–1158(7), 1966.
- [5] F. P. Kapron, D. B. Keck, and R. D. Maurer, “Radiation losses in glass optical waveguides,” *Applied Physics Letters*, vol. 17, pp. 423–425, 1970.
- [6] T. Miya, Y. Terunuma, T. Hosaka, and T. Miyashita, “Ultimate low-loss single-mode fibre at 1.55 μm ,” *Electronics Letters*, vol. 15, pp. 106–108(2), 1979.
- [7] G. P. Agrawal, *Fiber-Optic Communication Systems*. John Wiley & Sons, 3rd ed., 2002.
- [8] G. P. Agrawal, “Nonlinear fiber optics: its history and recent progress (invited),” *J. Opt. Soc. Am. B*, vol. 28, pp. A1–A10, 2011.
- [9] D. Marcuse, A. Telephone, and T. Company, *Theory of Dielectric Optical Waveguides*. Academic Press, 1991.
- [10] R. H. Stolen, E. P. Ippen, and A. R. Tynes, “Raman oscillation in glass optical waveguide,” *Applied Physics Letters*, vol. 20, pp. 62–64, 1972.
- [11] R. H. Stolen and A. Ashkin, “Optical Kerr effect in glass waveguide,” *Applied Physics Letters*, vol. 22, pp. 294–296, 1973.
- [12] R. H. Stolen, J. E. Bjorkholm, and A. Ashkin, “Phase-matched three-wave mixing in silica fiber optical waveguides,” *Applied Physics Letters*, vol. 24, pp. 308–310, 1974.
- [13] R. Stolen, “Phase-matched-stimulated four-photon mixing in silica-fiber waveguides,” *IEEE Journal of Quantum Electronics*, vol. 11, pp. 100–103, 1975.
- [14] K. O. Hill, D. C. Johnson, B. S. Kawasaki, and R. I. MacDonald, “cw three-wave mixing in single-mode optical fibers,” *Journal of Applied Physics*, vol. 49, pp. 5098–5106, 1978.
- [15] R. H. Stolen and C. Lin, “Self-phase-modulation in silica optical fibers,” *Phys. Rev. A*, vol. 17, pp. 1448–1453, 1978.
- [16] L. F. Mollenauer, R. H. Stolen, and J. P. Gordon, “Experimental observation of picosecond pulse narrowing and solitons in optical fibers,” *Phys. Rev. Lett.*, vol. 45, pp. 1095–1098, 1980.

- [17] L. F. Mollenauer and K. Smith, “Demonstration of soliton transmission over > 1000 km in fiber with loss compensated by Raman gain,” in *Conference on Lasers and Electro-Optics*, p. TUP5, 1988.
- [18] L. F. Mollenauer, “Solitons: the future of fibre communications,” *Physics World*, vol. 2, p. 29, 1989.
- [19] L. G. Wright, D. N. Christodoulides, and F. W. Wise, “Controllable spatiotemporal nonlinear effects in multimode fibres,” *Nature Photonics*, vol. 9, pp. 306–310, 2015.
- [20] A. Picozzi, G. Millot, and S. Wabnitz, “Nonlinear virtues of multimode fibre,” *Nature Photonics*, vol. 9, pp. 289–291, 2015.
- [21] D. Richardson, J. Fini, and L. Nelson, “Space division multiplexing in optical fibres,” *Nature Photonics*, vol. 7, pp. 354–362, 2013.
- [22] P. Winzer, “Optical networking beyond WDM,” *Photonics Journal, IEEE*, vol. 4, pp. 647–651, 2012.
- [23] L. G. Wright, D. N. Christodoulides, and F. W. Wise, “Spatiotemporal mode-locking in multimode fiber lasers,” *Science*, vol. 358, pp. 94–97, 2017.
- [24] N. O. Moussa, T. Mansuryan, C.-H. Hage, M. Fabert, K. Krupa, A. Tonello, M. Ferraro, L. Leggio, M. Zitelli, F. Mangini, A. Niang, G. Millot, M. Papi, S. Wabnitz, and V. Couderc, “Spatiotemporal beam self-cleaning for high-resolution nonlinear fluorescence imaging with multimode fiber,” *Scientific Reports*, 2021.
- [25] K. Krupa, A. Tonello, A. Barthélémy, T. Mansuryan, V. Couderc, G. Millot, P. Grelu, D. Modotto, S. A. Babin, and S. Wabnitz, “Multimode nonlinear fiber optics, a spatiotemporal avenue,” *APL Photonics*, vol. 4, p. 110901, 2019.
- [26] K. Krupa, A. Tonello, B. M. Shalaby, M. Fabert, A. Barthélémy, G. Millot, S. Wabnitz, and V. Couderc, “Spatial beam self-cleaning in multimode fibres,” *Nature Photonics*, vol. 11, pp. 237–241, 2017.
- [27] Z. Liu, L. G. Wright, D. N. Christodoulides, and F. W. Wise, “Kerr self-cleaning of femtosecond-pulsed beams in graded-index multimode fiber,” *Opt. Lett.*, vol. 41, pp. 3675–3678, 2016.
- [28] L. G. Wright, Z. Liu, D. A. Nolan, M.-J. Li, D. N. Christodoulides, and F. W. Wise, “Self-organized instability in graded-index multimode fibres,” *Nature Photonics*, vol. 10, pp. 771–776, 2016.
- [29] W. H. Renninger and F. W. Wise, “Optical solitons in graded-index multimode fibres,” *Nature Communications*, vol. 4, p. 1719, 2013.
- [30] Z. Zhu, L. G. Wright, D. N. Christodoulides, and F. W. Wise, “Observation of multimode solitons in few-mode fiber,” *Opt. Lett.*, vol. 41, pp. 4819–4822, 2016.

- [31] L. G. Wright, W. H. Renninger, D. N. Christodoulides, and F. W. Wise, “Spatiotemporal dynamics of multimode optical solitons,” *Opt. Express*, vol. 23, pp. 3492–3506, 2015.
- [32] A. Couairon and A. Mysyrowicz, “Femtosecond filamentation in transparent media,” *Physics Reports*, vol. 441, pp. 47–189, 2007.
- [33] K. D. Moll, A. L. Gaeta, and G. Fibich, “Self-similar optical wave collapse: Observation of the Townes profile,” *Phys. Rev. Lett.*, vol. 90, p. 203902, 2003.
- [34] G. A. Askaryan, “Effect of the gradient of a strong electromagnetic ray on electrons and atoms,” 1962.
- [35] E. Garmire, R. Y. Chiao, and C. H. Townes, “Dynamics and characteristics of the self-trapping of intense light beams,” *Phys. Rev. Lett.*, vol. 16, pp. 347–349, 1966.
- [36] F. Shimizu, “Frequency broadening in liquids by a short light pulse,” *Phys. Rev. Lett.*, vol. 19, pp. 1097–1100, 1967.
- [37] Y. Silberberg, “Collapse of optical pulses,” *Optics Letters*, vol. 15, pp. 1282–1285, 1990.
- [38] H. Kondakci and A. Abouraddy, “Diffraction-free space–time light sheets,” *Nature Photonics*, vol. 11, 2017.
- [39] K. O. Hill, D. C. Johnson, and B. S. Kawasaki, “Efficient conversion of light over a wide spectral range by four-photon mixing in a multimode graded-index fiber,” *Appl. Opt.*, vol. 20, pp. 1075–1079, 1981.
- [40] H. Tu, Z. Jiang, D. L. Marks, and S. A. Boppart, “Intermodal four-wave mixing from femtosecond pulse-pumped photonic crystal fiber,” *Applied Physics Letters*, vol. 94, p. 101109, 2009.
- [41] J. Cheng, M. E. Pedersen, K. Charan, K. Wang, C. Xu, L. Grüner-Nielsen, and D. Jakobsen, “Intermodal Čerenkov radiation in a higher-order-mode fiber,” *Optics Letters*, vol. 37, pp. 4410–4412, 2012.
- [42] J. Demas, P. Steinvurzel, B. Tai, L. Rishoj, Y. Chen, and S. Ramachandran, “Intermodal nonlinear mixing with Bessel beams in optical fiber,” *Optica*, vol. 2, pp. 14–17, 2015.
- [43] S. Perret, G. Fanjoux, L. Bigot, J. Fatome, G. Millot, J. M. Dudley, and T. Sylvestre, “Supercontinuum generation by intermodal four-wave mixing in a step-index few-mode fibre,” *APL Photonics*, vol. 4, p. 022905, 2018.
- [44] R. Dupiol, A. Bendahmane, K. Krupa, A. Tonello, M. Fabert, B. Kibler, T. Sylvestre, A. Barthelemy, V. Couderc, S. Wabnitz, and G. Millot, “Far-detuned cascaded intermodal four-wave mixing in a multimode fiber,” *Optics Letters*, vol. 42, pp. 1293–1296, 2017.
- [45] A. Bendahmane, K. Krupa, A. Tonello, D. Modotto, T. Sylvestre, V. Couderc, S. Wabnitz, and G. Millot, “Seeded intermodal four-wave mixing in a highly multimode fiber,” *J. Opt. Soc. Am. B*, vol. 35, pp. 295–301, 2018.

- [46] J. Yuan, Z. Kang, F. Li, X. Zhang, C. Mei, G. Zhou, X. Sang, Q. Wu, B. Yan, X. Zhou, K. Zhong, K. Wang, C. Yu, G. Farrell, C. Lu, H. Y. Tam, and P. K. A. Wai, “Experimental generation of discrete ultraviolet wavelength by cascaded intermodal four-wave mixing in a multimode photonic crystal fiber,” *Opt. Lett.*, vol. 42, pp. 3537–3540, 2017.
- [47] K. Krupa, A. Tonello, A. Barthélémy, V. Couderc, B. M. Shalaby, A. Bendahmane, G. Millot, and S. Wabnitz, “Observation of geometric parametric instability induced by the periodic spatial self-imaging of multimode waves,” *Physical Review Letters*, vol. 116, p. 183901, 2016.
- [48] C. M. Arabí, A. Kudlinski, A. Mussot, and M. Conforti, “Geometric parametric instability in periodically modulated graded-index multimode fibers,” *Phys. Rev. A*, vol. 97, p. 023803, 2018.
- [49] G. Lopez-Galmiche, Z. S. Eznaveh, M. A. Eftekhar, J. A. Lopez, L. G. Wright, F. Wise, D. Christodoulides, and R. A. Correa, “Visible supercontinuum generation in a graded index multimode fiber pumped at 1064 nm,” *Opt. Lett.*, vol. 41, pp. 2553–2556, 2016.
- [50] K. Krupa, C. Louot, V. Couderc, M. Fabert, R. Guenard, B. M. Shalaby, A. Tonello, D. Pagnoux, P. Leproux, A. Bendahmane, R. Dupiol, G. Millot, and S. Wabnitz, “Spatiotemporal characterization of supercontinuum extending from the visible to the mid-infrared in a multimode graded-index optical fiber,” *Optics Letters*, vol. 41, p. 5785, 2016.
- [51] D. Colladon, “On the reflections of a ray of light inside a parabolic liquid stream,” *Comptes Rendus*, vol. 15, p. 15, 1842.
- [52] J. Tyndall, *Six lectures on light: delivered in America in 1872-1873*. Longmans, 1873.
- [53] R. Kitamura, L. Pilon, and M. Jonasz, “Optical constants of silica glass from extreme ultraviolet to far infrared at near room temperature,” *Appl. Opt.*, vol. 46, pp. 8118–8133, 2007.
- [54] O. Humbach, H. Fabian, U. Grzesik, U. Haken, and W. Heitmann, “Analysis of OH absorption bands in synthetic silica,” *Journal of Non-Crystalline Solids*, vol. 203, pp. 19–26, 1996.
- [55] W. Griffioen, *Optical fiber mechanical reliability*. PhD thesis, Chemical Engineering and Chemistry, TU/e, 1995.
- [56] D. Bonamy, S. Prades, C. Rountree, L. Ponson, D. Dalmas, E. Bouchaud, K. Ravi-Chandar, and C. Guillot, “Nanoscale damage during fracture in silica glass,” *International Journal of Fracture*, vol. 140, pp. 3–13, 2006.
- [57] F. Célerié, S. Prades, D. Bonamy, L. Ferrero, E. Bouchaud, C. Guillot, and C. Marlière, “Glass breaks like metal, but at the nanometer scale,” *Phys. Rev. Lett.*, vol. 90, p. 075504, 2003.

- [58] Y. Bellouard, “On the bending strength of fused silica flexures fabricated by ultrafast lasers (invited),” *Opt. Mater. Express*, vol. 1, pp. 816–831, 2011.
- [59] A. V. Smith and B. T. Do, “Bulk and surface laser damage of silica by picosecond and nanosecond pulses at 1064 nm,” *Appl. Opt.*, vol. 47, pp. 4812–4832, 2008.
- [60] M. Perry, B. Stuart, P. Banks, M. Feit, V. Yanovsky, and A. Rubenchik, “Ultrashort-pulse laser machining of dielectric materials,” *Journal of Applied Physics*, vol. 85, pp. 6803–6810, 1999.
- [61] L. Sudrie, M. Franco, B. Prade, and A. Mysyrowicz, “Study of damage in fused silica induced by ultra-short IR laser pulses,” *Optics Communications*, vol. 191, pp. 333–339, 2001.
- [62] M. Ferraro, F. Mangini, M. Zitelli, A. Tonello, A. D. Luca, V. Couderc, and S. Wabnitz, “Femtosecond nonlinear losses in multimode optical fibers,” *Photon. Res.*, vol. 9, pp. 2443–2453, 2021.
- [63] M. Deroh, B. Kibler, H. Maillotte, T. Sylvestre, and J.-C. Beugnot, “Large Brillouin gain in germania-doped core optical fibers up to a 98 mol% doping level,” *Opt. Lett.*, vol. 43, pp. 4005–4008, 2018.
- [64] J. Wang, “Alumina as a dopant in optical fiber by OVD,” *Applied Physics A*, vol. 116, pp. 505–518, 2014.
- [65] K. Schuster, S. Grimm, A. Kalide, J. Dellith, M. Leich, A. Schwuchow, A. Langner, G. Schötz, and H. Bartelt, “Evolution of fluorine doping following the REPUSIL process for the adjustment of optical properties of silica materials,” *Opt. Mater. Express*, vol. 5, pp. 887–897, 2015.
- [66] A. C. S. V. HEEL, “A new method of transporting optical images without aberrations,” *Nature*, vol. 173, pp. 39–39, 1954.
- [67] K. Mori, H. Takara, and S. Kawanishi, “Analysis and design of supercontinuum pulse generation in a single-mode optical fiber,” *J. Opt. Soc. Am. B*, vol. 18, pp. 1780–1792, 2001.
- [68] T. Okuno, M. Hirano, T. Kato, M. Shigematsu, and M. Onishi, “Highly nonlinear and perfectly dispersion-flattened fibres for efficient optical signal processing applications,” *Electronics Letters*, vol. 39, pp. 972–974(2), 2003.
- [69] R. F. Cregan, B. J. Mangan, J. C. Knight, T. A. Birks, P. S. J. Russell, P. J. Roberts, and D. C. Allan, “Single-mode photonic band gap guidance of light in air,” *Science*, vol. 285, pp. 1537–1539, 1999.
- [70] H. Sakr, Y. Chen, G. Jasion, T. Bradley, J. Hayes, H. C. Mulvad, I. Davidson, E. N. Fokoua, and F. Poletti, “Hollow core optical fibres with comparable attenuation to silica fibres between 600 and 1100 nm,” *Nature Communications*, vol. 11, 2020.

- [71] A. Snyder and J. Love, *Optical Waveguide Theory*. Springer US, 1983.
- [72] D. Gloge and E. A. J. Marcatili, “Multimode theory of graded-core fibers,” *The Bell System Technical Journal*, vol. 52, pp. 1563–1578, 1973.
- [73] G. P. Agrawal, “Invite paper: Self-imaging in multimode graded-index fibers and its impact on the nonlinear phenomena,” *Optical Fiber Technology*, vol. 50, pp. 309–316, 2019.
- [74] A. Mafi, “Pulse propagation in a short nonlinear graded-index multimode optical fiber,” *Journal of Lightwave Technology*, vol. 30, pp. 2803–2811, 2012.
- [75] R. Paschotta, “Case study: Number of modes of a highly multimode fiber.” https://www.rp-photonics.com/case_study_number_of_modes.html. Accessed: May 2024.
- [76] J. C. Knight, T. A. Birks, P. S. J. Russell, and D. M. Atkin, “All-silica single-mode optical fiber with photonic crystal cladding,” *Opt. Lett.*, vol. 21, pp. 1547–1549, 1996.
- [77] B. J. Eggleton, C. Kerbage, P. S. Westbrook, R. S. Windeler, and A. Hale, “Microstructured optical fiber devices,” *Opt. Express*, vol. 9, pp. 698–713, 2001.
- [78] J. C. Knight, “Photonic crystal fibres,” *Nature*, vol. 424, pp. 847–851, 2003.
- [79] P. Russell, “Photonic crystal fibers,” *Science*, vol. 299, pp. 358–362, 2003.
- [80] V. Finazzi, T. Monro, and D. Richardson, “Small-core silica holey fibers: Nonlinearity and confinement loss trade-offs,” *JOSA B*, vol. 20, pp. 1427–1436, 2003.
- [81] J. Knight, J. Arriaga, T. Birks, A. Ortigosa-Blanch, W. Wadsworth, and P. Russell, “Anomalous dispersion in photonic crystal fiber,” *IEEE Photonics Technology Letters*, vol. 12, pp. 807–809, 2000.
- [82] K. Saitoh, M. Koshiba, T. Hasegawa, and E. Sasaoka, “Chromatic dispersion control in photonic crystal fibers: application to ultra-flattened dispersion,” *Opt. Express*, vol. 11, pp. 843–852, 2003.
- [83] K. Saitoh and M. Koshiba, “Numerical modeling of photonic crystal fibers,” *Journal of Lightwave Technology*, vol. 23, pp. 3580–3590, 2005.
- [84] G. P. Agrawal, *Nonlinear Fiber Optics*. Academic Press, 6th ed., 2019.
- [85] D. Gloge, “Weakly guiding fibers,” *Appl. Opt.*, vol. 10, pp. 2252–2258, 1971.
- [86] S. Ramachandran and P. Kristensen, “Optical vortices in fiber,” *Nanophotonics*, vol. 2, pp. 455–474, 2013.
- [87] E. Nazemosadat, H. Pourbeyram, and A. Mafi, “Phase matching for spontaneous frequency conversion via four-wave mixing in graded-index multimode optical fibers,” *J. Opt. Soc. Am. B*, vol. 33, pp. 144–150, 2016.

- [88] K.-P. Ho and J. Kahn, “Mode coupling and its impact on spatially multiplexed systems,” *Optical Fiber Telecommunications VIB: Systems and Networks: Sixth Edition*, 2013.
- [89] H. Taylor, “Bending effects in optical fibers,” *Journal of Lightwave Technology*, vol. 2, pp. 617–628, 1984.
- [90] C. Schulze, R. Brüning, S. Schröter, and M. Duparré, “Mode coupling in few-mode fibers induced by mechanical stress,” *J. Lightwave Technol.*, vol. 33, pp. 4488–4496, 2015.
- [91] L. Allen, M. W. Beijersbergen, R. J. C. Spreeuw, and J. P. Woerdman, “Orbital angular momentum of light and the transformation of Laguerre-Gaussian laser modes,” *Phys. Rev. A*, vol. 45, pp. 8185–8189, 1992.
- [92] C. Brunet and L. Rusch, “Invited paper: Optical fibers for the transmission of orbital angular momentum modes,” *Optical Fiber Technology*, vol. 31, pp. 172–177, 2016.
- [93] S. Chen and J. Wang, “Theoretical analyses on orbital angular momentum modes in conventional graded-index multimode fibre,” *Scientific Reports*, vol. 7, 2017.
- [94] M. Mirhosseini, O. S. M. na Loaiza, C. Chen, B. Rodenburg, M. Malik, and R. W. Boyd, “Rapid generation of light beams carrying orbital angular momentum,” *Opt. Express*, vol. 21, pp. 30196–30203, 2013.
- [95] C. Brunet, P. Vaity, Y. Messaddeq, S. LaRochelle, and L. A. Rusch, “Design, fabrication and validation of an OAM fiber supporting 36 states,” *Opt. Express*, vol. 22, pp. 26117–26127, 2014.
- [96] K. Sueda, G. Miyaji, N. Miyanaga, and M. Nakatsuka, “Laguerre-Gaussian beam generated with a multilevel spiral phase plate for high intensity laser pulses,” *Opt. Express*, vol. 12, pp. 3548–3553, 2004.
- [97] M. Beijersbergen, R. Coerwinkel, M. Kristensen, and J. Woerdman, “Helical-wavefront laser beams produced with a spiral phaseplate,” *Optics Communications*, vol. 112, pp. 321–327, 1994.
- [98] S. Khonina, V. Kotlyar, M. Shinkaryev, V. Soifer, and G. Uspleniev, “The phase rotor filter,” *Journal of Modern Optics*, vol. 39, pp. 1147–1154, 1992.
- [99] L. Marrucci, C. Manzo, and D. Paparo, “Optical spin-to-orbital angular momentum conversion in inhomogeneous anisotropic media,” *Phys. Rev. Lett.*, vol. 96, p. 163905, 2006.
- [100] P. Gregg, M. Mirhosseini, A. Rubano, L. Marrucci, E. Karimi, R. W. Boyd, and S. Ramachandran, “Q-plates as higher order polarization controllers for orbital angular momentum modes of fiber,” *Opt. Lett.*, vol. 40, pp. 1729–1732, 2015.
- [101] E. Collett, *Field Guide to Polarization*. SPIE Press, 2005.

- [102] P. Hlubina, D. Ciprian, and M. Kadulová, “Measurement of chromatic dispersion of polarization modes in optical fibres using white-light spectral interferometry,” *Measurement Science and Technology*, vol. 21, p. 045302, 2010.
- [103] J. Damask, *Polarization Optics in Telecommunications*. Springer, 2004.
- [104] R. Dyott, *Elliptical Fiber Waveguides*. Artech House, 1995.
- [105] J. Noda, K. Okamoto, and Y. Sasaki, “Polarization-maintaining fibers and their applications,” *Journal of Lightwave Technology*, vol. 4, pp. 1071–1089, 1986.
- [106] A. Ortigosa-Blanch, J. C. Knight, W. J. Wadsworth, J. Arriaga, B. J. Mangan, T. A. Birks, and P. S. J. Russell, “Highly birefringent photonic crystal fibers,” *Opt. Lett.*, vol. 25, pp. 1325–1327, 2000.
- [107] A. Michie, J. Canning, K. Lyytikäinen, M. Åslund, and J. Digweed, “Temperature independent highly birefringent photonic crystal fibre,” *Opt. Express*, vol. 12, pp. 5160–5165, 2004.
- [108] P. Hlubina and D. Ciprian, “Spectral-domain measurement of phase modal birefringence in polarization-maintaining fiber,” *Opt. Express*, vol. 15, pp. 17019–17024, 2007.
- [109] G. Thomas, B. Shraiman, P. Glodls, and M. Stephen, “Towards the clarity limit in optical fibre,” *Nature*, vol. 404, pp. 262–264, 2000.
- [110] J. Zhou, K. Tajima, K. Nakajima, K. Kurokawa, C. Fukai, T. Matsui, and I. Sankawa, “Progress on low loss photonic crystal fibers,” *Optical Fiber Technology*, vol. 11, pp. 101–110, 2005.
- [111] T. P. White, R. C. McPhedran, C. M. de Sterke, L. C. Botten, and M. J. Steel, “Confinement losses in microstructured optical fibers,” *Opt. Lett.*, vol. 26, pp. 1660–1662, 2001.
- [112] T. Okuno, M. Onishi, T. Kashiwada, S. Ishikawa, and M. Nishimura, “Silica-based functional fibers with enhanced nonlinearity and their applications,” *IEEE Journal of Selected Topics in Quantum Electronics*, vol. 5, pp. 1385–1391, 1999.
- [113] M. J. Weber, D. Milam, and W. L. Smith, “Nonlinear refractive index of glasses and crystals,” *Optical Engineering*, vol. 17, p. 175463, 1978.
- [114] P. Kabaciński, T. M. Kardaś, Y. Stepanenko, and C. Radzewicz, “Nonlinear refractive index measurement by SPM-induced phase regression,” *Opt. Express*, vol. 27, pp. 11018–11028, 2019.
- [115] D. Milam, “Review and assessment of measured values of the nonlinear refractive-index coefficient of fused silica,” *Appl. Opt.*, vol. 37, pp. 546–550, 1998.

- [116] T. R. Ensley and N. K. Bambha, “Ultrafast nonlinear refraction measurements of infrared transmitting materials in the mid-wave infrared,” *Opt. Express*, vol. 27, pp. 37940–37951, 2019.
- [117] S. R. Flom, G. Beadie, S. S. Bayya, B. Shaw, and J. M. Auxier, “Ultrafast Z-scan measurements of nonlinear optical constants of window materials at 772, 1030, and 1550 nm,” *Appl. Opt.*, vol. 54, pp. F123–F128, 2015.
- [118] G. Janssonas, R. Budriūnas, M. Vengris, and A. Varanavičius, “Interferometric measurements of nonlinear refractive index in the infrared spectral range,” *Opt. Express*, vol. 30, pp. 30507–30524, 2022.
- [119] N. Tzoar and M. Jain, “Self-phase modulation in long-geometry optical waveguides,” *Phys. Rev. A*, vol. 23, pp. 1266–1270, 1981.
- [120] D. Anderson and M. Lisak, “Nonlinear asymmetric self-phase modulation and self-steepening of pulses in long optical waveguides,” *Phys. Rev. A*, vol. 27, pp. 1393–1398, 1983.
- [121] F. DeMartini, C. H. Townes, T. K. Gustafson, and P. L. Kelley, “Self-steepening of light pulses,” *Phys. Rev.*, vol. 164, pp. 312–323, 1967.
- [122] R. Merlino, J. Heinrich, S.-H. Hyun, and J. Meyer, “Nonlinear dust acoustic waves and shocks,” *Physics of Plasmas*, vol. 19, 2012.
- [123] J. M. Dudley, G. Genty, and S. Coen, “Supercontinuum generation in photonic crystal fiber,” *Reviews of Modern Physics*, vol. 78, pp. 1135–1184, 2006.
- [124] C. Sulem and P. Sulem, *The Nonlinear Schrödinger Equation: Self-Focusing and Wave Collapse*. Springer New York, 2007.
- [125] Q. Lin and G. Agrawal, “Vector theory of cross-phase modulation: role of nonlinear polarization rotation,” *IEEE Journal of Quantum Electronics*, vol. 40, pp. 958–964, 2004.
- [126] C. R. Menyuk, “Stability of solitons in birefringent optical fibers. I: Equal propagation amplitudes,” *Optics Letters*, vol. 12, pp. 614–616, 1987.
- [127] C. R. Menyuk, “Stability of solitons in birefringent optical fibers. II. Arbitrary amplitudes,” *Journal of the Optical Society of America B*, vol. 5, pp. 392–402, 1988.
- [128] J. M. Soto-Crespo and E. M. Wright, “Generation of pulse trains in the normal dispersion regime of a dielectric medium with a relaxing nonlinearity,” *Applied Physics Letters*, vol. 59, pp. 2489–2491, 1991.
- [129] R. Dupiol, A. Bendahmane, K. Krupa, J. Fatome, A. Tonello, M. Fabert, V. Couderc, S. Wabnitz, and G. Millot, “Intermodal modulational instability in graded-index multimode optical fibers,” *Opt. Lett.*, vol. 42, pp. 3419–3422, 2017.

- [130] C. V. Raman, “A new radiation,” *Indian Journal of physics*, vol. 2, pp. 387–398, 1928.
- [131] Q. Lin and G. P. Agrawal, “Raman response function for silica fibers,” *Optics Letters*, vol. 31, pp. 3086–3088, 2006.
- [132] F. M. Mitschke and L. F. Mollenauer, “Discovery of the soliton self-frequency shift,” *Optics Letters*, vol. 11, pp. 659–661, 1986.
- [133] K. Rottwitt and J. H. Povlsen, “Analyzing the fundamental properties of Raman amplification in optical fibers,” *J. Lightwave Technol.*, vol. 23, p. 3597, 2005.
- [134] L. Rishøj, P. Kristensen, S. Ramachandran, and K. Rottwitt, “Experimental demonstration of intermodal nonlinear effects between full vectorial modes in a few moded fiber,” *Opt. Express*, vol. 21, pp. 28836–28841, 2013.
- [135] A. Hasegawa and F. Tappert, “Transmission of stationary nonlinear optical pulses in dispersive dielectric fibers. I. Anomalous dispersion,” *Applied Physics Letters*, vol. 23, pp. 142–144, 1973.
- [136] J. Takayanagi, T. Sugiura, M. Yoshida, and N. Nishizawa, “1.0–1.7- μm wavelength-tunable ultrashort-pulse generation using femtosecond Yb-doped fiber laser and photonic crystal fiber,” *IEEE Photonics Technology Letters*, vol. 18, pp. 2284–2286, 2006.
- [137] R. Pant, A. C. Judge, E. C. Magi, B. T. Kuhlmeier, M. de Sterke, and B. J. Eggleton, “Characterization and optimization of photonic crystal fibers for enhanced soliton self-frequency shift,” *Journal of the Optical Society of America B*, vol. 27, pp. 1894–1901, 2010.
- [138] G. Soboń, T. Martynkien, K. Tarnowski, P. Mergo, and J. Sotor, “Generation of sub-100 fs pulses tunable from 1700 to 2100 nm from a compact frequency-shifted Er-fiber laser,” *Photon. Res.*, vol. 5, pp. 151–155, 2017.
- [139] G. Soboń, T. Martynkien, D. Tomaszewska, K. Tarnowski, P. Mergo, and J. Sotor, “All-in-fiber amplification and compression of coherent frequency-shifted solitons tunable in the 1800–2000 nm range,” *Photonics Research*, vol. 6, pp. 368–372, 2018.
- [140] A. Picozzi, G. Millot, and S. Wabnitz, “Nonlinear virtues of multimode fibre,” *Nature Photonics*, vol. 9, pp. 289–291, 2015.
- [141] L. Rishøj, B. Tai, P. Kristensen, and S. Ramachandran, “Soliton self-mode conversion: revisiting Raman scattering of ultrashort pulses,” *Optica*, vol. 6, pp. 304–308, 2019.
- [142] M. N. Islam, C. D. Poole, and J. P. Gordon, “Soliton trapping in birefringent optical fibers,” *Optics Letters*, vol. 14, pp. 1011–1013, 1989.
- [143] N. Nishizawa and T. Goto, “Widely wavelength-tunable ultrashort pulse generation using polarization maintaining optical fibers,” *IEEE Journal on Selected Topics in Quantum Electronics*, vol. 7, pp. 518–524, 2001.

- [144] N. Nishizawa and T. Goto, “Trapped pulse generation by femtosecond soliton pulse in birefringent optical fibers,” *Optics Express*, vol. 10, pp. 256–261, 2002.
- [145] N. Nishizawa and T. Goto, “Characteristics of pulse trapping by use of ultrashort soliton pulses in optical fibers across the zero-dispersion wavelength,” *Optics Express*, vol. 10, pp. 1151–1159, 2002.
- [146] E. Shiraki, N. Nishizawa, and K. Itoh, “Ultrashort pulse generation from cw beam by trapped pulse amplification in birefringent fibers,” *Optics Express*, vol. 18, pp. 23070–23078, 2010.
- [147] E. Shiraki and N. Nishizawa, “Coherent ultrashort pulse generation from incoherent light by trapped pulse amplification in birefringent fibers,” *Optics Express*, vol. 20, pp. 11073–11082, 2012.
- [148] P. Hlubina, M. Szpulak, L. Knyblová, G. Statkiewicz, T. Martynkien, D. Ciprian, and W. Urbańczyk, “Measurement and modelling of dispersion characteristics of a two-mode birefringent holey fibre,” *Measurement Science and Technology*, vol. 17, pp. 626–630, 2006.
- [149] K. Blow and N. Doran, “The asymptotic dispersion of soliton pulses in lossy fibres,” *Optics Communications*, vol. 52, pp. 367–370, 1985.
- [150] J. C. Travers, M. H. Frosz, and J. M. Dudley, *Nonlinear fibre optics overview*, p. 32–51. Cambridge University Press, 2010.
- [151] K. Stefańska, S. Majchrowska, K. Gemza, G. Soboń, J. Sotor, P. Mergo, K. Tarnowski, and T. Martynkien, “Soliton trapping and orthogonal Raman scattering in a birefringent photonic crystal fiber,” *Opt. Lett.*, vol. 47, pp. 4183–4186, 2022.
- [152] O. Szewczyk, P. Pala, K. Tarnowski, J. Olszewski, F. Senna Vieira, C. Lu, A. Foltynowicz, P. Mergo, J. Sotor, G. Soboń, and T. Martynkien, “Dual-wavelength pumped highly birefringent microstructured silica fiber for widely tunable soliton self-frequency shift,” *Journal of Lightwave Technology*, vol. 39, pp. 3260–3268, 2021.
- [153] H. E. Lopez-Aviles, F. O. Wu, Z. S. Eznaveh, M. A. Eftekhari, F. Wise, R. A. Correa, and D. N. Christodoulides, “A systematic analysis of parametric instabilities in nonlinear parabolic multimode fibers,” *APL Photonics*, vol. 4, p. 022803, 2018.
- [154] A. Bendahmane, M. Conforti, O. Vanvincq, C. M. Arabi, A. Mussot, and A. Kudlinski, “Origin of spontaneous wave mixing processes in multimode GRIN fibers,” *Optics Express*, vol. 29, p. 30822, 2021.
- [155] T. Hansson, A. Tonello, T. Mansuryan, F. Mangini, M. Zitelli, M. Ferraro, A. Niang, R. Crescenzi, S. Wabnitz, and V. Couderc, “Nonlinear beam self-imaging and self-focusing dynamics in a GRIN multimode optical fiber: theory and experiments,” *Opt. Express*, vol. 28, pp. 24005–24021, 2020.

- [156] S. Longhi, “Modulational instability and space time dynamics in nonlinear parabolic-index optical fibers,” *Opt. Lett.*, vol. 28, pp. 2363–2365, 2003.
- [157] M. A. Eftekhar, L. G. Wright, M. S. Mills, M. Kolesik, R. A. Correa, F. W. Wise, and D. N. Christodoulides, “Versatile supercontinuum generation in parabolic multimode optical fibers,” *Opt. Express*, vol. 25, pp. 9078–9087, 2017.
- [158] Z. S. Eznaveh, M. A. Eftekhar, J. E. A. Lopez, M. Kolesik, A. Schülzgen, F. W. Wise, D. N. Christodoulides, and R. A. Correa, “Tailoring frequency generation in uniform and concatenated multimode fibers,” *Opt. Lett.*, vol. 42, pp. 1015–1018, 2017.
- [159] J. M. Stone and J. C. Knight, “Visibly “white” light generation in uniform photonic crystal fiber using a microchip laser,” *Opt. Express*, vol. 16, pp. 2670–2675, 2008.
- [160] J. Swiderski, “High-power mid-infrared supercontinuum sources: Current status and future perspectives,” *Progress in Quantum Electronics*, vol. 38, 2014.
- [161] C. Xia, M. Kumar, M.-Y. Cheng, O. P. Kulkarni, M. N. Islam, A. Galvanauskas, F. L. Terry, M. J. Freeman, D. A. Nolan, and W. A. Wood, “Supercontinuum generation in silica fibers by amplified nanosecond laser diode pulses,” *IEEE J. Sel. Topics Quantum Electron.*, vol. 13, pp. 789–797, 2007.
- [162] E. A. Anashkina, A. V. Andrianov, M. Y. Koptev, S. V. Muravyev, and A. V. Kim, “Towards mid-infrared supercontinuum generation with germano-silicate fibers,” *IEEE Journal of Selected Topics in Quantum Electronics*, vol. 20, pp. 643–650, 2014.
- [163] X. Wang, H. Lei, K. Xie, and J. Li, “All-silica fiber ultra-flat 2-3 μm supercontinuum source based on highly nonlinear silica fiber,” *IEEE Photonics Technology Letters*, vol. 35, pp. 381–384, 2023.
- [164] H. Lei, K. Xie, X. Wang, S. Wang, H. Luo, and J. Li, “NIR to MIR ultra-broadband supercontinuum laser source based on all-silica fibers,” *Opt. Express*, vol. 31, pp. 29403–29410, 2023.
- [165] D. Jain, R. Sidharthan, G. Woyessa, P. M. Moselund, P. Bowen, S. Yoo, and O. Bang, “Scaling power, bandwidth, and efficiency of mid-infrared supercontinuum source based on a GeO₂-doped silica fiber,” *J. Opt. Soc. Am. B*, vol. 36, pp. A86–A92, 2019.
- [166] K. Yin, B. Zhang, J. Yao, L. Yang, G. Liu, and J. Hou, “1.9–3.6 μm supercontinuum generation in a very short highly nonlinear germania fiber with a high mid-infrared power ratio,” *Opt. Lett.*, vol. 41, pp. 5067–5070, 2016.
- [167] L. Yang, Y. Yang, B. Zhang, X. Zhu, D. Zhao, S. Liu, and J. Hou, “Record power and efficient mid-infrared supercontinuum generation in germania fiber with high stability,” *High Power Laser Science and Engineering*, vol. 10, p. e36, 2022.

- [168] X. Wang, C. Yao, P. Li, Y. Wu, L. Yang, G. Ren, and C. Wang, “All-fiber high-power supercontinuum laser source over 3.5 μm based on a germania-core fiber,” *Opt. Lett.*, vol. 46, pp. 3103–3106, 2021.
- [169] M. Michalska, P. Hlubina, and J. Swiderski, “Mid-infrared supercontinuum generation to 4.7 μm in a ZBLAN fiber pumped by an optical parametric generator,” *IEEE Photonics Journal*, vol. 9, pp. 1–7, 2017.
- [170] G. Qin, X. Yan, C. Kito, M. Liao, C. Chaudhari, T. Suzuki, and Y. Ohishi, “Ultrabroadband supercontinuum generation from ultraviolet to 6.28 μm in a fluoride fiber,” *Applied Physics Letters*, vol. 95, p. 161103, 2009.
- [171] Y. Leventoux, G. Granger, Y. Arosa, I. Tilouine, K. Krupa, A. Tonello, V. Couderc, and S. Février, “Three octave visible to mid-infrared supercontinuum generation seeded by multimode silica fiber pumped at 1064 nm,” *Opt. Lett.*, vol. 48, pp. 4582–4585, 2023.
- [172] Z. Zhao, B. Wu, X. Wang, Z. Pan, Z. Liu, P. Zhang, X. Shen, Q. Nie, S. Dai, and R. Wang, “Mid-infrared supercontinuum covering 2.0–16 μm in a low-loss telluride single-mode fiber,” *Laser & Photonics Reviews*, vol. 11, p. 1700005, 2017.
- [173] Z. Eslami, P. Ryczkowski, L. Salmela, and G. Genty, “Low-noise octave-spanning mid-infrared supercontinuum generation in a multimode chalcogenide fiber,” *Opt. Lett.*, vol. 45, pp. 3103–3106, 2020.
- [174] A. Lemièrre, R. Bizot, F. Désévéday, G. Gadret, J.-C. Jules, P. Mathey, C. Aquilina, P. Béjot, F. Billard, O. Faucher, B. Kibler, and F. Smektala, “1.7–18 μm mid-infrared supercontinuum generation in a dispersion-engineered step-index chalcogenide fiber,” *Results in Physics*, vol. 26, p. 104397, 2021.
- [175] J. Lægsgaard and H. Tu, “How long wavelengths can one extract from silica-core fibers?,” *Opt. Lett.*, vol. 38, pp. 4518–4521, 2013.
- [176] D. Nodop, C. Jauregui, D. Schimpf, J. Limpert, and A. Tünnermann, “Efficient high-power generation of visible and mid-infrared light by degenerate four-wave-mixing in a large-mode-area photonic-crystal fiber,” *Opt. Lett.*, vol. 34, pp. 3499–3501, 2009.
- [177] C. Jauregui, A. Steinmetz, J. Limpert, and A. Tünnermann, “High-power efficient generation of visible and mid-infrared radiation exploiting four-wave-mixing in optical fibers,” *Opt. Express*, vol. 20, pp. 24957–24965, 2012.
- [178] L. Lavoute, J. C. Knight, P. Dupriez, and W. J. Wadsworth, “High power red and near-IR generation using four wave mixing in all integrated fibre laser systems,” *Opt. Express*, vol. 18, pp. 16193–16205, 2010.
- [179] A. Herzog, A. Shamir, and A. A. Ishaaya, “Wavelength conversion of nanosecond pulses to the mid-IR in photonic crystal fibers,” *Opt. Lett.*, vol. 37, pp. 82–84, 2012.

- [180] Y. Leventoux, G. Granger, K. Krupa, T. Mansuryan, M. Fabert, A. Tonello, S. Wabnitz, V. Couderc, and S. Février, “Frequency-resolved spatial beam mapping in multimode fibers: application to mid-infrared supercontinuum generation,” *Optics Letters*, vol. 46, p. 3717, 2021.
- [181] H. Sunak and S. Bastien, “Refractive index and material dispersion interpolation of doped silica in the 0.6-1.8 micrometer wavelength region,” *IEEE Photonics Technology Letters*, vol. 1, pp. 142–145, 1989.
- [182] P. Béjot, “Multimodal unidirectional pulse propagation equation,” *Phys. Rev. E*, vol. 99, p. 032217, 2019.
- [183] J. D. Harvey, R. Leonhardt, S. Coen, G. K. L. Wong, J. C. Knight, W. J. Wadsworth, and P. S. J. Russell, “Scalar modulation instability in the normal dispersion regime by use of a photonic crystal fiber,” *Optics Letters*, vol. 28, pp. 2225–2227, 2003.
- [184] T. Godin, Y. Combes, R. Ahmad, M. Rochette, T. Sylvestre, and J. M. Dudley, “Far-detuned mid-infrared frequency conversion via normal dispersion modulation instability in chalcogenide microwires,” *Optics Letters*, vol. 39, pp. 1885–1888, 2014.
- [185] H. Pourbeyram, P. Sidorenko, F. O. Wu, N. Bender, L. Wright, D. N. Christodoulides, and F. Wise, “Direct observations of thermalization to a Rayleigh–Jeans distribution in multimode optical fibres,” *Nature Physics*, vol. 18, pp. 685–690, 2022.
- [186] E. Podivilov, F. Mangini, O. Sidelnikov, M. Ferraro, M. Gervaziev, D. Kharenko, M. Zitelli, M. Fedoruk, S. Babin, and S. Wabnitz, “Thermalization of orbital angular momentum beams in multimode optical fibers,” *Physical Review Letters*, vol. 128, p. 243901, 2022.
- [187] B. Kibler and P. Béjot, “Discretized conical waves in multimode optical fibers,” *Physical Review Letters*, vol. 126, p. 023902, 2021.
- [188] P. Béjot and B. Kibler, “Spatiotemporal helicon wavepackets,” *ACS Photonics*, vol. 8, pp. 2345–2354, 2021.
- [189] A. Shiri, M. Yessenov, S. Webster, K. L. Schepler, and A. F. Abouraddy, “Hybrid guided space-time optical modes in unpatterned films,” *Nature Communications*, vol. 11, p. 6273, 2020.
- [190] P. Béjot and B. Kibler, “Quadrics for structuring invariant space–time wavepackets,” *ACS Photonics*, vol. 9, pp. 2066–2072, 2022.
- [191] A. Shiri, S. Webster, K. L. Schepler, and A. F. Abouraddy, “Propagation-invariant space-time supermodes in a multimode waveguide,” *Optica*, vol. 9, pp. 913–923, 2022.
- [192] P. Béjot and B. Kibler, “Taming light in all dimensions,” *Nature Photonics*, vol. 16, pp. 671–672, 2022.

- [193] D. Cruz-Delgado, S. Yerolatsitis, N. K. Fontaine, D. N. Christodoulides, R. Amezcua-Correa, and M. A. Bandres, “Synthesis of ultrafast wavepackets with tailored spatiotemporal properties,” *Nature Photonics*, vol. 16, pp. 686–691, 2022.
- [194] C. Day, “Intense X-shaped pulses of light propagate without spreading in water and other dispersive media,” *Physics Today*, vol. 57, pp. 25–26, 2004.
- [195] H. Kondakci and A. F. Abouraddy, “Optical space-time wave packets having arbitrary group velocities in free space,” *Nature Communications*, vol. 10, p. 929, 2019.
- [196] M. Yessenov, J. Free, Z. Chen, E. G. Johnson, M. P. Lavery, M. A. Alonso, and A. F. Abouraddy, “Space-time wave packets localized in all dimensions,” *Nature Communications*, vol. 13, p. 4573, 2022.
- [197] M. Yessenov, L. A. Hall, K. L. Schepler, and A. F. Abouraddy, “Space-time wave packets,” *Advances in Optics and Photonics*, vol. 14, pp. 455–570, 2022.
- [198] K. Tarnowski, S. Majchrowska, P. Béjot, and B. Kibler, “Numerical modelings of ultrashort pulse propagation and conical emission in multimode optical fibers,” *J. Opt. Soc. Am. B*, vol. 38, pp. 732–742, 2021.
- [199] M. Kolesik, E. M. Wright, and J. V. Moloney, “Interpretation of the spectrally resolved far field of femtosecond pulses propagating in bulk nonlinear dispersive media,” *Optics Express*, vol. 13, pp. 10729–10741, 2005.
- [200] D. Faccio, A. Couairon, and P. D. Trapani, *Conical waves, filaments and nonlinear filamentation optics*. Aracne Rome, 2007.
- [201] H. Sonajalg, M. Rätsep, and P. Saari, “Demonstration of the Bessel-X pulse propagating with strong lateral and longitudinal localization in a dispersive medium,” *Opt. Lett.*, vol. 22, pp. 310–312, 1997.
- [202] P. D. Trapani, G. Valiulis, A. Piskarskas, O. Jedrkiewicz, J. Trull, C. Conti, and S. Trillo, “Spontaneously generated X-shaped light bullets,” *Phys. Rev. Lett.*, vol. 91, p. 093904, 2003.
- [203] D. Majus, G. Tamošauskas, I. Gražulevičiūtė, N. Garejev, A. Lotti, A. Couairon, D. Faccio, and A. Dubietis, “Nature of spatiotemporal light bullets in bulk Kerr media,” *Phys. Rev. Lett.*, vol. 112, p. 193901, 2014.
- [204] M. A. Porras, A. Dubietis, E. Kučinskas, F. Bragheri, V. Degiorgio, A. Couairon, D. Faccio, and P. D. Trapani, “From X- to O-shaped spatiotemporal spectra of light filaments in water,” *Opt. Lett.*, vol. 30, pp. 3398–3400, 2005.
- [205] M. A. Porras, A. Dubietis, A. Matijošius, R. Piskarskas, F. Bragheri, A. Averchi, and P. D. Trapani, “Characterization of conical emission of light filaments in media with anomalous dispersion,” *J. Opt. Soc. Am. B*, vol. 24, pp. 581–584, 2007.

- [206] M. Kolesik, D. Faccio, E. Wright, P. D. Trapani, and J. Moloney, “Supercontinuum generation in planar glass membrane fibers: comparison with bulk media,” *Optics Letters*, vol. 34, pp. 286–288, 2009.
- [207] H. E. Hernández-Figueroa, M. Zamboni-Rached, and E. Recami, *Localized waves*. John Wiley & Sons, 2008.
- [208] D. Faccio, P. D. Trapani, S. Minardi, A. Bramati, F. Bragheri, C. Liberale, V. Degiorgio, A. Dubietis, and A. Matijosius, “Far-field spectral characterization of conical emission and filamentation in Kerr media,” *J. Opt. Soc. Am. B*, vol. 22, pp. 862–869, 2005.
- [209] M. Kolesik, E. M. Wright, and J. V. Moloney, “Dynamic nonlinear X waves for femtosecond pulse propagation in water,” *Phys. Rev. Lett.*, vol. 92, p. 253901, 2004.
- [210] D. Faccio, M. A. Porras, A. Dubietis, G. Tamošauskas, E. Kučinskas, A. Couairon, and P. D. Trapani, “Angular and chromatic dispersion in Kerr-driven conical emission,” *Optics Communications*, vol. 265, pp. 672–677, 2006.
- [211] Y. Nomura, H. Shirai, K. Ishii, N. Tsurumachi, A. A. Voronin, A. M. Zheltikov, and T. Fuji, “Phase-stable sub-cycle mid-infrared conical emission from filamentation in gases,” *Opt. Express*, vol. 20, pp. 24741–24747, 2012.
- [212] P. Béjot, J. Kasparian, S. Henin, V. Loriot, T. Vieillard, E. Hertz, O. Faucher, B. Lavorel, and J.-P. Wolf, “Higher-order Kerr terms allow ionization-free filamentation in gases,” *Phys. Rev. Lett.*, vol. 104, p. 103903, 2010.
- [213] O. G. Kosareva, V. P. Kandidov, A. Brodeur, C. Y. Chien, and S. L. Chin, “Conical emission from laser–plasma interactions in the filamentation of powerful ultrashort laser pulses in air,” *Opt. Lett.*, vol. 22, pp. 1332–1334, 1997.
- [214] E. T. J. Nibbering, P. F. Curley, G. Grillon, B. S. Prade, M. A. Franco, F. Salin, and A. Mysyrowicz, “Conical emission from self-guided femtosecond pulses in air,” *Opt. Lett.*, vol. 21, pp. 62–64, 1996.
- [215] M. Ferraro, F. Mangini, Y. Sun, M. Zitelli, A. Niang, M. C. Crocco, V. Formoso, R. Agostino, R. Barberi, A. D. Luca, *et al.*, “Multiphoton ionization of standard optical fibers,” *Photonics Research*, vol. 10, pp. 1394–1400, 2022.
- [216] M. N. Polyanskiy, “Refractiveindex.info database of optical constants,” *Scientific Data*, vol. 11, 2024.
- [217] R. DeSalvo, A. Said, D. Hagan, E. V. Stryland, and M. Sheik-Bahae, “Infrared to ultraviolet measurements of two-photon absorption and n_2 in wide bandgap solids,” *IEEE Journal of Quantum Electronics*, vol. 32, pp. 1324–1333, 1996.
- [218] S.-H. Cho, H. Kumagai, I. Yokota, K. Midorikawa, and M. Obara, “Observation of self-channeled plasma formation and bulk modification in optical fibers using high-intensity femtosecond laser,” *Japanese Journal of Applied Physics*, vol. 37, p. L737, 1998.

- [219] P. M. Walker, C. E. Whittaker, D. V. Skryabin, E. Cancellieri, B. Royall, M. Sich, I. Farrer, D. A. Ritchie, M. S. Skolnick, and D. N. Krizhanovskii, “Spatiotemporal continuum generation in polariton waveguides,” *Light: Science & Applications*, vol. 8, p. 6, 2019.
- [220] L. Wright, W. Renninger, D. Christodoulides, and F. Wise, “Nonlinear multimode photonics: nonlinear optics with many degrees of freedom,” *Optica*, vol. 9, pp. 824–841, 2022.
- [221] K. Krupa, V. Couderc, A. Tonello, D. Modotto, A. Barthélémy, G. Millot, and S. Wabnitz, “Refractive index profile tailoring of multimode optical fibers for the spatial and spectral shaping of parametric sidebands,” *J. Opt. Soc. Am. B*, vol. 36, pp. 1117–1126, 2019.

List of Figures

2.1	Schematic illustration of refractive index profile of a step-index fiber and a photograph of the fiber used in later experiments.	6
2.2	Schematic illustration of refractive index profile of a graded-index fiber and a photograph of the fiber used in later experiments.	7
2.3	Image from a scanning electron microscope showing the photonic crystal fiber used in the later experiments.	8
2.4	Calculated amplitude and intensity profiles of the first few $LP_{0,p}$ modes (left) and mode propagation constant (right) as a function of the radial mode number for the step-index fiber characterized by a $R = 52.5 \mu\text{m}$ pure-silica core and $NA=0.22$, assuming $\lambda = 1.035 \mu\text{m}$. In the left panels, the vertical dashed line at $r = R$ indicates the core-cladding boundary.	11
2.5	Calculated amplitude and intensity profiles of the first few $LP_{0,p}$ modes (left) and mode propagation constant as a function of the radial mode number for the graded-index fiber characterized by a $R = 50 \mu\text{m}$ core with a 24 mol% Ge doping in the core center, a parabolic index profile, and a pure silica cladding, assuming $\lambda = 1.035 \mu\text{m}$. In the left panels, the vertical dashed line at $r = R$ indicates the core-cladding boundary.	11
2.6	Calculated efficiencies of power coupling into the fundamental fiber mode for the beam with a Gaussian intensity profile launched into the investigated step-index MMF. The points show the calculated results as a function of incident beam radius, offset in the longitudinal and transverse directions, and error in angular orientation. The lines serve to guide the eye.	14
2.7	Helical structures and phase fronts of OAM beams with (a) $l = +1$, (b) $l = -1$, (c) $l = +2$, (d) $l = -2$	16
2.8	Examples of q plates. Lines indicate the local direction of the optical axis. . . .	17
2.9	Input beam (top row) and near-field images of the fiber output (bottom row) for different rotations of circular polarizer selecting the launched beam composition.	19
2.10	Refractive index calculated for the core center and cladding of the investigated GRIN fiber, along with the effective refractive index of the fundamental fiber mode.	20
2.11	Calculated phase and group effective refractive index for the fundamental mode of the investigated GRIN fiber.	21
2.12	Measured linear parameters of two modes $LP_{0,1}^x$ (blue) and $LP_{0,1}^y$ (red) of the investigated PCF: differential group refractive index and relative inverse group velocity.	23
2.13	Measured chromatic dispersion of the investigated PCF.	24

2.14	Measured phase and group birefringence determined using various techniques in the two investigated PCFs.	26
2.15	Measured attenuation coefficient in PCF (black) and its estimation for longer wavelengths (green).	28
2.16	Calculated effective areas of the fundamental and higher-order modes of the investigated GRIN and photonic crystal fiber.	29
2.17	Normalized Raman gain in silica fibers calculated for co-polarized (g_{\parallel}) and orthogonally polarized (g_{\perp}) pump and Stokes pulses.	35
3.1	Raman gain in silica fibers calculated for orthogonally polarized pulses based on model from Ref. [131]. Gain is normalized to the maximum of Raman gain for co-polarized pulses.	38
3.2	Transmission properties of the two photonic crystal fibers. Measured related inverse group velocities RIGV (a-b) and calculated chromatic dispersion D (c-d) of the mode polarized along x axis (blue) and y axis (red) in PCF 1 (a,c) and PCF 2 (b,d). Insets in (a,b) show SEM images of the fiber cross-section with arrows indicating direction of x and y axis and a white scale bar of $5\ \mu\text{m}$. Group birefringence (e) measured in PCF 1 and PCF 2. Measured attenuation (f) with an estimated maximum at $2.21\ \mu\text{m}$ indicated with green circle. Calculated mode effective area (g) and effective refractive index (h) of the two polarization modes of both PCFs. A vertical black line indicates a $1.56\ \mu\text{m}$ pump wavelength. . . .	40
3.3	Optical spectra recorded at the output of 20-meter-long section of PCF 1 (left) or PCF 2 (right) for increasing power of pump beam polarized along the x (top) or y (bottom) axis of the fiber. Line colors denote signal components polarized along the x (blue) or y (red) axis. Average power of the input beam is indicated in the top left corner of each panel. Polarization extinction ratio of solitons is given in the top right corner of each panel.	43
3.4	Central wavelength of solitons from Fig. 3.3 as a function of pump power for PCF 1 (left) and PCF 2 (right) after 20 m of propagation in the fiber. When x axis is excited, only the signal component polarized along the x axis is observed (blue circles). When y axis is excited, the signal component polarized along the x axis (blue asterisks) is observed in addition to the original component polarized along the y axis (red crosses).	44
3.5	Relationship between the fiber output power and the power of the input beam in short, 2-meter-long sections of PCF 1 (left) and PCF 2 (right) for input beam polarization aligned along x and y axis of the fiber. The calculated ratio of powers is indicated below markers for x polarization and above markers for y polarization.	45

3.6 Optical spectra recorded at the output of fiber sections of increasing lengths with an average power of the input beam equal to 60 mW for PCF 1 (left) or 70 mW for PCF 2 (right). The direction of the input beam polarization is along the x axis (top) or y axis of the fiber. Line colors denote signal components polarized along the x (blue) or y (red) axis. Fiber length is indicated in the top left corner of each panel. Polarization extinction ratio of solitons is given in the top right corner of each panel, and η denotes ratio of output soliton power to total output power. 47

3.7 Optical spectra recorded at the output of fiber sections of increasing lengths with an average power of the input beam equal to 70 mW for PCF 1 (left) or 80 mW for PCF 2 (right). The direction of the input beam polarization is along the x axis (top) or y axis of the fiber. Line colors denote signal components polarized along the x (blue) or y (red) axis. Fiber length is indicated in the top left corner of each panel. Polarization extinction ratio of solitons is given in the top right corner of each panel, and η denotes ratio of output soliton power to total output power. 48

3.8 Central wavelength of polarization components of the solitons as a function of propagation distance in PCF 1 (top row) and PCF 2 (bottom row) for four power levels of the input beam. When the x axis is excited, only the signal component polarized along the x axis is observed (blue circles). When the y axis is excited, the signal component polarized along the x axis (blue asterisks) is observed in addition to the original component polarized along the y axis (red crosses). 49

3.9 Optical spectra recorded at the output of 20-meter-long fiber sections with an average power of the input beam equal to 70 mW for PCF 1 (left) and 80 mW for PCF 2 (right) for different direction of the input pulse polarization with respect to the x fiber axis. Line colors denote signal components polarized along the x (blue) or y (red) axis. 50

3.10 Optical spectra recorded at the output of increasing lengths of PCF 1 with 70 mW input beam average power for equal excitation of the two fiber axes. Line colors denote signal components polarized along the x (blue) or y (red) axis. 51

3.11 Optical spectra calculated at the output of increasing lengths of PCF 1 for equal excitation of the two fiber axes assuming 80 mW input beam average power coupled with 50% efficiency. Line colors denote signal components polarized along the x (blue) or y (red) axis. Simulations performed assuming the orthogonal Raman polarization mixing term is turned off (dashed lines) or turned on (solid lines). Figure reproduced from [151]. 52

3.12 Calculated spectra (top) and temporal profiles (bottom) of generated soliton pulses at the output of 20-meter-long section of PCF 1, assuming 80 mW input power with 50% coupling efficiency. Line colors denote signal components polarized along the x (blue) or y (red) axis. Figure reproduced from [151]. . . 53

3.13	Central wavelength shift of polarization components of the solitons as the input pulse polarization is rotated with respect to the x axis of the fiber in PCF 1 (left) and PCF 2 (right). The input beam average power is 66 mW, and the fiber sections are 80 meter long in both cases.	54
3.14	Relation between central wavelengths of two polarization components of the soliton pulse investigated for different propagation distances (indicated in the legend) and pump average powers between 60 and 127 mW in PCF 1 (orange markers) and PCF 2 (pink markers) when the input pulse polarization is rotated 90° , 70° , and 45° with respect to the x axis of the fiber. Results for simulations performed for PCF 1 are indicated with blue markers. Two lines indicate group velocity matched wavelengths of the two polarization modes in each fiber (based on Fig. 3.2(a-b)). Background intensity indicates normalized orthogonal Raman gain from the pulse component polarized along the y axis (the gain spectrum is shown in Fig. 3.1).	55
4.1	(a) Phase-mismatch curves for FWM process with a selected spatial modes in Stokes (μ) and anti-Stokes (η) assuming pumping at $1.064 \mu\text{m}$ in the fundamental mode in a $22 \mu\text{m}$ -core GRIN fiber with a 5% Ge doping in the core center. Solid lines: obtained using calculated mode propagation constants; dotted lines: obtained using second order Taylor expansion of mode propagation constants around pump wavelength. (b) Phase-mismatch for intramodal FWM process with a Stokes, anti-Stokes, and pump in the fundamental mode, assuming pumping at $1.064 \mu\text{m}$, calculated using full mode propagation constant (solid line), or second-order (dotted line), fourth-order (dashed line), or sixth-order (dashed-dotted line) Taylor expansion of mode propagation constant around pump wavelength.	62
4.2	Phase-matching curves for FWM processes with a pump wavelength of $0.625 \mu\text{m}$. The Δk_M and $-\Delta k_W$ curves represent the material and waveguide dispersion contributions, respectively. $-\Delta k_W$ were calculated for several allowed values of integer G . Numbers in brackets represent example values of p of $\text{LP}_{0,p}$ modes that could be selected for Stokes, anti-Stokes, and two pump modes interacting in a FWM process and be characterized by a given G	64
4.3	Phase-matching curves for FWM processes involving different combinations of Stokes, anti-Stokes, and pump modes calculated using two approaches: a collective approach that accounts for material and waveguide dispersion contribution (thick dashed lines), and a rigorous approach that accounts for the effective refractive index of each mode (thin lines). The considered mode combinations are grouped by linestyle according to their phase-matched wavelength.	66
4.4	Experimental characterization of the Stokes peak generated in nonlinear wave mixing process in a $62.5 \mu\text{m}$ core fiber pumped at $1.064 \mu\text{m}$ reveals different modal components at offset wavelengths [Reprinted with permission from Leventoux <i>et al.</i> , Opt. Lett. 46, 3717-3720 (2021). Copyright 2021 Optical Society of America].	67

4.5 Measured parameters of the fiber: (a) Refractive index profile measured at 0.632 μm (blue dots) and corresponding fit used for the numerical analysis (black line). (b) Measured attenuation (blue dots) and absorption spectrum of bulk silica (Suprasil F300) from Ref. [54] (dashed line) in the mid-IR. 68

4.6 Calculated mode damping (a), effective area (b), and effective refractive index (c) of the first three $\text{LP}_{0,p}$ modes of the GRIN fiber under study. Calculated effective group refractive index and corresponding inverse group velocity of the $\text{LP}_{0,1}$ mode (d). 69

4.7 (a) Phase mismatch $\Delta\beta$ calculated for the FWM process in the fundamental mode. (b) Experimental spectrum recorded at the output of a 70 cm-long fiber segment when the aforementioned FWM process in the fundamental mode is optimized. Insets: near-field images of the three spectral peaks (anti-Stokes, pump, and Stokes waves) captured using appropriate spectral filters. 71

4.8 Corresponding spectra of anti-Stokes (a), pump (b), and Stokes (c) waves recorded at the output of fiber segments of increasing lengths. In (a-b), the input beam launch conditions were kept unchanged. In (c), for each fiber length the launch conditions were adjusted to obtain the highest intensity of the Stokes peak. 72

4.9 (a) Experimental gain measurements for the anti-Stokes wave centred at 0.625 μm as a function of propagation distance z , obtained for peak powers in the fundamental mode equal to 51 kW (red and yellow) and 36 kW (blue) (with fitting curves in dashed lines as guides to the eye). Horizontal solid segments also indicate the cutback fiber lengths. (b and c) Theoretical gain calculations for the anti-Stokes (b) and Stokes (c) waves for 36 kW (blue) and 51 kW (orange) peak power. Black dashed line indicates the estimated fiber attenuation in this spectral region. (d) Theoretical gain calculations for the anti-Stokes and Stokes waves as a function of peak power. Dashed orange and blue lines indicate peak powers plotted in (b-c). 73

4.10 (a-e) Near-field images of the spectrally filtered peaks indicated by arrows and colored dashed lines. Left sections are experimental measurements, whereas right sections provide corresponding calculated mode distributions for a given wavelength. In panel (e), both calculated $\text{LP}_{0,1}$ and $\text{LP}_{0,2}$ modes are shown. Red line in right sections indicates the inner edge of the fluorine-doped trench. (f) Phase mismatch $\Delta\beta$ calculated for intra- and intermodal FWM processes - details provided in text. (g) Experimental spectrum recorded at the output of a 70 cm-long fiber segment with an average power of 29.8 mW when a cascaded FWM process is optimized. 75

- 4.11 Experimental spectrum for 23 mW average power recorded at the output of a meter-long segment of step-index fiber with a 15.5 μm core diameter with the light launching conditions optimized to excite the fundamental mode. Magenta lines indicate the Stokes and anti-Stokes wavelengths of the intramodal FWM process. Insets: near-field images of the selected peaks captured using appropriate spectral filters. 79
- 4.12 (a) Phase mismatch calculated for the FWM process in the fundamental mode (magenta) and for the FWM process with anti-Stokes in $\text{LP}_{0,1}$ and Stokes in $\text{LP}_{0,2}$ mode (black). (b) Experimental spectrum recorded at the output of a 80 cm-long, 62.5 μm core GRIN fiber for 23 mW average power coupled into the fiber with the light launching conditions optimized to excite the fundamental mode. 81
- 5.1 Examples of helicon wavepackets in a fused silica rod with radius $R = 100 \mu\text{m}$. (a,c) Quadric surfaces obtained in normal and anomalous dispersion regimes. Green dots indicate discretized conic sections for each p coordinate. Black circles correspond to the selected modes used for the linear construction of helicon wavepackets depicted in (b,d) through iso-surfaces of their spatiotemporal intensity pattern at half-maximum. The successive subplots obtained every $\pi/(2|K_l|)$ corroborate the invariant nature of helicon wavepackets over propagation. The dashed orange line indicates the origin ($x = 0, y = 0$). Projections on planes are provided for a clear observation of rotation [Adapted with permission from ACS Photonics 2022, 9, 6, 2066–2072. Copyright 2022 American Chemical Society]. . 85
- 5.2 Experimental setup for investigating helicon wavepackets in MMF and for recording near-field images and angularly-resolved far-field spectra of spontaneous conical emission from a multimode fiber and bulk glass. ND: neutral density filter; HWP: half-wave plate; P: polarizer; M: mirror; L: lens; MMF: multimode fiber; QWP: quarter-wave plate; VP: q plate; SF: spectral filter; BS: plate beamsplitter; OSA: optical spectrum analyzer. The insets show photographs of the output beam in the far field for a bulk BK7 glass plate and MMF. 89
- 5.3 Input beam (top row) and near-field images of the fiber end face in linear regime (bottom row) for different rotations of the QWP_2 axis. The locations for the beam profiler used to capture these images are shown in Fig. 5.2: in *Beam shaping* panel for input beam characterization, and in *Detection system A* panel for fiber output characterization. 90

5.4	Conical emission recorded at the output of a 5-mm-thick sapphire plate. (a) Output pattern in the far field projected on a screen and photographed using a phone camera. (b-e) False-color near-field images recorded with the use of bandpass spectral filters with different central wavelengths. (f) Measured angle-resolved far-field spectrum. Solid white line provides the corresponding phase-matching using relation of $\theta(\omega)$. (g) Total spectrum measured with a focusing lens L_4 before (blue line) and after (orange line) (time separation: 45 minutes) performing the angle-resolved spectral measurements. Yellow line: integration of angle-resolved far-field spectrum from panel (f).	92
5.5	Conical emission recorded at the output of a 14-mm-thick plate made of BK7 glass. (a) Measured angle-resolved far-field spectrum for a 1.86 μJ pulse energy. Solid lines provide the corresponding phase-matching. (b) Full spectrum collected with a focusing lens for different pulse energies. Inset: Output pattern for 1.85 μJ projected on a screen photographed using a phone camera.	94
5.6	Angle-resolved far-field spectrum of conical emission obtained at the output of a 5.8 cm-long step-index MMF. (a) Experimentally measured angle-resolved far-field spectrum. (b) Corresponding numerical simulation of angle-resolved far-field spectrum based on MM-UPPE model. Calculated angles take into account the refraction taking place at the fiber output. Note that the numerical spatial grid cannot provide details for very small values of θ	96
5.7	Mode-resolved spectrum of conical emission obtained at the output of a 5.8 cm-long step-index MMF. (a-g) False-color near-field images of the $\text{LP}_{0,p}$ higher-order modes involved in both X-like tails at specific wavelengths. Top panels: experimental captures with a CCD camera using bandpass spectral filters with indicated central wavelengths. Bottom panels: corresponding numerical fiber modes. (h) False-color map of the numerical mode-resolved spectrum. Colored crosses: spectral positions of the higher-order modes captured in subplots (a-g) according to the distinct bandpass spectral filters. White squares and dashed lines: theoretical phase-matching region of the discretized conical wave. Inset: Fiber output pattern projected on a screen photographed using a camera. . . .	97
5.8	Nonlinear propagation of 275-fs pulses (1.2 μJ energy at 1035 nm) in step-index MMF. (a-c) False-color map of temporal, spectral, and spatial power profiles as a function of propagation distance z . (d-g) Snapshots of temporal (d,f) and spectral (e,g) power profiles showing formation and evolution of the first, intense optical shock (d,e) and a following, less intense shock (f,g) and corresponding spectral broadening.	100
5.9	Evolution of the mode-resolved spectrum during propagation. Panels show false-color map of the numerical mode-resolved spectrum (in log. scale, dB units) calculated before (first column), during (second column), and after (third column) formation of optical shocks I-IV indicated in Fig. 5.8(a) at different propagation distances. Squares and dashed lines show theoretical phase-matching regions of the discretized conical waves corresponding to the subsequent optical shocks. . .	101

5.10	Stability of the fiber output pattern in two power regimes. Top panels: Stable fiber output pattern (snapshot every second) for $1.3\ \mu\text{J}$ pulse energy. Middle and bottom panels: Evolution of the fiber output pattern recorded over one second for a coupled pulse energy around $3\ \mu\text{J}$. The fiber output pattern is projected on a screen and recorded using a phone camera.	103
5.11	Measured output spectrum and near-field images of the fiber output as a function of the coupled pulse energy for the launched optical beam consisting of (a) a mix of $l = 1$ and $l = 0$ fields (b) a $l = 1$ field.	104
5.12	Experimentally measured angle-resolved far-field spectrum and near-field images of the fiber output captured using bandpass spectral filter. The pulse energy of the input $l = 1$ beam is $3.9\ \mu\text{J}$, and $2.9\ \mu\text{J}$ is measured at the output of the fiber.	105
5.13	Numerical simulation for $l = 1$, $3.0\ \mu\text{J}$ pulses launched into the step-index MMF. False-color map of temporal (a), spectral (b), and spatial (c) power as a function of the propagation distance. Inset shows a false-color beam intensity distribution at the fiber output. Mode-resolved spectrum (d) and calculated near-field spectrally-filtered beam intensity distributions (e) at the fiber output.	106
5.14	Numerical simulation for an equal mix of $l = 0$ and $l = 1$ $1.05\ \mu\text{J}$ pulses launched into the step-index MMF. False-color map of temporal (a), spectral (b), and spatial (c) power as a function of the propagation distance. Inset shows a false-color beam intensity distribution at the fiber output. Mode-resolved spectrum (d) and calculated near-field spectrally-filtered beam intensity distributions (e) at the fiber output.	107

Appendix A

Academic achievements

Publications

Journal publications related to the dissertation:

- [K. Stefańska](#), P. Béjot, J. Fatome, G. Millot, K. Tarnowski, B. Kibler, *High-gain far-detuned nonlinear frequency conversion in a few-mode graded-index optical fiber*, Scientific Reports, 2024, 10.1038/s41598-024-65873-w;
- [K. Stefańska](#), P. Béjot, K. Tarnowski, B. Kibler, *Experimental observation of the spontaneous emission of a space-time wavepacket in a multimode optical fiber*, ACS Photonics, vol. 10, 3, 2023, 10.1021/acsp Photonics.2c01863;
- [K. Stefańska](#), S. Majchrowska, K. Gemza, G. Soboń, J. Sotor, P. Mergo, K. Tarnowski, T. Martynkien, *Soliton trapping and orthogonal Raman scattering in a birefringent photonic crystal fiber*, Optics Letters, vol. 47, 16, 2022, 10.1364/OL.463643;

Journal publications unrelated to the dissertation:

- O. Szewczyk, K. L. Tarnowski, A. K. Głuszek, D. Szulc, [K. Stefańska](#), P. Mergo, G. J. Soboń, *All-normal dispersion supercontinuum vs frequency-shifted solitons pumped at 1560 nm as seed sources for thulium-doped fiber amplifiers*, Optics Express, vol. 29, 12, 2021, 10.1364/OE.430292;
- B. R. Szczupak, J. Olszewski, M. Mądry, P. Pala, [K. Stefańska](#), G. Statkiewicz-Barabach, *The influence of germanium concentration in the fiber core on temperature sensitivity in Rayleigh scattering-based OFDR*, IEEE Sensors Journal, vol. 21, 18, 2021, 10.1109/JSEN.2021.3095550.

Publications in conference proceedings related to the dissertation:

- [K. Stefańska](#), P. Béjot, K. Tarnowski, B. Kibler, *Experimental observation of discretized conical wave in a multimode fiber*, European Optical Society Annual Meeting, Dijon, France, 2023, 10.1051/epjconf/202328711010;
- [K. Stefańska](#), P. Béjot, J. Fatome, G. Millot, K. Tarnowski, B. Kibler, *Mid-infrared generation beyond 3.5 μm in a graded-index silica fiber*, European Optical Society Annual Meeting, Dijon, France, 2023, 10.1051/epjconf/202328706026;
- [K. Stefańska](#), P. Béjot, J. Fatome, G. Millot, K. Tarnowski, B. Kibler, *Far-detuned frequency conversion beyond 3500 nm in a few-mode graded-index silica fiber*, IEEE Photonics Society Summer Topicals Meeting Series, Sicily, Italy, 2023, 10.1109/SUM57928.2023.10224428;

-
- [K. Stefańska](#), P. Béjot, K. Tarnowski, B. Kibler, *Discretized X-wave in a multimode optical fiber*, SPIE Photonics Europe, Strasbourg, France, 2022, 10.1117/12.2620978;
 - [K. Stefańska](#), P. Béjot, K. Tarnowski, B. Kibler, *Discretized X-wave in a multimode optical fiber*, *Frontiers in Optics + Laser Science*, online, 2021, 10.1364/FIO.2021.JTu1A.19;
 - [K. Stefańska](#), S. Majchrowska, K. Gemza, T. Martynkien, P. Mergo, K. Tarnowski, *Polarization conversion of solitons propagating in birefringent microstructured optical fibers*, *OSA Nonlinear Optics*, online, 2021, 10.1364/NLO.2021.NTu2A.7.

Publications in conference proceedings unrelated to the dissertation:

- A. Rampur, D.-M. Spangenberg, G. Stepniewski, D. Dobrakowski, K. Tarnowski, [K. Stefańska](#), A. Pazdzior, P. Mergo, T. Martynkien, T. Feurer, M. Klimczak, A. M. Heidt, *Temporal fine structure of all-normal dispersion fiber supercontinuum*, Conference on Lasers and Electro-Optics Europe & European Quantum Electronics Conference, Munich, Germany, 2021, 10.1109/CLEO/Europe-EQEC52157.2021.9542292.

Patents

- K. Dybka, M. Pietryna, M. Biduś, M. Dłubek, M. Dyrkacz, [K. Stefańska](#), T. Martynkien, G. Soboń, J. Sotor, O. Szewczyk, P. Mergo, M. Makara, *Pasywny nieliniowy modul światłowodowy / Passive nonlinear fiber optic module*, PL441719, 2024.

Participation in research projects

- Project *Nonlinear pulse propagation in multimode fibers: Experiments with spatiotemporal light and fiber characterizations* funded by the Bourse du Gouvernement Français;
- STER Programme Internationalisation of Wroclaw University of Science and Technology Doctoral School funded by the Polish National Agency for Academic Exchange;
- *Zjawiska nieliniowe w światłowodach wielomodowych - solitony wielomodowe i konwersja częstotliwości*, project Sonata Bis funded by the Polish National Science Center, Principal Investigator: dr hab. Karol Tarnowski;
- French-Polish Polonium Hubert Curien Partnership *Far-detuned frequency conversion in multimode fibers* funded by the French Ministry for Europe and Foreign Affairs, French Ministry for Higher Education and Research, and Polish National Agency for Academic Exchange;
- French-Polish Polonium Hubert Curien Partnership *Nonlinear light propagation in multimode fibers* funded by the French Ministry for Europe and Foreign Affairs, French Ministry for Higher Education and Research, and Polish National Agency for Academic Exchange.

Conference presentations

- Presentation *Towards spontaneous helicon wavepacket generation in multimode optical fibers*, Slovak-Czech-Polish Optical Conference, scheduled for 02-06.09.2024, Štrbské Pleso, Slovakia
- Presentation *Mid-infrared generation beyond 3.5 μm in a graded-index silica fiber*, European Optical Society Annual Meeting, 11-15.09.2023, Dijon, France
- Presentation *Experimental observation of discretized conical wave in a multimode fiber*, European Optical Society Annual Meeting, 11-15.09.2023, Dijon, France
- Invited presentation *Far-detuned frequency conversion beyond 3500 nm in a few-mode graded-index silica fiber*, Multimode Nonlinear Photonics IEEE SUM, 17-19.07.2023, Giardini Naxos, Italy
- Presentation *Daleka konwersja częstotliwości w kilkumodowym światłowodzie gradientowym*, Polish Optical Conference, 04-07.07.2023, Toruń, Poland
- Presentation *Observation of soliton trapping in microstructured optical fibers with different group birefringence*, Polish-Slovak-Czech Optical Conference, 05-09.09.2022, Wojanów, Poland
- Presentation *Discretized X-Wave in a Multimode Optical Fiber*, SPIE Photonics Europe, 03-07.04.2022, Strasbourg, France
- Poster *Discretized X-Wave in a Multimode Optical Fiber*, Frontiers in Optics, 01-04.11.2021, online
- Presentation *Polarization conversion of solitons propagating in birefringent microstructured optical fibers*, OSA Nonlinear Optics 2021, 9-13.08.2021, online
- Presentation *Pomiar interferometryczny dyspersji międzymodowej w światłowodzie mikrostrukturalnym o wysokiej dwójłomności*, Ogólnopolska Fizyczno-Optyczna Konferencja FOKA, 11-13.12.2020, Wrocław, Poland

Active participation in workshops and schools

- Poster *High-gain far-detuned FWM in graded-index fiber*, Multimode-Multichannel Guided Photonics Workshop organized by Laboratoire PhLAM and Institut Langevin, 14-15.05.2024, Villeneuve-d'Ascq, France
- Poster *Discretized conical wave and helicon wavepackets in multimode fibers*, Multimode-Multichannel Guided Photonics Workshop organized by Laboratoire PhLAM and Institut Langevin, 14-15.05.2024, Villeneuve-d'Ascq, France
- Poster *Space-time wavepackets in optical fibers: discretized conical emission in a multimode fiber*, School on Nonlinear optics in fibers and in integrated optics, 22-28.10.2023, Cargèse, France
- Poster *Soliton Trapping in Birefringent Photonic Crystal Fibers*, Siegmán International School on Lasers organized by Optica and Dublin City University, 18-24.06.2023, Dublin, Ireland
- Poster *Discretized Conical Wave in a Multimode Optical Fiber*, Siegmán International

School on Lasers organized by Optica and University of Warsaw, 25.06-02.07.2022, Chęciny, Poland

- Presentation *Discretized conical wave in a multimode optical fiber*, Multimode Photonics Workshop organized by Sapienza Università di Roma, 22-25.08.2022, Rome, Italy